INTERNATIONAL DOCTORAL
SCHOOL OF THE USC

Sara
Leardini

PhD Thesis

New detection concepts in noble-element TPCs

Santiago de Compostela, 2024

Doctoral Programme in Nuclear and Particles Physics

ESCOLA DE DOUTORAMENTO
INTERNACIONAL DA USC

DOCTORAL THESIS

NEW DETECTION CONCEPTS IN NOBLE-ELEMENT TPCS

Author

Sara Leardini

Supervisor/s: Diego González Díaz, Shikma Bressler

Tutor: Diego González Díaz

PHD PROGRAMME IN NUCLEAR AND PARTICLES PHYSICS

SANTIAGO DE COMPOSTELA

2024

ללילה 🐱

USC
UNIVERSIDADE
DE SANTIAGO
DE COMPOSTELA

Contents

Resumen **1**

Resumo **3**

Summary **5**

Objectives and Methodology **7**

Introduction **11**

I State of the art **13**

1 Physics of neutrinos **15**
1.1 The problem of neutrino mass 16
1.2 Neutrinoless double beta decay 19
1.3 Neutrino mixing matrix 22
1.4 Neutrino scatterings 25

2 Scintillation in gases **27**
2.1 Interaction of particles with matter 28
2.1.1 Charged particles 28
2.1.2 Neutral massive particles 28
2.1.3 Photons 29
2.2 Generic scintillation concepts in noble gases 29
2.3 Primary scintillation 31
2.3.1 First continuum 31
2.3.2 Second continuum 32
2.3.3 Third continuum 33
2.3.4 Infrared continuum 34
2.4 Secondary scintillation 35
2.4.1 Electroluminescence 35
2.4.2 Electroluminescence from electron avalanches 36

USC UNIVERSIDADE DE SANTIAGO DE COMPOSTELA

2.4.3 Neutral bremsstrahlung . . . 37
2.4.4 Electron drift in noble gases . . . 37
2.5 Gas mixtures with noble gases . . . 38
2.6 Scintillation in liquid . . . 40

3 Gas discharge physics 41
3.1 Useful general concepts . . . 41
3.1.1 Townsend mechanism . . . 42
3.1.2 Streamer discharges . . . 45
3.2 Applied cases . . . 47
3.2.1 Low pressure . . . 47
3.2.2 Long gaps . . . 49
3.2.3 Breakdown phenomena in gaseous detectors . . . 50

4 Time Projection Chambers 55
4.1 The TPC concept . . . 55
4.2 Amplification structures . . . 58
4.2.1 Wires . . . 58
4.2.2 MPGDs . . . 60
4.3 Readout techniques . . . 62
4.3.1 Electronic readout . . . 62
4.3.2 Optical readout . . . 64
4.4 Experiments . . . 66
4.4.1 DUNE . . . 66
4.4.2 NEXT . . . 71

5 Challenges in TPCs 73
5.1 Electroluminescence in gas . . . 73
5.2 Detection of noble gas scintillation . . . 75
5.3 Dual-phase TPC gas-liquid interface . . . 78
5.4 Charge multiplication in liquid phase . . . 80
5.5 Sparks inside the detector . . . 81

II Part II 87

6 Resistive materials for spark quenching 89
6.1 RWELL . . . 90
6.1.1 Characterization of DLCs . . . 90
6.1.2 Operation in a detector . . . 102

USC UNIVERSIDADE DE SANTIAGO DE COMPOSTELA

6.2 RPWELL 118
6.2.1 Characterization of Fe_2O_3/YSZ ceramics 118
6.2.2 Operation in a detector 131

7 Bubble-assisted LHMs **137**
7.1 Equilibrium of the gas bubble under a THGEM-electrode hole: theory 139
7.2 Observation of captive bubbles in liquid Argon 144
7.3 Numerical simulations of the bubble electrodynamics 148
7.4 Experimental validations by X-ray micro-CT 150
7.4.1 Validation of the bubble hydrostatics in water and in silicone oil 150
7.4.2 Validation of the bubble electrodynamics in silicone oil 151
7.5 Conclusions 153

8 Ar/CF_4 secondary scintillation **157**
8.1 Experimental setup 157
8.2 Data taking and analysis 159
8.3 Results 161
8.3.1 Spectra at different concentrations 161
8.3.2 Charge and optical gain 162
8.4 Discussion and conclusions 165

9 FAT-GEMs for electroluminescence **169**
9.1 PMMA-based FAT-GEMs 171
9.1.1 Fabrication process 171
9.1.2 Radiopurity 173
9.1.3 Working principle 174
9.1.4 Setup 174
9.1.5 Data taking and analysis 177
9.1.6 Simulations 178
9.1.7 Results for untreated FAT-GEMs 180
9.1.8 Results for TPB-coated FAT-GEMs 182
9.1.9 Discussion 185
9.1.10 Conclusions 187
9.2 PEN-based FAT-GEMs 190
9.2.1 Concept and possible configurations 190
9.2.2 Production 192
9.2.3 Expected light collection performance 194

USC UNIVERSIDADE DE SANTIAGO DE COMPOSTELA

9.2.4 High voltage tests and validation in xenon gas 197
9.2.5 Conclusions 198

Results and Conclusions **201**

Bibliography **204**

List of publications **237**

Permission of content reuse **245**

Resumo **263**

USC UNIVERSIDADE DE SANTIAGO DE COMPOSTELA

Resumen

El campo de las búsquedas de eventos raros puede contar con un gran aliado: la Cámara de Proyección Temporal (TPC). Introducida por D. Nygren en los años 70, fue posteriormente desarrollada en diferentes versiones (de fase dual, gaseosa a alta presión, de fase líquida única...). A pesar de todos los avances tecnológicos que ya han ocurrido, las TPCs aún deben adaptarse a requisitos cada vez más estrictos, ya que los experimentos requieren cada vez más sensibilidad. Esto implica un esfuerzo continuo de investigación y desarrollo, que también ha impulsado este trabajo. En particular, esta tesis propone algunas soluciones prácticas a problemas comunes encontrados en las TPCs: se mostrarán el desarrollo de dos materiales resistivos ajustables capaces de proporcionar protección contra chispas en condiciones criogénicas, junto con los resultados de su funcionamiento en un detector a 90 K; posteriormente, se tratará un aspecto particular de un concepto local de fase dual (LHMs asistidos por burbujas), es decir, la dinámica de las bolsas de gas debajo de la estructura de multiplicación; la tesis continuará con un estudio de la centelleo secundario de mezclas de Ar/CF4, relevante, entre otros, para TPCs de alta presión, como la propuesta para el detector DUNE NDGAr; finalmente, se presentará la caracterización de estructuras gruesas y fácilmente escalables (FATGEMs) para electroluminiscencia con rendimientos de luz y resoluciones energéticas competitivos.

USC
UNIVERSIDADE DE SANTIAGO DE COMPOSTELA

USC
UNIVERSIDADE
DE SANTIAGO
DE COMPOSTELA

Resumo

O campo das buscas de eventos raros pode contar cun gran aliado: a Cámara de Proxección Temporal (TPC). Introducida por D. Nygren nos anos 70, foi posteriormente desenvolvida en diferentes versións (de fase dual, gasosa a alta presión, de fase líquida única...). A pesar de todos os avances tecnolóxicos que xa aconteceron, as TPCs aínda teñen que adaptarse a requisitos cada vez máis esixentes, xa que os experimentos precisan cada vez máis sensibilidade. Isto implica un esforzo continuo de investigación e desenvolvemento, que tamén impulsou este traballo. En particular, esta tese propón algunhas solucións prácticas a problemas comúns atopados nas TPCs: mostrarase o desenvolvemento de dous materiais resistivos axustables capaces de proporcionar protección contra faíscas en condicións crióxenicas, xunto cos resultados do seu funcionamento nun detector a 90 K; posteriormente, tratarase un aspecto particular dun concepto local de fase dual (LHMs asistidos por burbullas), é dicir, a dinámica das bolsas de gas debaixo da estrutura de multiplicación; a tese continuará cun estudo da centelleo secundario de mesturas de Ar/CF4, relevante, entre outros, para TPCs de alta presión, como a proposta para o detector DUNE NDGAr; finalmente, presentarase a caracterización de estruturas grosas e facilmente escalables (FATGEMs) para electroluminiscencia con rendementos de luz e resolucións enerxéticas competitivos.

USC
UNIVERSIDADE DE SANTIAGO DE COMPOSTELA

USC
UNIVERSIDADE
DE SANTIAGO
DE COMPOSTELA

Summary

The field of Rare Event Searches can count on a great ally: the Time Projection Chamber (TPC). Introduced by D. Nygren in the 70s, it was subsequently developed into different versions (dual-phase, gaseous with high pressure, liquid single-phase...). Despite all the technological advancements which already occurred, TPCs still have to adapt to more and more stringent requirements, as the experiments need more and more sensitivity. This implies a continuous R&D effort, which has driven this work, too. In particular, this thesis proposes some practical solutions to common problems encountered in TPCs: the development of two tunable resistive materials capable of spark protection in cryogenic conditions will be shown, together with results of their operation in a detector at 90 K; afterwards, a particular aspect of a local dual-phase concept (bubble-assisted LHMs) will be treated, that is, the dynamics of the gas pockets underneath the multiplication structure; the thesis will continue with a study of secondary scintillation of Ar/CF_4 mixtures, relevant, among others, for high pressure TPCs such as the one proposed for the DUNE NDGAr detector; finally, the characterization of easily scalable, thick structures (FATGEMs) for electroluminescence with competitive light yields and energy resolutions will be presented.

USC
UNIVERSIDADE DE SANTIAGO DE COMPOSTELA

USC
UNIVERSIDADE
DE SANTIAGO
DE COMPOSTELA

Objectives and Methodology

The objective of this thesis is to provide proposals that address some typical problems encountered in noble-element TPCs. In particular, it will focus on spark protection for detectors operating in cryogenic conditions, a local dual-phase configuration that overcomes the interface problem, the study of a gas mixture able to wavelength-shift the VUV light of argon into visible light while keeping adequate quenching, and the characterization of a structure optimized for electroluminescence in gaseous TPCs. In particular:

- Spark protection: detectors operating in high voltage conditions may suffer from sparks, which may make its operation unstable or even damage them. A known solution at room temperature is to resort to resistive materials that provide protection from sparks; for this purpose, the material must possess the right resistivity (in a range of 10-10^4 MΩ/sq for resistive foils, 10^9-10^{12} $\Omega \cdot$ cm for resistive plates). In this work, analogue materials suitable for cryogenic operation (especially in liquid argon, at 90 K) were searched for; the focus was on two materials: diamond-like carbon (DLC) and Fe_2O_3/YSZ ceramics. The characteristics of DLC were investigated through the use of a physical property measuring system (PPMS) from Quantum Design, and of a home-made cryostat in helium atmosphere, connected to a picoammeter for resistivity measurements and to a PT100 sensor for temperature monitoring, and immersed in a nitrogen bath. Ceramic plates were measured through the picoammeter and the PT100 in direct contact with the nitrogen bath. The suitable samples were then tested inside a detector, WISArD, located at the Weizmann Institute of Science, in the so-called RWELL configuration (for DLC) and RPWELL configuration (for ceramics), in which the resistive material is sandwiched between the amplification structure (in this case, a THGEM) and the readout anode. The measurements were performed at 90 K, in saturated argon vapor, ensuring purity through continuous circulation of the argon through a hot getter. The analysis of the materials characterization and of the test inside the detector was performed with dedicated Python scripts.

- Local dual-phase: at the moment, the gas-liquid interface of dual-

USC UNIVERSIDADE DE SANTIAGO DE COMPOSTELA

phase TPCs is very challenging to control; for this reason, alternatives such as the bubble-assisted liquid hole multipliers (LHM) were proposed. This concept exploits a local dual phase, consisting of a gas bubble trapped underneath the amplification structure (typically a THGEM). Tests performed previously to this work on the bubble-assisted LHM yielded a lower photon detection efficiency than expected. This could have depended on the equilibrium point of the gas-liquid interface: in fact, if the gas were not filling the hole, the electrons could have benefitted less from the high-field region to produce electroluminescence. For this reason, a study on the dynamics of the bubble was performed: a model based on hydrostatic and electrodynamic equations was developed, simulated in COMSOL, and validated through μCT imaging. To get the equilibrium points for the bubble with this model, the contact angle is necessary: my contribution to this work was to measure the contact angles of the liquid-gas interface of argon with different materials, including copper and FR4, of which the THGEMs are made of. For this, the measurements were taken inside the WISArD detector at the Weizmann Institute of Science: slabs of different materials were immersed in liquid argon, and bubbles were created underneath them through heating wires or spontaneous bubbling. Pictures of 200 bubbles (400 contact angles) were taken through a viewport and processed through a Python script; the contact angle was then extracted by using a plugin of ImageJ, called DropSnake; finally, the angle distribution was histogrammed and fitted in MATLAB.

- Gaseous wavelength-shifting: mixing a noble gas to a molecular additive can reduce diffusion, and stabilize the detector operation through quenching the gas/absorbing VUV photons. However, some additives may make the S1 signal disappear, losing information about the time of interaction. Ar/CF_4 mixtures are able to keep the S1 information, by wavelength-shifting the VUV light of noble gases to visible light, much easier to detect with common light sensors. In order to better understand the emission of Ar/CF_4 mixtures, a spectroscopic study of the secondary scintillation was performed at the GDD laboratory at CERN: a setup with parallel plate electrodes was irradiated with an x-ray gun under different conditions in terms of CF_4 concentration, gas pressure and electric field. A collimating lens and an optical fiber directed the light into a CCD spectrometer, previously calibrated through a visible and a UV lamp of known spectra. The current at the anode was monitored through a picoammeter. The data were subsequently processed through Python scripts.

- Structures for electroluminescence: at the moment, the main tools

USC UNIVERSIDADE DE SANTIAGO DE COMPOSTELA

used to obtain electroluminescence in the gas phase are meshes or wires, able to provide excellent energy resolution and sensitivity to single electrons. However, it is challenging to scale this kind of structures, which could be a complication in big-size experiments. For this reason, a new easily-scalable, thick perforated structure, called FAT-GEM, was conceived. In this work, different versions of this structure were characterized, among which i) a version optimized for secondary scintillation, provided with a reflector on the cathode side and TPB, a wavelength shifter, inside the holes, and ii) a version developed also for S1 detection, fully transparent and with a bulk made of PEN, also able to wavelength-shift the VUV light. To characterize the structures in terms of energy resolution and light yield, a setup equipped with a ^{55}Fe source placed on the cathode plane was employed. The vessel was filled with xenon or argon gas at different pressures, and the light collected through a PMT-preamplifier-amplifier-MCA chain. The PMT was previously calibrated with a green LED and a MATLAB script. The rest of the data was analyzed by means of Python scripts.

The experiments, unless otherwise specified, were conducted at the USC.

USC
UNIVERSIDADE DE SANTIAGO DE COMPOSTELA

USC
UNIVERSIDADE
DE SANTIAGO
DE COMPOSTELA

Introduction

The search for new particles has always had to grow hand-in-hand with technological development. Long time has passed since the first cloud chambers, which allowed to discover particles that are relatively easy to detect, such as positrons [1] and muons [2]. These devices relied on visual images of particle tracks formed by ionized particles interacting with the medium; while innovative for their time, cloud chambers had inherent limitations in speed and resolution, prompting a search for more effective detection methods.

The advent of electronic detectors marked a revolutionary shift in the field, transitioning from visual to charge-based detection systems. This innovation allowed for the rapid and precise measurement of particle interactions, significantly enhancing the capabilities of experimental physics. Various technologies emerged, including wire chambers and drift chambers, precursors of the Time Projection Chamber (TPC), a pivotal invention that combines spatial resolution with three-dimensional tracking capabilities, revolutionizing the way experiments are conducted in high-energy physics.

In recent years, the focus of particle physics research has shifted towards the discovery of rare events, such as those associated with dark matter or neutrino interactions. This shift requires the development of new technologies capable of supporting larger and more sensitive TPCs. As the search for elusive phenomena intensifies, researchers are revisiting optical detection methods, exploiting new advanced imaging techniques.

Regardless of the choice of readout medium, building such experiments is extremely challenging, and requires a huge R&D effort. The purpose of this work is to address some common problems encountered in TPCs, such as sparks in the detector, handling of the gas-liquid interface in dual-phase TPCs, detection of VUV light and producing electroluminescence with big-scale amplification structures.

This thesis is divided as follows. The first part (chapters 1-5) contains the state-of-the-art of the current knowledge relevant to TPCs. In Chapter

USC UNIVERSIDADE DE SANTIAGO DE COMPOSTELA

1 a brief description of neutrino physics is provided, as neutrino detection is one of the main targets of Rare Event searches. In Chapter 2 the scintillation in noble elements (in gaseous and liquid phase) is discussed, as argon and xenon, pure or in mixtures, are among the most common media in TPCs. In Chapter 3 gas discharge physics is presented, a field that includes fascinating phenomena such as lightnings and kirlian photographs, but also events that are potentially destructive for a detector. Chapter 4 describes TPCs in detail, delving into the amplification structures available and the readout techniques (electronic and optical). Chapter 5, finally, explains some of the common problems that can appear in TPCs. I hope that this part will be clear and enjoyable [3] for future students beginning their path in detector development.
The second part (chapters 6-9) shows the proposed solutions to some of these problems: spark protection for detectors operating in cryogenic conditions (Chapter 6), a local dual- phase configuration that overcomes the interface problem (Chapter 7), the study of a gas mixture able to wavelength-shift the VUV light of argon into visible light while keeping adequate quenching (Chapter 8), and the characterization of a structure optimized for electroluminescence in gaseous TPCs (Chapter 9).
This second part, mostly reproduced from published papers, comes from efforts of all the co-authors, to which I address all my gratitude, as this PhD work would have not be possible without them, both at professional and personal level.

USC UNIVERSIDADE DE SANTIAGO DE COMPOSTELA

Part I

State of the art

USC
UNIVERSIDADE DE SANTIAGO DE COMPOSTELA

USC
UNIVERSIDADE
DE SANTIAGO
DE COMPOSTELA

Physics of neutrinos

1

Neutrinos are elusive particles detected for the first time in the 1950s, decades after their existence was hypothesised to explain the continuous energy spectrum of electrons produced through beta decay: if it were a two-body decay, the electron should have had a fixed energy. However, finding the solution to the puzzle was not easy, in that neutrinos do not interact neither through electromagnetic nor strong force. Even after their discovery, they never stopped surprising: they unexpectedly turned out having a mass, forcing researchers to think how to adapt the Standard Model of particle physics to the new fact; this is not enough, however, since both the nature of such mass and the mass hierarchy of the various neutrinos are at present unknown. Moreover, learning how to detect the cosmic neutrino background (analogous to the cosmic microwave background) could provide information about the universe when it was only one second old! Finally, many believe that neutrinos hold the key to explain why in the universe there is more matter than antimatter: if the charge-parity (CP) symmetry was violated strongly enough by neutrinos, an equal initial amount of matter and antimatter could have lead to the current prevalence of matter.
This chapter will describe the place of neutrinos in the standard model, why they have a mass and what the nature of their mass could be; thereafter, it will describe how the nature of neutrino masses and other parameters regarding neutrino physics are experimentally determined, ending with a short description of neutrino scatterings with nuclei.

USC
UNIVERSIDADE DE SANTIAGO DE COMPOSTELA

1.1 The problem of neutrino mass

The Standard Model of particle physics successfully describes the fundamental particles that constitute (anti)matter and their interactions. The particles included in this model are six quarks, six leptons (charged leptons and neutrinos), the gauge bosons (mediators of the fundamental forces), and the Higgs boson (Fig. 1.1).

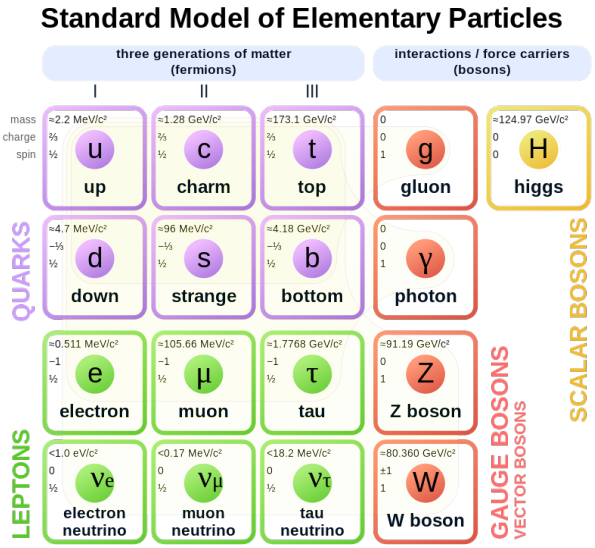

Figure 1.1: Particles that make up the standard model of particle physics. The neutrinos are leptons (hence, fermions) and come in three known generations: electron, muon and tau neutrinos. Image by MissMJ, from [4].

Particles in the Standard Model acquire mass through a Yukawa interaction with the Higgs field; for example, the Yukawa interaction for electrons reads:

$$\mathcal{L}_{Yukawa} = f_e \bar{l}_L \Phi e_R + h.c. \tag{1.1}$$

where f_e is the coupling constant, $\bar{l}_L = \begin{bmatrix} \nu_L \\ e_L \end{bmatrix} \gamma^0$ is the leptonic doublet with left chirality (times the Dirac matrix γ^0), Φ is the Higgs field, and e_R is the electron singlet with right chirality.
Analogous terms can be written for quarks and heavier generations of electrons; neutrinos, on the other hand, are assumed to be massless in the Standard Model.
Experiments in the last decades demonstrated, however, that neutrinos os-

USC UNIVERSIDADE DE SANTIAGO DE COMPOSTELA

cillate [5, 6, 7], that is, they change their flavour along their path. This is not possible, unless neutrino do actually have mass. In fact, the probability of transition between one flavor and another in vacuum reads

$$P(\nu_l \to \nu_{l'}) = \mid \sum_{j=1}^{3} U^*_{l'j} e^{-iE_j t} U_{lj} \mid =$$

$$\delta_{ll'} - 2\sum_{j>k} \Re(U^*_{l'j} U_{l'k} U_{lj} U^*_{lk})(1 - \cos(\frac{\Delta m^2_{kj} L}{2E})) + \tag{1.2}$$

$$+2\sum_{j>k} \Im(U^*_{l'j} U_{l'k} U_{lj} U^*_{lk}) \sin(\frac{\Delta m^2_{kj} L}{2E})$$

(with U being the mixing matrix, E the energy and L the length of the path of the neutrino, and the indexes j, k referring to the three known mass eigenstates $\nu_{1,2,3}$). From eq. 1.2 it is clear that there must be a mass difference between one mass eigenstate and another for oscillations to take place; in particular, at least two mass eigenstates must have $m > 0$ to explain the observed oscillations.

In principle, one could write a mass term for neutrinos in the same way as eq. 1.1; this would require, however, introducing a neutrino with right chirality, which does not interact with the other particles of the standard model neither through strong nor electroweak forces, therefore it cannot be detected. Besides this, eq. 1.1 only contains the so-called Dirac term, which is the only term allowed for electrically charged particles; the most general mass term, however, can include a Majorana term, too. If the neutrinos would be Majorana particles, a left-handed chiral state would be enough to describe the process of acquiring mass, being $\Psi_R = C\bar{\Psi}^T_L = \Psi^C_L$ (Ψ^C is the charge conjugate field of Ψ). The implications of neutrinos being Majorana particles are that they would be their own antiparticle, and that neutrinoless double beta decay would be possible.

The nature of the neutrino mass, as already mentioned, is not the only puzzling question that the discovery of oscillations posed. In fact, at the moment only the differences between the three mass values are known, but not their absolute magnitude[1]:

$$\Delta m^2_{2,1} = 7.37^{-0.16}_{+0.16} \cdot 10^{-5} eV^2 \tag{1.3}$$

$$\Delta m^2_{3,1} = 2.562^{-0.030}_{+0.043} \cdot 10^{-3} eV^2 \tag{1.4}$$

or

$$\Delta m^2_{2,3} = 2.545^{-0.032}_{+0.034} \cdot 10^{-3} eV^2 \tag{1.5}$$

[1] Values in eq. 1.3-1.5 from [8]

USC UNIVERSIDADE DE SANTIAGO DE COMPOSTELA

Moreover, as one can grasp from eq. 1.3-1.5, while for $\Delta m^2_{2,1}$ it was established that m_1 is smaller than m_2, it is still a mystery whether m_3 is the biggest or the smallest of the three masses: in the former case, the mass hierarchy is called *normal* (NH, eq. 1.4 holds), in the latter, it is called *inverted* (IH, eq. 1.5 holds); the two possibilities are depicted in Fig. 1.2.

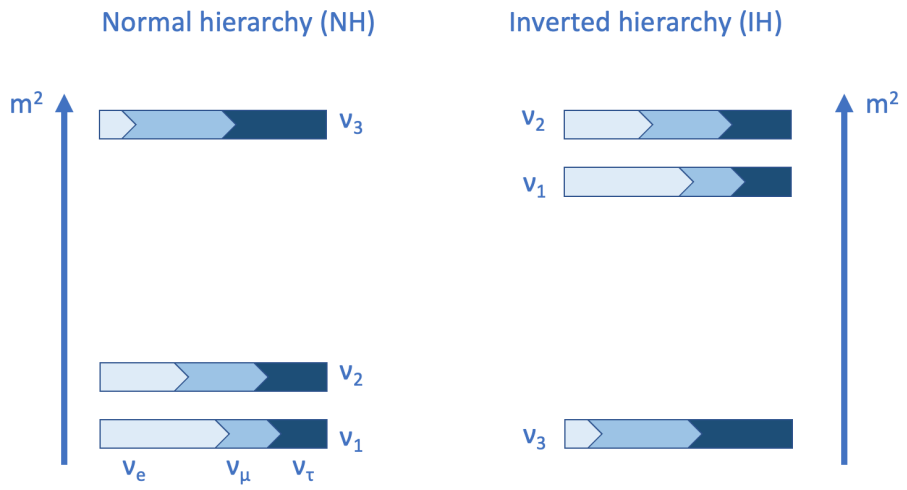

Figure 1.2: The three mass eigenstates of neutrino may have two different mass orderings: ν_3 could be the heaviest neutrino (normal hierarchy, on the left) or the lightest (inverted hierarchy, on the right). The sign of the mass difference between ν_1 and ν_2 has already been constrained by measurements of solar neutrinos.

When a global analysis of oscillation data from various experiments probing the neutrino mass ordering is performed (more in Sec. 1.3), a preference towards the normal hierarchy (2.7σ [9]) is found. It must be also mentioned that cosmological data from the Planck collaboration [10] pose a constraint over the total mass of neutrinos: $\sum m_\nu < 0.12$ eV; considering that $\sum m_\nu \sim 0.1$ eV for the inverted hierarchy (while it is smaller, $\sum m_\nu \sim 0.06$ eV for the normal hierarchy), should the boundaries from cosmology become even tighter, they may rule it out[2] (Fig. 1.3). Following a different approach from cosmology and oscillation experiments, KATRIN collaboration is attempting to measure directly the mass of electron antineutrinos below the eV scale [11].

[2]Of course, the inverted hierarchy could as well be the right one and the cosmological limit is now extremely close to the expected value for $\sum m_\nu$!

USC UNIVERSIDADE DE SANTIAGO DE COMPOSTELA

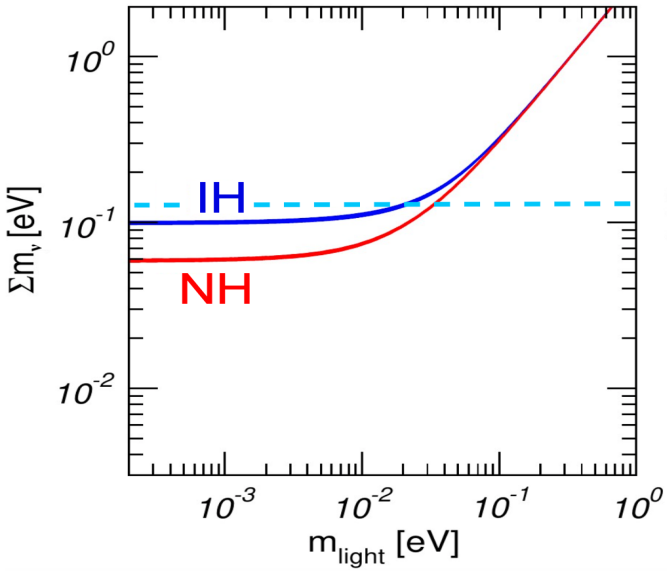

Figure 1.3: Regions at 2σ resulting from the global analysis of oscillation data from the last NuFIT plots (V5.2, [9, 12]). Superimposed to the NuFIT plot, the dashed light-blue line shows the cosmological limit from [10].

1.2 Neutrinoless double beta decay

Double beta decay is a nuclear process in which two neutrons in the same atomic nucleus undergo beta decay at the same time. In ordinary two-neutrino double beta decay ($2\nu\beta\beta$), the final products of the decay would be an atom with $Z_f = Z_i + 2$, two electrons and two anti-neutrinos; if neutrinos were Majorana particles, however, the two neutrinos could annihilate, emitting only the two electrons (Fig. 1.4). It is clear that this process would violate the lepton number by two units.
In general, double beta decay can occur in atoms whose number of protons and neutrons are both even: the odd-odd configuration after a simple beta decay would be less bound, thus a double beta decay is energetically favoured [13] (fig 1.5). Two-neutrino double beta decay were observed in ^{48}Ca [14], ^{76}Ge [15], ^{82}Se [16], ^{96}Zr [17], ^{100}Mo [18], ^{116}Cd [19], ^{128}Te [20], ^{130}Te [21], ^{136}Xe [22], ^{150}Nd [23], and ^{238}U [24]. Defining $Q_{\beta\beta}$ as the amount of energy released in the double beta decay, if two neutrinos are emitted the electrons can acquire an arbitrary amount of this energy up to $Q_{\beta\beta}$. In the case of neutrinoless double beta decay, a sharp peak at the value $Q_{\beta\beta}$ should be observed (fig 1.6).

USC UNIVERSIDADE DE SANTIAGO DE COMPOSTELA

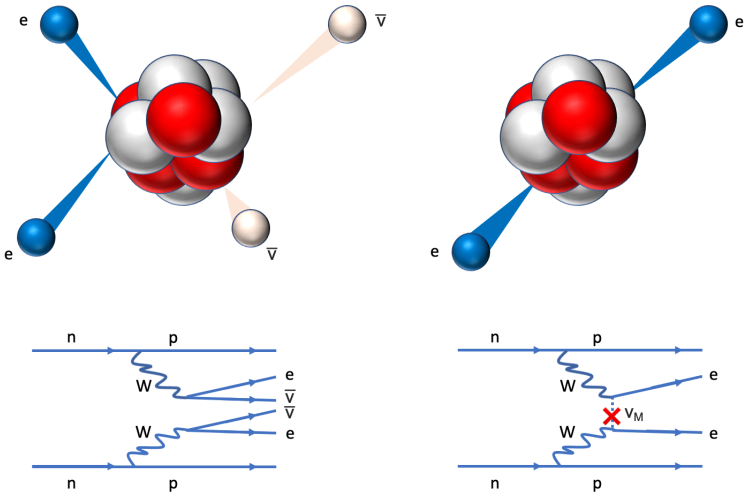

Figure 1.4: Depiction of a two-neutrino double beta decay (top left) and of a neutrinoless double beta decay (top right), with the corresponding Feynman diagrams (bottom left and right, respectively).

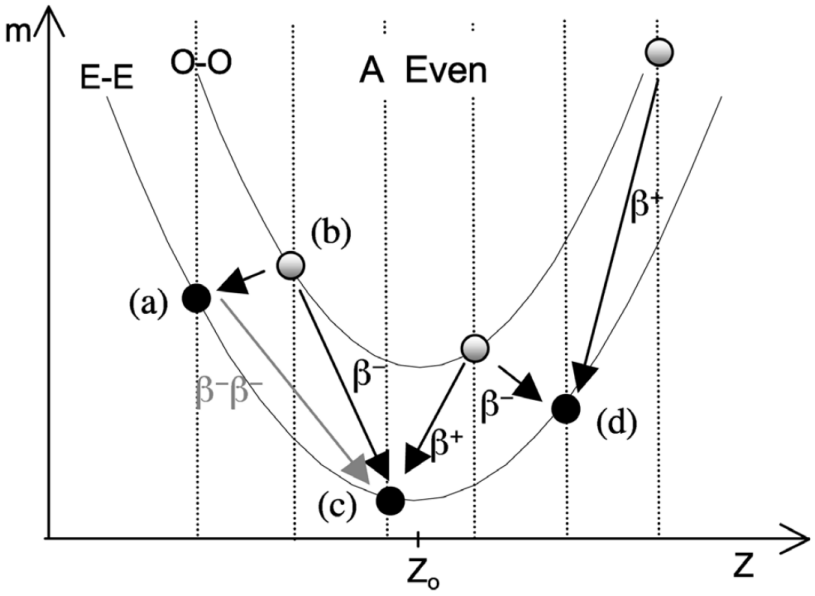

Figure 1.5: Ground state mass parabola for isobaric nuclei with A even. The odd-odd proton-neutron pairs (open circles) have higher mass than even-even pairs (black circles) due to the nuclear pairing energy, which gives more bound configurations for nucleons of the same kind. Image from [25].

The neutrinoless double beta decay half life is given by

USC UNIVERSIDADE DE SANTIAGO DE COMPOSTELA

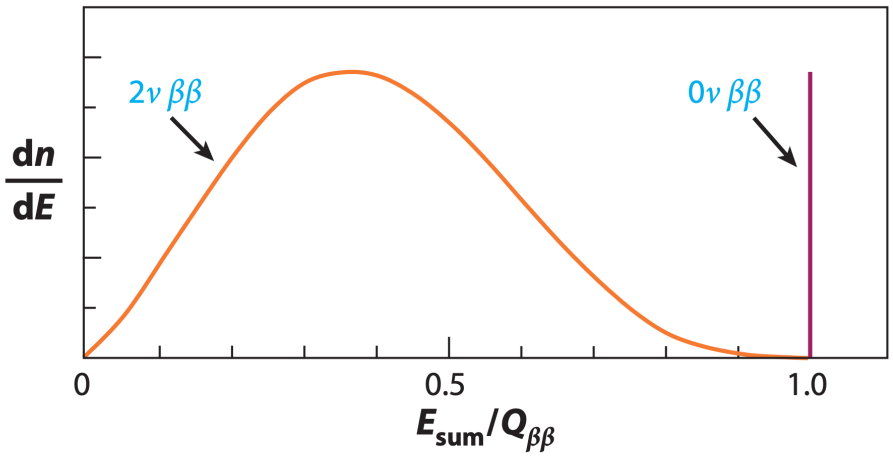

Figure 1.6: Energy spectrum of electrons emitted in a double beta decay. In orange is the energy spectrum from a two-neutrino double beta decay: the energy is shared between electrons and neutrinos, hence the energy of electrons can take any value from zero to $Q_{\beta\beta}$; in purple is the energy spectrum of electrons for neutrinoless double beta decay: all the energy goes into electrons, hence the value is always $Q_{\beta\beta}$. Image from [13].

$$\frac{1}{\tau^{0\nu}_{1/2}} = G^{0\nu}|M^{0\nu}|^2(\frac{m_{ee}}{m_e}) \tag{1.6}$$

where $G^{0\nu}$ is a phase space factor, $M^{0\nu}$ is the nuclear matrix element[3]:

$$|M^{0\nu}|^2 = |<\phi_f|\hat{O}^{0\nu\beta\beta}|\phi_i>|^2, \tag{1.7}$$

and m_{ee} is the effective Majorana mass of ν_e:

$$m_{ee} = |\sum_i U^2_{ei} m_{\nu_i}|. \tag{1.8}$$

From the values of the mixing matrix U (it will be described in detail in section 1.3), it results that the sum in eq. 1.8 will be greater if the correct neutrino mass hierarchy is inverted, and smaller if it is normal, implying a half life in the range $10^{26} - 10^{27}$ years for the former case, $\gtrsim 10^{28}$ years for the latter (fig 1.7).

[3]Here $\hat{O}^{0\nu\beta\beta}$ is the transition operator between the initial and final state (ϕ_i and ϕ_f, respectively) of the process.

USC UNIVERSIDADE DE SANTIAGO DE COMPOSTELA

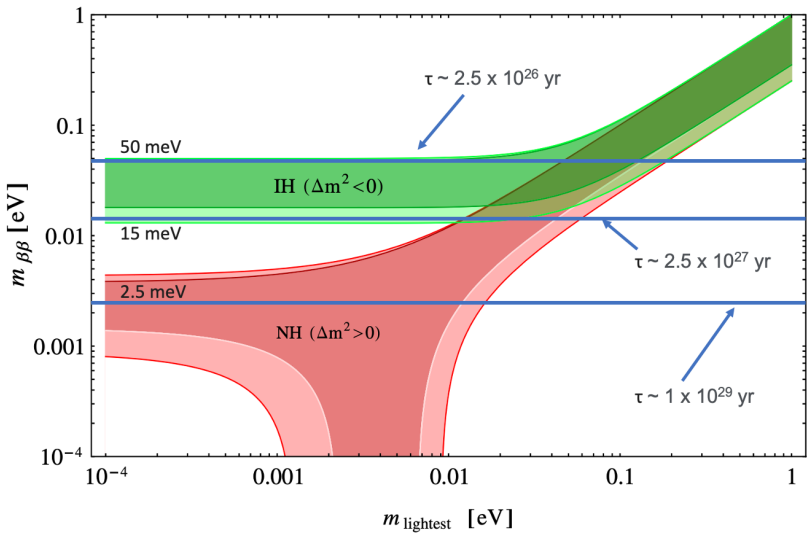

Figure 1.7: Possible values of m_{ee} as a function of the mass of the lightest neutrinos, in the case of normal hierarchy of neutrino masses (pink band) or inverted hierarchy (green band), from [26]. The blue lines (from [27]) indicate the corresponding value of $\tau^{0\nu}_{1/2}$ considering ^{100}Mo as a target.

Several experiments are currently looking for neutrinoless double beta decays: among those, NEMO (^{100}Mo), KamLAND-ZEN, nEXO, NEXT (^{136}Xe), CUORE (^{130}Te), estabilishing a lower limit for $\tau^{0\nu}_{1/2}$ of $\sim 10^{27}$ years. It must be noted that current experiments are sensitive only to the inverted hierarchy of neutrino masses. The future generation of experiments aims at extending sensitivity in order to explore normal hierarchy, too.

1.3 Neutrino mixing matrix

In the previous sections, the so-called *mixing matrix* has been mentioned multiple times. The mixing matrix, also called Pontecorvo-Maki-Nakagawa-Sakata (PMNS) matrix, takes this form in case neutrinos are Dirac particles:

USC UNIVERSIDADE DE SANTIAGO DE COMPOSTELA

$$U = \begin{pmatrix} U_{e1} & U_{e2} & U_{e3} \\ U_{\mu 1} & U_{\mu 2} & U_{\mu 3} \\ U_{\tau 1} & U_{\tau 2} & U_{\tau 3} \end{pmatrix} =$$
$$\begin{pmatrix} 1 & 0 & 0 \\ 0 & \cos\theta_{23} & \sin\theta_{23} \\ 0 & -\sin\theta_{23} & \cos\theta_{23} \end{pmatrix} \begin{pmatrix} \cos\theta_{13} & 0 & \sin\theta_{13}e^{-i\delta} \\ 0 & 1 & 0 \\ -\sin\theta_{13}e^{i\delta} & 0 & \cos\theta_{13} \end{pmatrix} \begin{pmatrix} \cos\theta_{12} & \sin\theta_{12} & 0 \\ -\sin\theta_{12} & \cos\theta_{12} & 0 \\ 0 & 0 & 1 \end{pmatrix}. \quad (1.9)$$

The matrix contains three mixing angles ($\theta_{12}, \theta_{13}, \theta_{23}$) and a CP violation phase (δ, from now denoted as δ_{CP}). If neutrinos are Majorana particles, U should be multiplied by the diagonal matrix $diag(e^{i\alpha}, e^{i\beta}, 1)$, which contains two additional CP violation phases.
All the parameters appearing in the matrix are not given by theory, but have to be measured. The sources of neutrinos employed are the nuclear reactions (mainly the p-p chain) happening inside the Sun, the interactions of cosmic rays with the Earth's atmosphere, the nuclear fission reactors on Earth, and particle accelerators[4]. Depending on the position of the detector with respect to the neutrino source, one may need to take into account the effect of matter on the neutrino oscillations and modify accordingly eq. 1.2, which holds in vacuum [28, 29]; the effect of matter is particularly relevant for long baseline accelerator experiments, for atmospheric neutrinos detected after crossing the whole Earth, and for solar neutrinos when traveling inside the Sun core (Fig. 1.8).
Here is how the three angles and the Dirac phase are determined experimentally:

1. For the mixing angle θ_{12}, solar neutrino experiments (like SNO [30] and Borexino [31]) play a pivotal role in the determination of its value. In fact, the electron neutrinos produced by nuclear reactions in the Sun are mainly composed of ν_1 (see Fig. 1.2); measuring the discrepancy between the number of electrons neutrinos that are measured and the one expected by the solar model allows to obtain θ_{12}.

2. The mixing angle θ_{23} mainly governs the oscillations between muon neutrinos and tau neutrinos. Atmospheric neutrino experiments (e.g. Icecube [32] and Super-Kamiokande [33]) have been key in measuring θ_{23}. Long baseline neutrino experiments such as NOvA [34] and T2K [35] (conducted through production of neutrinos in an accelerator) also contributed to the measurement of θ_{23}.

[4]There are other neutrino sources, such as supernovae or the Earth's core (geoneutrinos), but they are typically detected to study the source itself and not to extract neutrino parameters.

USC UNIVERSIDADE DE SANTIAGO DE COMPOSTELA

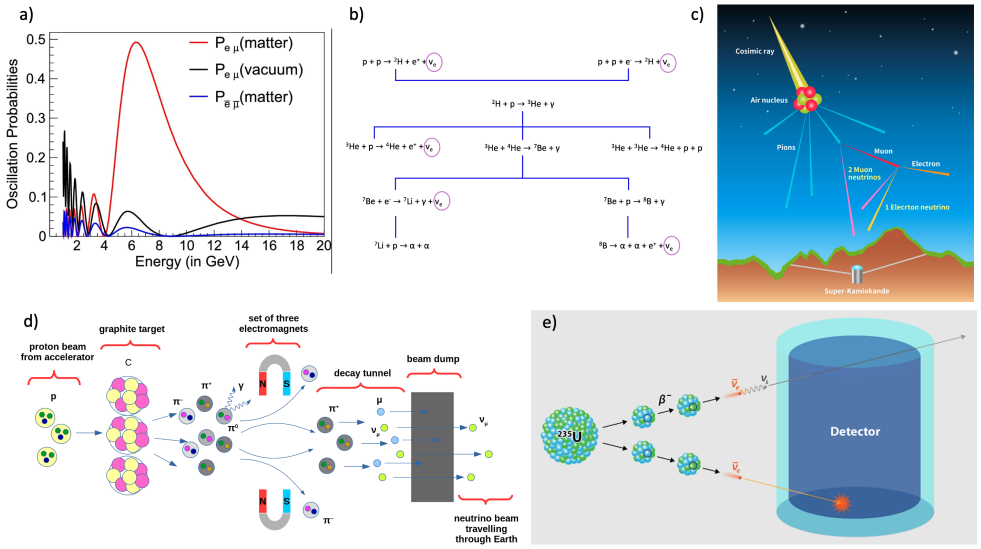

Figure 1.8: a): example of effect of matter on the oscillation probability of atmospheric neutrinos: the probability is strongly enhanced in matter (red line) with respect to vacuum (black line) over a path L = 8000 km for $\sim 4 - 12$ GeV neutrinos (from [36]).
b): p-p fusion chain, the main nuclear process happening inside the Sun, which leads to the production of one or two electron neutrinos.
c): production of atmospheric neutrinos through the interaction of a cosmic proton/alpha particle with the air: a subsequent hadronic shower leads to the decay of charged pions into muons and muon antineutrinos (or antimuons and muon neutrinos); the muons in turn decay into an electron, an electron antineutrino, and a muon neutrino. As final result, there will be muon (anti)neutrinos and electron (anti)neutrinos in ratio 2:1 (image by Kamioka Observatory, ICRR (Institute for Cosmic Ray Research, The University of Tokyo [37]).
d): production of accelerator neutrinos; the process is similar to the one occurring in the atmosphere, in that proton colliding generate pions that can decay into muons and muon antineutrinos (or antimuons and muon neutrinos). However, in this case a beam of only neutrinos (or only antineutrinos) can be created by deflecting the pions through suitable magnets (image by Batmann, [38]).
e): production of reactor neutrinos: the fission of ^{235}U generates radioactive species which undergo β^- decay. As a result, electron antineutrinos are emitted (image by APS/Alan Stonebraker [39]).

3. The mixing angle θ_{13} is mainly determined with reactor neutrino experiments which are placed close to the nuclear plant, such as Daya Bay [40] and RENO [41].

4. In the context of neutrino oscillations, CP violation manifests as a difference (more precisely, a shift) in the oscillation probabilities between neutrinos and antineutrinos; δ_{CP} quantifies this asymmetry. It is currently measured by long baseline experiments (and to a lesser extent with atmospheric neutrinos), by looking at the transitions $\nu_\mu \rightarrow \nu_e$ and $\bar{\nu}_\mu \rightarrow \bar{\nu}_e$.

USC UNIVERSIDADE DE SANTIAGO DE COMPOSTELA

The data from the many experiments (of which I have cited only some examples) have been fitted all together by using both bayesian and frequentist analysis [42]. The results of the global fit, including Δm^2_{21} and $|\Delta m^2_{31}|$ are shown in Fig. 1.9: a mixing angle $\theta_{13}(< 9^o) << \theta_{12}, \theta_{23}(\sim 49^o)$ emerges from the analysis, together with a strong preference for CP violation.

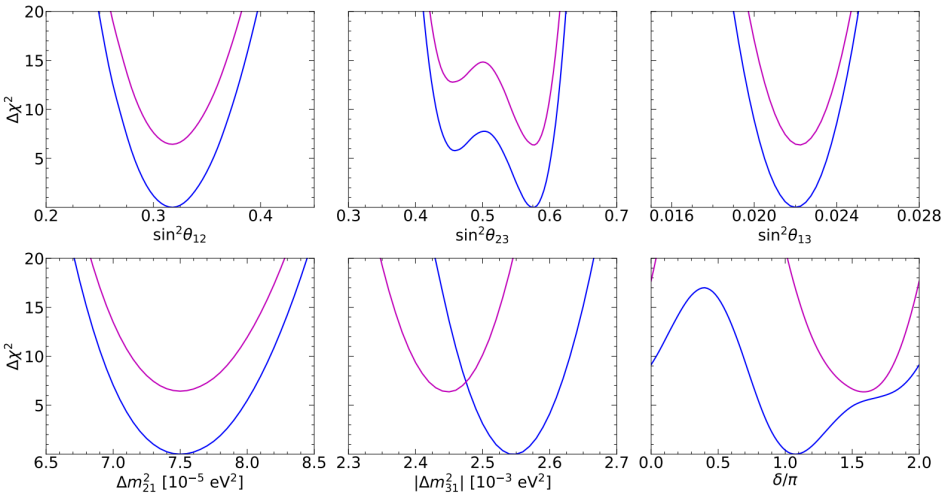

Figure 1.9: Results of the global fit for the neutrino oscillation parameters [42]; the blue line refers to the normal hierarchy, the magenta line to the inverted hierarchy.

A last interesting fact to mention in this quest is the presence of some anomalies detected by short-baseline experiments [43] with accelerator neutrinos and by reactor neutrinos, respectively. The first one is a statistically significant excess of ν_e appearance at sub-GeV scale; the latter is a deficit of electron antineutrinos measured close to the reactor (L $<$ 2 km). An additional anomaly, called *gallium anomaly*, is reported by experiments exploiting beta decay of ^{71}Ga [44]; also in this case, less $\bar{\nu}_e$ than expected are measured.

1.4 Neutrino scatterings

So far, it has not been mentioned how neutrinos interact with the rest of matter, so for the sake of completeness here follow a few words about it. As said, neutrinos don't feel the electromagnetic and the strong force: they only interact through the weak force (and well, of course through gravity). At first approximation, the interactions can be divided into charge current (CC) and neutral current (NC) interactions: in CC interactions, a neutrino

USC UNIVERSIDADE DE SANTIAGO DE COMPOSTELA

interacts with a particle through the exchange of a W boson, the result of the reaction being the charged lepton with the same flavour as the neutrino plus other particles; NC interactions involve the exchange of a Z boson between the neutrino and the target particle, without changing the flavor of the neutrino. Zooming into the different energies that neutrinos can have when interacting with the nucleus of a detector's atom, a finer subdivision can be made:

1. At $\geq$ TeV scale, we have deep inelastic scattering (Fig. 1.10 a). A high-energy neutrino interacts with a quark inside a nucleon via the exchange of a W boson or a Z boson. The interaction transfers energy and momentum from the neutrino to the quark. The struck quark will produce a hadronic jet, resulting with the nucleon completely broken up.

2. At MeV-GeV scale, according to the specific energy, there can be inelastic scattering, including resonances (Fig. 1.10 b), in which the nucleon is left unaltered, but new particles are also produced (e.g. pions), and quasi-elastic scattering (Fig. 1.10 c), in which the exchange of W boson leaves the target nucleon intact with minimal changes (that is, if it was a neutron, it will turn into a proton and vice versa).

3. At $\sim$ keV scale, coherent elastic scattering occurs (Fig. 1.10 d): the neutrino interacts with the entire nucleus of the atom, which recoils as a whole, through NC. For the low energies involved, this scattering was detected only in 2017 [45].

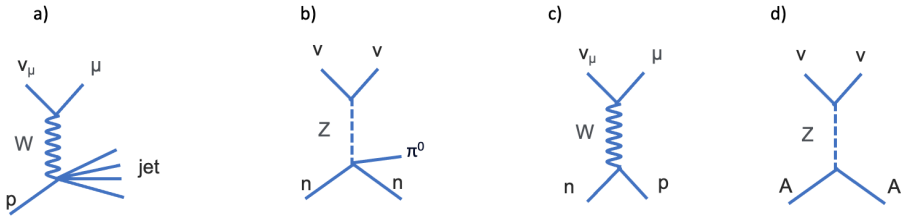

Figure 1.10: Examples of neutrino scatterings with the nuclei/nucleons of the atoms of a potential detector: a) deep inelastic scattering, b) resonance, c) quasi elastic scattering, d) coherent elastic scattering. In the NC interactions the flavor of the neutrinos is not specified, as any would work, as far as it is conserved. The diagrams shown are not the exhaustive list of all processes that could lead to scatterings a-d. Moreover, scatterings of neutrinos with atomic electrons are not shown.

USC UNIVERSIDADE DE SANTIAGO DE COMPOSTELA

2 Scintillation in gases

When it comes to detecting particles, a natural choice for the detector material is represented by noble elements (except radon, no one wants to use that). The reasons are manifold, starting from the high transparency to their own excimer emission, the high scintillation yield, and the possibility of cleaning them to high purity levels thanks to their low reactivity. In particular, xenon and argon are the most used noble elements in particle physics, alone or in mixtures: xenon is more sensitive to nuclear recoils thanks to the heavier nucleus, has no natural isotope with problematic decay time, and has a longer-wavelength spectrum, which is easier to detect. On the other hand, argon is cheaper, and elastic nuclear interactions with low-mass particles are easier to detect since it is a lighter atom; the issue with the natural isotope ^{39}Ar, which constitutes a troublesome source of background, could be sorted out by resorting to underground Ar, with an additional chemical purification [46]. To make good use of these elements and extract physical information out of their interaction with the particles of interest, it is of paramount importance to understand their scintillation mechanisms, which will be described in this chapter: first of all, a brief generic description of the interaction of different particles with matter will be provided. Thereafter, the primary and secondary scintillation of pure noble gases will be described, ending with gas mixtures and the behavior of scintillation in the liquid phase.

USC UNIVERSIDADE DE SANTIAGO DE COMPOSTELA

2.1 Interaction of particles with matter

When a particle interacts with a medium, it will lose energy through various mechanisms, depending on its own energy and on which kind of particle it is. On a first approximation, the incident particles could be classified into charged particles, neutral massive particles, and photons.

2.1.1 Charged particles

A charged particle will lose an average amount of energy per unit length in a medium according to the Bethe Bloch formula:

$$\frac{-dE}{dx} = 2\pi N_a r_e^2 m_e c^2 \rho \frac{Z}{A}\frac{z^2}{\beta^2}[\ln \frac{2m_e\gamma^2\beta^2c^2W_M}{I^2} - \beta^2 - \delta - 2\frac{C}{Z}] \qquad (2.1)$$

where, in order of appearance, N_a is the Avogadro number, r_e the classical electron radius, m_e the electron mass, ρ the medium density, Z and A the atomic number and atomic mass of the medium, z, β and γ the charge and the relativistic factors of the incident particle, W_M the maximum energy transfer in a single collision, I the mean excitation potential, and finally δ and C correction factors that become relevant for light (relativistic) particles or low energy particles, respectively.
It is important to remember that the Bethe Bloch formula provides a mean energy loss; for each $\beta\gamma$ value, the energy loss actually follows a non-symmetrical distribution displaying a long tail towards high energies (Landau-like distribution, Fig. 2.1).

Looking at the Bethe Bloch curve, it is apparent that as a minimum ionizing particle deposits energy in the medium, hence losing momentum, the energy loss per unit length will increase considerably, leading eventually to the particle to be stopped in the medium (Fig. 2.2 left). The high energy deposition at the end of the trajectory is called Bragg peak.

2.1.2 Neutral massive particles

Interactions of neutrinos with matter were already described in Section 1.4; unlike neutrinos, which interact via the weak nuclear force, neutrons interact through the strong nuclear force, making them far more likely to interact with matter, particularly with atomic nuclei. The interactions range from

USC UNIVERSIDADE DE SANTIAGO DE COMPOSTELA

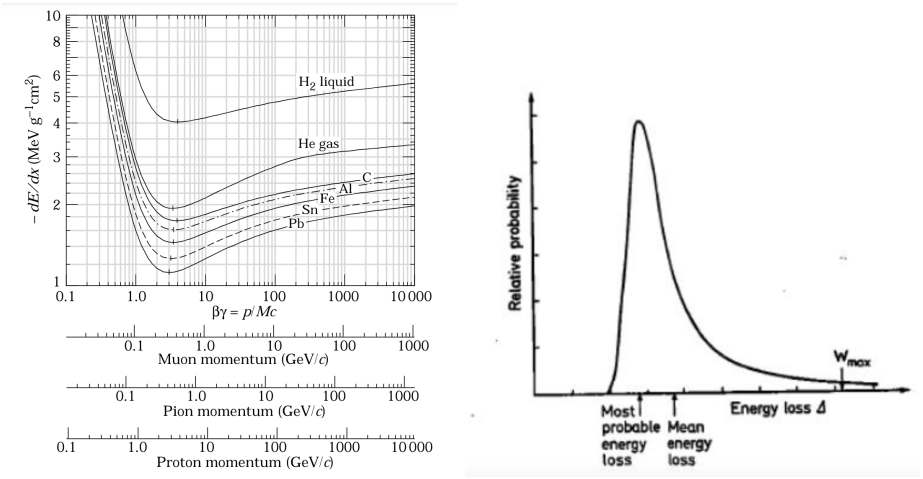

Figure 2.1: Left: Bethe Bloch formula for different particles and media. The particles whose energy corresponds to the minimum of the curve are called Minimum Ionizing Particles (MIPs). Image from [47]. Right: Landau-like distribution that describes the energy loss for a particle at a fixed $\beta\gamma$, skewed towards high energy losses (from [48]).

elastic scattering with nuclei, at low energies, to hadronic showers at the highest energies.

2.1.3 Photons

According to its energy, the photon will interact with matter in different ways (Fig. 2.2 right): at the lowest energies, it will excite the material's atoms, managing eventually to ionize the medium when its energy is big enough (photoelectric effect); at intermediate energies, Compton scattering will become relevant. Finally, when the photon energy reaches twice the electron mass, pair production can take place.

2.2 Generic scintillation concepts in noble gases

When a particle interacts with the noble element of a gaseous detector, it leads to excitation and ionization of the medium. The prompt de-excitation and recombination of the medium yields the so-called primary scintillation (S1); if the ionization electrons (called *primary electrons*, since they stem directly from the interaction of the particle with the gas volume) are drifted with an electric field into a high electric field region, they can in turn excite/ionize the medium, producing secondary scintillation (S2). The energy needed to produce a photon/electron is given respectively by the W_{sc} and

USC UNIVERSIDADE DE SANTIAGO DE COMPOSTELA

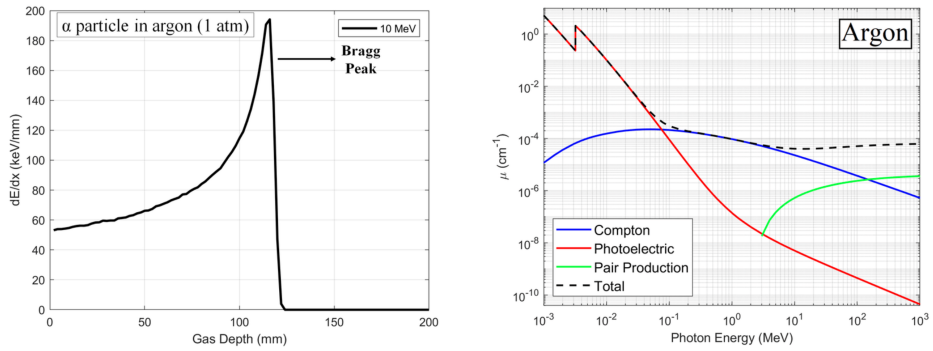

Figure 2.2: Left: Bragg peak of a 10 MeV alpha particle in argon: the particle is fully stopped after crossing 120 mm of gas at 1 bar. Right: Interaction of photons with argon gas as a function of the photon energy. Both images from [49].

W_I parameters[1], which have in general convoluted dependencies and must be determined experimentally for each gas and particle type.
The emission spectrum is also peculiar: given the typical high pressure of the detector ($\gtrsim$100 mbar!), the result of the S1 and S2 scintillation is not the spectrum with atomic lines typically studied in quantum mechanics courses; in fact, the phenomenon is dominated by the energy transfers between the gas atoms, that can form excited dimers (*excimers*):

$$NG^* + NG + NG \rightarrow NG_2^* + NG \tag{2.2}$$

The emission of these excimers depends on the distance between the two atoms involved[2], leading to the formation of *continua* instead of individual lines (Fig. 2.3, right). The primary and secondary scintillation will display different features, in that for S1 the excited states, formed directly by the incoming particle, are almost uniformly distributed; the excited states of secondary scintillation, on the other hand, are produced by low energy ionization electrons, populating mostly the least energetic states as a consequence (Fig. 2.3, left).

[1] Or by it inverse, the yield (photons/MeV or electrons/MeV).
[2] That is, whether the excimer is weakly or strongly bound, and whether it is fully vibrationally-relaxed or not.

USC UNIVERSIDADE DE SANTIAGO DE COMPOSTELA

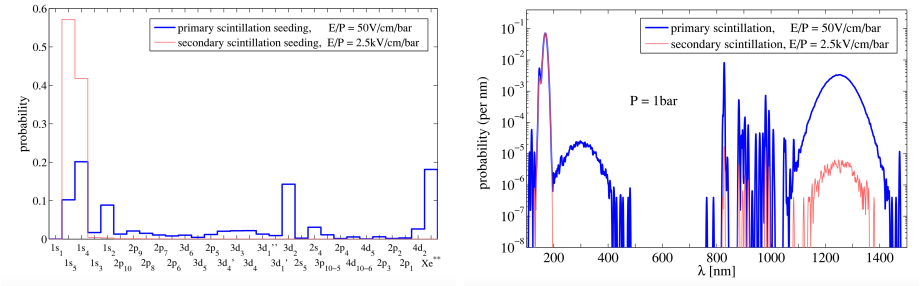

Figure 2.3: Left: simulated distribution of excited states for primary scintillation (blue) and secondary scintillation (red) in xenon. Right: with the same color code, the different continua of xenon are showed; residuals of the first continuum at $\sim$ 145 nm, the second continuum centered at 172 nm, the third continuum peaked at $\sim$ 300 nm, and the infrared continuum at wavelengths $\lambda > 1000$ nm. Some infrared atomic lines are also present between 800 and 1000 nm. The lack of the third continuum for the secondary scintillation is a consequence of the population of low-energy states only, as it will be explained in the following sessions. Images from [50].

2.3 Primary scintillation

2.3.1 First continuum

It is formed through the transition from weakly bound excimers (and/or high lying vibrational states) of the noble gas excimer:

$$NG^*(s_4) + NG + NG \rightarrow NG_2^*(0_u^+) + NG$$

(weakly bound excimer formation)

$$NG_2^*(0_u^+) \rightarrow NG + NG + h\nu$$

(first continuum),

or

$$NG^*(s_5) + NG + NG \rightarrow NG_2^*(1_u/0_u^-) + NG$$

(weakly bound excimer formation)

$$NG_2^*(1_u/0_u^-) \rightarrow NG + NG + h\nu$$

(first continuum).

USC UNIVERSIDADE DE SANTIAGO DE COMPOSTELA

At high pressure (some 100's mbar) these states tend to form strongly bound and fully relaxed excimers [51], that yield a highly universal emission spectra, characterised by the shape of the potentials of the excimer and ground state dimer (second continuum).

2.3.2 Second continuum

The second continuum is the main scintillation mechanism in typical detector conditions (i.e., at pressures higher than 100 mbar in case of gas and at even higher densities in case of liquid or solid phases). Analogously to the first continuum, it originates from the $NG_2^*(0_u^+)$ and $NG_2^*(1_u/0_u^-)$ states, which in this case are vibrationally relaxed [52]:

$$NG_2^*(0_u^+) + NG \rightarrow NG_2^*(^1\Sigma_u(v)) + NG$$

(excimer binding)

$$NG_2^*(^1\Sigma_u(v)) + NG \rightarrow NG_2^*(^1\Sigma_u(v=0)) + NG$$

(excimer cooling)

$$NG_2^*(^1\Sigma_u(v=0)) + NG \rightarrow NG_2(^1\Sigma_g) + NG + h\nu$$

(second continuum)

or

$$NG_2^*(1_u/0_u^-) + NG \rightarrow NG_2^*(^3\Sigma_u(v)) + NG$$

(excimer binding)

$$NG_2^*(^3\Sigma_u(v)) + NG \rightarrow NG_2^*(^3\Sigma_u(v=0)) + NG$$

(excimer cooling)

$$NG_2^*(^3\Sigma_u(v=0)) + NG \rightarrow NG_2(^1\Sigma_g) + NG + h\nu$$

(second continuum),

USC UNIVERSIDADE DE SANTIAGO DE COMPOSTELA

where $^1\Sigma_u$ and $^3\Sigma_u$ are called, respectively, singlet and triplet excimer states, and exhibit different decay times τ (Table 2.1), the singlet decay time being considerably faster than the triplet.

Gas	Singlet (ns)	Triplet (ns)
Argon [53]	4-5	3000
Krypton [54]	3.6	265
Xenon [50]	4.5	100

Table 2.1: Compilation of decay times for the second continuum singlet (fast component) and triplet (slow component) in some noble gases.

Recombination

At high density (high pressure or low temperature, or in condensed phases) and low electric fields, charge recombination plays an important role for the primary scintillation, especially for highly ionizing particles such as α particles or heavier nuclei [55, 56]. In gas, the light from recombination appears as a long tail in the primary scintillation pulse, reaching a considerable contribution (even 50% of the total primary light!) at low fields (Fig. 2.4 b). Fig. 2.4 (a) shows how the contribution from recombination varies with pressure. On the other hand, the contribution from lower ionization particles such as electrons from beta decays is negligible even at zero field and pressures as high as 10 bar (Fig. 2.4 c).

2.3.3 Third continuum

The third continuum emission stems from species and pathways that are not entirely understood yet, which anyway require more energy than the second continuum precursors to be produced (this is why it is typically not observed for the secondary scintillation); some processes that lead to this emission were proposed for example in [59, 60, 53], involving states like NG_n^{+*}, or NG_n^{++}, with $n = 2, 3$. Third continuum emission was investigated especially in xenon, krypton and argon [61, 62, 53, 57, 63], finding a fast decay time (from 5 to 9 ns, depending on the gas) and no dependence from electric field, meaning that recombination is not affecting the third continuum. A ratio $3^{rd}/2^{nd}$ continuum $\sim 20\%$ was reported for argon at 1.5 bar, while for xenon the contribution of third continuum is more modest ($< 10\%$). During my PhD I have contributed on a time and band resolved study [57] of xenon

USC UNIVERSIDADE DE SANTIAGO DE COMPOSTELA

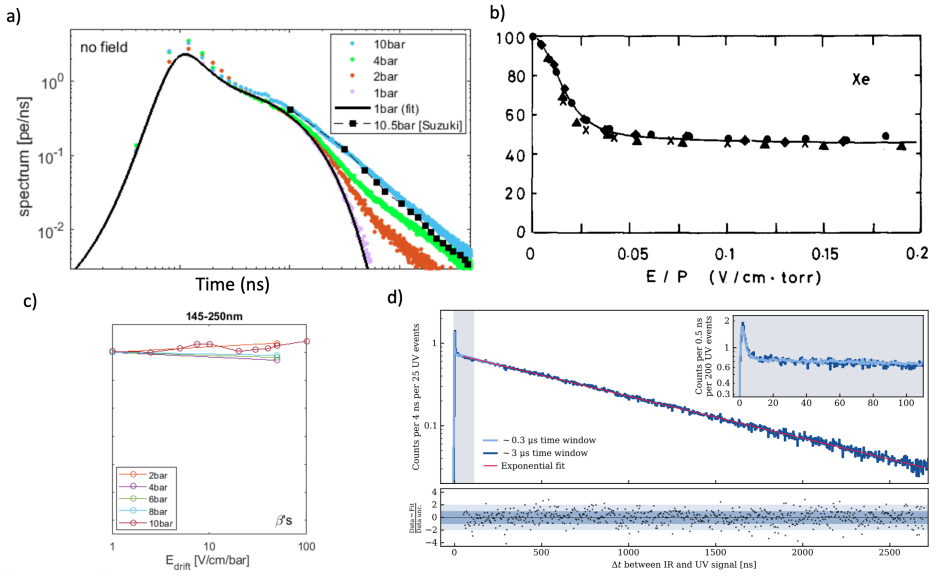

Figure 2.4: a): contribution from recombination as a function of pressure in xenon, when no electric field is applied. The contribution from recombination becomes more relevant at high pressure, in that the higher density makes recombination more likely to happen (from [57]). b): the light from recombination can reach even 50% of the total primary light when no electric field is applied; the example in xenon is taken from [55]. c): no recombination with beta particles is observed in xenon, as expected (from [57]). d): tail with a long decay time observed in the infrared; it is unlikely that it is due to recombination, as it does not disappear by increasing the electric field (from [58]).

scintillation, with a focus on the third continuum, but the results will not be presented more deeply in this thesis.

2.3.4 Infrared continuum

The continuum in the near infrared, observed for the case of xenon, is believed to be the result of the excimer state $C0_u^+$ (associated to the high-lying atomic $2p^5$ level) decaying to $A0_g^+$ [64] (which will later emit in the second continuum). The subsequent emission in the second continuum of the $A0_g^+$ state should pose an upper limit on the infrared decay time of 2 ns for xenon; however, recent studies [65, 58] observed a long tail ($O(\mu s)$) in the infrared emission which is yet to be explained (Fig. 2.4 d).

USC UNIVERSIDADE DE SANTIAGO DE COMPOSTELA

2.4 Secondary scintillation

It has been already mentioned in the previous section that applying an electric field diminishes the contribution of recombination. This is because the electrons are drifted away from the ions, towards the anode; at this point, many options are available, detector-wise: electrons can be collected as they are, or multiplied with a strong enough electric field (all this will be discussed in Chapter 3). However, there is another option: the electrons, drifting in the gas, will excite further atoms, producing the aforementioned secondary scintillation.

2.4.1 Electroluminescence

The light produced by field-assisted electrons, also called electroluminescence (EL) light [66], is much easier to detect than the primary electrons: without charge amplification, the amount of photons produced increases linearly with the electric field (proportional EL region[3]):

$$Y_z/N \simeq K(E^* - E^*_{th}) \tag{2.3}$$

where Y_z is the light yield per unit length (photons/e^-/cm), N the gas number density, K a proportionality factor, and E^* the density-reduced electric field E/N (or, equivalently for gases at constant temperature, E/P) [67]. E^*_{th} is the threshold value for the density-reduced electric field below which no electroluminescence takes place.
Usually the EL process is extremely efficient (a total yield Y of hundreds of photons/e$^-$ can be easily achieved [68]), making the relative variance of the signal $Q = (\sigma_Y/Y)^2$ extremely small. This makes electroluminescence a prime tool for applications requiring good energy resolution $\mathcal{R}$, this being, for an incident particle with energy E:

$$\mathcal{R} = 2.355\sqrt{F + Q + \frac{1}{n_{pe}}\left(1 + \frac{\sigma_G^2}{G^2}\right)}\sqrt{\frac{1}{n_e}} \tag{2.4}$$

at FWHM[4]. Here, F is the *Fano factor*[5] of the noble gas at energy E, n_{pe} is

[3]Note that the proportional region for EL is not the so-called *proportional mode* for electron avalanches!

[4]Sometimes the energy resolution is reported in terms of σ_E/E, which differs from eq. 2.4 only by the factor 2.355.

[5]The Fano factor expresses the ratio between the observed variance in the number of electrons and the poissonian variance, and is a number between 0 and 1; in noble gases it is typically 0.1-0.2 [69].

USC UNIVERSIDADE DE SANTIAGO DE COMPOSTELA

the number of detected photons (photoelectrons) per electron, σ_G/G is the relative width of the single-photon distribution function of the photosensor, and $n_e = E/W_I$ is the number of ionization electrons. Choosing a good light sensor and having a small Q, the main limit would be the intrinsic Fano factor.

If the electric field is increased up to the point that charge amplification sets in, the linear region will be abandoned and EL photons will exponentially increase (Fig. 2.5); in this work, unless specified otherwise, the plain term *electroluminescence* will refer only to the proportional EL region.

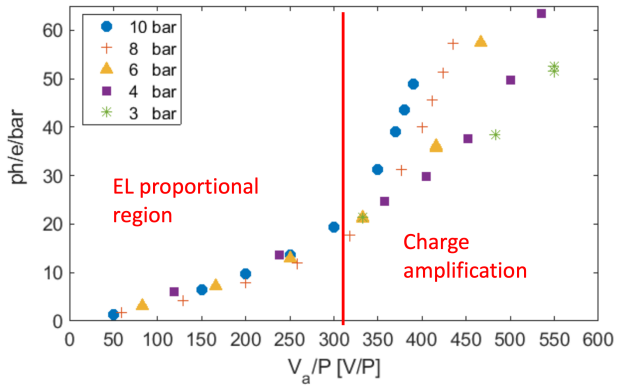

Figure 2.5: Electroluminescence proportional region, where the number of produced photons increases linearly with the electric field; the yields scale with pressure, as expected. When charge amplification sets in, the electric field/ number of electroluminescence photons relation deviates from linearity, and the scaling with pressure is also lost. Modified from [57].

2.4.2 Electroluminescence from electron avalanches

Using electron avalanches in GXe and GAr at 1 bar, an astounding number respectively of 10^5 and 10^4 photons per primary electrons was obtained [70]. Studies with gas mixtures [71] showed that the number of photons per secondary electrons, on the other hand, is constant as a function of the charge gain (Fig. 2.6 left). The stability of the gas against breakdown (see chapter 3) will limit the maximum optical gain achievable; advantages and disadvantages of using electron avalanches for detecting secondary scintillation will be discussed in sec. 5.1.

USC UNIVERSIDADE DE SANTIAGO DE COMPOSTELA

2.4.3 Neutral bremsstrahlung

At electric fields below the electroluminescence threshold, some non-excimer based secondary scintillation is still present in a broad range of UV, visible and/or near IR wavelengths (Fig. 2.6 right). This contribution is due to low energy electrons interacting with induced dipoles on the whole neutral atoms of the gas: for this reason, it was named *neutral bremsstrahlung*. Analogously to electroluminescence, the yields of neutral bremsstrahlung show proportionality with the path length of the electrons, and the number density of the gas [72]. Neutral bremsstrahlung has been observed for the first time in argon [73] and xenon [74] gas in the last years, and has been proposed as a way to explain some weak sub-threshold emission in krypton [75].

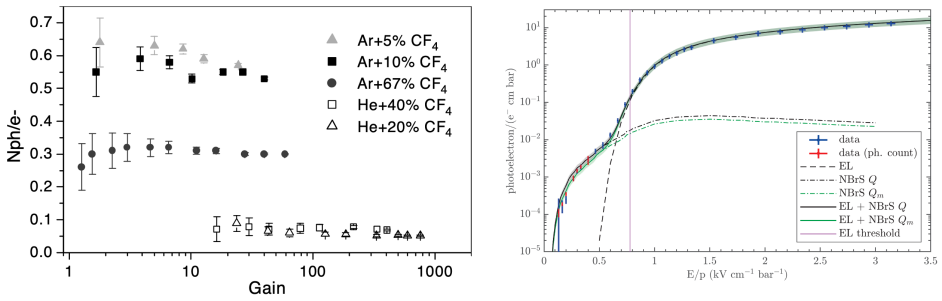

Figure 2.6: Left: number of photons per secondary electron as a function of charge gain for different gas mixtures. Image from [71]. Right: neutral bremstrahlung in xenon: a source of secondary scintillation is clearly visible below the electroluminescence threshold. Image from [74].

2.4.4 Electron drift in noble gases

The electrons drifted by the electric field E will drift in the noble gas with a drift velocity

$$v_d = -\frac{eE}{m\nu_c} = -\mu E \tag{2.5}$$

where μ is the electron mobility and depends on the average frequency between two consecutive collisions of the electron with the gas atoms. The collisions with the gas that the electrons experience will eventually lead to a spread of the electron swarm (diffusion), both in the direction of the electric field (longitudinal diffusion D_L) and perpendicularly to it (transverse diffusion D_T). On first approximation [76]:

$$D_L = \frac{kT_e}{e}(\mu + E\frac{\delta\mu}{\delta E}) \tag{2.6}$$

USC UNIVERSIDADE DE SANTIAGO DE COMPOSTELA

$$D_T = \frac{kT_e}{e}\mu \tag{2.7}$$

where T_e is the electron 'temperature' given by their velocity distribution (in general, $T_e > T_{gas}$). This ellipsoid-shaped broadening of the electron swarm can impact the performance of the detector, in terms for example of topology reconstruction of an event [77]. Moreover, if some impurity with electron affinity is present inside the gas (for example O_2), attachment of electrons to these species can occur, reducing the number of charges n that are effectively collected (and eventually produce light):

$$n = n_0 e^{-hx} \tag{2.8}$$

where h is a field-dependent attachment coefficient per unit length [78]. A vast compilation of these parameters for different gases can be found in [79].

2.5 Gas mixtures with noble gases

Very often noble gases are mixed with other molecules to perform an experiment. There may be different reasons to do that:

1. Reducing diffusion. While collisions in a pure noble gas are mostly elastic, adding a different molecular species with vibrational and rotational degrees of freedom, electrons can transfer a considerable higher amount energy to the latter through inelastic scatterings. This process is called *electron cooling*, as T_e can decrease even down to the thermal limit. As a result, the diffusion is effectively reduced even with a tiny amount of additive, and the drift velocity is enhanced as the number of elastic scatterings decreases (Fig. 2.7). As an example, a simple amount of 0.05% of CO_2 in xenon reduces transverse diffusion by a factor of four [80].

2. Absorbing photons. At electric fields high enough to induce charge multiplication, the VUV photons emitted by the noble gas can start secondary avalanches, potentially leading to sparks inside the detector (more in chapter 3). Therefore, an additive which absorbs these VUV photons can keep the detector operation stable. An analogous effect can be achieved if the excimers are quenched by the additive, absorbing their excess energy through transfer reactions. Of course, if your goal is to work with electroluminescence, absorption of photons and quenching are a disadvantage of using certain mixtures. In fact, the threshold to have electroluminescence and the rate of increase of the yields as a function of electric field can be negatively affected by

USC UNIVERSIDADE DE SANTIAGO DE COMPOSTELA

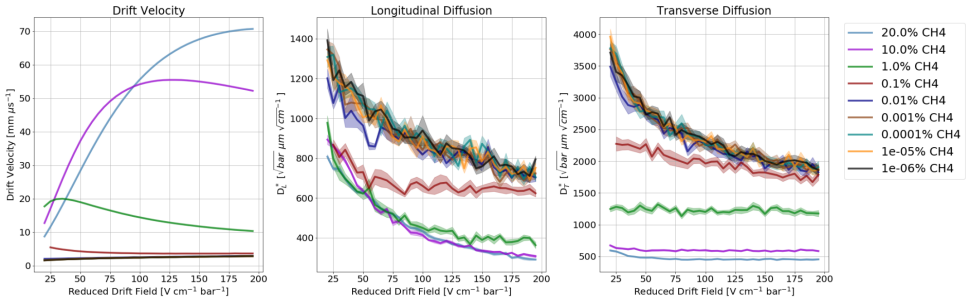

Figure 2.7: Simulated effect, on drift velocity and diffusion, of adding CH_4 to gaseous argon. The effect of a mixture on the drift parameters is unpredictable a priori, hence some simulation tool is needed, such as Pyboltz, which produced the results shown in these plots [81].

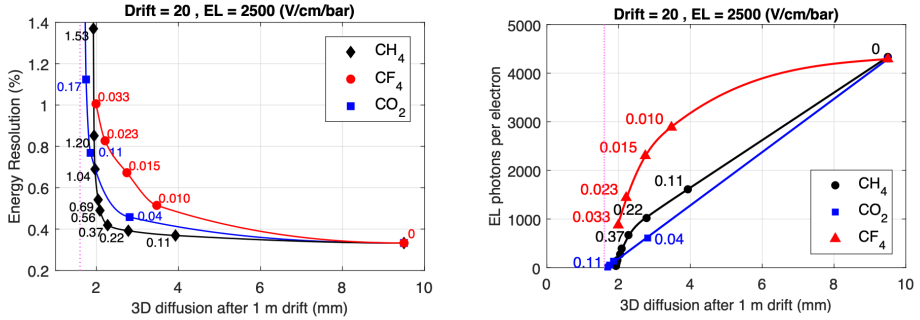

Figure 2.8: Effect of some typical quenchers (CH_4, CF_4 and CO_2) added to xenon to energy resolution (left) and EL yield (right) for different concentrations, from [77].

the presence of some common additives (Fig 2.8). As far as only electron cooling is concerned, the idea of using a lighter noble gas, such as helium in xenon, also looks promising [81] due to the effective energy transfer towards a low-mass species; a mixture of xenon and helium was actually simulated and tested [82, 83, 84], showing an improvement of transverse diffusion without a significant impact on energy resolution and light yield.

Contrary to many common additives, there are also some molecules, such as TMA in xenon [85], which can enhance the detector performance in terms of energy resolution while still effectively quenching the gas. This happens by exploiting the Penning effect: the excited atom of the noble gas transfers enough energy to ionize the quencher molecule. In this way, the ionization signal is enhanced, leading to a better energy resolution. Combinations of noble gases and additive which can effectively exploit this phenomenon are called Penning mixtures.

USC UNIVERSIDADE DE SANTIAGO DE COMPOSTELA

3. Wavelength shifting. If the additive is in turn a good scintillating gas, such as CF_4 or N_2, transfer reactions from excited states of the noble element can lead to light detectable at more convenient wavelengths. For example, a study of primary scintillation for Ar/CF_4 mixtures [86] showed a transfer $Ar^* + CF_4 \rightarrow Ar + CF_3^*(2A_2'', 1E')$, with CF_3^* eventually emitting in a band centered at $\lambda = 630$ nm.

2.6 Scintillation in liquid

Primary scintillation in noble liquid is a well known phenomena, already exploided in liquid scintillator experiments. The second continuum in xenon appears approximately at the same wavelengths as in gas (there is a shift of few nanometers), although the triplet decays around three-fold faster [87, 88, 89]. The second continuum was observed in liquid argon, too, showing a dependence of the triplet time constant on the electric field applied, due to quenching with Ar_2^+ ions (unquenched decay time $\tau_3 \simeq 2.1\mu$s) [90]. An analogous feature to the third continuum in gas has also been observed, although it is not sure whether the underlying process is the same [91].

Regarding S2, several works have measured electroluminescence in LXe, observing it already at electric fields lower than the ones required for charge multiplication: [92] and [93], using respectively thin wires and microstrip plates, both report a threshold field $400 < E_{th} < 500$ kV/cm for electroluminescence, and $700 < E_{th} < 800$ kV/cm for electron avalanches. Recently, the idea of exploiting electroluminescence in a LXe-based detector is being explored, for example in [94, 95, 96, 97, 98].

For liquid argon, [99] and [100] observed electroluminescence with a threshold of $E_{th} \sim 60$ kV/cm, around a factor of 10 lower than in LXe; thus, it is believed [101] that the observed light was actually produced in a local gaseous pocket, or that it is due to neutral bremsstrahlung in the liquid. The latter was indeed confirmed in liquid argon recently [102]: this source of scintillation may constitute an interesting alternative to excimer-based electroluminescence for neutrinos noble liquid-based experiments (see Chapter 5).

USC UNIVERSIDADE DE SANTIAGO DE COMPOSTELA

Gas discharge physics

3

The study of breakdown phenomena began its journey at the beginning of the nineteenth century, when arc discharge was discovered independently by V. V. Petrov [103] and H. Davy [104]. The first discharge mechanism to be identified was the Townsend mechanism in 1903, followed by the theory of streamers and sparks in 1940s. Other than the undeniable fascination that all breakdown phenomena carry with themselves (just think about lighting, or leaves glowing with purple light), and practical uses they can have (glow lamps, plasma balls or Kirlian photography, Fig. 3.1), they are of paramount importance in detector physics, since they have destructive potential on the structures typically used in experiments, other than posing a threat to the readout electronics.
In this chapter, the Townsend theory of discharge (Sec. 3.1.1) and the streamer theory (Sec. 3.1.2) will be explained, applying them to the low-pressure case, to the long sparks case, and finally to gaseous detectors for particle physics (Sec. 3.2).

3.1 Useful general concepts

To understand the breakdown in a gas, it is important to understand how an avalanche is formed in general under the effect of an electric field: the aforementioned Townsend mechanism can explain how electron multiplication takes place in a gas before the breakdown, and also some breakdown

USC UNIVERSIDADE DE SANTIAGO DE COMPOSTELA

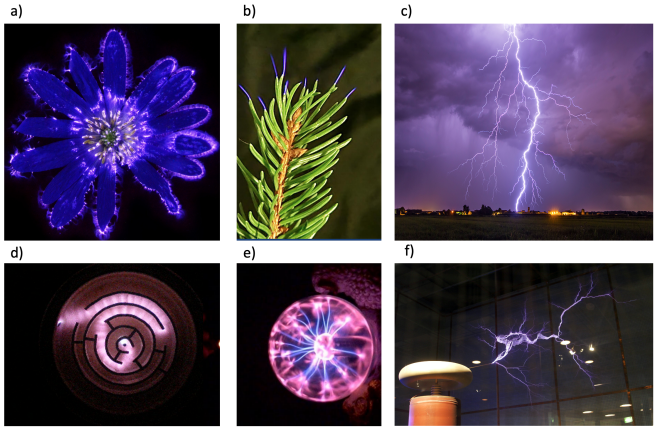

Figure 3.1: Some fascinating breakdown-related phenomena this chapter aims at shedding light to: (a) Kirlian photography of a flower (by Robin Noorda, Tropism Art & Science Collective [105]), (b) corona discharge on a tree [106], (c) a lighting (by Alessandro Piazza [107]), (d) a glow discharge solving a maze [108], (e) the famous plasma ball [109], and (f) a Tesla coil (by Fir0002/Flagstaffotos [110]). Not depicted are less pleasant breakdown-related events, such as the electric shocks you get on a dry day touching your car or sparks in your beloved detector.

phenomena, although not *all* of them, as it will be shown with the streamer theory. The general recipe to have avalanches and/or sparks, is always to have two electrodes (a cathode and an anode), of whatever shape, and some gas in between. Depending on the shape of the electrodes, on their distance, and on the gas pressure, the breakdown phenomenon will appear differently, but the mechanisms underneath will always be the two presented in this section. For simplicity, in the following treatment parallel plate electrodes will be mostly assumed.

3.1.1 Townsend mechanism

Let's imagine to have two parallel plates, one of which is the cathode, and one the anode, separated by a gas gap, with a uniform field E. If some event (such as an interaction with a cosmic ray or natural radioactivity products, or simply field emission) frees an electron from the cathode (set at the position x=0), this electron will be accelerated by the electric field applied, being able to ionize other gas atoms/molecules. Assuming the two electrodes at a distance d and an initial number of pairs produced n_{e0}, the number of ionizing events per unit area for the gas thickness dx will be:

$$dn_e = \alpha n_e dx, \tag{3.1}$$

USC UNIVERSIDADE DE SANTIAGO DE COMPOSTELA

resulting in

$$n_e(d) = n_{e0}e^{\alpha d}. \tag{3.2}$$

The expression $e^{\alpha d}$ is called *gain*. α is the so-called first Townsend coefficient, and depends on the energy acquired by the electrons, so ultimately on its mean free path (linked to the gas pressure and the gas characteristics) and the electric field applied; for low values [111], α can be approximated as

$$\alpha = PAe^{-BP/E}, \tag{3.3}$$

A and B being factors that depend on the gas.

The n_e positive ions created in this process will eventually drift towards the cathode; calling W the effective work function of the cathode, if an ion possesses an energy $E \geq 2W$, it can free another electron, creating a secondary avalanche. The positive ions generated by the secondary avalanche will free other electrons, producing subsequent generations of avalanches (Fig. 3.2). The same phenomenon could be produced by photons emitted by gas atoms/molecules excited by the drifting electrons, and hitting the cathode; this is called ion/photon feedback.

Defining γ as the ratio between the number of electrons released from the cathode and the number of incident ions (or photons) and $n_{e,i}$ the number of electrons created in the i-th generation, the (i+1)th generation will increase the number of electrons reaching the anode by $\gamma n_{e,i}$. With theoretically an infinite number of generations, the geometric progression will tend to

$$n_{e,tot} = \frac{n_{e0}e^{\alpha d}}{1 - \gamma(e^{\alpha d} - 1)}. \tag{3.4}$$

If $\gamma(e^{\alpha d} - 1) < 1$, and the source of primary ionization is removed, the number of electrons reaching the anode will become zero: the discharge is not self-sustaining. However, when $\gamma(e^{\alpha d} - 1)$ becomes ≥ 1, even removing the source of primary ionization we can keep having a self-sustaining discharge, that may eventually lead to a spark. This condition for the equality can be simplified to

$$\alpha d = \ln(\frac{1}{\gamma} + 1). \tag{3.5}$$

USC UNIVERSIDADE DE SANTIAGO DE COMPOSTELA

Remembering eq. 3.3, eq. 3.5 becomes

$$PAe^{BP/E}d = PAe^{BPd/V_b}d = \ln(\frac{1}{\gamma} + 1), \tag{3.6}$$

which yields the following expression for the breakdown voltage V_b:

$$V_b = \frac{BPd}{\ln \frac{APd}{\ln(\frac{1}{\gamma}+1)}}. \tag{3.7}$$

From eq. 3.7 it can be seen that the breakdown voltage is a function of the product between the pressure of the gas and the distance between the electrodes: this is the Paschen Law (Fig. 3.3), discovered experimentally by Paschen in 1889 [112] before Townsend theory was developed.

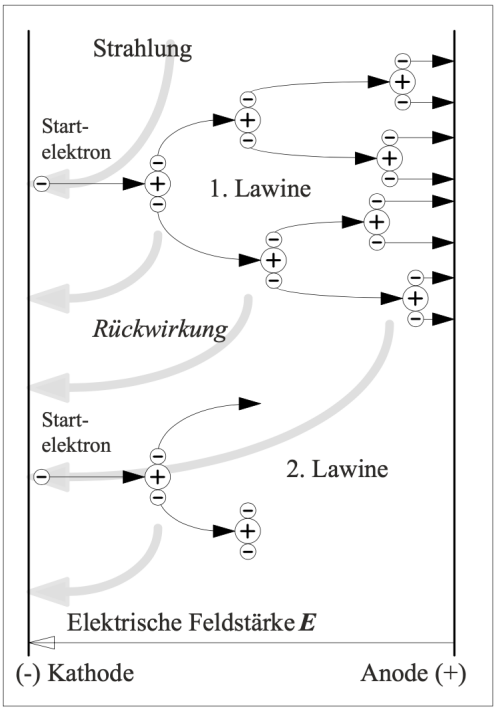

Figure 3.2: Avalanche caused by external radiation, giving rise to an exponential ionization process, and subsequent generations of avalanches initiated by positive ions (or photons) colliding with the cathode. Image from [113].

If the field is not uniform, for example in the case we are using wires or MPGDs as an anode, or if the primary ionization does occur in different

USC UNIVERSIDADE DE SANTIAGO DE COMPOSTELA

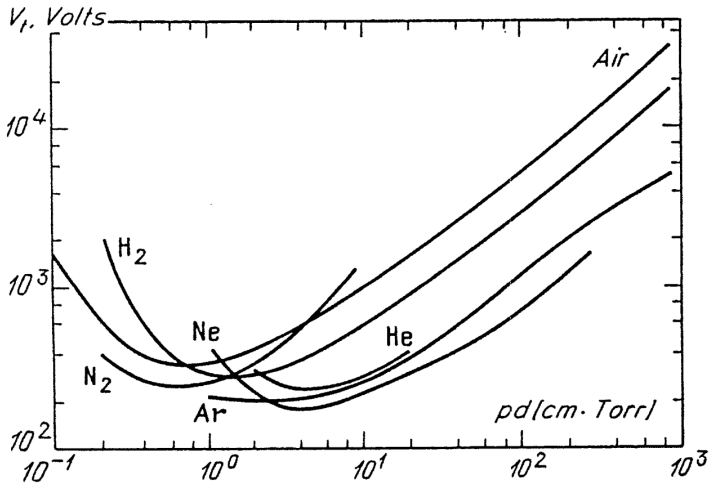

Figure 3.3: Paschen curves for different gases. Image from [114].

locations inside the gas, the gain[1] in eq. 3.2 becomes

$$M = \exp(\int_0^d \alpha(E(x))dx) \tag{3.8}$$

and all the following equations presented for the parallel plate case with ionization at the cathode have to be modified accordingly.

Finally, in the case of long gaps, or for electronegative gases, attachment of electrons has also to be taken into account; this effect will slow down the development of the avalanche; if β is the attachment coefficient, the most general expression for M becomes

$$M = \exp(\int_0^d [\alpha(E(x)) - \beta(E(x))]dx) \tag{3.9}$$

3.1.2 Streamer discharges

Townsend theory of discharges, despite being able to explain a broad range of phenomena, has some limitations [115]:

1. The formation of secondary avalanches depends on the work function

[1] In this case also called *multiplication factor*.

USC UNIVERSIDADE DE SANTIAGO DE COMPOSTELA

of the cathode material;

2. The timescales for the formation of a spark are of the order of tens of microseconds;
3. The secondary avalanches must start from the cathode;
4. When the gap is large, or the pressure is high, Paschen's law is not valid anymore.

These limitations make Townsend theory unable to explain the observation of sparks with a much shorter timescale (<1 μs [116]). Moreover, these sparks are independent from the cathode material, and appear to happen from anywhere in the gas gap. To overcome these limitations, streamer theory was developed by Raether, Meek and Loeb.

According to this theory, the steps to produce a spark are the following (see also Fig. 3.4):

1. An electron avalanche is initiated; due to the different velocities of electrons and ions, a short negative head forms towards the anode, and a long positive tail appears towards the cathode. The field is distorted by the space-charge of the avalanche.
2. As a result of space-charge, the charged particles in the avalanche undergo inelastic collisions with the gas, enhancing the ionization at a rate higher than that expected from the external field alone.
3. This additional multiplication accumulates at the tail of the primary avalanche, where the electric field is higher due to the presence of positive ions; eventually a plasma is formed, starting from the anode.
4. Eventually a whole conductive channel of plasma (called streamer) is formed between the anode and the cathode: you get a spark. The characteristic sound of a spark is due to a shock wave, since the temperature (hence pressure) in the channel is very high ($\sim 10^4$ K).

The occurrence of sparks set a limit to the gain that can be achieved in a detector; in particular, the empirical so-called Raether limit is

$$\alpha d < 20, \tag{3.10}$$

corresponding to a number of electrons in the avalanche $n_{e0}e^{\alpha d} \sim 10^8$ [117]. However, it is worth noting that the limit can change depending on different

USC UNIVERSIDADE DE SANTIAGO DE COMPOSTELA

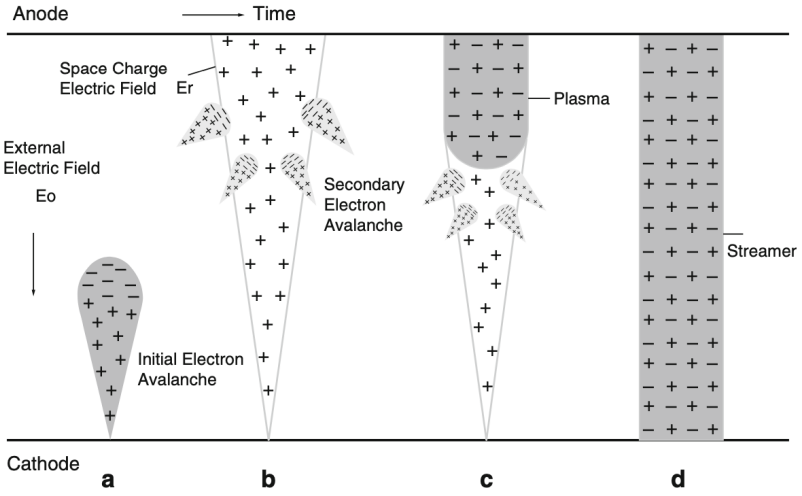

Figure 3.4: Formation of a streamer in the gas gap between two parallel eletrodes. Image from [118].

factors such as the gas, the structures used for the detector, or the number of primary electrons. A detailed study about the maximum gain achievable before a spark occurs in some MPGD structures can be found in [119].

3.2 Applied cases

3.2.1 Low pressure

When the pressure of the gas is low (around $10^{-5} - 10^{-2}$ mbar), the voltage-current curve that is observed is depicted in Fig. 3.5:

1. Region with incomplete electron collection (A-B): the field is not high enough to collect all the electrons at the anode, recombination can take place in the gas.
2. Saturation regime (B-C): the field between the electrodes is high enough to collect all the electrons produced by the primary ionization of an incident particle, but there is no avalanche.
3. Townsend regime (C-D): the electrons manage to acquire enough energy to create first-generation avalanches. As the voltage increases, further generations of avalanches appear, until the breakdown voltage is reached.

USC UNIVERSIDADE DE SANTIAGO DE COMPOSTELA

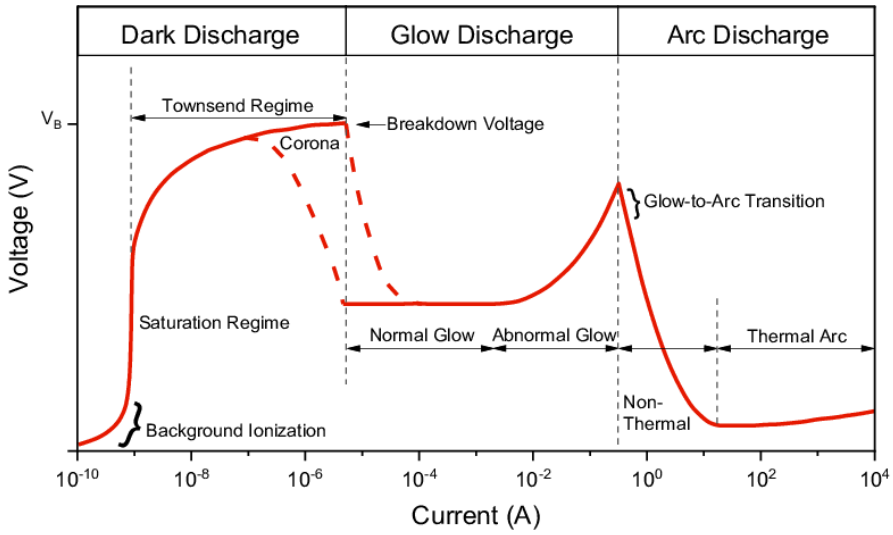

Figure 3.5: Volt-Ampere characteristic curve of a low pressure gas. The voltage values are the result of the interplay between the power source and the charges behavior in the gas gap. Image from [120].

4. Corona discharge (D-E): a corona discharge appears only when the electric field is non-uniform. For example, it can appear close to an electrode with a small radius of curvature [121]. The characteristic glow of a corona discharge (Fig. 3.6a) is caused by recombination within the highly ionized gas (plasma) in the immediate vicinity of such electrode. The rest of the space between the electrodes does not glow since it is not highly ionized. Depending whether the corona happens at the cathode or at the anode, two different mechanisms come into play: while the corona happening close to the cathode (negative corona) relies on the generation of secondary avalanches by extracting electrons from the electrode, yielding a uniform glow, this is not possible for a corona taking place at the anode (positive corona). In this case, the corona can set in when formation of streamers becomes possible due to high enough charge density; some filaments around the electrode become visible.

5. Glow discharge (F-G): a region between the anode and the cathode is in plasma state and glows (Fig. 3.6b). An increase of the current leads to an increase of the plasma section, keeping the current density constant; to increase the current by orders of magnitude, a tiny increase of voltage is sufficient.

6. Abnormal glow discharge (G-H): the whole section is filled with plasma; an increase in current requires a higher voltage, and it translates into an increase in current density.

USC UNIVERSIDADE DE SANTIAGO DE COMPOSTELA

7. Arc discharge (I-K): the number of charge carriers further increases due to thermoionic emission from the cathode; the discharge channel becomes thin and its conductivity increases due to the higher ionization, causing a significant voltage drop.

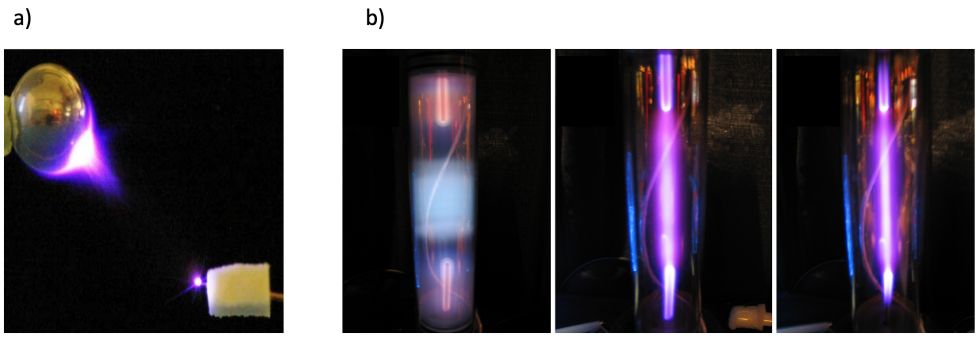

Figure 3.6: a): corona discharge from electrodes with not uniform field [122]. b): transition from glow to arc discharge in argon (by Wikigian [123]).

The phenomena just explained mostly depend on the Townsend mechanism and not on the streamer discharges, with the exception of corona discharges occurring at the anode (and strictly speaking, of arcs, which mostly rely on the thermoionic effect). This curve is mostly relevant for plasma physics, and not for gaseous detectors, where usually the pressures are too high to show glow discharge. The exception is, again, posed by corona discharges, which can appear at higher pressures, too.

3.2.2 Long gaps

When the gap between the electrodes becomes long enough, it will be increasingly hard to have a uniform electric field, no matter the shape of the electrodes. At high voltages, a corona will appear at first around the electrode with the highest field. By increasing the voltage even more, streamers will eventually start to propagate towards the other electrode, creating a branched pattern, and leaving behind a single hot, conductive channel, called *leader*. If the leader reaches the opposite electrode (or a counterpropagating leader), the conductive channel is neutralized by electrons rapidly flowing through it, causing the *return stroke*. Lighting and the Tesla coil branched light are typical examples of long sparks.

USC UNIVERSIDADE DE SANTIAGO DE COMPOSTELA

3.2.3 Breakdown phenomena in gaseous detectors

Gaseous detectors for particle physics typically operate at a higher pressure than in Sec. 3.2.1 (usually ≥ 1 bar); however, we can draw a curve similar to Fig. 3.5, where regions 1-5 in Fig. 3.7 roughly correspond to regions A-D for low-pressure gases (note that the axes are reversed). The distinct regions will allow to build detectors that use different operational modes:

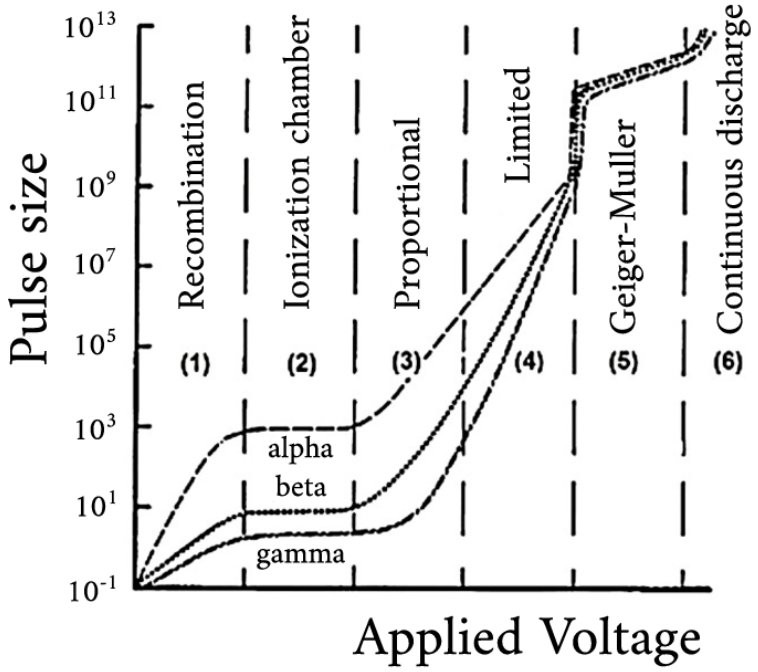

Figure 3.7: Different operational regimes for gaseous detectors. Image from [124].

1. Recombination mode: if the field is not high enough, most of the electrons and ions produced by an incident particle will recombine before being collected, not allowing for a detector with charge readout. However, the light produced by recombination may be used with scintillators using an optical readout. Increasing the voltage, more and more electrons are collected.

2. Ionization mode: the field is high enough to collect all the primary electrons at the anode, but not high enough for the electrons (ions) to produce new pairs: the current collected will not depend on a further increase of the voltage (until we enter the proportional mode), but only on the energy of the incident particle. Ionization chambers work in this region; moreover, the value for the drift field of TPCs is chosen

USC UNIVERSIDADE DE SANTIAGO DE COMPOSTELA

to be in this range of values. Using optical readout, this is also the realm of detectors that exploit electroluminescence.

3. Proportional (or avalanche) mode: when the voltage increases further, electrons acquire enough kinetic energy to ionize other atoms/-molecules in the gas, creating avalanches. The current collected will be proportional to the primary electrons. In this region we find, for example, MWPCs and Micromegas/GEMs - based detectors.

4. Limited proportionality mode: positive ions drift towards the cathode much slower than electrons to the anode; as the number of ions increases, the space charge[2] deforms the electric field, causing a loss of proportionality in the detector.

5. Geiger-Müller mode: in this region, space-charge is so high to limit further multiplication. This point is reached at an approximately fixed number of avalanches [125], produced by photons interacting with the gas, which fill the whole detector space. In this way large pulses are produced, which do not provide information about the energy of the incident particle. However, it is fairly simple to detect single particles in this mode. Geiger-Müller detectors work in this regime.

If the voltage is increased even further, the detector will enter in a self-sustaining discharge mode, in which the presence of current will be independent from the interaction with an incoming particle: the breakdown voltage has been reached.

Townsend or streamer?

What happens when breakdown in a gaseous detector is reached? The phenomena described in Sec. 3.2.1 are typically not seen in this case: for example, glow discharge occurs at lower pressures;corona discharge can be seen in case of some defect in the detector, creating a sharp edge, but here we want to think about a flawless detector.

What is commonly observed, in this case, is the onset of a spark, due either to the Townsend or the streamer mechanism. Conventionally, it has been reported that the transition from Townsend mechanism to streamer mechanism happens when $Pd \gtrsim 0.27$ bar cm (or 200 Torr cm) [116]. However, both phenomena have been observed, for example, in a parallel plate avalanche

[2]Note that the space charge comes from a single avalanche, and not from previous events.

USC UNIVERSIDADE DE SANTIAGO DE COMPOSTELA

chamber at constant pressure and gap between the electrodes [116] if the noble gas was mixed with different additives[3]: in Fig. 3.8 the presence of two distinct mechanisms for breakdown (the slower Townsend mechanism and the fast streamer one) is apparent.

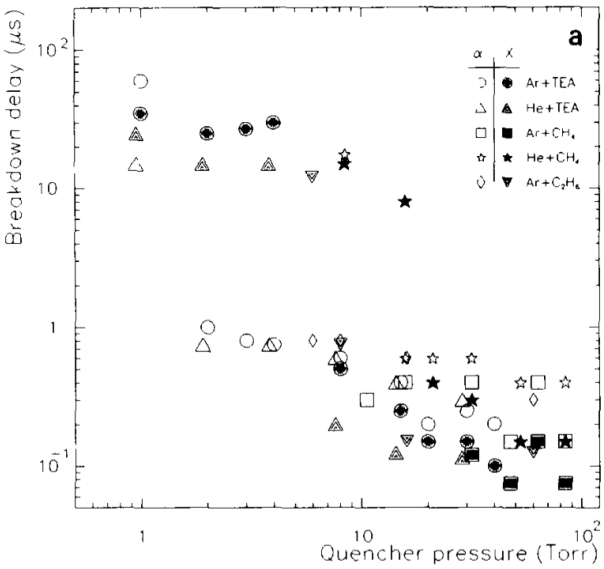

Figure 3.8: Observation of two distinct breakdown mechanisms in a parallel plate avalanche chamber for different gas mixtures. Although the distance between the electrodes and the pressure are kept constant, in the same mixture (and concentration) both the Townsend mechanism (slower) and the streamer mechanism (fast) occur, the transition depending on the source of primary charge. Image from [116].

To explain this observation, one must remember the two conditions for breakdown:

$\gamma(e^{\alpha d} - 1) \geq 1$ for Townsend discharge
$n_{e0}e^{\alpha d} \sim 10^8$ for streamer discharge

The first criterion that will be met will determine which kind of breakdown will happen. As explained in Sec. 3.1.1, Townsend mechanism relies on the positive ions (or photons) impinging on the cathode and freeing further electrons[4]. Adding some quencher (such as TEA, CF_4, CH_4) to a noble gas,

[3] In other words, you can adjust the transition from Townsend to streamer mechanisms by changing the gas.

[4] The mechanism of quenching ions or photons is different: for ions, the quencher easily neutralizes the noble gas ions and becomes an ion itself (charge transfer); since the quencher is less chemically reactive, there will be a lower chance of producing feedback freeing electrons at the cathode; for photons, two mechanisms come into play, which are VUV photon absorption or, more efficiently, collisional quenching of the excited noble gas

USC UNIVERSIDADE DE SANTIAGO DE COMPOSTELA

or even having some accidental impurity, limits the feedback process, that is, suppresses the Townsend discharge mode. Thus, quenchers will make it more likely that the limit for streamer discharge will be met first; this often translates into being able to reach higher gains if the noble gas is well quenched [126]. Nevertheless, under some conditions (for example, in the case of the gaseous phase of a dual-phase TPC, at cryogenic temperature) it may not be possible to add a quencher: in this case, the Townsend mechanism may be the dominant cause of a spark. This topic will be examined more in depth in chapter 5.

atoms prior to emission.

USC UNIVERSIDADE DE SANTIAGO DE COMPOSTELA

USC
UNIVERSIDADE
DE SANTIAGO
DE COMPOSTELA

Time Projection Chambers

4

Having a nice theory and predictions to probe, joined with the knowledge of scintillation and charge multiplication in gases, is only half of the journey: you have yet to set up an experiment. Even considering only the neutrino field, there is a huge diversity of detectors and materials that are employed for the scope: researchers have resorted to solid-state crystals, liquid and gaseous noble gases, tanks of water, getting as far as employing the Mediterranean Sea [127] or the Antarctica ice[1] [128]. Describing all these experiments and their techniques would be fascinating, but beyond the scope of this thesis. For this reason, this chapter will be limited to a widespread kind of detector in the particle physics field: the time projection chamber (TPC). Afterwards, some amplification structures and readout techniques will be described, keeping in mind that they are not of exclusive use for TPCs; finally, two neutrino experiments will be described, among those which use TPCs.

4.1 The TPC concept

TPCs were invented in the 1970s by D. Nygren[2] [129]. The concept evolved from drift chambers [131], that were already operated at that time: a gas-

[1] They didn't dig any tunnel from CERN to Gran Sasso, though.

[2] To hear the story of the development of the first TPC from the inventor himself, see [130].

USC UNIVERSIDADE DE SANTIAGO DE COMPOSTELA

filled chamber, with anode wires, that was able to reconstruct the incident particle's distance from the signalling wire thanks to the drift time of primary electrons; the drift time was known by means of, for example, a scintillator, while to compute the distance one needed to know the drift velocity of the electrons along the path. Despite these devices were an excellent idea, they suffered from a severe diffusion problem over long distances, coupled to a presumed incompatibility with magnetic fields due to "ExB" effects. It was thus realized that, if the magnetic field would have been applied parallel to the electric field, the transverse diffusion would have been reduced by a factor

$$\frac{1}{1+(\omega\tau)^2} \tag{4.1}$$

with ω being the cyclotron frequency and τ the mean collision time [132]. The original TPC design was a gas-filled volume, with a cathode placed in the center of the volume and two anodes at the end caps. The magnetic field was generated by a coil wrapped around the gas volume. When a particle interacts with the gas inside the volume, as already seen in chapter 2, it generates light due to excitation and de-excitation of the gas atoms/molecules (if the gas scintillates), and primary electrons due to their ionization. Together with a diffusion-reduced drift, the novelty of the TPC is the possibility of reconstructing all the spatial coordinates of the interaction point: the x-y coordinates (the plane perpendicular to the cathode and anode planes) would be given by wires placed with different angles, or by pads behind the anode; the z coordinate (perpendicular to the anode and cathode planes), by using the time difference between the prompt light signal (S1) and the signal produced by the drifting electrons (S2) (Fig. 4.1). While the signal

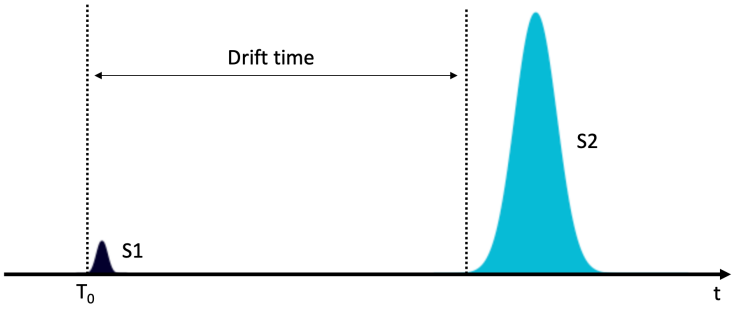

Figure 4.1: Typical S1 and S2 signal from a TPC with optical sensors; the time difference between the two signals allows to reconstruct the coordinate parallel to the electric field, while the other two coordinates are obtained from the readout configuration.

produced by the electrons could be detected either collecting the charge or the secondary scintillation light, for S1 an optical sensor must be placed at

USC UNIVERSIDADE DE SANTIAGO DE COMPOSTELA

least at one of the endcaps. This is not the case for gaseous TPCs used in accelerator experiments (including the first prototype!), where the initial time of interaction (T_0) is obtained by using the beam spill time and auxiliary timing detectors around the TPC[3].
Right after, a TPC variant with liquid argon (LArTPC) was developed: in fact, the high density of the liquid is a natural reducer of the large diffusion that occurs in gas; this kind of TPCs do not resort to a magnetic field, which is unpractical with the large active volumes required for rare event searches and the broad topological features of tracks in this field [133]. Nowadays, different noble element in liquid state are used, the most common ones being argon and xenon, with two different designs: pure liquid TPC (single-phase) and a combination of liquid and gas (dual-phase).
Dual-phase TPC exploits a relatively small gaseous region on top of the main liquid volume, obtained by following the saturation curve of the noble element during liquefaction (Fig. 4.2). The cathode is placed at the bottom of the liquid, usually with photomultipliers (PMTs), or silicon photomultipliers (SiPMs), underneath. The electrons are shifted towards the gaseous phase, where the anode is placed. An extraction field helps the passage of the electrons through the gas-liquid interface. In the gaseous phase, primary electrons undergo some process to amplify the signal; this could be charge amplification (making it possible to collect either the produced charge or light) or electroluminescence.

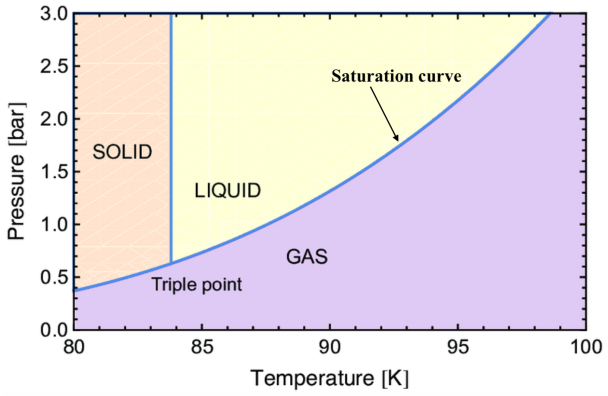

Figure 4.2: Phase diagram of argon zoomed on typical operational values for TPCs. Coexistence of gaseous and liquid phase can be obtained by setting a temperature and pressure combination that lays on the saturation curve. Image adapted from [134].

In the single-phase TPC, on the other hand, the whole space is filled

[3]The idea of developing a fully optical TPC for an accelerator experiment will be discussed in Sec. 4.4.1

USC UNIVERSIDADE DE SANTIAGO DE COMPOSTELA

with liquid; an electric field is applied between the cathode and the anode (typically made of wires), where the primary electrons generated by the particle interaction are collected. The possibility to collect only primary electrons for S2 restricts the use of single-phase TPCs to experiments with energy deposition at least of the MeV scale. Regarding S1, a common way to detect the signal is to put PMTs behind the S2 readout wires.
In addition to liquid-based TPCs, high-pressure TPCs have also been developed, which do not apply any magnetic field. In this case, an amplification stage for electrons/electroluminescence is deployed, analogously to the dual-phase TPC.
Chapter 5 will discuss about challenges faced when dealing with the different kinds of TPCs (shown in Fig. 4.3). For a compilation of TPC variants that were not discussed here (a teaser: some ideas are positive- or negative-ion TPCs, bubble chamber TPCs and spherical TPCs), refer to [133].

4.2 Amplification structures

As mentioned before, it becomes handy to have a way to amplify the S2 signal, especially when it comes to low deposition of energy. For this purpose, one can resort to charge amplification of primary electrons, usually achieved with wires or micropattern gaseous detectors (MPGDs), or to production of electroluminescence light (often attained with meshes in current experiments). Here follows a short description of various amplification structures.

4.2.1 Wires

Wires are historically one of the first tools that allowed to multiply the primary charge produced by a particle interaction: one example is the *proportional counter*, a cylindrical device filled with gas, whose walls were negatively biased (cathode); at the center of the cylinder, a wire (the device's anode) could at the same time drift the electrons from the far region, where the electric field is weaker, and multiply the charge in its immediate vicinity, where the field becomes stronger as $1/r$.
An evolution of the proportional counter was the multi-wire proportional chamber [139], which employed multiple wires, parallel to each other and equally spaced (Fig. 4.4 left). The wires were positioned between two cathode planes. For an accurate description of these devices, see [140].
The usage of multiple wires eventually allowed to stack different wire planes, each one tilted by a certain angle with respect to the other. By combining the information from the different planes, it is possible to reconstruct the

USC UNIVERSIDADE DE SANTIAGO DE COMPOSTELA

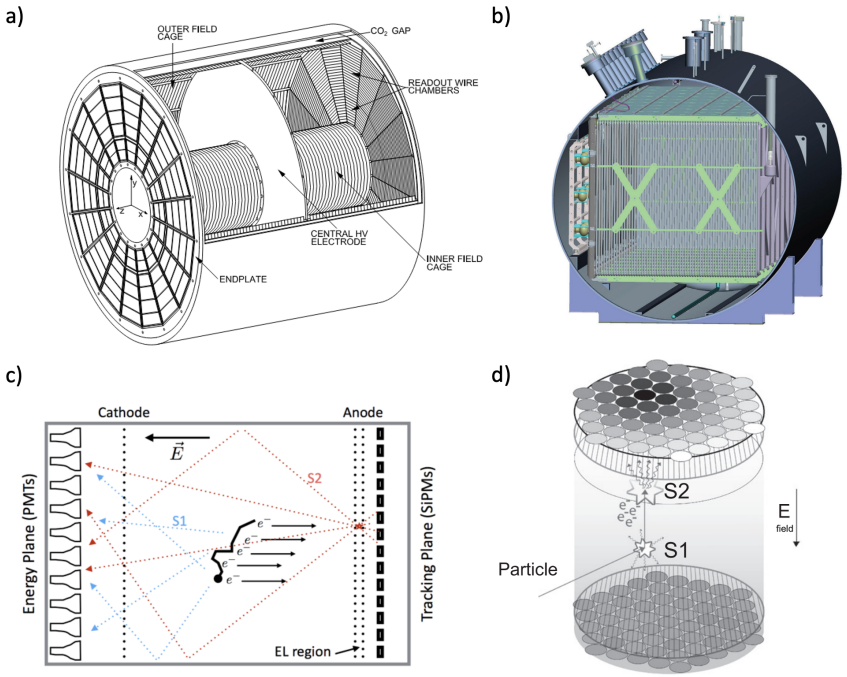

Figure 4.3: Different TPC concepts illustrated in text: a) the original concept of a gaseous TPC with a magnetic field parallel to an electric field (in particular, the drawing shows the ALICE TPC). The cathode is at the center of the TPC, and the readout anodes are wires placed at the two endcaps. The 0.5 T solenoidal magnetic field is not depicted here. From [135]. b) Single-phase TPC (here, MicroBooNE LAr TPC); the cathode is placed on the right, while three layers of anode wires are on the left. The three distinct wire layers are tilted by 60° one with respect to the other, allowing to reconstruct two of the spatial coordinates. Behind the wires, there is a PMT plane for S1. From [136]. c) Example of high pressure gaseous TPC without magnetic field (NEXT HPGXe TPC). S1 is detected by PMTs placed behind the cathode, while S2 detection exploits electroluminescence, obtained through planes of wires. From [137]. d) Specimen of a dual-phase TPC (here, from the LUX experiment). S1 is detected in the liquid by PMTs placed behind the cathode, while electrons are extracted to the gaseous phase with an electric field and there undergo some signal amplification (in this case, using electroluminescence). From [138].

position of the particle track in the x-y section (parallel to the wire planes). A wire plane can also be used in TPCs to reduce the ion feedback: this plane, called *gating grid*, would be composed of parallel wires that can be alternately biased with a positive or a negative voltage. When this alternate bias is applied, all the field lines end up on the gating grid wires, impeding the passage of any charged particle (closed gate mode); to open the gate in order to detect an event, all the gating grid wires are put at the same potential, precisely the one that makes the voltage drop in the drift region uniform (Fig. 4.4 center and right).

Finally, the concept of wires can be used to produce meshes, widely used

USC UNIVERSIDADE DE SANTIAGO DE COMPOSTELA

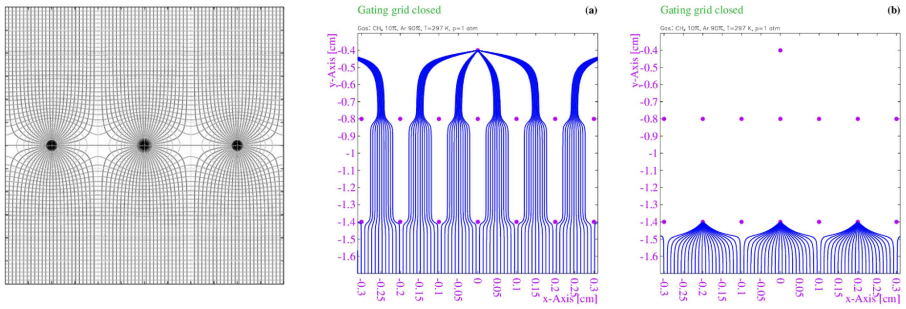

Figure 4.4: Left: Field lines and equipotential around the anode wires in a MWPC, from [140]. Center: configuration endowed with a gating grid, set in the open gate mode. Right: same configuration, this time in closed gate mode. From [141].

for obtaining electroluminescence. These can be created by weaving wires (woven mesh) or putting simply together arrays of wires; meshes can also be produced without starting from pre-existing wires, through electroforming (the patterned structure is built atom-by-atom) or etching. In this case, the electroluminescence takes place between two meshes, the closest to the cathode, called *gate*, contributing both to the drift field and the electroluminescence field, and the farthest, the anode, defining the EL field.

4.2.2 MPGDs

Introduced at the end of the 1980s, with the invention of the microstrip gas counter (MSGC) [142], MPGDs were a novelty with respect to wire chambers, in that the multiplication field is not defined anymore by the voltage difference applied between the cathode and the anode, but the different regions (drift region, multiplication, and induction) are well defined and separated through the structure itself [143]. MPGD structures allow for a more compact geometry with respect to the wires, allowing for a better spatial resolution, a better ion colletion and a lower ion back flow. Over time, many different MPGDs have been designed, however the most widespread structures at present moment are MicroMesh Gas detectors (Micromegas) [144] and the Gas Electron Multipliers (GEMs) [145]:

1. Micromegas are composed of a micromesh (few μm thick) parallel to a strip or pad plane, which are often some 100's of μm apart (see Fig. 4.5 left). The region between the mesh and the strip is the amplification gap, where a high field can be applied. On the other hand, the region between the cathode and the mesh is the drift gap

USC UNIVERSIDADE DE SANTIAGO DE COMPOSTELA

(labeled as conversion gap in Fig. 4.5), where it is possible to apply a lower electric field.

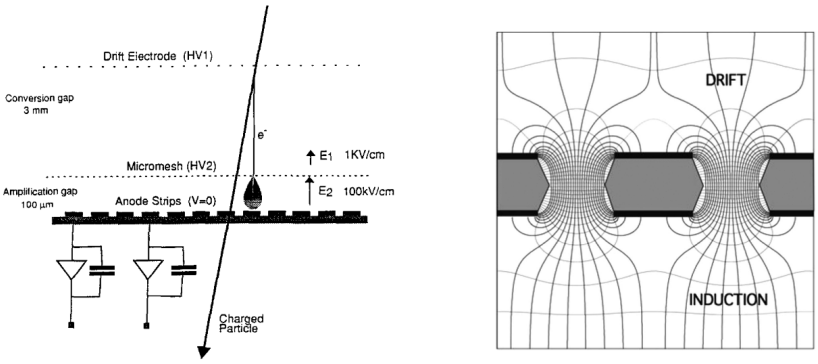

Figure 4.5: Left: schematic drawing of a Micromegas (from [144]). Right: electric field inside the GEM holes (from [145]).

2. GEMs are a sandwich-like structure, where the filling is a thin insulating layer (typically 50 μm of kapton) and the bread slices are two copper electrodes, about 5 μm thick. Small holes ($\sim$ 70 μm diameter) are drilled in the structure, with a pitch of typically twice the hole diameter, different possible symmetries (e.g. hexagonal and square) and hole shapes (for example conical and biconical), and the potential presence of a rim around the holes. The structure, analogously to the Micromegas, divides the volume into different regions: the drift region between the cathode and a copper electrode, the multiplication region inside the holes, where high fields can be achieved, and an induction region between the second copper electrode and the readout plane. If the readout is put in contact with the GEM, for increasing the signal induced on the pick-up pads/strips, we talk about WELL configuration. Often, multiple GEMs are stacked together, allowing to reach gains even orders of magnitude higher than a single layer ([146] reported an increase of about an order of magnitude at each added GEM); in principle, cascading GEMs and Micromegas is also possible. Following the GEM concept, thicker GEMs have been also developed (TH-GEMs), of around 500 μm thickness, where the typical materials are FR4 for the insulator and copper for the electrodes (lately also glass THGEMs have been developed). In this case, the pitch and hole size are also bigger ($\sim$ 0.4 mm and 1 mm, respectively). For a nice review about THGEMs and its variants, see [143].

USC UNIVERSIDADE DE SANTIAGO DE COMPOSTELA

4.3 Readout techniques

The next step after amplification (or the simple drift of the primary electrons) is to read out the signal. While S1 is read out through photo-sensitive devices[4], S2 can be detected in two ways: by reading directly the charge (electronic readout), or by detecting the photons produced by the electrons through the processes described in chapter 2 (optical readout). Here follows a description of the two methods.

4.3.1 Electronic readout

When a charge q[5] moves inside the detector, it induces a current on all the electrodes[6], whose trend on the electrode n (assuming all the other electrodes are grounded) is described by the Shockley-Ramo theorem:

$$I^n_{ind}(t) = -\frac{q}{V_W}\vec{E}^n_W[\vec{x}(t)] \cdot \vec{v}(t) \tag{4.2}$$

where $\vec{v}(t)$ is the velocity of the moving charge, and $\vec{E}^n_W$ is the so-called weighting field of the electrode n at the position x where the charge is located at the time t. The weighting field of the electrode n is defined as the electric field that would be there if there were no charge, all the other electrodes were grounded, and the electrode n had applied a potential V_W [149]. By integrating eq. 4.2, one finds that when all the charges have arrived to the different electrodes, the total charge induced on the electrode n is equal to the charge that has reached that particular electrode (see [149] for a detailed treatment). From this, it can be concluded that the current on an electrode that doesn't receive charge will be bipolar (in general, the current is positive for a positive charge entering the electrode or a negative charge leaving the electrode, negative vice versa[7]). If we add an impedance element to the electrode, so that it is not grounded anymore, this complicates a bit the calculation of the induced currents (again, see [149] for details), however it holds true that the total charge induced on an electrode is equal

[4] Actually, one could imagine techniques to exploit photoelectric effect from S1 photons and detect charge. [147] performed the coating of the THGEM cathode side with CsI, exactly to induce photoelectric effect; however, the aim is to detect electroluminescence out of the electrons. For a compilation of novel ideas about how to obtain S1 and S2 hardware-wise, refer to [148].

[5] For this dissertation, q contains the sign of the charge.

[6] Notice that the current is induced during the movement of the charge, and not when the charge reaches the electrode!

[7] A pre-amplifier will invert the signals.

USC UNIVERSIDADE DE SANTIAGO DE COMPOSTELA

to the charge that has arrived to that electrode. A typical impedance element could be a pre-amplifier, often used as the next component of the readout chain. The signal can be read collectively, to have a single total charge value, or preserving the spatial information, if reading wire-by-wire, or using pads/strips. In the latter case, if a signal from a charge is induced in a pad/strip, a bipolar current signal will be induced in nearby pads/strips.

Pre-amplifiers are used in order to make the signals from the readout

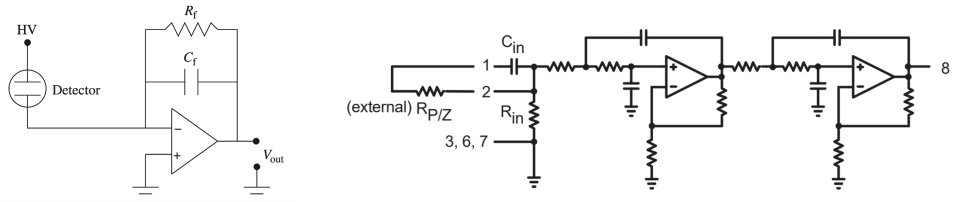

Figure 4.6: Example of circuits for a pre-amplifier (left, from [150]) and a shaper (right, from [151]).

wires/pads broader in time and higher in amplitude, decreasing the systematic errors when measuring these quantities [150]. A common pre-amplifier is the charge-sensitive amplifier[8], whose circuit is pictured in Fig. 4.6 (left): the detector charge output is fed to an operational amplifier (op-amp), which performs the integration of the signal on the capacitor C_f; the maximum amplitude of the output signal will be proportional to the input charge, and to $1/C_f$: hence, the capacity of C_f is selected to be small. In order to discharge the device, a feedback resistor R_f is also provided: after reaching the peak, the output signal decays with the time constant given by $R_f C_f$. The choice of $R_f C_f$ must be done in order not to give too long a tail, which may lead to severe pile-up of signals, and not too short a timescale, which may affect the proportionality of the maximum amplitude.

Often, the signal from the pre-amplifier is further processed by a pulse shaper, which is typically made of concatenated CR and RC filters (Fig. 4.6 right). Shapers turn the pre-amplifier signal into a gaussian-like one, characterized by a peak voltage proportional to the input charge [78] (see Fig. 4.7). The amplitude of such a pulse can eventually be read by a multichannel analyzer (MCA), an analog to digital converter (ADC) which can produce a histogram representing the pulse height spectrum [152].

[8]For a description of different pre-amplifiers, such as current-sensitive amplifiers, see [150]

USC UNIVERSIDADE DE SANTIAGO DE COMPOSTELA

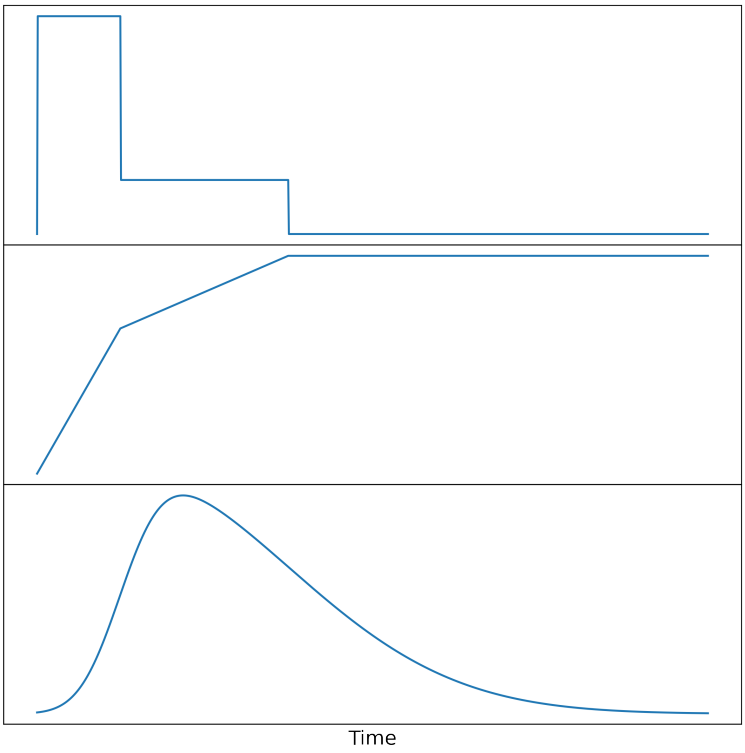

Figure 4.7: Top: current induced by the charge produced by a track parallel to the anode: the short pulse is given by the electrons, while the long pulse is induced by the slower ions (pulses not to scale). Center: signal produced by the pre-amplifier when receiving the pulse depicted in the top image (the current is integrated over time). The decay of the tail with time constant RC is not shown. Bottom: illustrative pulse yielded by the shaper (the time alignment and shape are not precise), whose peak value is proportional to the charge received from the pre-amp.

4.3.2 Optical readout

The alternative to the electronic readout is to read the light output. This can be done with different devices: PMTs, for example, are extremely sensitive devices, able to detect single photons, and diverse models are built to withstand different conditions, in terms of temperature and pressure, or to detect distinct wavelength ranges. These devices (shown in Fig. 4.8) are constituted by a vacuum tube equipped with a photocathode, several electrodes called *dynodes*, and an anode. If the photon to detect, impinging on the photocathode, produces an electron through photoelectric effect, this electron will then be amplified by the dynode chain with a cascade effect: each dynode has a more positive potential than the previous one, and when hit by an electron, it releases f new electrons, yielding finally a total gain

$$G = f^n \tag{4.3}$$

USC UNIVERSIDADE DE SANTIAGO DE COMPOSTELA

where n is the number of dynodes.

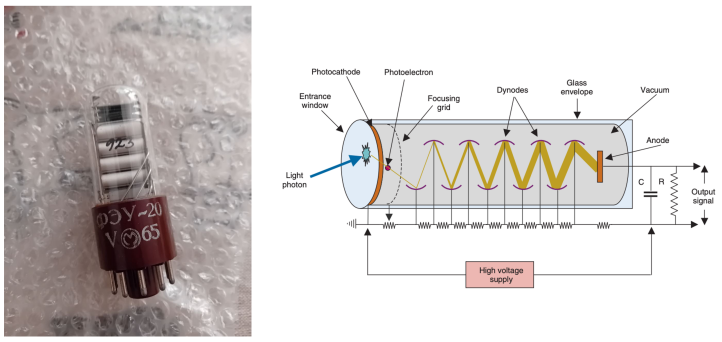

Figure 4.8: Left: picture of an old PMT. Right: scheme of a PMT tube, from [153].

Not all the photons that hit the photocathode will manage to free an electron (photoelectron); the probability for this to happen depends on the energy of the photon, even above the photoelectric effect threshold, and is usually well below 1 even for the wavelengths to which the sensitivity is maximum. This is also affected by the fact that the PMT tube material may filter out certain wavelengths, especially when considering VUV photons. Moreover, as the photoelectrons will be emitted isotropically, only half of them could possibly reach the dynodes. The combination of these factors defines the quantum efficiency of the PMT.
Analogous considerations can be done for other devices sensitive to single photons, such as photodiodes (e.g. SiPMs), which employ p-n junctions. PMTs or SiPMs can be arranged into arrays, similarly to pads in electronic readout, providing 2D spatial information; the pre-amp - shaper - MCA chain can also be connected to such devices, in order to collect the events energy distribution in a simple way.

If the amount of light is copious and emitted in the visible wavelengths, the opportunity to use cameras opens up. The usage of cameras is particularly handy, in that they provide readily available images with high spatial resolution [154]. The most widespread cameras are using CCD or CMOS sensors, whose pixels are all photodiodes. The difference between these devices resides in how the pixels are read (Fig. 4.9): for CCDs, signals from pixels are transferred along the columns and then to a unique amplifier and ADC chain; CMOS, on the other hand, have an amplifier for each pixel, and an ADC for each column: this makes the readout less noisy, but also slower [155]. In addition, currently there exists a camera (Timepix3 [156]) in which each pixel signal is read independently, featuring excellent speed and time resolution, namely 1.6 ns, used for example in the ARIADNE detector

USC UNIVERSIDADE DE SANTIAGO DE COMPOSTELA

[157, 158].
These different readout techniques can be used with different combinations, employing for example: PMTs for both S1 and S2, like in the XENON experiment [159] (or also SiPMs); PMTs/SiPMs for S1, and a camera to see ionization tracks, building a so-called *optical TPC* (OTPC); PMTs/SiPMs for S1, and electronic readout for S2; PMTs/SiPMs for S1, and both optical and electronic readout for S2.

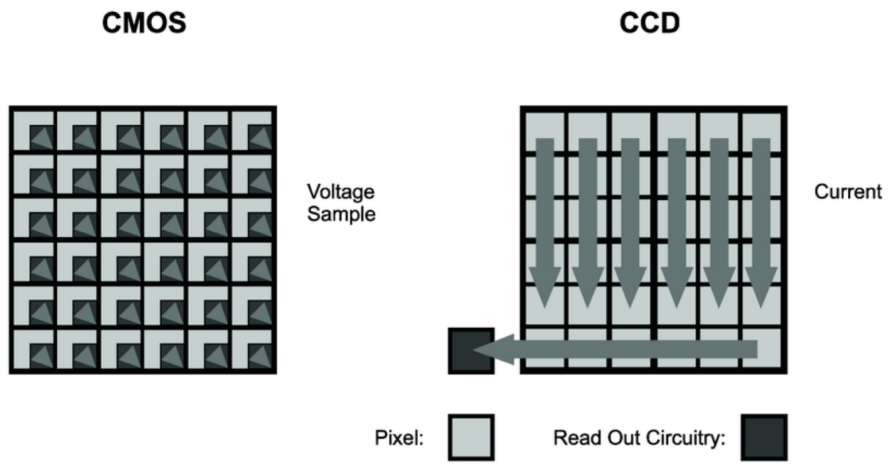

Figure 4.9: Readout mechanism of a CMOS camera (left) and a CCD camera (right), from [160].

4.4 Experiments

As real-life examples, two neutrino experiments will be presented: the first one is DUNE, a multi-purpose neutrino experiment that is currently under construction in the United States, and that will make extensive use of single-phase liquid argon TPCs. The second one is NEXT, a $0\nu\beta\beta$ experiment undergoing in Spain, which employs a high-pressure gaseous xenon TPC.

4.4.1 DUNE

DUNE will be a long baseline accelerator experiment: the beam of $\nu_\mu/\bar{\nu}_\mu$ (peaked at $\sim$ 2.5 GeV [161]) will be provided by Fermi National Accelerator Laboratory, in Illinois, where a near detector will be also placed; a far detector, as the name suggests, will be placed 1300 km far, at the Sanford

USC UNIVERSIDADE DE SANTIAGO DE COMPOSTELA

Underground Research Facility (SURF), in South Dakota (Fig. 4.10), an ideal distance to maximise the appearance probability of $\nu_e/\bar{\nu}_e$ at 2.5 GeV. The main goal of the experiment is to study neutrino oscillations parameters, including the δ_{CP} phase to probe the matter-antimatter asymmetry, and the neutrino mass hierarchy [162]. It will also be sensitive to solar neutrinos, but not only: it will participate to the collective effort of multimessenger astronomy, too. In fact, being able to detect neutrinos emitted from supernovae (SN), it will allow to deepen the knowledge of these celestial bodies, probing the core collapse mechanism, SN evolution in time, and black hole formation [163]. The near detector will also be employed to characterize a wide range of neutrino cross sections [164].

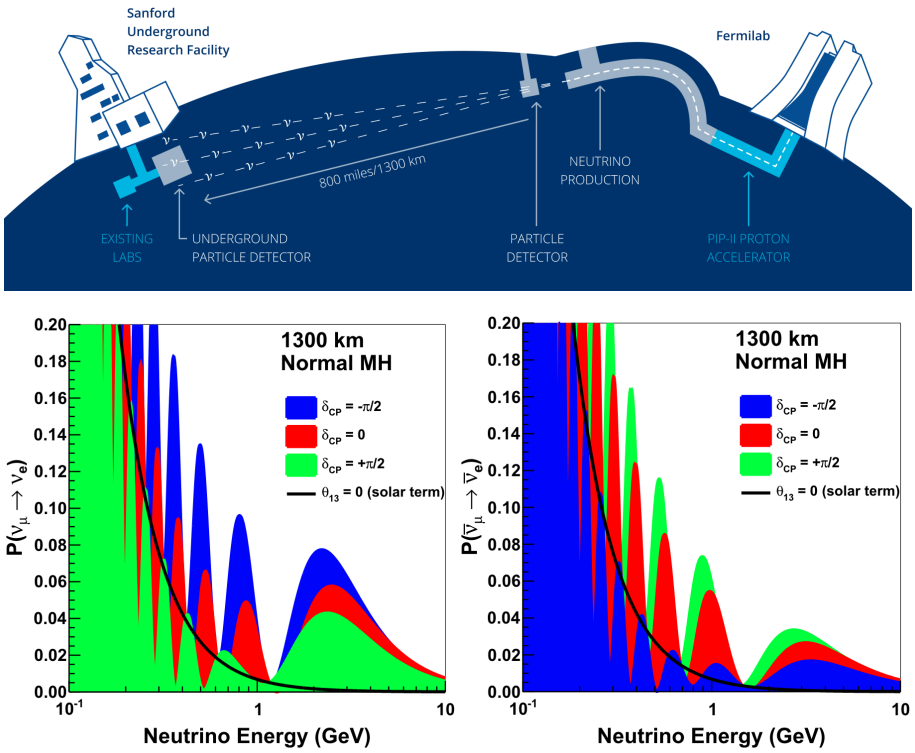

Figure 4.10: Top: scheme of DUNE experiment; the beam of $\nu_\mu/\bar{\nu}_\mu$ will be produced at Fermi National Accelerator Laboratory, in Illinois, and detected in-situ by a near detector (574 m from the source [161]). After traveling for 1300 km, the neutrinos will reach the far detector, at the Sanford Underground Research Facility (SURF), in South Dakota (image credit: Fermilab [165]). Bottom: appearance probability of $\nu_e/\bar{\nu}_e$ at the far detector, for different δ_{CP} values, in the case NH is the correct mass ordering. From [164].

USC
UNIVERSIDADE
DE SANTIAGO
DE COMPOSTELA

Near detector

The DUNE near detector (ND), placed at Fermi National Accelerator Laboratory is an essential component of the experiment, in that it will be employed to monitor the beam, and know with precision its initial composition. The three modules that compose ND will be placed 574 m from the neutrino source, aligned along the beam, and are described in depth in [166]; one of the three modules, SAND (System for on Axis Neutrino Detection) will be continuously monitoring the beam; on the other hand, there will be the possibility to slide the other two modules (NDLAr and the Temporary Muon Spectrometer, which will be upgraded into NDGAr in phase II of the experiment) away from the beam. This will exploit a feature of the neutrino beam, namely the energy distribution dependence as a function of the detection angle, to overconstrain the models to fit the collected data. Indeed, the fit parameters will have to fit different datasets at the same time, reducing potential biases. The system that will allow to move the NDLAr and NDGAr modules is called DUNE-PRISM (Fig. 4.11).

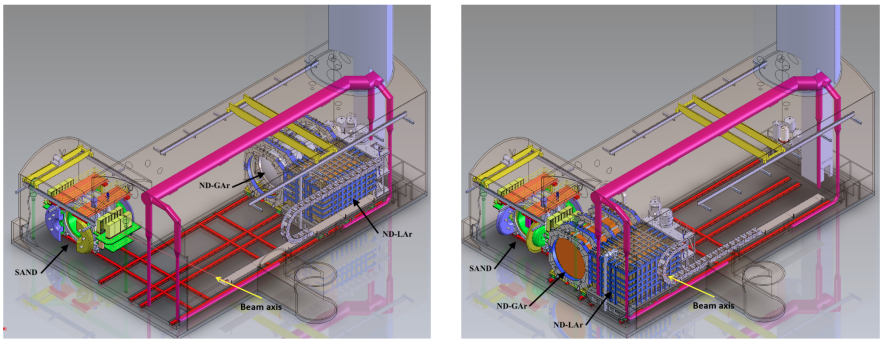

Figure 4.11: drawing of the near detector facility, showing the PRISM mechanism: while SAND is always on the beam trajectory, NDLAr (the most upstream with respect to the incoming beam) and NDGAr can slide, assuming every position from the one in the left figure to the one in the right one, taking data with different energy distributions depending on the angle with the beam. The image (from [167]) is for explicative purposes of the sliding mechanism, as some of the design of the detectors is outdated: for an up-to-date depiction, refer to Fig. 25 of [168].

As mentioned, SAND will be the only unmovable module of the near detector. It is a onion-like detector, containing two different trackers in the innermost layers, surrounded by an electromagnetic calorimeter (ECAL); in the outermost layer, a superconducting magnet of 0.6 T, inherited from KLOE, is placed in conjunction with its iron return yoke.

NDLAr will be a single-phase TPC operating with liquid argon. It uses a modular approach (ArgonCube technology), dividing the total volume

USC UNIVERSIDADE DE SANTIAGO DE COMPOSTELA

into smaller independents parts, each one equipped with its own cathode and readout. The latter is made of a pixelised charge readout for S2, and of two functionally identical SiPM-based systems able to detect single UV photons for S1.

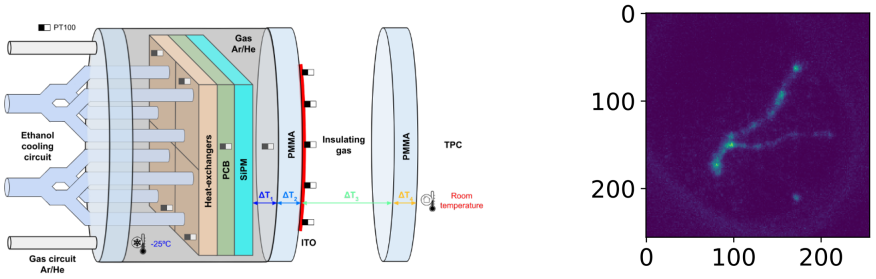

Figure 4.12: Left: scheme of the non-vacuum-based cryostat to cool down the SiPMs, from [169]: the SiPM are hosted in a PMMA container; the ethanol is cooled down to -25◦ and then transported to heat exchangers, which transfer the heat from the SiPM to the liquid. To keep the active volume at room temperature, a gas gap is included between the SiPM and the PMMA window, to which an active heating system (ITO coating) is applied. An additional argon region is interposed between the heating system and the TPC gas through another PMMA window. Right: some tracks observed in an Ar/CF_4 mixture with candidate structures (two glass-GEMs) for the OTPC prototype (from [170]).

Since the majority of neutrinos that will interact with NDLAr will be muon neutrinos, they will produce mainly GeV-scale muons upon interactions with NDLAr. Unfortunately, the LArTPC is not able to contain such particles above ~ 0.7 GeV/c. Since the muon momentum and charge are necessary for the neutrino energy determination, an additional module is needed downstream: this is what NDGAr was designed for. The base design for this module was a refurbishment of ALICE TPC (depicted in Fig. 4.3a), filled with high-pressure gas (10 bar), and surrounded by an ECAL, a magnetic coil, and a muon system. To provide useful data, the gas inside the TPC must be argon, since the FD modules will all be LArTPCs. R&D efforts are ongoing to turn the NDGAr TPC into an OTPC, wavelength-shifting the argon VUV light by means of a small addition (1%) of CF_4. S1 signal for the interaction time T_0 could be detected by means of SiPMs placed behind the cathode, and cooled down by a non-vacuum-based cryostat to keep the dark rate sufficiently low [169]; S2, on the other hand, could be amplified by means of stacked MPGDs, and observed by using a camera, such as a TimePix (Fig. 4.12 right). During my PhD I have contributed to the characterization of a prototype for the SiPM cryostat (Fig. 4.12 left) and of a suitable gas mixture, and I am participating at the effort for the commissioning of an OTPC demonstrator, but most of this work will not be reported in this thesis. Chapter 8, however, will be related to this project, since it will report a study on Ar/CF_4 secondary scintillation spectra and

USC
UNIVERSIDADE
DE SANTIAGO
DE COMPOSTELA

gains.

Far detector

The far detector (FD) of DUNE in the present moment is constituted by two modules (see for example [171]), both based on the single-phase LArTPC concept, each one containing 10 kton of argon of fiducial volume. There is, however, the possibility of building up to four modules in total; hence, there is room for novel ideas, since the technology for the additional modules have not been established yet. In this framework, the ARIADNE project proposes an optical readout solution for dual-phase LAr TPCs [172]: in 2018, the experiment was operated at the T9 beamline at CERN. It consisted of a 1 ton dual-phase TPC, equipped with four Electron Multiplying CCD (EMCCD) cameras to detect the secondary scintillation light produced in the gas phase thanks to a FR4 THGEM, after extracting the electrons from the liquid, and appropriately wavelength-shifted; four PMTs, also coated with a wavelength shifter and placed behind the cathode, captured the S1 signal, thus allowing in principle to reconstruct a 3D image of the tracks. A scheme of the setup is shown in Fig. 4.13 (left).

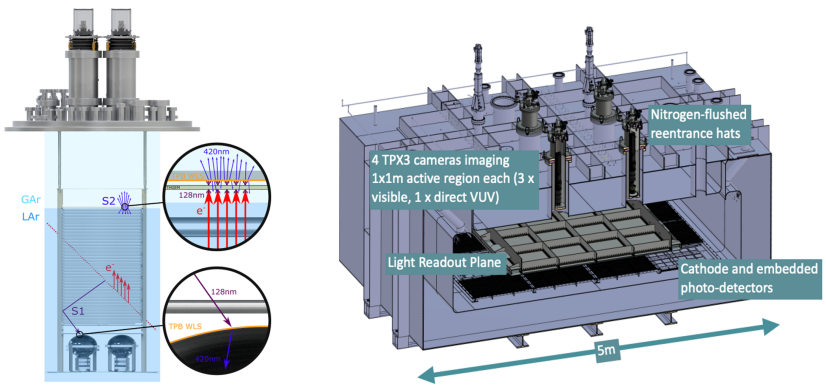

Figure 4.13: Left: scheme of the ARIADNE experiment before the upgrade (from [173]) Right: the protoDUNE cold box, adapted to host the ARIADNE experiment (from [158]).

The tracks captured with the cameras were the first optical images of argon interactions in a dual-phase LArTPC at a beamline [173]. The experiment was subsequently scaled up (ARIADNE$^+$, Fig. 4.13 right), with some further upgrades: the FR4 THGEM was replaced with a glass-GEM [174], and the EMCCD cameras was substituted with four TimePix3 cameras

USC UNIVERSIDADE DE SANTIAGO DE COMPOSTELA

which, together with the aforementioned excellent time resolution, provides a native 3D readout. The detector was installed inside the protoDUNE cold box, at the CERN Neutrino Platform, and succesfully tested in 2022 [158], demonstrating the promise of this technology for kilo-tonne LAr-based experiments like DUNE. Readouts based on resistive-protected structures coupled to strip readouts or to back-bonded QPix or LArPix chips represents an appealing possibility, too ([175, 176]).

4.4.2 NEXT

NEXT is an experiment probing the mass nature of neutrinos, looking for $0\nu\beta\beta$ decay. The experiment has been already operated in the NEXT-White version [177], the ten-time-bigger NEXT-100 is currently under development [178]. An active volume of xenon has been selected for the experiment, since this is the only gaseous element with a naturally occurring isotope undergoing double-beta decay (^{136}Xe).

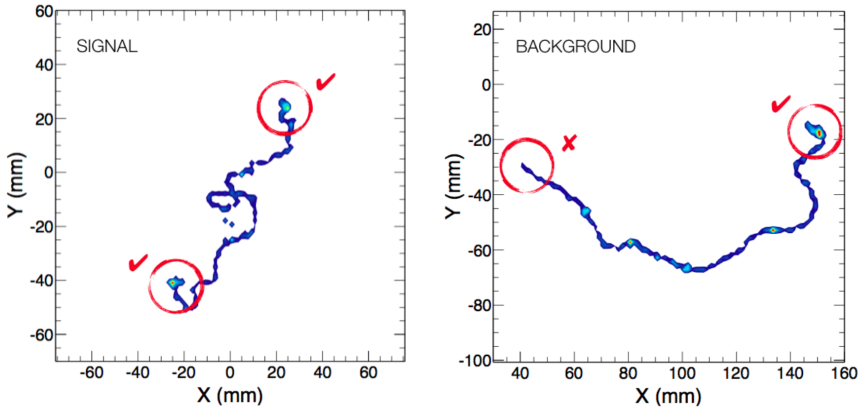

Figure 4.14: Simulated topology of a $0\nu\beta\beta$ decay (left) and a background event with a single electron (right). The $0\nu\beta\beta$ decay presents the two characteristic blobs corresponding to the Bragg peak of the emitted electrons. Image from [179].

The gas is kept at high pressure (10 bar) inside a TPC, and electroluminescence is produced thanks to planes of wires (the scheme of the detector has been shown in Fig. 4.3). The S2 signal is then detected by a grid of SiPMs, placed behind the anode, which provide the event topology, and by PMTs located under the cathode, which instead give a measurement of the event's energy (together with T0 from S1). Both detections are fundamental for the experiment, since the recognition of a $0\nu\beta\beta$ over background is a combination of two factors: one is the characteristic topology of the event, with the two emitted electrons leaving a track each, into opposite directions,

USC UNIVERSIDADE DE SANTIAGO DE COMPOSTELA

with a final blob corresponding to the Bragg peak (Fig. 4.14); the second one is the energy of the event, which must correspond precisely to the $Q_{\beta\beta}$ value of ^{136}Xe (2457.8 keV). It is clear that, for the second goal, an excellent energy resolution is needed; thanks to EL, a value slightly lower than 1% FWHM was obtained at $Q_{\beta\beta}$ [180].

USC UNIVERSIDADE DE SANTIAGO DE COMPOSTELA

5 Challenges in TPCs

Despite the already existing astounding ideas and advancements in building precise, sensitive and humongous detectors for particle physics, setting up an experiment never comes for free in terms of R&D. There are still many hurdles and room for improvement in the field. This chapter aims at providing a list, not exhaustive, of some of the challenges R&D researchers in noble elements-based TPCs bang their head against in laboratories all over the world. Since argon and xenon are the most widespread elements used in detectors, they will be the main focus of the following dissertation.

5.1 Electroluminescence in gas

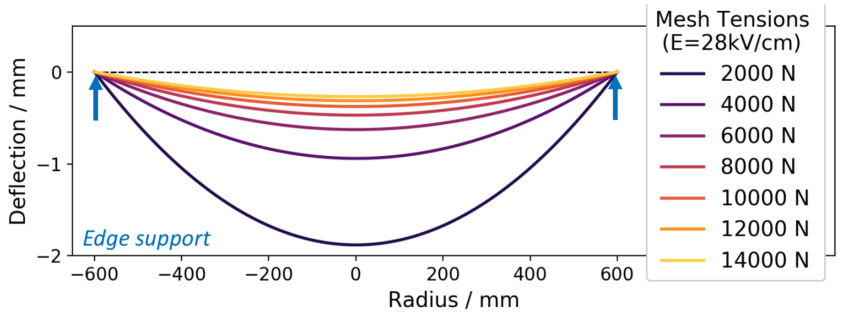

Figure 5.1: Effect of the electric field on a mesh: the central part of the structure bends (sagging), deforming the electric field. Image from [181].

USC UNIVERSIDADE DE SANTIAGO DE COMPOSTELA

Particle physics experiments widely use electroluminescence in the gas phase, be it in either high-pressure or dual-phase TPCs: it is employed for $\beta\beta0\nu$ experiments, such as NEXT, dark matter experiments, like XENONnT, DarkSide and PandaX, and some coherent neutrino scattering experiments (i.e. RED and GanESS) are also planning to resort to it. In order to achieve enough light yield at high gas densities (high P and/or low T), strong electric fields have to be applied. This is usually achieved by means of meshes or arrays of wires. This kind of structures display great performance in terms of energy resolution and single photon detection: NEXT reports an energy resolution of 0.91% at E = 2615 keV, close to the $Q_{\beta\beta}$ of ^{136}Xe [180]; DarkSide is able to extract a single electron from the liquid and detect $\sim$ 20 phe/electron out of it thanks to electroluminescence [182]. However, the bigger the size of the experiments, the more complicated the usage of meshes becomes, as they are devices that cannot be modular: hence, commissioning them prior to real operation would already require enormous setups. Moreover, the whole detector would be limited in the maximum applicable voltage, should the mesh have some local defect. Electrostatic forces must also not be forgotten: such big devices undergo sagging (Fig. 5.1), deforming the electric field.

Structures that can exploit modularity could be MPGDs such as GEMs, THGEMs or glass-GEMs, the latter being also stiff as a single large-area structure, more radiopure than FR4 and optically transparent [174, 183]. However, the thickness of THGEMs (either made of FR4 or glass) is O(0.5 mm), GEMs are even ten-fold thinner: very good for producing photons in charge avalanches, but definitely not for electroluminescence[1]. Using electron avalanches coupled with optical readout is a widespread technique, providing competitive results in terms of spatial and potentially time resolution (using e.g. a TimePix camera), and allowing for real-time imaging of particle tracks when coupled to a CCD or CMOS camera [184, 185, 170] (see Fig. 5.2). Stacking multiple GEMs allows to reach high optical gains, other than shielding a potential SiPM/PMT plane on the cathode side (dedicated to the detection of primary scintillation) from the secondary scintillation emission. An energy resolution of 25% FWHM has been reported with a triple GEM configuration in an Ar/CO_2 70/30 mixture using a 5.9 keV x-ray source [186].

Despite all the advantages just described, using avalanches also carries some issues: more fluctuations in the signal that lead to a worse energy resolution, ion feedback and the risk of sparks, which limit the rate capability by creating dead times in the detector. This makes the use of avalanches

[1] Remember that electroluminescence in this context is used for light produced by primary electrons without charge multiplication.

USC UNIVERSIDADE DE SANTIAGO DE COMPOSTELA

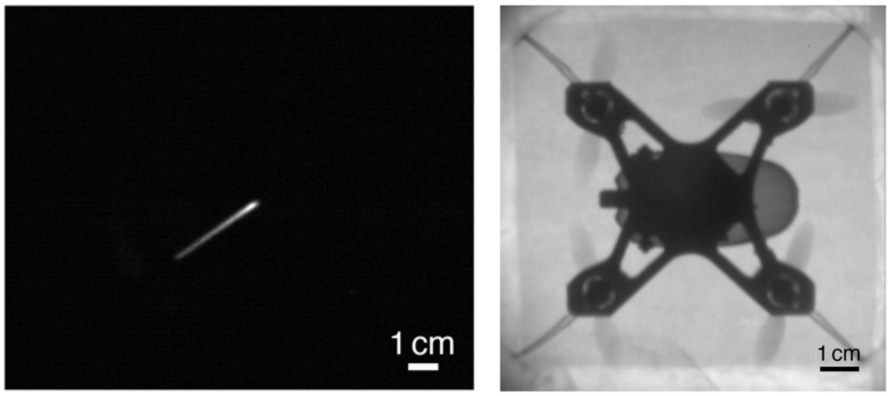

Figure 5.2: Left: alpha particle track obtained with a triple-GEM (avalanche mode) coupled to a 6 megapixel CCD camera: the Bragg peak at the end of the particle track is clearly visible, allowing for direction reconstruction. Right: an example of triple-GEM optical readout potential outside of particle physics: for instance, it can be used for radiography. The image shows the radiograph of a miniature drone obtained with the same setup as the alpha track; a video of the flying drone was even taken with the same technique. Images from [185].

not suitable for some experiments, which need a high rate capability, or an energy resolution as close as possible to the Fano factor, or detection of single electrons: these kind of experiments must resort to electroluminescence. Recently, to combine the advantages of MPGDs structures with the ones of electroluminescence, sturdy, thick (5 mm!) patterned structures have been designed with PTFE [187], PMMA [188] or PEN [189]. A scheme of the PTFE structure, from the AXEL collaboration, is reported in Fig. 5.3. The PMMA and PEN structures, on the other hand, will be discussed in detail in chapter 9 as part of this PhD project.

5.2 Detection of noble gas scintillation

As explained in chapter 2, noble gases emit most of the light in the VUV range: for this reason, detecting the second continuum has been the primary choice in many experiments. Nevertheless, VUV light is easily absorbed by many materials, including glass. Moreover, while it is easy to find PMT models that are sensitive enough to Xe second continuum emission (for instance R7378, R11410-21, R8520-406 from Hamamatsu [190, 191]), using most of SiPMs with Xe, or detecting Ar second continuum at all, is more of a challenge. Despite some models do exist, often alternatives need to be resorted to, in order to shift the light to longer wavelengths: some reasons could be because the quantum efficiency to VUV light is still too low, or

USC UNIVERSIDADE DE SANTIAGO DE COMPOSTELA

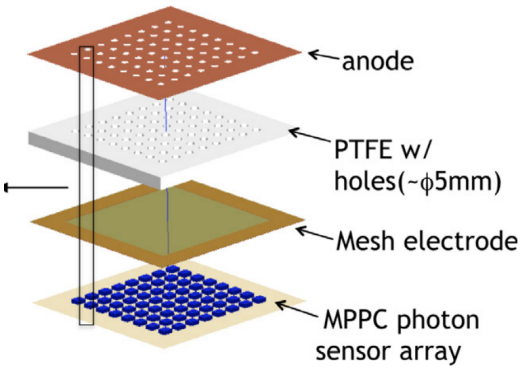

Figure 5.3: Scheme of the PTFE "electroluminescence collection cell" developed by the AXEL collaboration for electroluminescence in GXe. The structure is 5 mm thick, in order to have a good EL yield. Image from [187].

because the device is operated at cryogenic temperature, which is not compatible with the specific sensor model. Another reason may be that the experiment plans to use CCD or CMOS cameras, which have the peak of sensitivity in the visible light. In order to shift the wavelength of the light, two methods are commonly used:

1. Solid wavelength shifting: typically it is achieved by coating some area of the detector (such as plates placed in front of the PMTs [192], the PMT window itself [193], the vessel surface [194]), or the reflector tube running along the field cage, with a wavelength-shifting material. One of the most commonly used solid wavelength-shifters is tetraphenylbutadiene (TPB), whose absorption and emission spectrum is reported in Fig. 5.4. TPB has a high wavelength shifting efficiency (WLSE) and a fast re-emission time [195]. On the other hand, evaporation of TPB at large scale is complicated since it requires high vacuum during the deposition [196]; the material was also observed to dissolve in liquid xenon [197] over a time of only 20 hours and in liquid argon in similar timescales [198], potentially degrading the WLSE and the quality of the xenon. Recently polyethylene naphthalate (PEN) has also been proposed as wavelength shifting material [199], in the form of films [200] or even bulk for the electroluminescence structure itself [189].

2. Gaseous wavelength shifting: another way to obtain light in the visible spectrum is to add a certain amount of gas able to absorb the VUV of the noble gas and re-emit it at longer wavelengths. Typical substances used for this purpose in noble gases are CF_4, TMA [201], N_2 [202], and TEA [71]. Even small quantities of heavier noble gases

USC UNIVERSIDADE DE SANTIAGO DE COMPOSTELA

can effectively shift light in the lightest species (like xenon in argon [203]), since the transfer reactions between them are so effective that the gas will scintillate at the longer wavelength of the additive [204]. Using gaseous wavelength-shifting, time constants can be shortened, compared to the case in which you let the gas emit, and then shift the wavelength. Moreover, the wavelength-shifted light is easier to transport and collect, making it convenient in terms of light yield to have the wavelength shifter directly inside the gas.
Following the spirit of using additives in the gas as wavelength shifer, Chapter 8 will focus on the study of Ar/CF_4 secondary scintillation as part of my PhD project.

Studies of liquid argon doped with xenon [203, 205, 206, 207] show that it is in principle possible to mix a small amount of additives at cryogenic temperatures even below the freezing point of the wavelength shifter, at least up to a level of $\sim$ 1000 ppm. In [206] 2% N_2 was also successfully added to liquid argon, however the work didn't focus on the wavelength shifting properties of the mixture.

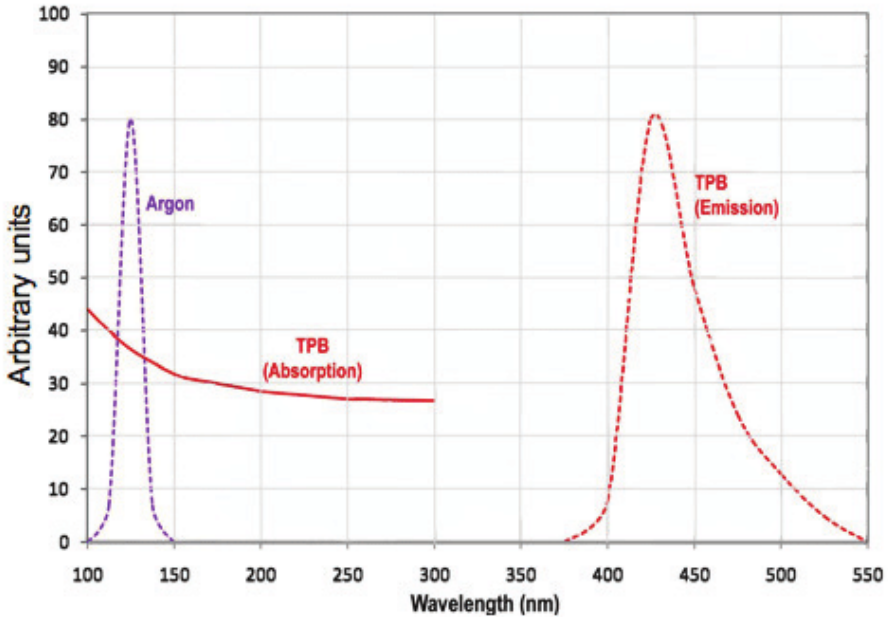

Figure 5.4: TPB absorption and emission spectra, compared to argon second continuum. The VUV emission is converted into a violet-bluish-colored light peaked at λ $\sim$420 nm. TPB is highly efficient absorbing VUV light, and re-emitting it at wavelengths that are commonly easier to detect by optical sensors. Image from [208].

The need to detect VUV light may be also overcome by resorting to other scintillation channels rather than the second continuum, namely the

USC UNIVERSIDADE DE SANTIAGO DE COMPOSTELA

third continuum, neutral bremsstrahlung or the infrared emission discussed in Chapter 2.

5.3 Dual-phase TPC gas-liquid interface

Many experiments in the field of Rare Events Searches resort to the dual-phase TPC technology. Nevertheless, operating it poses technical challenges, in that a painstaking control is needed of the liquid-gas interface: waves, or changes in the liquid level due to pressure/temperature variations, may impair the electron transmission between the two phases; moreover, the lack of parallelism between the transmission/multiplication structure and the interface would make the signal non-uniform, impacting on the energy resolution and the discrimination between signal and background [209].

A proposed solution to this problem is to create a local gas-phase by means of a bubble trapped underneath a GEM/THGEM fully immersed in the liquid (bubble-assisted liquid hole multiplier, or LHM). The technology was tested in LXe [210] and LAr [211]: in both cases, some heating wires are placed between the anode (bottom of the GEM) and the optical sensor, in order to create the bubble, although spontaneous bubbling is also observed; traveling through the bubble gas, electrons emit copious electroluminescence light (∼400 photons/e in Xe-LHM [212]). The bubble-assisted LHM is sketched in Fig. 5.5 (a), while a picture of the bubble between the THGEM and the heating wires is shown in Fig. 5.5 (b); Fig. 5.5 (c) displays the reconstruction of an anular ^{241}Am α source in LXe and LAr using the bubble-assisted LHM: the resolution is $\sim 200\mu$m RMS in the case of xenon, while it is worse for argon, due partly to the lower EL yield, and partly to the fact that the image was reportedly taken under not optimal conditions [213]. For the 5.5 MeV ^{241}Am alpha source, an energy resolution $\sigma/E = 5.5\%$ for S2 was achieved in LXe, while in LAr $\sigma/E = 13.5\%$. A more detailed treatment of the bubble-assisted LHM, with a focus on the bubble dynamics inside the structure holes, will be provided in chapter 7 as part of my PhD work.

Another option to deal with the interface problem is the floating hole multiplier (FHM), depicted in Fig. 5.6: a GEM-like structure with a lower density than the liquid (e.g. FR4 THGEMs for LXe) is left floating on the gas-liquid interface, ensuring in this way that the extraction field will "follow" the surface perturbations. Measurements taken in xenon with a 4.7 MeV α source yielded an energy resolution $\sigma/E = 10.1\%$ for S2 and an yield of 650 phe/α particle at the PMT photocathode for S1 [214].

Finally, another way to deal with the interface problem, is to get rid

USC UNIVERSIDADE DE SANTIAGO DE COMPOSTELA

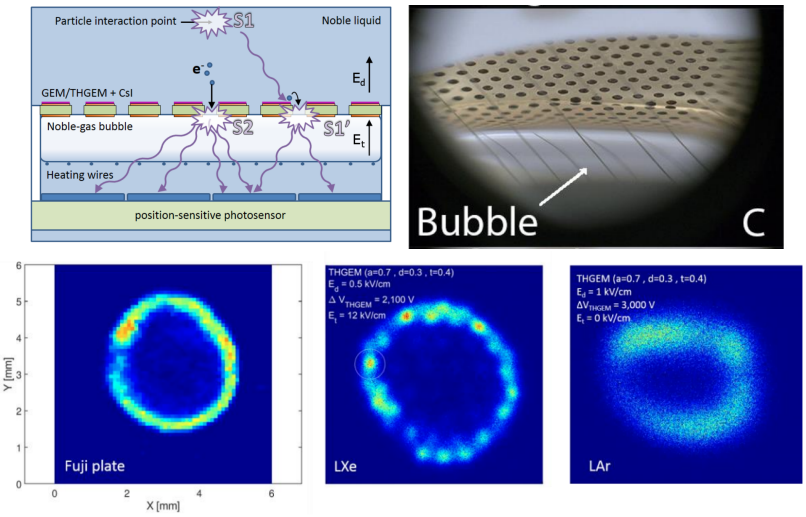

Figure 5.5: Top left: experimental setup to study the bubble-assisted LHM [211]; apart from the production of S2 within the bubble, the system is equipped with CsI coating on the THGEM cathode; thus, VUV photons from S1 can induce photoelectric effect, allowing to get an additional S1' signal through electroluminescence. Top right: picture of a bubble of GXe trapped underneath a TH-GEM immersed in LXe (the image is reversed) [216]. Bottom left: auto-radiographic ^{241}Am alpha-source image, recorded with a Fuji phosphor-imaging plate; center: image of the same source reconstructed using the bubble-assisted LHM in xenon; right: preliminary image of the same source reconstructed using the bubble-assisted LHM in argon [213].

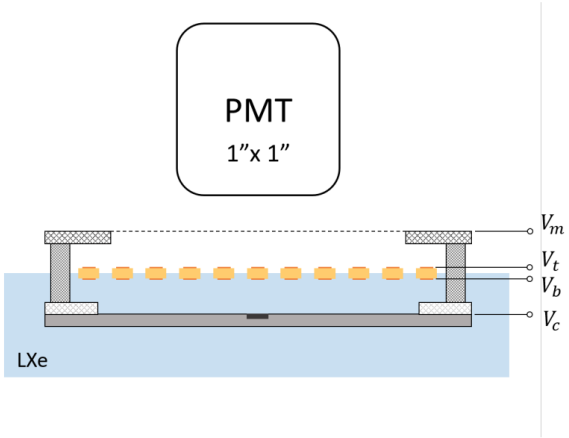

Figure 5.6: Concept of a floating hole multiplier: the GEM-like structure, thanks to the lower density with respect to the noble liquid, is able to float, following the changes on the gas-liquid interface. Electroluminescence occurs in the gaseous phase. Image from [214].

USC UNIVERSIDADE DE SANTIAGO DE COMPOSTELA

of the interface altogether, that is, to resort to a single-phase TPC. This idea has been nurtured for a long time at the moment of writing, and actually implemented/planned in experiment such as MicroBoone [215] and DUNE, detecting directly primary electrons. This choice is indeed suitable for experiments with relatively high energy deposit ($\gtrsim$ MeV), but unviable when lower energies are involved, such as in coherent neutrino scattering. Moreover, particles that cause nuclear recoils (NR) in the medium, such as neutrinos undergoing coherent scattering, or some dark matter candidates, transfer most of the energy, as the name suggests, to the nuclei, at the expense of ionization. Therefore, they have a much lower S2 yield which, with present technologies, absolutely needs some amplification to be detected[2].

5.4 Charge multiplication in liquid phase

Single-phase TPC is great: the low diffusion in the medium provides better spatial resolution than in gas, and not dealing with the gas-liquid interface makes handling the experiment much easier. However, it is well known that the devil makes the pots but not the lids: in this case, one of the lids is electron multiplication. In the absence of avalanches, experiments that need to detect nuclear recoil interactions cannot resort to a single-phase TPC, as at most few tens of electrons are produced from this kind of interaction, while the noise levels are usually higher.

In liquid xenon, some stable avalanches were actually observed: in [217] avalanches were observed using a microstrip plate, with a multiplication factor of order 10; in [218, 219, 92] the production of avalanches was achieved by means of thin wires (diameter ≤ 10 μm). [92] reports a threshold for electron multiplication of 725 kV/cm. Despite these observations, at the best of my knowledge no single-phase LXe TPC exploiting charge multiplication does exist at the moment, due to the low gains and technical difficulties to work at high fields.

Even more grim does the scenario for liquid argon look: [220] produced a remarkable stable avalanche gain of ~ 100 using a sharp needle (~ 0.25 μm radius) in Ar/Xe mixtures; in [221] an array of tips produced multiplication in pure liquid argon, but the behavior of the avalanches reported in literature in the pure medium is mostly erratic and not reproducible [222]. Currently there are R&D efforts towards stable charge amplification in LAr from the LArCADe project, that is attempting to attain it by means of

[2]Single-phase experiments for nuclear recoils have been/are being constructed, such as XMASS and DEAP, but they aim to detect solely the S1 signal.

USC UNIVERSIDADE DE SANTIAGO DE COMPOSTELA

nano-fabricated tip arrays at the anode [223].

5.5 Sparks inside the detector

As explained in Sec. 3.2.3, under certain conditions a spark could occur inside a detector, due to either the Townsend or streamer mechanism. When this happens, some components may undergo serious damage, e. g. in the multiplication structure (Fig. 5.7) or in the readout chain; the dead time of the detector can also increase [224].

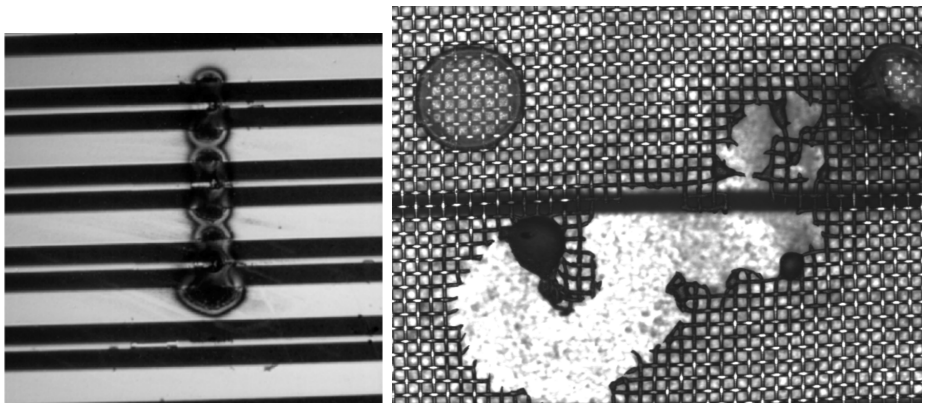

Figure 5.7: Damages caused by sparks in a micro-strip gas chamber (MSGC), from [140], and a Micromegas, from [225].

In gaseous detectors, as mentioned in Sec. 3.2.3, a typical way to deal with this problem is to add some molecular quencher, whose function was explained in Sec. 2.5. Depending on the molecular additive, some problems can be encountered:

1. Attachment (at low fields or of dissociative type in the multiplication region), quenching or photon absorption can degrade the energy resolution and decrease the yields (S2); high quenching can also affect the S1 signal. In Fig. 5.8 the effect on the signals is shown for $ArCF_4$ (low quenching) and $ArCH_4$ (high quenching) mixtures: S1 completely disappears when 2% CH_4 is added to argon.
2. At cryogenic temperatures, it is difficult to add quenchers since many have higher melting points, and high purity is required in order to properly drift the electrons, as well as to collect the primary scintillation light (S1).

USC UNIVERSIDADE DE SANTIAGO DE COMPOSTELA

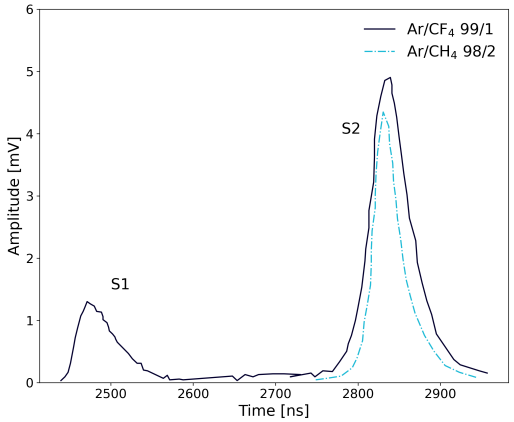

Figure 5.8: Effect of high quenching (Ar/CH_4 98/2) on the S1 signal, compared to low quenching (Ar/CF_4 99/1): in the former case S1 is completely absent. The signals are taken in the band 250-400 nm and are from data presented in [226].

3. Even in presence of a quenched gas, sparks can still occur if the Raether limit is reached.

Another way to handle the issue of sparks is to resort to resistive materials[3]. This idea was pioneered in 1971 [227], by using semiconductive glass in a parallel plate chamber, and further brought forward in 1981 [228], when the resistive plate chamber (RPC) was developed. RPCs are parallel plate detectors, filled with quenched gas, whose electrodes are covered with a material (typically bakelite, or any of its pseudonyms) of high bulk resistivity ($\rho \sim 10^{10} - 10^{11} \Omega$ cm). In the presence of a resistive electrode, when a streamer develops, the charge locally builds up in the material, causing a decrease of the electric field, thus limiting the development of the discharge (Fig. 5.9).

Following the RPC breakthrough, and using the same working mechanism, the idea of implementing resistive materials for spark quenching was applied to MPGDs, too. For GEM-like structures, the resistive thick GEM (RETGEM) concept was developed by V. Peskov in the mid-2000s [230]: resistive kapton was glued to both sides of the PCB board before applying the copper electrodes. Starting from the WELL configuration, μ-RWELLs were also produced [231]: the readout plane is coated with a resistive layer,

[3]The approaches of quenchers and resistive materials are, in fact, not mutually exclusive. Resistive materials can be employed in quenched gases for protection if a spark occurs, and quenching can be useful to reduce diffusion, feedback and streamer development even when using resistive-protected structures.

USC UNIVERSIDADE DE SANTIAGO DE COMPOSTELA

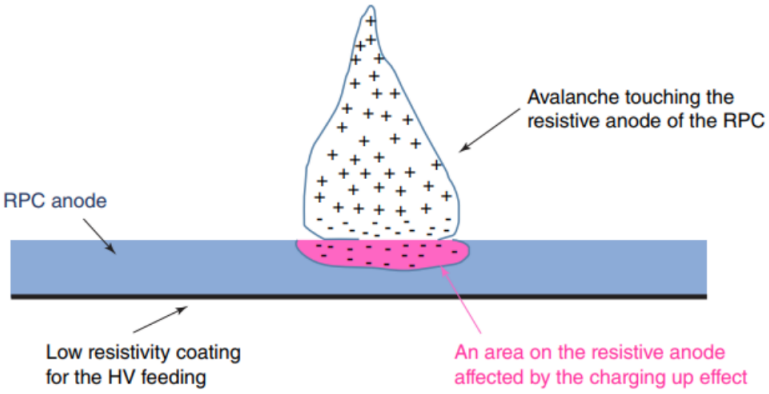

Figure 5.9: Effect of a resistive anode on a streamer: a local charging up in the material leads to a decrease of the electric field, limiting the development of the discharge (from [229]).

and then merged with a GEM structure. RWELLs and RPWELLs, built starting from a THGEM, also utilize the WELL configuration (Fig. 5.10): the former features a resistive layer between the THGEM bottom and the readout plane, which allows to evacuate the charge through the surface of the resistive material, while the latter makes use of a resistive plate, exploiting its bulk resistivity. Analogous concepts were developed, for instance, for Micromegas [232, 233] and MSGCs [234].

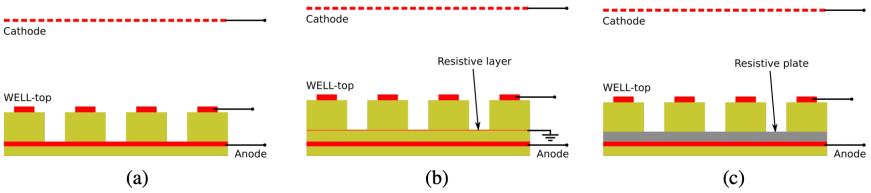

Figure 5.10: Depiction of a WELL configuration (a), an RWELL (b) and an RPWELL (c). Image from [235].

Resistive materials may also provide other benefits to the detectors other than spark quenching, the main ones being [236]: adjusting the charge-induction profile from moving charges to improve space resolution, by spreading the signal over a bigger readout area [237, 238, 239]; reducing local charging-up and suppressing surface discharges in high voltage feedthroughs [240], MPGDs like MSGCs [241, 242], and TPC field-cages [166] (Fig. 5.11).

In order to obtain an effective performance from the resistive material, it is important to choose the appropriate resistivity, be it either bulk ρ_v or

USC UNIVERSIDADE DE SANTIAGO DE COMPOSTELA

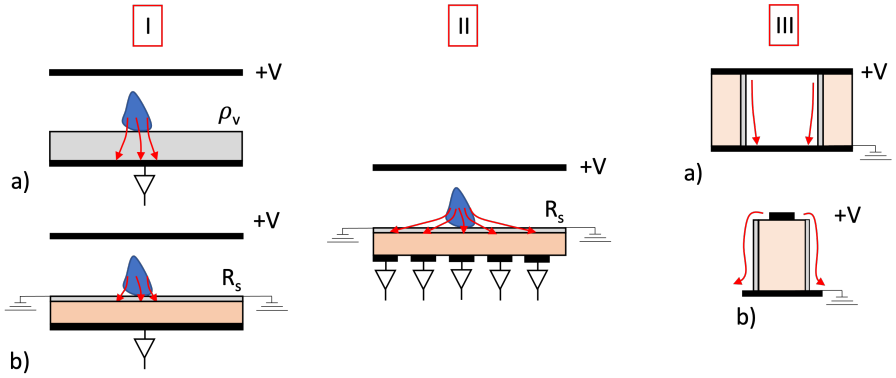

Figure 5.11: Most common situations of practical interest for use of resistive materials in gaseous and liquid particle detection technology. Ia-Ib) spark quenching: current flow is limited to a small area, reducing the electrostatic energy available in case an avalanche reaches a too large size. II) cluster-size tuning: current flow is adjusted in order to facilitate signal induction over a larger region, leading to oversampling and better spatial reconstruction of the charge centroid. III) mitigation of charging-up and surface discharges: current flow through uniform resistive materials minimizes charging-up and provides suitable boundary conditions matching the electrostatic potential in the active medium. Image and caption from [236].

surface R_S. For linear, homogeneous and isotropic coatings, sheets or plates, they relate through $R_S = \rho_v/t$, where t is the material thickness. Approximate orders of magnitude can be found in Table 5.1, for either coatings or plates.

case	R_S[MΩ/□]	ρ_v[GΩ · cm]
Ia	-	0.1-1 to 10^3-10^4[243]
Ib	10-1000 [244]	-
II	0.5-2.5 [237, 239]	-
$IIIa$	1000-10000 [166, 245]	-
$IIIb$	1000-10000 [240]	-

Table 5.1: Surface and bulk resistivity values employed by various authors in most typical applications. In I) the lower limit is imposed by loss of spark quenching and the upper one by loss of rate capability (charge build-up). For typical geometries, the values given in II) lead to cluster sizes at the millimeter scale. In III) the lower limit is given by current consumption, the upper limit is setup-dependent. Table and caption from [236].

The values presented in Table 5.1 fall in a range of low interest for industrial purposes, since materials with these resistivities are "bad insulators". However, nowadays a decent range of suitable materials do exist for oper-

USC UNIVERSIDADE DE SANTIAGO DE COMPOSTELA

ation at room temperature, such as Diamond-like carbon (DLC), carbon-loaded kapton (CLK) [230], Semitron ESD2251, semiconductive glass, bakelite, Fe_2O_3/YSZ-based ceramics [246] and 3D-printed thermoplastic plates doped with carbon nanotubes [247].

Focusing on spark quenching purposes[4], these challenges have also to be addressed:

1. Rate capability: for practical purposes, in this context the detector can be seen as an RC circuit, where the main component of resistance is given by the resistive material. Since the charge will be evacuated with a timescale given by RC, it follows that the higher the resistivity of the protection, the longer it will take to clear the charge after an event or a spark. For this reason, a reduction of the detection efficiency occurs at high rate of events. Thus, the resistivity of the material has to be tuned appropriately, finding a compromise between a sufficient protection and an adequate rate capability, as shown in Table 5.1, case Ia and Ib.

2. Usage at cryogenic temperatures: many resistive materials display an Arrhenius behavior with temperature: $\ln(\rho(T)) = a + b/T$ [248]. Hence, at cryogenic temperature most of such materials behave as perfect insulators, leading to the aforementioned charging-up problems. Some plastic materials such as the 3D-printed thermoplastic [249] or CLK may be promising for such operations due to their flat response with temperature; on the other hand, a ferric-based ceramics was successfully operated at LXe temperature in a Ne/CH_4 atmosphere [250]. Chapter 6 will be dedicated to the characterization and operation of resistive materials suitable for liquid noble-element detectors, as part of my PhD project.

3. Coupling to the structures: ensuring good contact between the GEM-like structure and the resistive material is important in order not to decrease the efficiency of the detector. Sometimes the two surfaces are glued together, requiring a challenging procedure: indeed, the structure is exposed to the risk that some glue may enter inside the holes, becoming a source for discharges [251]. At cryogenic temperature, the different thermal expansion coefficients of the various materials come also into play, complicating the picture further [5].

[4] Some of these problems can apply also to the other usages of resistive materials.

[5] For small surfaces, as the ones that will be discussed in the next chapter, a sufficiently good contact can be achieved by pressure.

USC UNIVERSIDADE DE SANTIAGO DE COMPOSTELA

USC
UNIVERSIDADE
DE SANTIAGO
DE COMPOSTELA

Part II

Part II

USC
UNIVERSIDADE
DE SANTIAGO
DE COMPOSTELA

USC
UNIVERSIDADE
DE SANTIAGO
DE COMPOSTELA

6 Resistive materials for spark quenching

Chapters 3 and 5.5 have pictured the phenomenon of sparks inside a detector, and its destructive potential. In Sec. 5.5 it was showed that, despite the need for resistivities ranges that are usually not of industrial interest, a wide range of materials for resistive protection has been developed nowadays for operation at room temperature. With the aim of seeking resistive protection for cryogenic operations, a part of my PhD was dedicated to characterizing the properties of some promising materials (mainly DLCs and ceramics), building RWELLs and RPWELLs out of them, and testing them inside a detector at liquid argon temperature.

USC UNIVERSIDADE DE SANTIAGO DE COMPOSTELA

6.1 RWELL

The following section (6.1.1) is based on the paper:

Diamond-like carbon coatings for cryogenic operation of particle detectors

S. Leardini [a], Y. Zhou [c d], A. Tesi [b], M. Morales [a], D. González-Díaz [a], A. Breskin [b], S. Bressler [b], L. Moleri [b], V. Peskov [a]

[a] IGFAE, Universidade de Santiago de Compostela, Spain
[b] Weizmann Institute of Science, Department of Particle Physics and Astrophysics, Rehovot, Israel
[c] State Key Laboratory of Particle Detection and Electronics, University of Science and Technology of China, Hefei 230026, China
[d] Department of Modern Physics, University of Science and Technology of China, Hefei 230026, China

Journal and Article Information
Journal name: Nuclear Instruments and Methods in Physics Research Section A: Accelerators, Spectrometers, Detectors and Associated Equipment
Publisher: Elsevier
ISSN: 1872-9576
Year of publication: 2023
DOI: 10.1016/j.nima.2023.168104

6.1.1 Characterization of DLCs

DLC coating

The DLC samples that were studied were produced at the University of Science and Technology of China (Hefei). The DLC was deposited on top of a kapton or FR4 substrate, two common detector substrates of different mechanical and surface properties (Fig. 6.1), through a technique called magnetron sputtering [242]. A Teer 650 device (from Teer Coating Ltd) at the SKL in Hefei was used, allowing evaporations up to surface dimensions of 25 $\times$ 25 cm^2. The substrates were cleaned with ethanol and dried in an oven at 70 °C. The sputtering lasted for about 20-60 min, resulting in film thicknesses generally in the range 10's-100's nm (more details on the process can be found on [242]). In total, six DLC-coated Kapton samples of different surface resistivities were produced, named with letters A-F, and two DLC-coated FR4 samples, a and f, made with sputtering conditions

USC UNIVERSIDADE DE SANTIAGO DE COMPOSTELA

similar to A and F. Different film thicknesses and resistivities were obtained by changing the sputtering time. As a reference, the thickness of the most conductive FR4 sample presented in this work was estimated to be compatible with $t = 160 \pm 10$ nm, the uncertainty reflecting the variation between the measurement performed in Hefei (with a step profiler) and the one conducted at USC-RIAIDT (by grazing-angle X-ray reflectometry on a twin sample evaporated on silicon substrate).

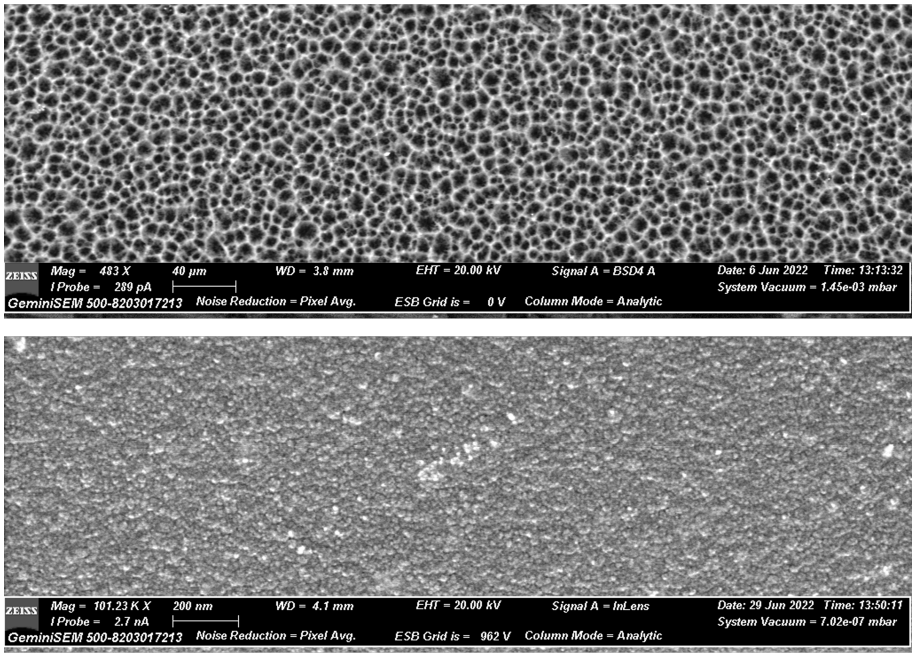

Figure 6.1: Images taken with scanning electron microscope of the DLC films on FR4 (40 μm scale, top) and Kapton (200 nm scale, bottom). The scales have been chosen to highlight the main features observed.

Cryogenic setup

The surface resistivity as a function of temperature was determined with a physical property measuring system (PPMS, Model 6000) from Quantum Design, which assures thermal equilibrium at every measuring step. The samples were measured following a square four-point probe method over a ~ 1 cm^2 area. Two geometrical corrections were applied according to [252]: the first one (F1) takes into account the effects due to finite thickness t of the sample, while the second one (F3, following the notation from [252]) corrects for border effects if the electrodes are placed close to the sample edges (at a distance d). The corrections for these samples (see Fig. 6.2) amounted to about 30%.

USC UNIVERSIDADE DE SANTIAGO DE COMPOSTELA

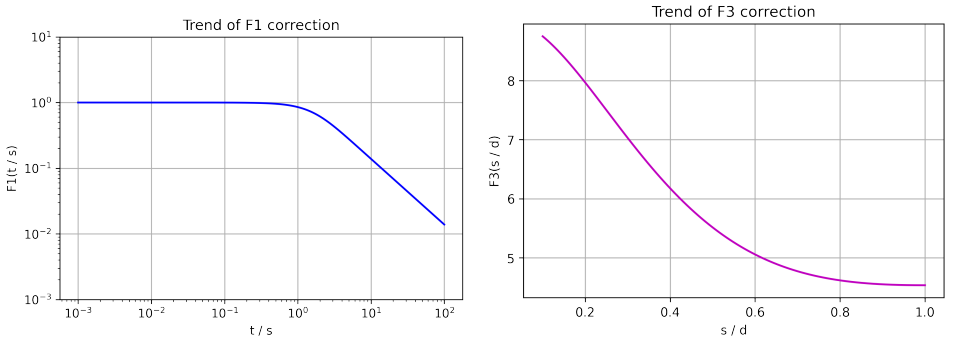

Figure 6.2: Corrections to apply to the measurements performed with the four-point probe, following [252]. Here s is the distance between the electrodes, t the sample thickness and d the distance between the electrodes and the sample edge.

Unfortunately, the PPMS sensitivity reaches up to $R_S = 30$ MΩ/□, which lays at the lower-end of the resistivities that had to be measured, so a cryogenic setup was purposefully built to cover the entire range. The sample was prepared by applying two silver epoxy [253] stripes, which approximately enclosed a 1 cm^2-square; it was then placed on the floor of a stainless steel vessel, electrically insulated with a thin Kapton layer and covered with APIEZON N grease to ease thermal coupling between the sample and the metal. Two spring-loaded probes allowed to bias a silver epoxy strip and to read the return current on the second one through a Keithley 6487 picoammeter. The system was operated in helium atmosphere (1.5 bar) after being evacuated down to 10^{-3} mbar with a Pfeiffer Duo 016B pump. This allowed to mitigate the effect of water freezing, which affected the resistivity measured otherwise (as well as the system mechanics). To reach cryogenic temperatures, the vessel was immersed in a LN-filled Dewar acting as a cryostat, until reaching 77 K. Then it was removed from the nitrogen bath, letting it warm up through its thermal inertia (drift mode) while measuring the resistivity at defined time steps. A PT100 sensor placed on the kapton, close to the sample, allowed to measure the temperature at the same time through an Arduino micro-controller board. A sketch of the setup is shown in Fig. 6.3.

The system was commissioned by comparing the measurements for the least resistive sample with the ones obtained with the PPMS; the two measurements showed an agreement within 10 %, confirming that a sufficiently good thermal equilibrium is reached in the DLC samples through this procedure (Fig. 6.4). Identical conclusions were extracted in a special PPMS run performed in drift mode, where the sample is also let warm up in a helium atmosphere, unimpeded.
The error bars in this work have been extracted from the standard devia-

USC UNIVERSIDADE DE SANTIAGO DE COMPOSTELA

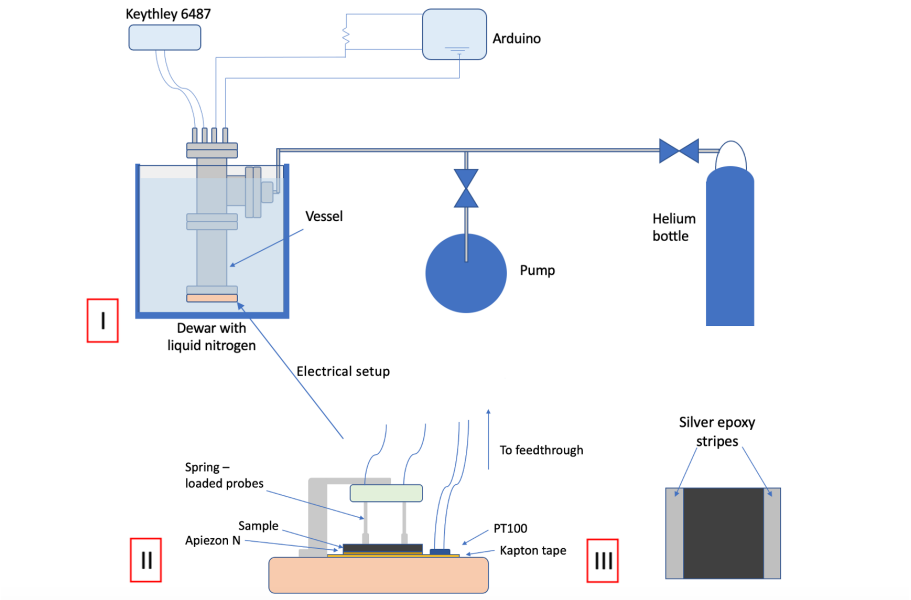

Figure 6.3: Scheme of the setup used for electrically characterizing DLC-coated samples. I) Full view: the sample is laying on the part of the vessel colored in orange. The vessel is immersed in liquid nitrogen inside a Dewar, and connected to a Pfeiffer Duo 016B pump and a helium bottle. It also communicates with a Keithley 6487 and an Arduino thanks to the upper feedthrough. II) Close-up of the electrical setup inserted into the vessel: a Kapton layer electrically insulates the sample from the vessel bottom, while an additional layer of Apiezon N grease improves the thermal coupling. The sample is connected to two spring-loaded probes to measure the surface resistivity; close to the sample, a PT100 is used to measure the temperature inside the vessel. III) Top view of the sample: the two silver epoxy electrodes define a 1 cm $\times$ 1 cm square.

tion of two independent measurements. This deviation must be understood as an estimate of the systematic uncertainty from the setup. A statistical interpretation in terms of confidence intervals is not straightforward without accomplishing a relatively high number of measurements, and was not deemed necessary given the scope of the investigation and the small relative deviations between measurements, generally at the level of 10-20%.

I-V curves

The characteristic I-V curves of the samples were obtained both at room and liquid nitrogen temperature, showing a perfect ohmic trend (Fig. 6.5-lines represent the fit results). This simplifies the characterization as a function of temperature: the applied voltage was generally chosen to provide a good precision for the resistivity measurement at LN temperature (starting point

USC UNIVERSIDADE DE SANTIAGO DE COMPOSTELA

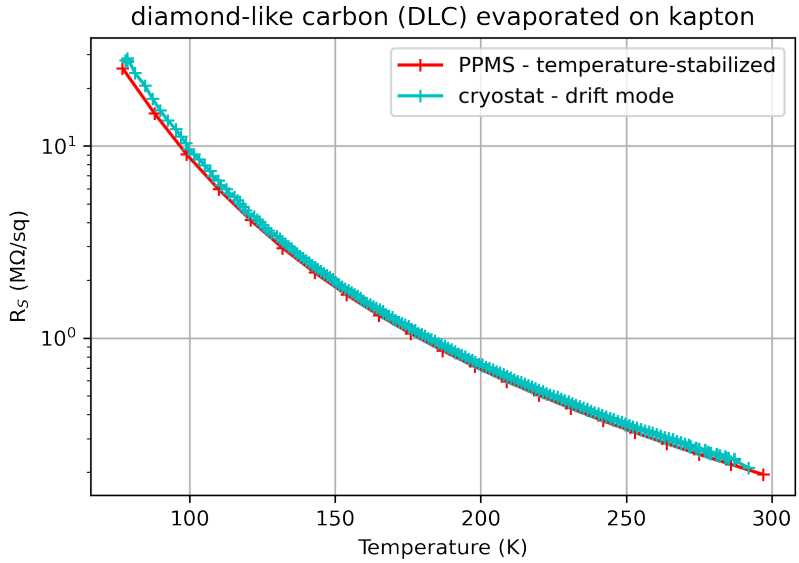

Figure 6.4: R-T curves for sample A as measured with PPMS (red) and with the dedicated setup described in section 6.2.2, developed for high-resistivity measurements (light blue).

of the scan).

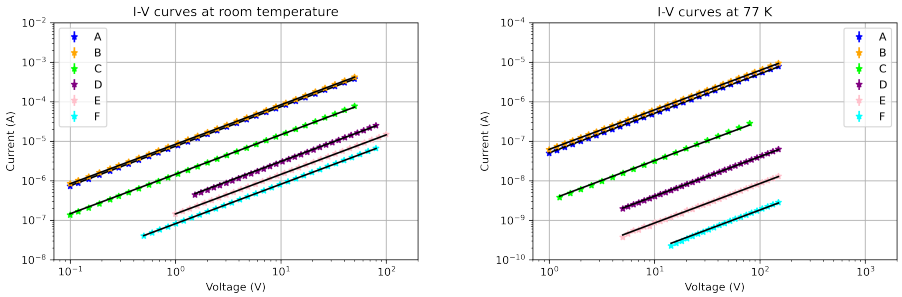

Figure 6.5: *I-V* curves of the DLC-coated Kapton samples at room temperature (left) and liquid nitrogen temperature (right). Results for the FR4 samples (a, f) are not shown, but display the same trend. Super-imposed, the fit to $I = V/R$ lines.

Uniformity and dependence from substrate

The electrical uniformity of the coatings was studied by measuring on four representative 1 cm^2-regions. Illustratively, results for sample A, 10 $\times$ 10 cm^2 in size, are shown in Fig. 6.6. The four measurements show an agreement within 20%, down to *LN* temperature, a result compatible with

USC UNIVERSIDADE DE SANTIAGO DE COMPOSTELA

the 23% uniformity values reported earlier in [242]. The other samples were tested for uniformity at room temperature, providing analogous results.

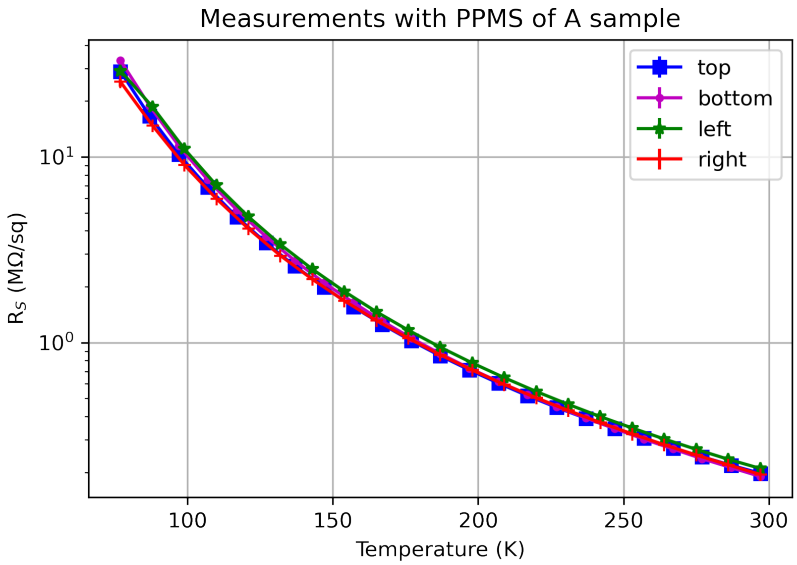

Figure 6.6: *R-T* curves from sample A taken with the PPMS device at USC-RIAIDT, for 1 cm^2 regions chosen over the sample (10×10 cm^2 in size).

Kapton and FR4 are used regularly for manufacturing gaseous detectors, so they are interesting for understanding which role the substrate may play in the properties of the film. Fig. 6.7 shows the result of such study for the couples A-a, F-f, made under similar sputtering conditions. Although the results are not compatible within the errors, the lack of a systematic effect (the deviation goes to opposite directions for the two couples) between FR4 and Kapton points to a small dependence with the substrate. Variations are likely due to small changes in the initial conditions of the sputtering machine.

R-T curves

R-T curves are shown in Fig. 6.8, with error bars estimated from the deviation between two independent measurements taken with the setup described in Fig. 6.3 (for the A sample, the four available measurements from the PPMS were used instead).

USC UNIVERSIDADE DE SANTIAGO DE COMPOSTELA

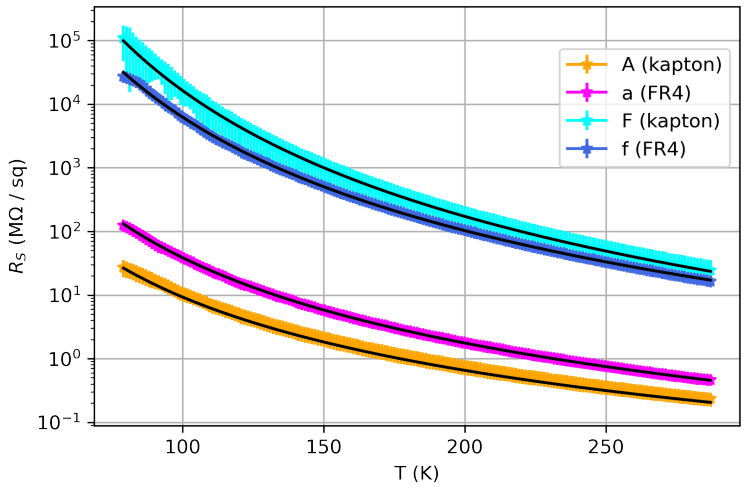

Figure 6.7: Comparison of samples with Kapton and FR4 substrates, grouped in couples for which similar parameters of the sputtering machine were attempted (A-a, F-f). The lack of a systematic deviation points to small changes of the sputtering process as the main source of discrepancy. The line represents the fit to the function described later in text.

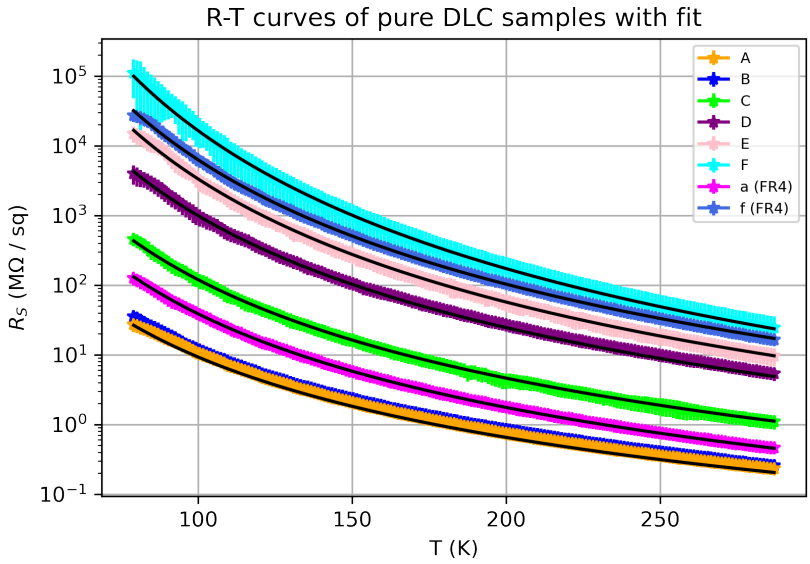

Figure 6.8: *R-T* curves for all DLC-coated samples, together with a fit to a 2-dimensional variable-range electron hopping model (black solid lines), following eq. 6.1.

For thin coatings based on amorphous carbon it has been shown, using for instance percolation theory, that the coating resistance is highly

USC UNIVERSIDADE DE SANTIAGO DE COMPOSTELA

anisotropic with the following dependence:

$$R = R_{S,300} * \exp\left(\left(\frac{T_0}{T}\right)^a - \left(\frac{T_0}{300}\right)^a\right) \tag{6.1}$$

being $a = 1/4$ for the resistance across the bulk (3D) and $a = 1/3$ for the resistance over the surface (2D) [254]. The form of eq. 6.1 has been chosen such that the pre-factor $R_{S,300}$ represents the surface resistance at 300 K. T_0 is an effective temperature given by:

$$T_0 = \frac{\beta}{k_B \cdot g \cdot r} \tag{6.2}$$

where k_B is the Boltzmann constant, β a factor of order 1, g the density of states at the Fermi level of the film material, and r the localization radius around it. This type of conduction mechanism is called *variable-range hopping* (vrh) [255].

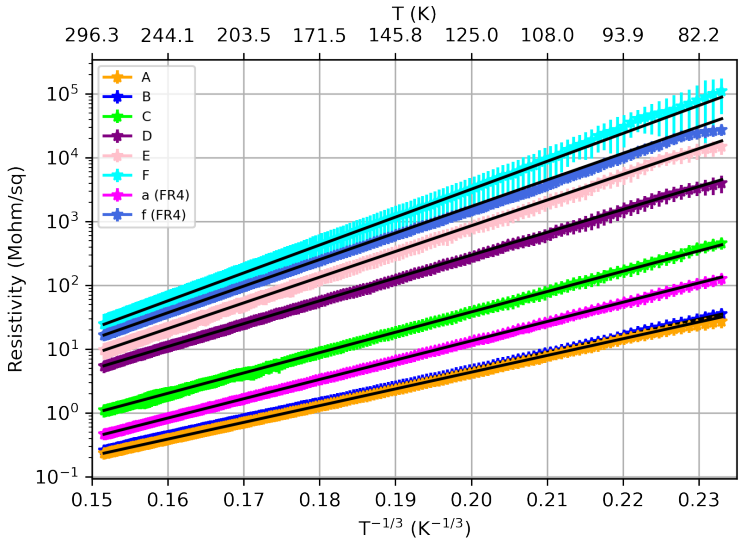

Figure 6.9: R_S as a function of $T^{-1/3}$ (lower x-axis) and T (upper x-axis) in a logarithmic representation, demonstrating the 2-dimensional variable range hopping assumption. Only for very low temperatures small deviations appear, an effect likely attributable to the measurement setup.

A logarithmic representation of the resistivity curves as a function of $T^{-1/3}$ confirms in fact the expectation from 2D-vrh (Fig. 6.9), reproducing early observations by Hauser on amorphous carbon [256]. The parameters T_0 and $R_{S,300}$, found by fitting each curve individually and keeping $a = 1/3$,

USC UNIVERSIDADE DE SANTIAGO DE COMPOSTELA

display a power-law correlation in our data, as $T_0 \sim R^{\nu}_{S,300}$, with $\nu = 0.3$ (Fig. 6.10). Such a power-law dependence is expected in 2D-vrh conduction (e.g., eq. 9.4.5 in [254]).

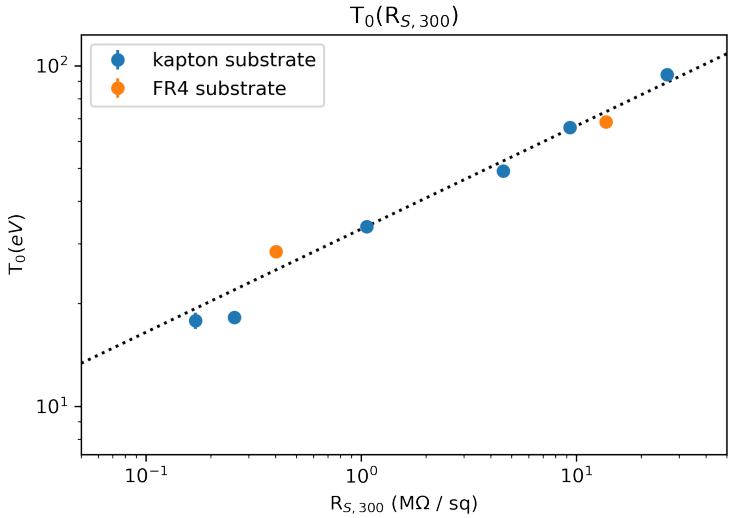

Figure 6.10: Parameter T_0 as a function of the room temperature resistivity, $R_{S,300}$, together with a fit to a power-law. Blue points refer to the Kapton substrate and orange ones to FR4.

Using function 6.1 and the relation between T_0 and $R_{S,300}$, iso-resistivity curves can be obtained numerically for each starting value of $R_{S,300}$ (Fig. 6.11). These numerically-generated curves are well described by a function of the form

$$R_{S,300} = C * \exp(T^b) \tag{6.3}$$

with $0.38 < b < 0.5$ in the range considered. This plot allows to predict the room-temperature surface resistivity that needs be targeted at the sputtering machine, to obtain the desired resistivity at the temperature of operation. With the range of $R_{S,300}$ studied in this work (top and bottom lines in the figure, corresponding to films A and F), it is clear that the ranges of potential interest as per table 5.1 are reasonably well covered, in particular when aiming at operation at liquid argon and liquid xenon conditions.

USC UNIVERSIDADE DE SANTIAGO DE COMPOSTELA

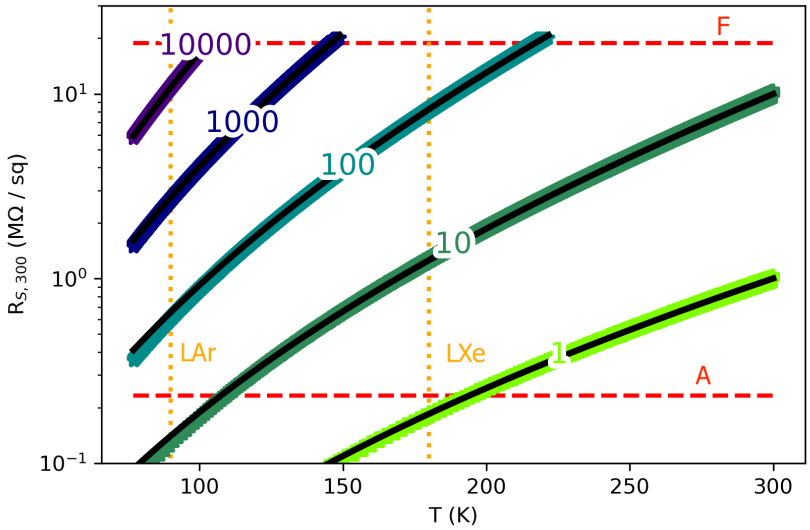

Figure 6.11: Iso-resistivity curves as a function of temperature, generated numerically. Once the desired R_S-value (1, 10, 100, 1000, 10000 MΩ/□) is chosen for a certain operating temperature, the corresponding room temperature value ($R_{S,300}$) can be determined. The latter is in principle configurable at the sputtering machine, through the total sputtering time. Overlapped to the numerically-generated curves, the black line is the approximate fit to function 6.3. Dashed lines A and F represent the two most extreme $R_{S,300}$ values in this study.

Long-term stability

Long-term stability is a crucial aspect for applicability in particle-physics experiments, expected to run over time spans of years. First, a relevant effect of humidity was excluded, by studying sample B directly in open air (R.H. around 40%) and in helium atmosphere, with the two measurements agreeing within 0.5%. By simply storing the samples in plastic bags, for more than 1 year, all kept their conductivity within less than a factor $\times 2$ variation.

Another concern is the appearance of charge-depletion effects, that limit for instance ionic conductors. Therefore, the stability of one of the least and most resistive samples (B and F) was probed at LN temperature, in the 2-stripe configuration (Fig. 6.2.2). To accelerate the migration of charge carriers, a voltage of 500 V was applied for about five hours, while keeping the vessel inside LN. Both samples showed variations of current of $\leq 2\%$ (Fig. 6.12), which points towards a good stability of the material. Furthermore, measurements in helium atmosphere at room temperature, where the ageing can be greatly accelerated, showed no significant variation for transported

USC UNIVERSIDADE DE SANTIAGO DE COMPOSTELA

charges as large as 2 C/cm^2. The absence of charge-depletion effects, combined with the observed T-dependence, are compatible with a 2-dimensional variable-range conduction mechanism based on electron hopping.

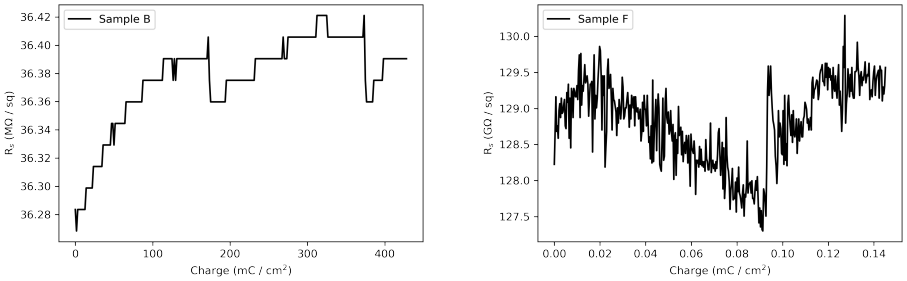

Figure 6.12: Long term stability test for samples B (left) and F (right) at LNT. Both samples show variations of current $\leq 2\%$ when 500 V are applied for more than 5 hours in a helium atmosphere.

Although the transported charges are fairly low, it must be noted that cryogenic detectors often work at very low interaction rates. In the case of DUNE Far-Detector [257], for instance, background rates are expected to be dominated by ^{39}Ar decays [258]; with this background, the charge density Q at the anode of a resistive-protected multiplication structure (e.g., [250]) would be about 60.5 μC/cm^2 over $t = 10$ years, even if assuming a (probably optimistic) gain $G = 100$. This value is surpassed in our ageing tests even for the most resistive film (Fig. 6.12-right). The calculation comes from a ^{39}Ar decay rate of $\nu \sim 1.4$ kHz/m^3 and an average energy per decay $E = 220$ keV [259], assuming a drift length $L = 10$ m:

$$Q = \frac{eG\nu ELt}{W_I} \tag{6.4}$$

Keeping in mind that the conduction mechanism of DLC does not seem to change in the T-range studied (as inferred from the good agreement with the 2D-vrh hypothesis), the stability observed up to 2 C/cm^2 at room temperature is expected to apply to LN too; if this is true, these coatings could be employed also in high-rate applications, at either temperature. Ageing effects related to chemical reactions or deposits from the avalanche process cannot be evaluated by this simple procedure, and require sustained detector operation.

USC UNIVERSIDADE DE SANTIAGO DE COMPOSTELA

Conclusions

We propose the use of resistive diamond-like carbon (DLC) coatings for applications related to gaseous and liquid particle detectors operating in cryogenic conditions, down to liquid nitrogen temperature. Our characterization of DLC samples on Kapton substrates (10×10 cm^2) reveals a good behaviour in terms of linearity, surface uniformity (electrical and physical), easiness of adjustment of the electrical properties, and long-term stability across a range of temperatures; these add to other properties well established in literature such as low chemical reactivity and radiation tolerance. In particular, the surface-resistivity range R_S = 1-10000 MOhm/$\square$ has been reasonably covered by the films studied here, in the temperature range comprising the LXe and LAr liquefaction points. This resistivity range is expected to cover a variety of problems beyond spark-quenching: examples are cluster-size tuning, field-cage or feed-through lining, and more.

The electrical behaviour with temperature and time is compatible with a conductivity mechanism based on 2-dimensional variable-range electron hopping. This important observation opens the path to a better and more detailed understanding of the surface and bulk conductivities of DLC coatings used in modern particle-physics instrumentation.

USC
UNIVERSIDADE DE SANTIAGO DE COMPOSTELA

The following section (6.1.2) is based on the paper:

The cryogenic RWELL: a stable charge multiplier for dual-phase liquid argon detectors

A. Tesi[1,a], **S. Leardini**[1,2], **L. Moleri**[1], **D. Gonzalez-Diaz**[2], **A. Jash**[1], **A. Breskin**[1], **S. Bressler**[1]
[1] Department of Particle Physics and Astrophysics, Weizmann Institute of Science, Rehovot, Israel
[2] Instituto Galego de Física de Altas Enerxías, Univ. de Santiago de Compostela, Santiago de Compostela, Spain

Journal and Article Information
Journal name: The European Physical Journal C
Publisher: EDP Sciences, Società Italiana di Fisica and Springer Berlin Heidelberg
ISSN: 1434-6052
Year of publication: 2023
DOI: 10.1140/epjc/s10052-023-12162-x

6.1.2 Operation in a detector

Experimental setup

Some DLCs samples (all with kapton substrate) characterised in the previous session were tested as resistive protection at liquid argon temperature at Weizmann Institute of Science. During this study, three detector concepts were investigated: THGEM, THWELL, and RWELL; as a reminder, the three configurations are schematically presented in Fig. 6.13. The first investigated configuration consisted of a double-sided 3x3 cm^2, 0.8 mm thick THGEM (0.5 mm diameter holes distributed in a hexagonal pattern with 1 mm pitch, and ∼0.1 mm hole rim) followed by an induction gap of 2 mm and an induction field E_i = 5 kV/cm (see Fig. 6.13a). The second structure was a 0.8 mm thick THWELL detector: a 3x3 cm^2, 0.8 mm thick single-sided THGEM structure (same specifications as before) directly coupled to a metallic anode (see Fig. 6.13b). The RWELL was realized pressing the single-sided THGEM electrode against the metallic anode, interposing a DLC sample between them (see Fig. 6.13c). To create electrical contacts the DLC layer and the readout were connected to copper wires using cryogenic conductive epoxy (Master Bond EP21TDCS-LO). An electrically-insulating cryogenic epoxy (Stycast 2850FT) was subsequently used to encapsulate the components on top of the readout anode PCB board (see Fig. 6.14).
DLC films with different surface resistivities were tested, in order to as-

USC UNIVERSIDADE DE SANTIAGO DE COMPOSTELA

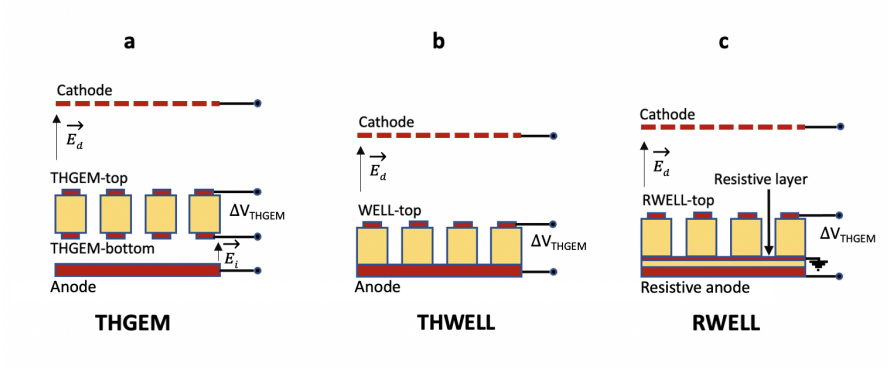

Figure 6.13: Scheme of **(a)** a THGEM (LEM) detector followed by an induction gap and a readout anode; **(b)** a THWELL detector, with a metallic anode at its bottom; **(c)** a RWELL detector, with a thin-film resistive anode decoupled from the metallic anode by an insulating plate. In all three cases, the drift gap was equal to 15 mm and the THGEM structure (double-sided in a) and single-sided in b), c)) was 0.8 mm thick.

sess the quenching properties at cryogenic temperatures. The response of the RWELL configuration with the lowest resistivity (sample A, with R_S ~10 MΩ/□ at 90 K) was found to be similar to those of non-resistive readouts, thus it is not reported here. In Table 6.1, the values for the relevant R_S at room temperature and at 90 K are given.

DLC sample	R_S at RT	R_S at 90 K
F	∼ 14 MΩ/□	∼ 20 GΩ/□
C	∼ 1 MΩ/□	∼ 200 MΩ/□

Table 6.1: Surface resistivity at room temperature and at 90 K for two different DLC samples.

All the electrodes (i.e. cathode, THWELL, resistive layer and readout electrode) were biased by an HV power supply (CAEN N1471H) or via a charge-sensitive preamplifier (Cremat: Model CR-110 with CR-150-R5 evaluation board). The latter was equipped with a protection circuit composed of surge arresters (8EC 90, EPCOS-TDK Electronics) in parallel and a series resistor of 220 Ω. The time evolution of the detector gain was studied in order to establish stable operation conditions. For gain stabilization studies, the signals from the preamplifier were fed to an amplifier (Ortec Model 450); the amplified signals were digitized by a multi-channel analyzer (Amptek MCA 8000D). For all the other measurements, waveforms from the preamplifier were acquired using a digital oscilloscope (Tektronix MSO 5204B). Histograms of the preamplifier signal amplitude were also acquired using the oscilloscope. Currents from the electrodes were read out by a digitizer (NI USB-6008) and monitored using LabVIEW SignalExpress [260].

USC UNIVERSIDADE DE SANTIAGO DE COMPOSTELA

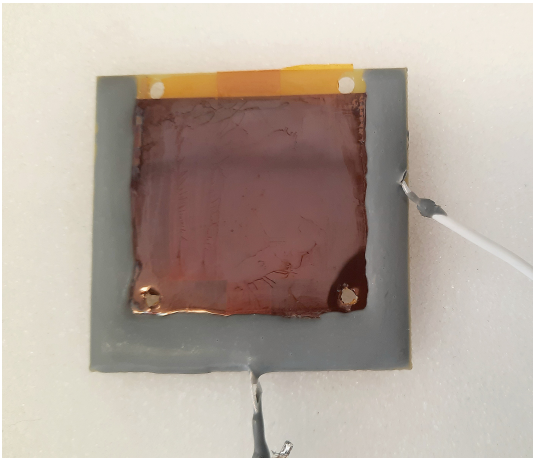

Figure 6.14: Resistive anode composed by a DLC layer fixed on a PCB board with electrically-insulating cryogenic epoxy. The electric connections, realized with cryogenic conductive epoxy, are encapsulated and connected with coaxial wires.

Cryostat

The measurements were performed in a dedicated LAr cryostat, WISArD (Weizmann Institute of Science liquid Argon Detector) described in detail in [211] (Fig. 6.15): the system is composed of an outer vacuum chamber (OVC) and an inner vacuum chamber (IVC). The former is kept in vacuum during operation, to ensure thermal insulation; the latter is a 150 mm tall cylindrical chamber (100 mm diameter) that can be filled with ∼250 ml of LAr.

The assembly is suspended from the top flange, equipped with feedthroughs for voltage biasing and readout. The cryostat is also equipped with four viewports having different positions and angles, that however were not used for this experiment. Argon liquefaction is done on cooling fins cooled by a Cryomech PT90 pulse tube refrigerator. Temperature of the liquefaction fins is maintained by a closed-loop feedback using a CryoCon temperature controller (Model 24). The liquefied argon flows in through a 1.5 m long double-wall, vacuum-insulated transfer tube into the chamber.

Each detector configuration was operated in the saturated vapor phase of argon at 90 K. The operation in the vapor phase rather than in the liquid minimized losses due to electron recombination and extraction (see Fig. 3 in [262]); in this way a higher number of ionization electrons could be collected. This was realized by inserting the detector assembly inside a Teflon cup, as depicted in Fig. 6.16. Argon was liquefied into the cryostat until a temperature of 90 K was measured in the gaseous phase at the level of the assembly (temperature sensor in Fig. 6.16). The pressure inside

USC UNIVERSIDADE DE SANTIAGO DE COMPOSTELA

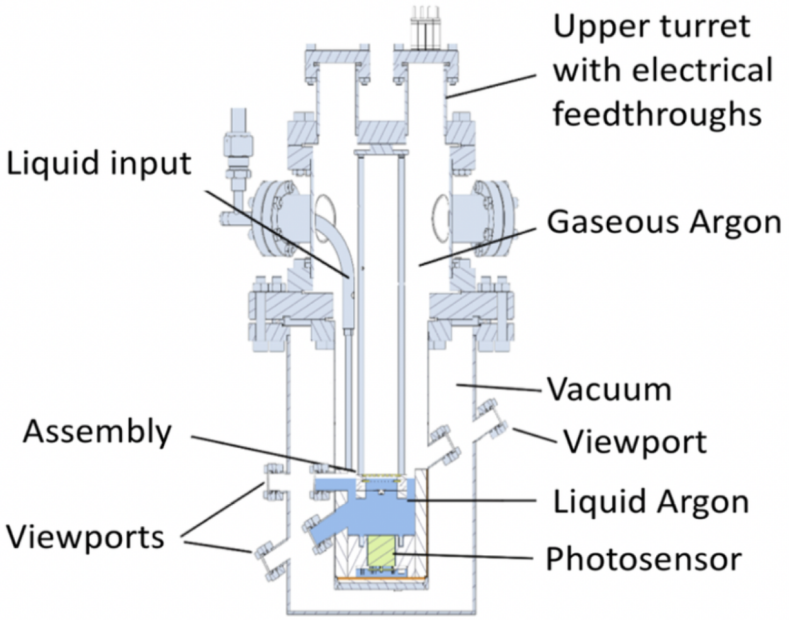

Figure 6.15: Depiction of WISArD, the LAr cryostat at Weizmann Institute of Science where different experiments described in this thesis were performed. The IVC, filled with liquid argon, is surrounded by the OVC, kept in vacuum for thermal insulation. Three viewports allow to observe the assembly from the side; an additional viewport is placed on the top flange. The photosensor, visible in the drawing, was not there during the experiments presented. Image from [261].

the cryostat throughout all the operations corresponded to the saturation pressure $P_s = 1.2$ bar at 90 K.
The level of the liquid was monitored using temperature sensors located in the proximity of the cup edges, inside the cup adjacent to the detector anode, and in other parts of the system. This prevented the liquid from penetrating into the detector region.
In order to grant thermal stability, according to previous experience, the detector was not operated during the first six hours following liquefaction.

Gas purity

Gas purity plays a crucial role in LAr-TPCs, where a sub-ppb level of electronegative impurities is targeted [263] in order to minimize electron capture during the drift in the liquid or gas. Moreover, impurities can absorb avalanche-induced VUV photons that are responsible for secondary

USC UNIVERSIDADE DE SANTIAGO DE COMPOSTELA

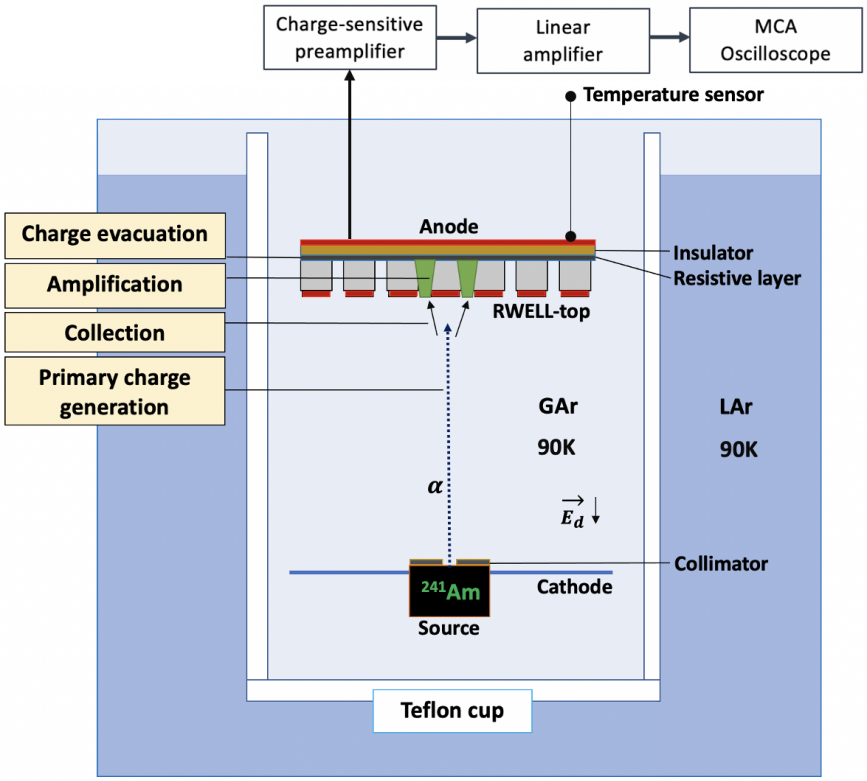

Figure 6.16: Scheme of the cryogenic setup for investigating the detectors (here an RWELL). The assembly and the involved physical processes are detailed. The detector was operated at 90 K, 1.2 bar.

avalanches, allowing for higher maximum gains than in pure gas. For these reasons, gaseous multipliers in Ar are strongly affected by the presence of impurities [126]: for a realistic comparison of the multipliers, the investigation had to count on a very pure Ar vapor, and on measurements conducted preferably in the same conditions for all structures. For this reason, prior to any measurement, the system was vacuum-pumped for at least 12 h reaching a pressure of $\sim 1 \times 10^{-4}$ mbar. A residual gas analyzer (SRS RGA200) was used to measure the level and composition of residual impurities. It was found that the main sources of contamination were H_2O, Ne, HF, N_2, CO. On the other hand, the level of impurities in the Ar gas bottle was 99.999%, with $H_2O \leq 2$ ppm, $O_2 \leq 2$ ppm, $C_nH_m \leq 0.5$ ppm and $N_2 \leq 5$ ppm, as specified by the producer. During operation, the gas was recirculated and purified with a hot getter (Entegris HotGetter PS3-MT3-R-2) in order to reach a nominal impurity content of the order of 1 ppb.

USC UNIVERSIDADE DE SANTIAGO DE COMPOSTELA

Physics of the detector

For all the experiments, an ^{241}Am source emitting 5.5 MeV alpha particles with a rate of about 10 Hz was installed on a metallic plate cathode at a distance of 15 mm from the multiplying electrode. The source was opportunely confined using a metallic collimator of 4 mm thickness and 5 mm diameter, so that the tracks could only form angles $\geq 60°$ with the detector surface. A 12 μm Mylar foil was installed at the collimator emitting face to attenuate the alpha energy to about 4 MeV. This granted full containment of the alpha-particles in the drift volume (≈7 mm range in gaseous argon at 90 K, 1.2 bar calculated with SRIM [264] assuming a gas density of 6.65 kg/m^3 [265]. Uncertainties related to the longitudinal and lateral straggling accounted for ≈280 μm and ≈300 μm, respectively.).
Each 4 MeV alpha particle generates ∼10^5 primary electrons (taking W_I = 26.3 eV[266]) in the drift region. The electrons are drifted towards the THGEM holes under a field $E_d = 0.5$ kV/cm for all the configurations. Increasing the bias across the multiplier electrode, defined as ΔV_{THGEM} results in a high electric field within the holes, allowing for the onset of avalanche multiplication of the primary charges. The amplification factor (i.e. detector gain) increases exponentially with ΔV_{THGEM}, typically in the range of 2.7-3.2 kV in our configuration. Charge from avalanche electrons is evacuated to the ground through the anode in the THGEM and THWELL multipliers and along the resistive-anode surface in the RWELL. An electrical signal is induced onto all the electrodes by the movement of charges (electrons and ions) during the entire process, as described by the Shockley-Ramo theorem (eq. 4.2). The collection signal, induced by the movement of the primary charges in the drift gap, was recorded from the cathode in dedicated measurements where $\Delta V_{THGEM} = 0$ kV. The amplification signal, induced by the movement of the avalanche charges, was recorded from the anode with ΔV_{THGEM} in the range of detector operation. The effective detector gain can be estimated by the following normalization:

$$G_{Eff} = \frac{P_{Amplif}}{P_{Coll}} \tag{6.5}$$

where P_{Amplif} and P_{Coll} are the Gaussian mean values of the spectra of amplification and collection signals, respectively. Notice that the anode signal of a THGEM operated in multiplication mode is mostly due to the fast movement of electrons within the induction gap - typically 4 μs in our setup at cryogenic temperature - whereas in THWELL and RWELL the signals contain both electron and slower ion components [143]. It is important to mention that the resistive anode, decoupled from the readout electrode by a thin insulator (here 0.1 mm thick Kapton), causes a small decrease in the effective gain because of a reduced weighting potential. This effect is negligible when the insulator is thin [235].

USC UNIVERSIDADE DE SANTIAGO DE COMPOSTELA

Gain stabilization and voltage scan

The gain of each detector configuration was characterized by increasing by steps the voltage ΔV_{RWELL} across the RWELL, while $E_d = 0.5$ kV/cm was kept constant. An increase of ΔV_{RWELL} corresponded to an increase of the detector gain, followed by a small reduction (about 20%), until reaching stabilization after several hours. This effect is due to the charging-up of the THGEM insulating substrate (holes' walls and rims) [267]. For each voltage configuration, a minimum of 100 spectra of 120 s each were acquired. In Fig. 6.17, the gain stabilization for the 20 GΩ-RWELL detector operated at 90 K, 1.2 bar is shown as an example. The initial ΔV_{RWELL} was set to 2.7 kV, sufficient to obtain well-defined spectra above noise, and it was subsequently increased up to 3.175 kV in steps of 50 V or 100 V. After a certain value of ΔV_{RWELL}, the detector entered a region of electrical instability. This was different for each detector configuration. For the THGEM and THWELL, a single discharge made the detector unstable, and a power cycle was required. For the RWELL, discharges were quenched by the resistive layer and the detector could be operated stably despite a loss in energy resolution due to small gain fluctuations (e.g. $\Delta V_{RWELL} = 3.15$ and 3.175 kV in Fig. 6.17).

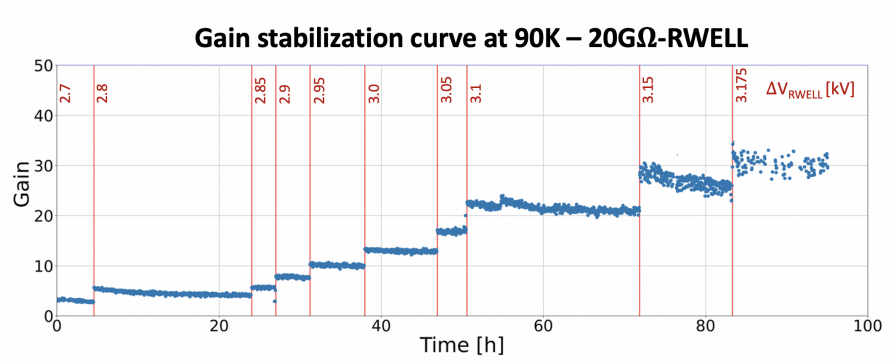

Figure 6.17: Gain stabilization for the 20GΩ-RWELL detector operated with alpha-particles at 90 K, 1.2 bar. The voltage configurations are indicated by red vertical bars and the corresponding values in kV are reported above them. The gain decreased over time (20% gain reduction) until stabilization. For 3 kV $< \Delta V_{RWELL} <$ 3.175 kV, the detector operated in the presence of quenched discharges. Gain fluctuations are also visible at $\Delta V_{RWELL} = 3.15$ and 3.175 kV.

For the RWELL, three regions of operation were identified: i) discharge-free behavior up to 3 kV, ii) stable operation in the presence of quenched discharges for 3 kV $< \Delta V_{RWELL} <$ 3.175 kV and iii) presence of constant currents above 3.175 kV. The measurement was stopped when the detector entered the latter region. For the THGEM and THWELL, two regions of operation were identified: discharge-free behavior up to $\Delta V_{THGEM} = 3.2$ kV

USC UNIVERSIDADE DE SANTIAGO DE COMPOSTELA

and $\Delta V_{\mathrm{THWELL}} = 2.9$ kV, and an unstable region of intense discharges above it; there the measurements were stopped.

Collection signals, spectra, and efficiency

The process of primary charge drift and collection is independent from the adopted detector configuration. An average collection signal from a dataset of 1000 waveforms is shown in Fig. 6.18, left. Its risetime provides a good estimate of the cathode-anode transit time of the ionization electrons, given that any alpha track orientation would induce signals of different shape yet with the same total duration (cathode-anode transit time). Thus all signals peak at about the same time when recorded through a charge amplifier. For our typical drift field of $E_d = 0.5$ kV/cm, the average risetime (from 10% to 90% of the signal maximum) corresponds to 5.5 μs, yielding a drift velocity estimate of $v_e = 2.7$ mm/μs, which is in approximate agreement with the simulated value at 90 K and 1.2 bar (from Magboltz [268]).
In Fig. 6.18, right, a typical spectrum of collection-signal amplitudes recorded for a sample of 4.5×10^3 waveforms is shown. The spectrum is normalized to the count value of the most probable amplitude. It was calibrated by injecting a known amount of charge through a 2 pF capacitor. The mean value of the distribution corresponds to ~1.5 x 10^5 primary electrons.

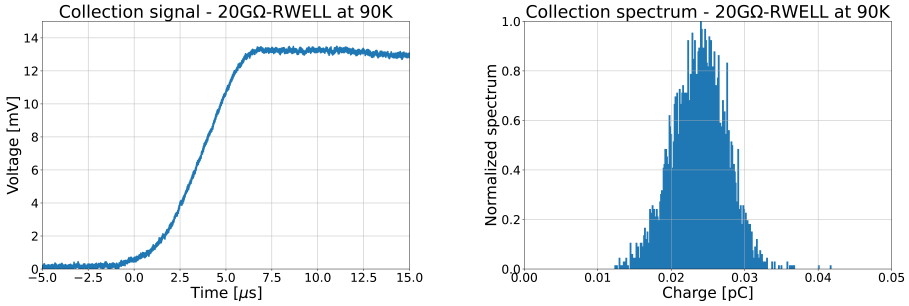

Figure 6.18: Left: Average charge-collection waveform from the preamplifier, for an RWELL detector operated with alpha particles at 90 K, 1.2 bar. Right: signal amplitude spectrum calibrated to charge.

As a comparison, a scan of the WELL detector at 90 K, 1.2 bar is reported in Fig. 6.19: the left plot shows the signal amplitudes of the WELL, taken from the anode, as a function of ΔV_{WELL}. Each point was recorded using the preamplifier-digital oscilloscope chain and represents the mean value of the distribution of signal amplitudes, each one containing 10^3 entries. The uncertainties were extrapolated as the σ of the charge distributions.

USC UNIVERSIDADE DE SANTIAGO DE COMPOSTELA

The signal amplitude from the cathode, recorded at $\Delta V_{\mathrm{WELL}} = 0$ kV and the usual drift field, is also reported for comparison; it is the same for the RWELL (Fig. 6.18, left). In Fig. 6.19, right, an initial rise of the collection efficiency can be observed when increasing the voltage across the WELL; a plateau is eventually reached at about $\Delta V_{\mathrm{WELL}} = 1.2$ kV, remaining constant until the onset of charge multiplication at about $\Delta V_{\mathrm{WELL}} = 1.5$ kV. A charge gain $\mathrm{G_{Abs}}$ ∼8 can be derived from Fig. 6.19, left, at $\Delta V_{\mathrm{WELL}} = 2.9$ kV. Since the detector is operating with full collection efficiency at these voltages, $\mathrm{G_{Eff}}$ (defined in Eq. 6.5) is equivalent to $\mathrm{G_{Abs}}$. These conclusions apply to the RWELL case as well.

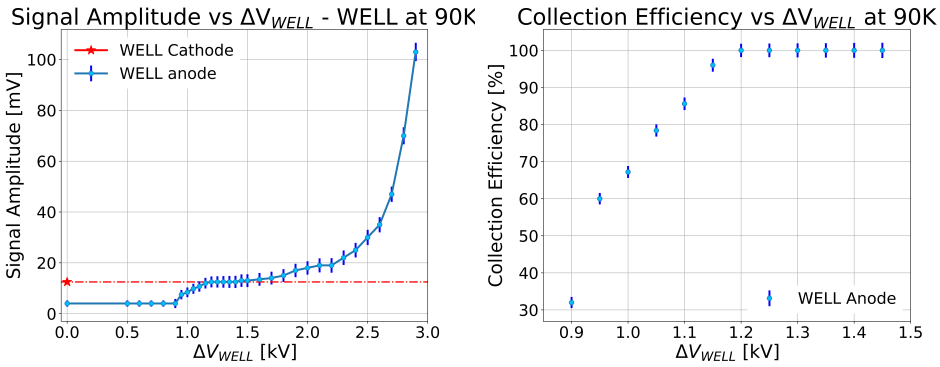

Figure 6.19: Left: Scan of the WELL detector operated at 90 K, 1.2 bar in terms of the anode signals' amplitudes from the preamplifier as a function of ΔV_{WELL}, with $\mathrm{E_d}$ = 0.5 kV/cm. The cathode signal amplitude is also reported for comparison (see red star). Right: WELL collection efficiency as a function of ΔV_{WELL}, with $\mathrm{E_d}$ = 0.5 kV/cm.

20GΩ-RWELL at 90 K - Amplification signals and spectra

The detector voltage was scanned in the range $\Delta \mathrm{V_{RWELL}}$ = 2.7-3.2 kV. In Fig. 6.20 left, the calibrated charge spectra are shown. Histograms were recorded using the MCA and each one contained ∼5×10^3 entries. All spectra were normalized to their area and to the maximum at $\Delta \mathrm{V_{RWELL}} = 2.7$ kV. The low-energy tail is attributed to the partial energy deposition of alpha particles exiting the collimator at large angles.

A risetime study was carried out to identify potential sources of feedback: possible candidates were photon feedback and/or ion feedback from the cathode, and ion feedback from the THGEM itself. For this purpose, a waveform-by-waveform analysis was made and the most probable value (*mpv*) was taken from a Gaussian fit to the risetime distributions. The risetime was defined as the time difference between 10% and 90% of the wave-

USC UNIVERSIDADE DE SANTIAGO DE COMPOSTELA

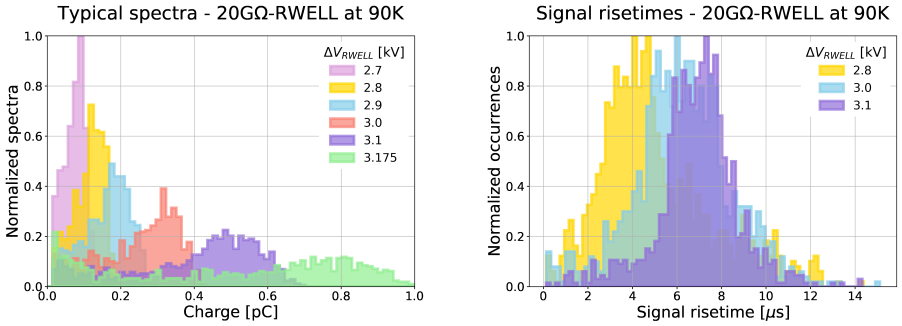

Figure 6.20: Left: reconstructed α-spectra obtained from an RWELL detector irradiated with α-particles at 90 K, 1.2 bar; Right: risetime distributions obtained in the same thermodynamic conditions.

form maximum. Exemplary histograms are shown in Fig. 6.20 right. An increase of the risetime as a function of ΔV_{RWELL} was observed in Fig. 6.21 (orange circles), from around 4 μs to 8 μs. Despite the limited signal/noise, a drift velocity analysis was carried out using the technique introduced for α-particles in [269], which reports the following relation between the drift velocity and the risetime:

$$v_d = kL\sqrt{t_{max}^2 - t_{min}^2} \tag{6.6}$$

where k is a constant related to the definition of risetime (taken as the time between 10% and 90% of the pulse maximum), and L is the track length: in this case, the expected alpha track length of 4 cm (in 1.2 bar of argon at RT) was divided by 3.4, to account for the increased density at 90 K. The risetime distribution is used to find t_{max}^2 and t_{min}^2, taken as the risetimes corresponding to a drop by 10% of the peak. Following this procedure, a constant value of $v_d \sim 1.8$ mm/μs was found (about 30% less than the simulated value quoted in the previous section). This indicates that the main contribution to the spread of the risetime distributions comes from the different orientations of the α-particles[1], while the increase of the *mpv* with ΔV_{RWELL} stems from the detector response. A quadratic subtraction of

[1]For the collection risetime the timescale is dominated by the drift time of electrons, and the signal induced by the primary charges taken with the charge amplifier doesn't suffer much from these variations. Indeed, in the case of a track perpendicular to the structures, all the electrons will start inducing the signal at the same moment t0; the signal (before amplification) will become smaller and smaller as the electrons reach the collection anode; the farthest electron from the collection anode will stop inducing the signal at a time t1, that will correspond to the maximum in the amplifier (integrated) signal. In the case of a track parallel to the structures, all the electrons will start inducing the signal at t0 and stop inducing the signal at t1. Therefore, also in this case t1 will correspond to the maximum of the amplifier (integrated) signal. On the contrary, the variation of the angle for alpha events leads to significant difference in the shape of the avalanche signal, right because the avalanches will have a significantly different duration

USC UNIVERSIDADE DE SANTIAGO DE COMPOSTELA

the low-field risetimes, performed in order to isolate the effect, is superimposed in Fig. 6.21 (blue circles). The time constant associated with photon feedback [116, 270] is shown for illustration (magenta dashed line). Even if a good match is visible, the observed agreement might be coincidental. Field modifications due to ion space charge or charge accumulation at the plate may induce a similar effect given that the contribution from the ion-drift across the THGEM structure amounts to ≈1 μs [2]: a field reduction down to 20%, even if a priori very extreme, would cause a similar increasing trend with ΔV_{RWELL}. On the other hand, ion feedback from the cathode, at the timescale of ms, would lead to well-separated spurious signals that were only present at ΔV_{RWELL} = 3.175 kV (up to 40% of the events, with a discharge rate of ≈ 1%). Perhaps the best indication that breakdown is slow (either photon or ion-driven), in contrast to a conventional streamer mechanism, is the fact that the surface resistance required in present conditions is considerably larger than that required in VUV-quenched gases at room temperature.

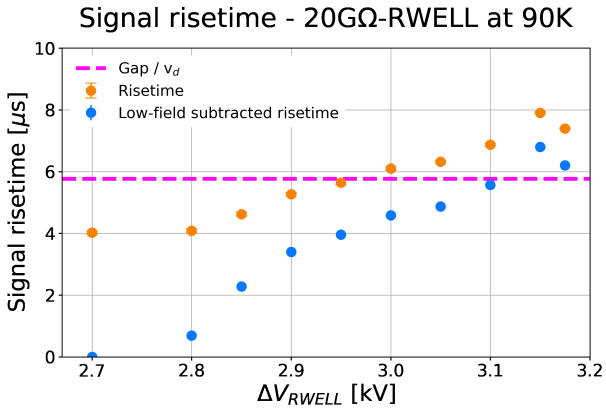

Figure 6.21: Most probable signal risetime as a function of the applied voltage for the RWELL detector operated at 90 K, 1.2 bar, with E_d = 0.5 kV/cm (orange circles). The low-subtracted risetime (blue circles) and the photon feedback time constant (magenta dashed line) are also reported.

Behavior with temperature

Fig. 6.22 depicts the RWELL gain as a function of ΔV_{RWELL} at different temperatures. Gain uncertainties represent the gain variations of the stabi-

if all the electrons arrive at the same time (parallel track) or over a certain time interval (perpendicular track).

[2] Computed by considering the mobility μ =(3e/16Nσ) $(2\pi/m_R k_B\ T)^{1/2}$ (where m_R is the reduced mass of argon and the ion, N the gas number density, k_B the Boltzmann constant, and σ the collision cross section) [271], and scaling accordingly the mobility of positive ions Ar^+ in 1 bar of Ar at RT.

USC UNIVERSIDADE DE SANTIAGO DE COMPOSTELA

lization curve.

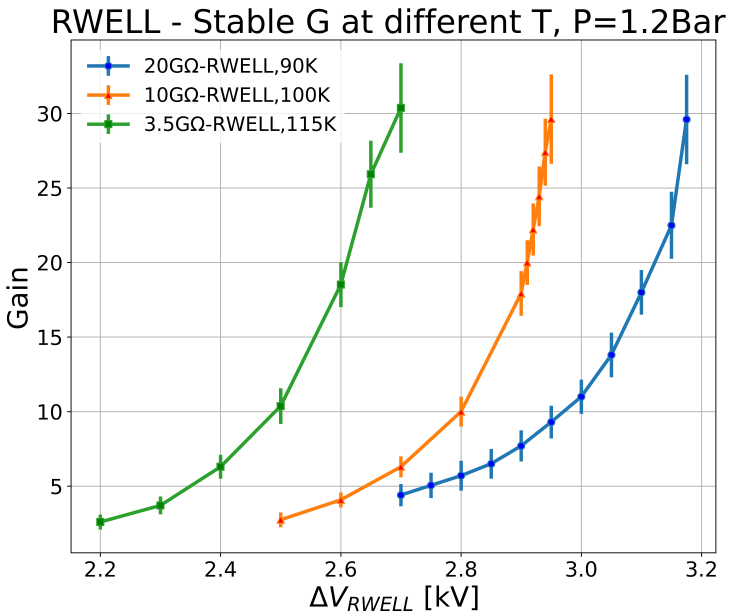

Figure 6.22: RWELL gain, measured in stable operation conditions, as a function of the applied voltage at different temperatures. The resistivity of the DLC layer at each temperature is also reported. From [272].

Since the gas pressure was kept constant along the experiments, in first approximation the gas density is only temperature-dependent, $\rho_g \sim T^{-1}$. As showed in Sec. 6.1.1, the DLC resistivity decreased with increasing temperature, from 20 GΩ/□ at 90 K to 10 GΩ/□ at 100 K and 3.5 GΩ/□ at 115 K. The detector characterization was performed first at 90 K, then the LAr level was reduced by warming up the system and extracting gas until the temperature reached the levels of 100 K and 115 K. The maximal achievable stable gain in the presence of quenched discharges was approximately 30 regardless of the temperature and DLC resistivity. The three curves manifest the same exponential trend, which is a feature of avalanche multiplication. Above a detector gain close to 18, the presence of quenched discharges was observed (≈ 0.25 μC); they did not prevent the RWELL operation and did not affect its performance. Above a gain of 30, the appearance of constant currents led to the detector tripping.

USC UNIVERSIDADE DE SANTIAGO DE COMPOSTELA

Comparative study

Past studies with LEM structures in dual-phase argon TPCs were carried out in different conditions: 87 K, 0.98 bar, cosmic muons, and unknown argon purity [273]. Thus, such results in terms of maximum achievable gain can not be directly compared to the ones obtained in this study. In order to demonstrate the potential advantages of the resistive configuration, the RWELL detector response was compared with that of THWELL and THGEM (LEM) in the same experimental system, irradiation source and conditions, at 90 K and 1.2 bar. Note that the RWELL was operated with DLC anodes of 200 MΩ/□ and 20 GΩ/□. The data were recorded after a gain stabilization cycle in purified Ar (see above). In all cases, E_d was kept at 0.5 kV/cm and the induction field in the THGEM configuration was set to 5 kV/cm. Gain curves for all the tested detectors are shown in Fig. 6.23.

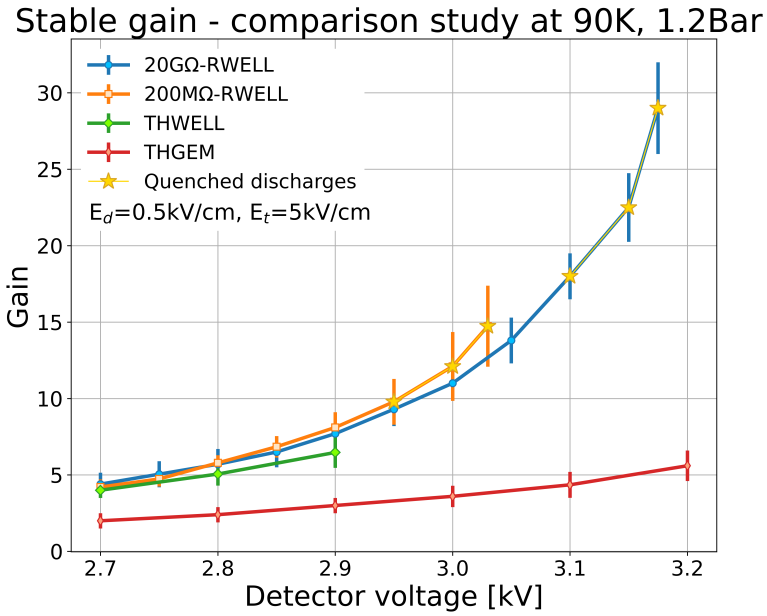

Figure 6.23: Comparison study showing the stable gain for a THGEM+2mm induction gap, a THWELL, a 200MΩ-RWELL and a 20GΩ-RWELL, at 90 K and 1.2 bar. In all cases, the THGEM structure was 0.8 mm thick.

The uncertainties on the gain were extracted from the gain stabilization measurements as the σ of the distribution. It is possible to observe that both RWELL detectors outperform their non-protective counterparts. The maximal stable-gain values achieved are summarized in Table 6.2:

USC UNIVERSIDADE DE SANTIAGO DE COMPOSTELA

Detector	THGEM	THWELL	200MΩ-RWELL	20GΩ-RWELL
Max stable Gain	6	8	15	30

Table 6.2: Maximal stable-gain values for the investigated structures.

The respective 2- and 4-fold gain increase of the RWELL configuration compared to the THWELL can be explained by the discharge quenching features of the resistive layer. Discharges occurring in the two non-protected detectors, WELL and THGEM, generally led to the tripping of the detector and often damaged the preamplifier. In both RWELL configurations, the presence of quenched discharges was observed: at $10 < G < 15$ for the 200MΩ-RWELL and $18 < G < 30$ for the 20GΩ-RWELL. Discharges could be sustained throughout the detector operation without affecting the stable gain, the discharge charge ($\approx$0.25 μC) was $\sim$15-fold lower than the one of unprotected detectors ($\geq$ 3.75 μC), and destructive effects to the electronics were strongly mitigated. Beyond $\Delta V_{RWELL} = 3.05$ kV for the 200MΩ-RWELL and $\Delta V_{RWELL} = 3.175$ kV for the 20GΩ-RWELL, both RWELL configurations were not operable due to the presence of constant currents.

Discharge probability

We define the discharge probability P_d as the number of discharges occurring per detected alpha particle per unit of time:

$$P_d = \frac{N_d}{E_r \times t} \tag{6.7}$$

where N_d represents the number of discharges recorded, E_r is the rate of detected events and t is the measurement time. E_r was measured using a surface-barrier silicon detector[3] and was found to be $\approx$10 Hz.

In Fig. 6.24, the discharge probability of the RWELL is depicted as a function of gain at different temperatures (90 K - 200 MΩ/□, 90 K - 20 GΩ/□, 100 K - 10 GΩ/□, 115 K - 3.5 GΩ/□).

Note the fast rise in discharge probability with the lowest resistivity RWELL, while the other three behave similarly. This is related to the fact that, for a higher R_S, the charge evacuation process is slower and consequently, the effective electric field at the bottom of the hole is reduced during the entire

[3] Ortec F Series Partially Depleted Silicon Surface Barrier Radiation Detector

USC UNIVERSIDADE DE SANTIAGO DE COMPOSTELA

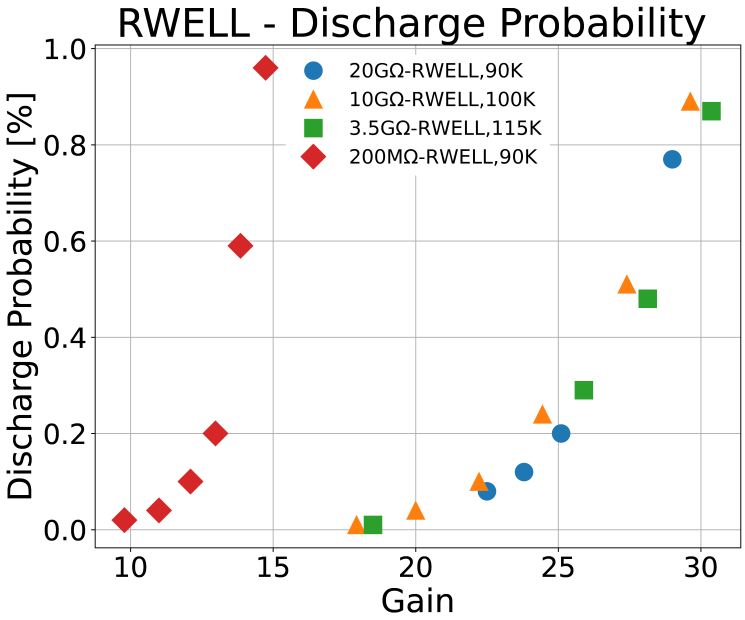

Figure 6.24: Discharge probability as a function of the RWELL gain for four different configurations: 200MΩ/□ at 90 K and 20 GΩ/□ at 90 K, 10 GΩ/□ at 100 K, 3.5 GΩ/□ at 115 K. Irradiation done with 4 MeV alpha particles, pressure: 1.2 bar.

development of the avalanche, leading to quenching. In all cases, at maximal gain values, the discharge probability reaches ∼1%.

Conclusions

The availability of DLC films with tunable surface resistivity has permitted, for the first time, the implementation of the cryogenic RWELL. It was operated under 4 MeV alpha particles in purified Ar at 90 K and 1.2 bar. With resistive anodes of 200 MΩ/□ and 20G Ω/□, the RWELL exhibited discharge-quenching capabilities and could reach gains of ∼15 and ∼30, respectively. Relative to RWELL detectors operated at room temperature, much higher R_S values were needed to reach lower discharge quenching factors [274, 235]. A comparison with a THWELL and with a THGEM (LEM) + 2mm induction gap demonstrated the superiority of the resistive configurations in terms of stability and gain (the latter was 6 and 8 for the THGEM and THWELL, respectively, with alpha particles).

The RWELL was operated also in the presence of moderate discharges,

USC UNIVERSIDADE DE SANTIAGO DE COMPOSTELA

the latter being ∼15-fold smaller than those in THWELL. In general, non-resistive configurations could not be operated in the presence of discharges, which also happened to damage the electronic readout. For all the configurations with $R_S > 3.5$ GΩ/□, it was possible to operate the detector with $P_d \leq 0.01\%$ (upper bound estimation limited by the source rate and measurement time) up to a gain ∼18, after which the discharge probability sharply increased to ≈1% at a gain of ∼30. The dependence of the discharge probability on R_S cannot be explained by simple considerations based on the streamer mechanism, which would lead to quenching resistances lower than the ones employed here (in line with observations in quenched mixtures at RT). For this reason, the process of discharge quenching at cryogenic conditions requires further investigation.
A factor 2.5-5 higher stable gain values was reached with the RWELL compared to a bare THGEM/THWELL in our current setup under the same conditions. This demonstrates the potential advantage of coupling a resistive anode to the multiplier, also in noble gas at cryogenic conditions. A direct comparison with the results presented in literature obtained with LEM detectors [275] was not possible due to the different conditions of operation (e.g. gas density and purity, type of primary ionization, different electrode parameters, etc.).

To conclude, the successful operation of the RWELL detector at cryogenic temperature represents an important milestone. Though requiring further investigations, it has the potential for improved scalable readout in future large-volume dual-phase detectors. The scaling up depends on industrial THGEM-electrode production limits and DLC-coating facilities. Electrode sizes reaching 50x50 cm^2 were already reported [276]; DLC-film coating currently reaches 20×100 cm^2 [277]. DLC films proved to be robust, minimally affected by aging, and cheap to produce [242].

USC UNIVERSIDADE DE SANTIAGO DE COMPOSTELA

6.2 RPWELL

The following section (6.2.1) is based on the paper:

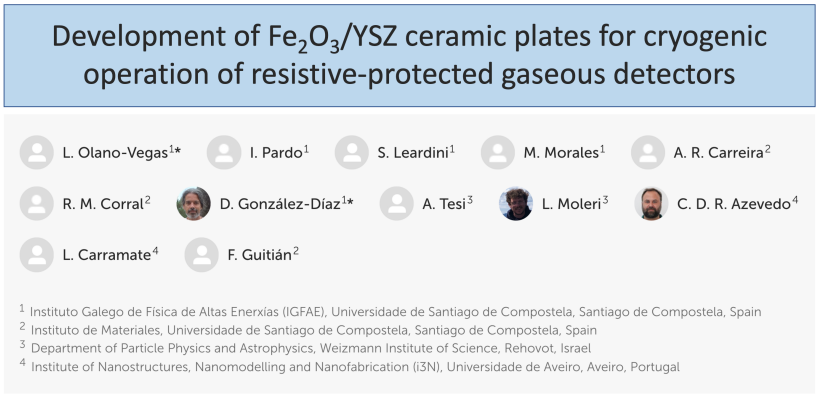
Development of Fe_2O_3/YSZ ceramic plates for cryogenic operation of resistive-protected gaseous detectors

L. Olano-Vegas[1*] I. Pardo[1] S. Leardini[1] M. Morales[1] A. R. Carreira[2]
R. M. Corral[2] D. González-Díaz[1*] A. Tesi[3] L. Moleri[3] C. D. R. Azevedo[4]
L. Carramate[4] F. Guitián[2]

[1] Instituto Galego de Física de Altas Enerxías (IGFAE), Universidade de Santiago de Compostela, Santiago de Compostela, Spain
[2] Instituto de Materiales, Universidade de Santiago de Compostela, Santiago de Compostela, Spain
[3] Department of Particle Physics and Astrophysics, Weizmann Institute of Science, Rehovot, Israel
[4] Institute of Nanostructures, Nanomodelling and Nanofabrication (i3N), Universidade de Aveiro, Aveiro, Portugal

Journal and Article Information
Journal name: Frontiers in Detector Science and Technology
Publisher:
ISSN: 2813-8031
Year of publication: 2023
DOI: 10.3389/fdest.2023.1234229

6.2.1 Characterization of Fe_2O_3/YSZ ceramics

Fabrication

The ceramic plates were produced through slip casting at the Ceramics Institute of Galicia (ICG/i-MATUS). Yttria-stabilized zirconia (YSZ) with crystallite sizes of 22 nm, and hematite (Fe_2O_3) of grain size below 5 µm (purity above 99%) were employed. Raw materials were weighted on a precision scale and admixed with 25% water and 1% deflocculant (Dolapix PC67). The resulting slurry was stirred in a mill filled with zircon balls for 24 h, after which it was poured into a plaster mold of internal dimensions $50 \times 50 \times 3$ mm^3. It was then put on a vibrating table for some minutes and, once the sample was consolidated, it was dried in air.

The sintering process started with the sample heated in an oven up to 900°C, in air atmosphere (pre-sintering). After the sample had further consolidated and contracted down to about the final dimensions of 40 mm

USC UNIVERSIDADE DE SANTIAGO DE COMPOSTELA

× 40 mm, it was thinned with SiC sandpaper down to 1-3 mm to ensure plano-parallelism. The final sintering was accomplished at 1250-1300°C for about 2 h, again in air atmosphere, after which the sample was cooled down at about 2°C/min. Although magnetite formation (Fe_3O_4) can be expected only above 1345°C, a magnetic hysteresis analysis confirmed its absence from the final samples.

Finally, the external oxide layer stemming from the sintering process was removed by thinning the samples further down by about 100 µm. The criteria employed was that the surface electrical resistance would remain constant upon further polishing. Ceramic pieces are shown for illustration in Fig. 6.25-left (pre-sintered) and right (sintered).

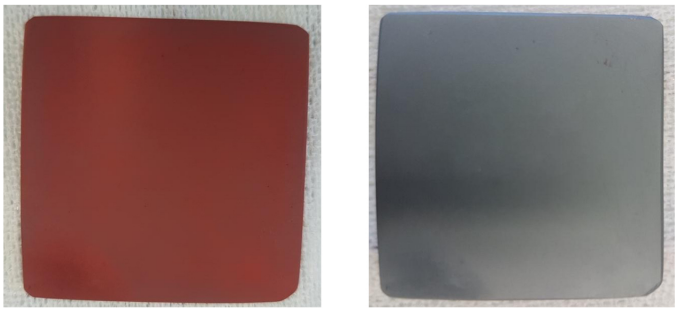

Figure 6.25: Left: pre-sintered ceramic plate (after polishing and edge-rounding) made from Fe_2O_3/YSZ (mass fraction 85/15), at the ICG. Right: fully-sintered ceramics plate (4 cm × 4 cm × 0.2 cm).

Samples were studied by X-ray dispersion and found to be largely free from contaminating species (Fig. 6.26). The results from the diffractogram were generally found to be consistent with the mass fraction targeted during the production of the slurry. Surface analysis showed good homogeneity, compatible with the grain sizes from the raw materials, without strong indications of clustering (Fig. 6.27). A study of the characteristic X-ray emission was compatible with the absence of species other than Fe, Zr, Y, and O.

Experimental setup for electrical characterization

For plate-based resistive protection of gaseous detectors, the product of the bulk resistivity times the sample thickness represents the main metric driving system performance (e.g., [278]). Accordingly, a thorough characterization of the bulk resistivity was performed following the recommendations in [279]. A guard-ring was dimmed necessary only for low-temperature measurements of the ceramics with low Fe_2O_3 concentration (30%wt), otherwise measurements would be shunted by surface currents. Fig. 6.28 describes

USC UNIVERSIDADE DE SANTIAGO DE COMPOSTELA

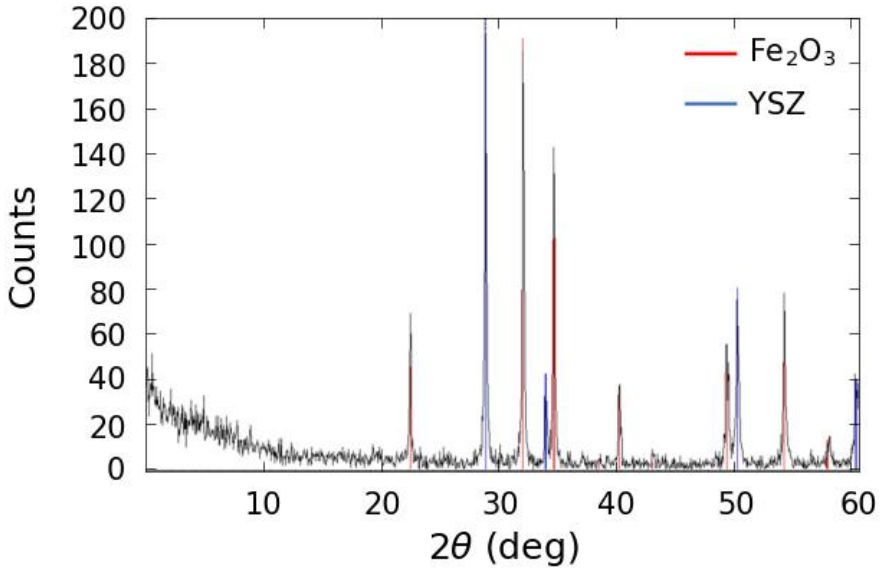

Figure 6.26: Results from X-ray dispersion on Fe_2O_3/YSZ ceramics (mass fraction 75/25), showing the main Fe_2O_3 and YSZ peaks.

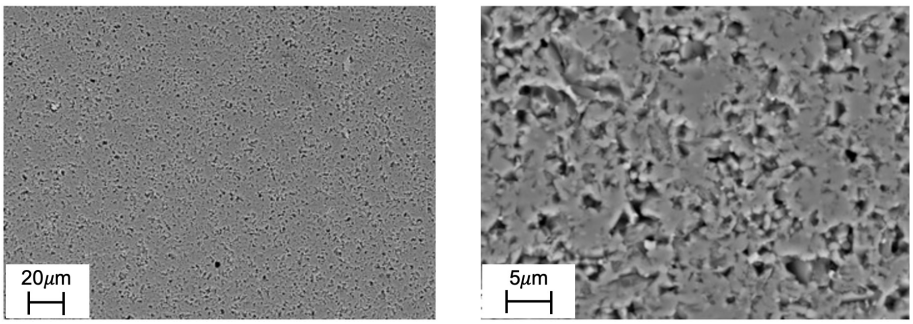

Figure 6.27: SEM images from Fe_2O_3/YSZ ceramics (mass fraction 75/25), at 20 µm (left) and 5 µm (right) scales.

the setup. The characteristic size of the electrodes was chosen to be at least 10 times larger than the plate thickness (1-3 mm, hence electrodes were in the range 1-10 cm^2), to keep fringe-field effects at the 10% level or below [280]. Connections were made through electrical leads clamped to the sample, that was immersed directly in a liquid N_2 (LN) bath in the case of measurements performed at LN-temperature (LNT). Different electrodes were studied: silver epoxy [253], Ag-loaded paint [281], Pt (deposited via magnetron sputtering), Au and Cr (deposited via physical evaporation at 100 nm thickness). All samples were thoroughly polished prior to adhering the electrodes in order to exclude the presence of oxide skin. The electrical resistivity was determined with a Keithley 6487 device. Measurements were

USC UNIVERSIDADE DE SANTIAGO DE COMPOSTELA

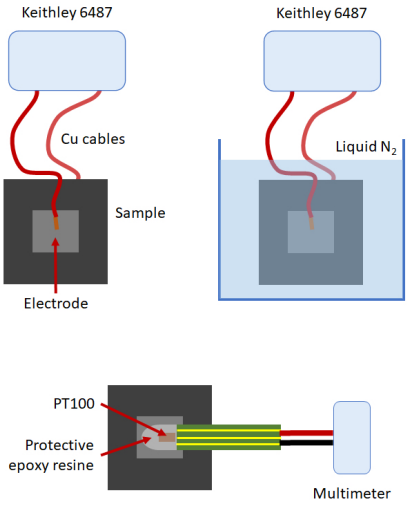

Figure 6.28: Description of the measurements of the electrical resistivity: electrodes were deposited on both faces of the sample, electrical leads clamped, and the readout performed through a Keithley 6487 picoammeter. Top: configuration for RT (left) and LNT (right). Bottom: PT-100 epoxied to the sample for resistivity measurements as a function of temperature. Temperature measurements were directly recorded with a multimeter.

performed up to the limits of the apparatus, namely: i) loss of sensitivity at low voltage due to noise, ii) exceeding the current limit for high voltages (20 mA), iii) exceeding the maximum voltage (500 V).

At LNT, measurements with the different electrodes were generally found to be compatible within ±25%, however deviations of up to 3 orders of magnitude appeared at room temperature (RT), as shown in Fig. 6.29. In this latter case, Cr-electrodes yielded the lowest resistivity and a good ohmic behavior, while the rest exhibited some form of charge blocking that was reduced as the field increased, approaching the Cr values. Therefore, the contact of the Cr-electrode was deemed good across all temperatures explored in this work, and a systematic uncertainty assigned to the LNT measurements based on the dispersion between different electrode types.[4] Point-to-point variations of the resistivity were studied in different regions within the sample (near the four corners and at the center). Their relative spread, in the range 8-30%, was used as an estimator of the sample uniformity.

[4]For few of the LNT series, and given that the low-frequency noise in the setup was not completely stable during the measurements, silver paint electrodes (thickness of few 100 µm) yielded a sensitivity down to lower voltages and were used instead.

USC UNIVERSIDADE DE SANTIAGO DE COMPOSTELA

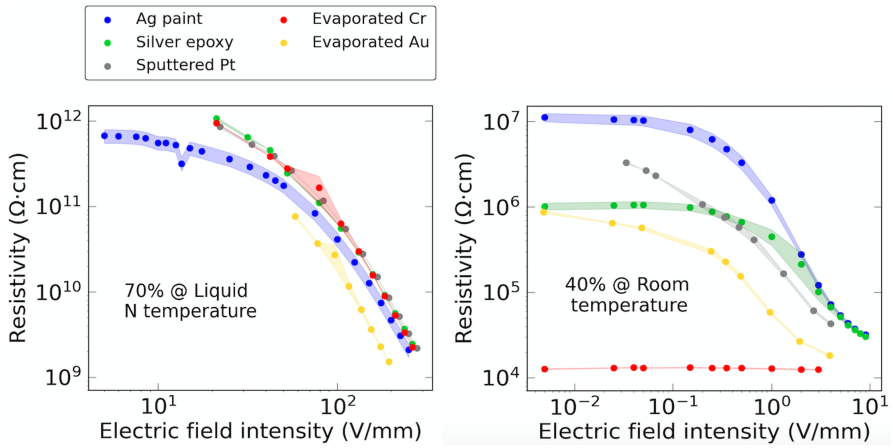

Figure 6.29: Impact of the electrode type on the measured resistivity. Left: behavior at LNT for the 70%wt Fe_2O_3 ceramics. Right: behavior at RT for the 40%wt Fe_2O_3 ceramics. Bands represent the statistical uncertainty only. The slightly different field range covered by each series comes from the different electrode sizes and noise levels.

Measurements as a function of temperature were taken in 'drift' mode, i.e., by removing the sample from the LN bath and letting it gradually warm up, unimpeded. A PT-100 was epoxied directly to the sample (Fig. 6.28-bottom). The first 5 seconds upon removal from the bath were excluded from the measurement to allow the sample to reach equilibrium, and the average of two identical series was taken. The combined uncertainty was estimated from their standard deviation, the point-to-point variations, and the electrode-to-electrode variations, added quadratically.

Last, measurements of the dielectric constant were performed, as its value impacts the signal induction process and the recovery time of resistive-protected detectors (e.g., [238, 282, 283]). For practical reasons, a first assessment based on a standard LCR-meter with a limited range of 0.1 kHz - 1 MHz was performed.

Dependence with electric field

Resistivity measurements as a function of the external electric field for LNT and RT are given in Fig. 6.30. All samples have thicknesses in the range 1-3 mm. A steep loss of linearity can be seen at LNT while no such effect could be observed at RT (except at much smaller fields, limited by the maximum current drawn by the picoammeter). During detector operation,

USC UNIVERSIDADE DE SANTIAGO DE COMPOSTELA

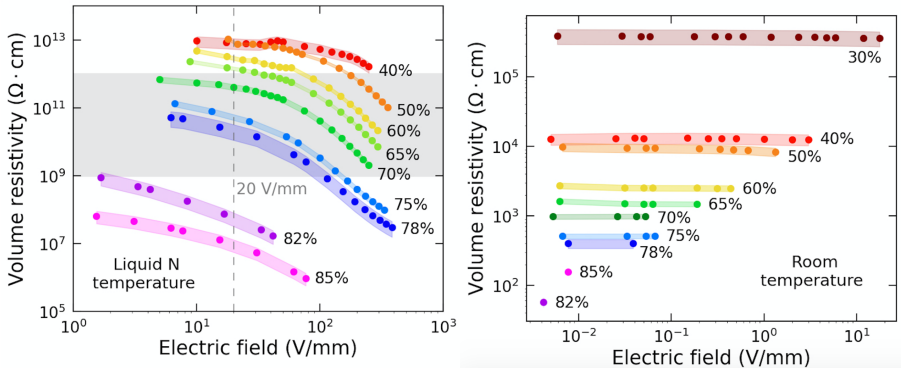

Figure 6.30: Bulk resistivity as a function of electric field at different temperatures. Top: measurements at LNT (the 30%wt sample was out of range). Bottom: measurements at RT. The shaded band in the top figure indicates the range of suitable values for detector operation and the dashed vertical line is the maximum voltage drop at the sample expected during operation. Uncertainty bands are obtained through quadratic addition of the point-to-point spread with the statistical uncertainty of the measurement. The systematic uncertainty from the electrode-to-electrode variations was quadratically added for the LNT case.

a maximum (steady state) voltage drop of few 10's of V across the ceramic sample can be anticipated, above which the gas amplification would start to deteriorate substantially. Hence, the 20 V value is highlighted with a vertical line for reference. A grey horizontal band, corresponding to values that are experimentally known to offer good spark quenching, was added following [116]. It can be seen that, assuming a maximum voltage drop during operation in the order of few 10's of V, samples in the Fe_2O_3 concentration range of 65-78%wt would be well suited for operation close to LNT/LArT. For a low particle flux on the detector, resistivities as high as 10^{13} Ω·cm might be considered, potentially enabling the use of ceramics with concentrations down to 40%wt.

The non-linearity observed in Fig. 6.30-top can be expected to play a role during detector operation, as the aforementioned 20 V refers to steady-state (*ss*) conditions, while a streamer can cause local drops much higher than those, easily in the order of hundreds. The spark-quenching power depends on the entire evolution of the field in the amplification gas and through the plate during the discharge process. Hence it is reassuring to see that some of the samples stay within the grey zone up to much higher voltage drops than those expected in *ss*. Last, depending on the application, *ss* voltage drops well over 100 V can occur in some detectors operating at high event rates (see e.g. [284] for Multi-gap Resistive plate chambers -

USC UNIVERSIDADE DE SANTIAGO DE COMPOSTELA

MRPCs), yet providing a usable response. The experimental range chosen in this work aims at covering this range of conditions.

In order to assess the electrical breakdown of the ceramics, several series of increasing and decreasing voltages in the range 0-5.5 kV were applied to both a 60% and a 75% sample at LNT through a CAEN471 power supply, and the current monitored. A monotonous behavior was observed up to 3 kV, above which the reproducibility of the *I-V* curve was lost. This voltage was then applied to the samples for several minutes, observing no instability. Hence, one can safely assume that the breakdown voltage is above 3 kV for mm-samples in the aforementioned concentration range, a priori suited for LNT/LArT operation. Strictly, for operation at around 3 kV voltage drop across the detector (as described later in section 6.2.2), that value represents the maximum possible value of the *ss* voltage drop across the plate, under any circumstance (e.g., a self-sustained glow discharge in the gas).

Dependence with temperature

Resistivity measurements as a function of temperature are given in Fig. 6.31 for the most representative samples. Results from a previous 35%wt-ceramic have been included as a dashed line [250], although a direct comparison is not possible given the less mature fabrication procedure and different post-processing. Measurements at stabilized temperature (LNT, RT) are included as open circles, and a weighted fit to an Arrhenius-like exponential law ($\log(\rho) = \mathrm{a} - \mathrm{b} \cdot T$) is shown as a dotted trend. The slopes are compiled in Table 6.3. The overall behavior supports the fact that, for practical purposes, good thermal uniformity is achieved in the sample during warm-up, and that the PT100 follows the sample temperature with good precision. Samples in the range 30-40%wt cross the shaded band at around the temperature of LXe (LXeT), as expected from [250].

Sample (%wt Fe_2O_3)	**a**	**$b \cdot 10^{-2}$ (K^{-1})**
82	12.08 ± 0.01	3.59 ± 0.01
70	15.07 ± 0.04	4.12 ± 0.02
40	16.27 ± 0.08	4.15 ± 0.03
35	17.54 ± 0.08	4.14 ± 0.03
30	19.20 ± 0.08	4.66 ± 0.03

Table 6.3: Parameters of the Arrhenius-like fit of the volume resistivity of Fe_2O_3/YSZ ceramic samples vs temperature: $\log(\rho) = \mathrm{a} - \mathrm{b} \cdot T$. Coefficient a is defined such that $\exp(a)$ has units of [Ω·cm].

Based on the observed temperature dependencies, it is possible to rep-

USC UNIVERSIDADE DE SANTIAGO DE COMPOSTELA

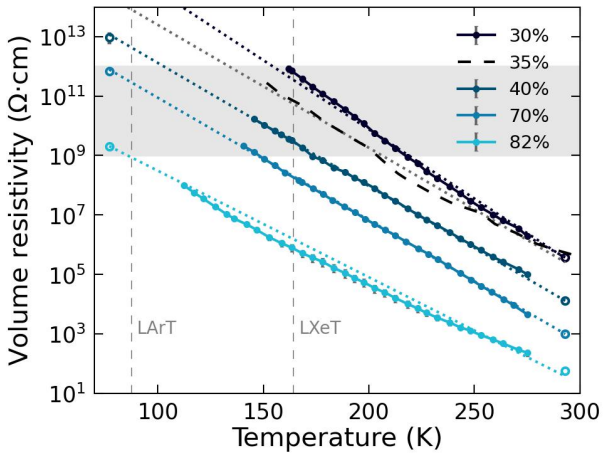

Figure 6.31: Low-field resistivity as a function of temperature, obtained for the most representative samples. Measurements in 'drift-mode' are indicated with full circles, while the empty circles correspond to measurements at stabilized temperature. The curve for the 35% sample (in dashed line) was extracted from [250].

resent the low-field resistivities as a function of the concentration of Fe_2O_3, as done in Fig. 6.32. Here, a reference measurement for pure Fe_2O_3 ceramics, performed at 293 K, has been included too. It is interesting to see that the trend as a function of Fe_2O_3 concentration is similar in the temperature range 77-293 K, except that it becomes steeper, as the temperature decreases, in the extremes of the 30-82%wt range. This becomes clearer when comparing the 77 K and 293 K series, for which this concentration range is more densely covered (open circles represent interpolations based on the fits to Fig. 6.31). The reduction in electrical resistivity of Fe_2O_3 ceramics upon addition of $\sim$ 15% YSZ amounts to a whopping nine-orders-of-magnitude gap. The resistivity measured for the 85%wt sample at RT provides a hint that such a concentration might be close to the inversion point.

Dependence with time/transported charge

The samples showed no strong dependence on humidity or time after storing them for about a year. Additional measurements were performed to indirectly assess the nature of the conductivity mechanism at room temperature and below, by applying voltage over time in a sustained manner. The situation is advantageous in that a very large charge can be transported at room temperature by profiting from the relatively large conductivity displayed in those conditions. Therefore, two sets of measurements were taken: i) at

USC UNIVERSIDADE DE SANTIAGO DE COMPOSTELA

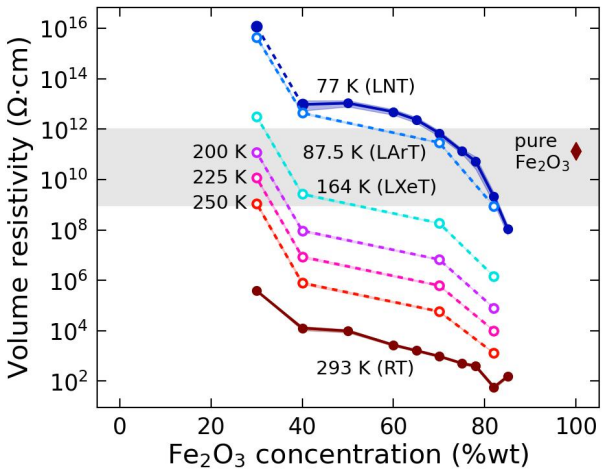

Figure 6.32: Dependence of the volume resistivity with Fe_2O_3 concentration for low fields. Solid lines: resistivity measurements at stabilized temperature (RT in brown, LNT in dark blue). Here the error bands include the uncertainty due to variations with electrode type, the sample uniformity and statistical uncertainty. Dashed lines: resistivity values estimated from an exponential fit to the T-dependence. Diamond: resistivity of a pure-Fe_2O_3 sample at 293 K.

LNT, for the maximum voltage of the picoammeter (500 V) and ii) at RT, for the maximum current (20 mA). Only the statistical uncertainty from the picoammeter was taken into account. The results are shown in Fig. 6.33. At room temperature, no strong increase is seen up to 1 C/cm^2, a large number by high energy physics standards. Even if it is noticeable a 40% increase after about 4000 s, that might be attributed to the lack of stringent temperature control during these measurements, the sample clearly stabilizes after that. A measurement at LNT up to comparable charges should be carried out at a later stage, as it can not be confirmed at the moment that the conductivity mechanism is the same across temperatures. It should be noted, however, that for transported-charge densities well in excess of those anticipated by some future experiments (< 100 μC/cm^2, as evaluated in Sec. 6.1.1), no effect could be seen at LNT either, for the 70%wt sample (Fig. 6.33-right). This result is encouraging, as the above conditions approach closely those for which detector operation was demonstrated (section 6.2.2).

Dependence with frequency

The transparency of a resistive plate to the signal induced by an avalanche in the gas depends on both its resistivity and capacitance. On the one

USC UNIVERSIDADE DE SANTIAGO DE COMPOSTELA

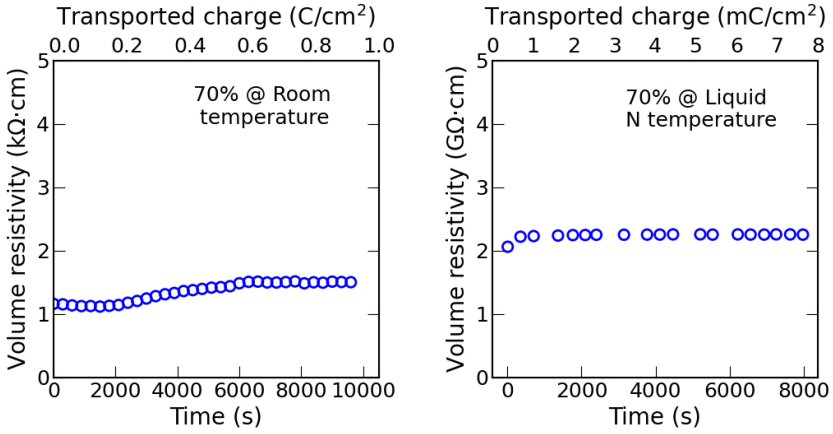

Figure 6.33: Stability of the electrical resistivity over time for a 70%wt Fe_2O_3 ceramics under sustained high voltage operation. The left figure (RT) was taken at the maximum current of the picoammeter. The right figure (LNT), at the maximum voltage (500 V).

hand, surface resistivities (R_s) above 10's of MΩ/□ are known not to disturb signal induction at the time scale of avalanche formation [238, 283]. For homogeneous materials such as the ones described here, where the relation $\rho/d = R_s$ may be assumed (d being the sample thickness), this condition is fulfilled by many orders of magnitude. On the other hand, if the coupling capacitance between the plate and pick-up electrode is too low, an additional loss can occur. Remembering the Shockley-Ramo theorem (eq. 4.2), and considering that for a parallel-plate geometry the drift velocity of the charge carriers $\vec{v}_d$ and the weighting field $\vec{E}_w$ are parallel, a 'coupling factor' might be defined as the ratio between the weighting field modulus in the protected structure and the unprotected one, as:

$$f = \frac{E_w|_{protected}}{E_w|_{unprotected}} \tag{6.8}$$

E_w is in this case nothing but the anode-cathode capacitance of the amplification structure, per unit area and divided by ϵ_0 ($E_w = C_A/\epsilon_0$, e.g. [285]). Specifically, for the RPWELL/WELL geometries (Fig. 5.10), the coupling factor evaluates to:

$$f = \frac{E_w|_{RPWELL}}{E_w|_{WELL}} \simeq \frac{\epsilon_r}{\epsilon_r + d/g}, \tag{6.9}$$

where ϵ_r is the dielectric constant of the plate, g the depth of the holes and d the plate thickness. In the limit when the plate has a very large dielectric constant or its thickness is much smaller than the hole depth, $f \to 1$.

USC UNIVERSIDADE DE SANTIAGO DE COMPOSTELA

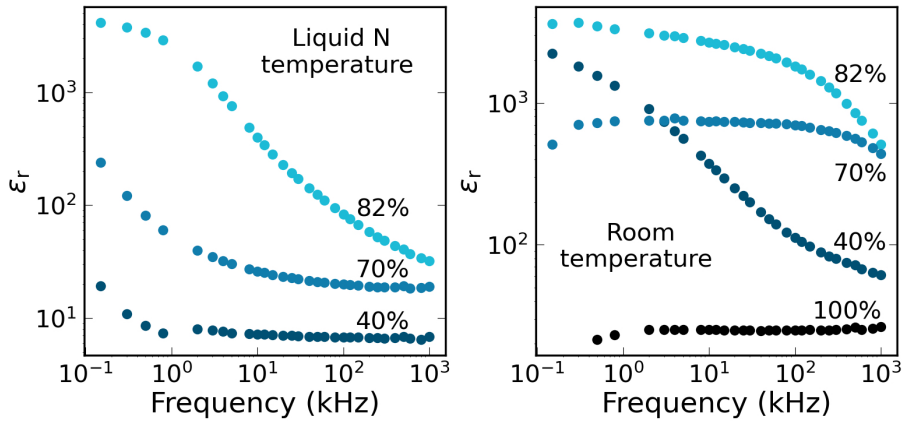

Figure 6.34: Dielectric constant (ϵ_r) measured as a function of frequency at LNT (left) and RT (right), for selected samples.

Fig. 6.34 shows the dielectric constant measured up to MHz, for illustrative purposes. If no additional relaxation mechanism would be present up to the GHz (avalanche) scale, the value of ϵ_r(1MHz) might be used to evaluate eq. 6.9, that we provide for illustration in Table 6.4. Although for insulators it is common to find relaxation at low frequencies (i.e., well below MHz), an additional elucidation of this aspect remains important.

Sample (%wt Fe_2O_3)	ϵ_r	**Coupling factor**
82	32.32	0.93
70	18.88	0.88
40	6.75	0.73

Table 6.4: Estimated coupling factor (defined in text) for RPWELL structures of 0.8 mm-deep holes and 2 mm-thick resistive plates, at LNT.

Interestingly, these results point to a relatively high dielectric constant for operation close to LNT/LArT, as the 70%wt sample displays a value ϵ_r(1MHz) $\simeq$ 20 in these conditions, about $\times$2-4 larger than other resistive materials that are usually found in resistive-plate detectors [282, 286]. Measurements for pure hematite at room temperature are found to be in the same range, in agreement with existing estimates [287].

Conduction mechanism

Tunability of the resistivity of hematite ceramics by nine orders of magnitude, through addition of YSZ in different proportions, makes Fe_2O_3/YSZ ceramics suitable for gaseous-detector assemblies at temperatures from liq-

USC
UNIVERSIDADE DE SANTIAGO DE COMPOSTELA

uid nitrogen up to room temperature. Of particular interest are the 75%wt, 35%wt, and 100%wt samples, which show resistivities in the range 10^9-10^{12} Ω·cm at the LAr, LXe boiling temperatures and room temperature, respectively. The approximate agreement between the resistivity values of the new ceramic batch and an earlier version developed in [250] suggests that the overall characteristics of the final samples do not depend critically on the fabrication details.

Apart from the suitable resistivity range, the high breakdown voltage observed (above 3 kV) together with the strong hints of electronic conductivity and stability over time and transported charge, represent (a priori) essential assets for the intended application. Both literature and our measurements support the electron-conductivity hypothesis:

1. On the low Fe_2O_3-concentration end (few %wt), Fe- and Fe_2O_3-doped YSZ ceramics have been extensively studied with concentrations up to around 5% mol and at high temperatures. Under these conditions, the conductivity is predominantly ionic. When the content of Fe-based impurities exceeds the solubility limit at around 6% mol (2.84%wt), paths of hematite have been reported to generate across the sample [288, 289, 290].

2. On the medium Fe_2O_3-concentration region (20-50%wt), the aforementioned effect seems to induce electron movement at the Fe sites, either through disaggregated Fe ions at the grain-boundary [288][5] or by electron hopping through Fe cations in the zirconia lattice [291, 289, 292]. At these unusual concentrations, mixed electronic-ionic conductivity has been reported at high temperature [289, 293], while the range below room temperature seems not to have been explored.

3. On the high Fe_2O_3-concentration end, below the YSZ percolation threshold, electron conductivity based on the polaron-hopping mechanism is known to take place [291, 294], and an enhancement in the conductivity is expected due to the higher amount of free electrons resulting from Zr donation [291].

Some (or all) of the above electron-conductivity mechanisms are expected to become dominant for low temperatures in case of medium and high Fe_2O_3-concentrations, given that the activation energy will be too low to enable ion conductivity [289].

[5]The possibility of the existence of a new phase at the grain-boundary has been advocated on that work too.

USC UNIVERSIDADE DE SANTIAGO DE COMPOSTELA

The existence of mixed electron-ion conductivity at room temperature is hinted in our data by indications of charge-blocking at low fields (Fig. 6.29-bottom) as well as the non-monotonous behavior of the relaxation time with Fe_2O_3 concentration (Fig. 6.34-right). While, based purely on the stability of the conductivity with transported charge, ion conductivity seems to be subdominant, additional indications can be found at LNT. In such conditions, charge blocking disappears for low electric fields and the relaxation times evolve monotonically with Fe_2O_3 concentration, facts that can be interpreted as a result of the conduction process becoming 'simpler' at low temperatures, and expectedly dominated by a form of electron conduction.

Conclusions

We demonstrate the maturity of Fe_2O_3/YSZ ceramic plates made in-house for use in gaseous detectors as resistive protection, across temperatures, specifically from 77 K (LNT) up to 300 K (RT). Fe_2O_3/YSZ ceramics are robust, display low-outgassing and their resistivity is tunable through adjustment of the Fe_2O_3 content. Optimal Fe_2O_3 concentrations are found to be 30-40%wt (LXeT), 65-75%wt (LArT) and 100%wt (RT). In the 65-75%wt range, for which 'in-detector' operation has been presented here for the first time at around LArT, the material has an approximately linear response up to 20 V voltage drop, and displays a breakdown voltage above 3 kV. Very good signal-coupling is expected by virtue of a relatively large dielectric constant around $\epsilon_r \sim 20$. No electrical-aging effect (e.g., exhaustion of charge carriers) was observed up to 8 mC/cm^2 (LNT) and 1 C/cm^2 (RT). According to these results, and existing literature, the dominant conductivity form of this family of ceramics is likely of electron origin, thus guaranteeing stability during run-time.

USC UNIVERSIDADE DE SANTIAGO DE COMPOSTELA

The following section (6.2.2) is based on the paper:

Cryogenic RPWELL: a novel charge-readout element for dual-phase argon TPCs

A. Tesi[3,1], S. Leardini[3,1,2], L. Moleri[1], M. Morales[2], D. Gonzalez-Diaz[2], A. Jash[1], A. Breskin[1] and S. Bressler[1]

Author affiliations

[1] Department of Particle Physics and Astrophysics, Weizmann Institute of Science, Rehovot, Israel

[2] Instituto Galego de Física de Altas Enerxías, Universidad de Santiago de Compostela, Santiago de Compostela, Spain

Author notes

[3] Contributed equally.

Journal and Article Information
Journal name: Journal of Instrumentation
Publisher: IOP Publishing
ISSN: 1748-0221
Year of publication: 2024
DOI: 10.1088/1748-0221/19/02/P02019

6.2.2 Operation in a detector

Experimental Setup and Methodology

Analogously to the RWELL test, the experiments were conducted at Weizmann Institute of Science in the WISArD cryostat, already described in Sec. 6.1.2. Two 2 mm thick Fe_2O_3/YSZ ceramics plates were tested, with 75% wt Fe_2O_3 and 65% wt Fe_2O_3 respectively. The bulk resistivity R_V at 90 K was 8×10^{10} Ω·cm for the former, and 10^{12}Ω·cm for the latter, at ∼20 V/mm (low-voltage drop, amenable to the experimental conditions). The RPWELL assembly consisted of a 3x3 cm^2 area and 0.8 mm thick single-sided THGEM (0.5 mm diameter holes distributed in a hexagonal pattern with 1 mm pitch, 0.1 mm hole-rim) pressed onto the resistive plate. The latter is attached to a plain metallic anode using cryogenic conductive epoxy (Master Bond EP21TDCS-LO). The charge signals are read out from the anode.

A drift field of $E_d = 0.5$ kV/cm was implemented in the region between the RPWELL and the metallic cathode, located 15 mm away from the top THGEM electrode. The detector was irradiated with a ^{241}Am source, at

USC UNIVERSIDADE DE SANTIAGO DE COMPOSTELA

a rate of about 10 Hz. The source was installed on the cathode plate; it was collimated with a 4 mm thick collimator of 5 mm diameter aperture, and attenuated (using a 12 μm thick Mylar foil) down to ∼4 MeV, in order to keep the alpha-particle range at ≈10 mm. Alpha-induced ionization electrons were collected from the drift region along the field lines into the RPWELL holes, where charge multiplication occurred. Avalanche electrons are evacuated to the anode through the resistive plate, while ions back-flow to the RPWELL top electrode.

The assembly was mounted as explained in Sec. 6.1.2 for the RWELL, and the same hardware was employed; the same considerations regarding purity also apply. A reduced sketch of the experimental setup is depicted in Fig. 6.35; for a more complete view, 6.16 can be taken as a reference.

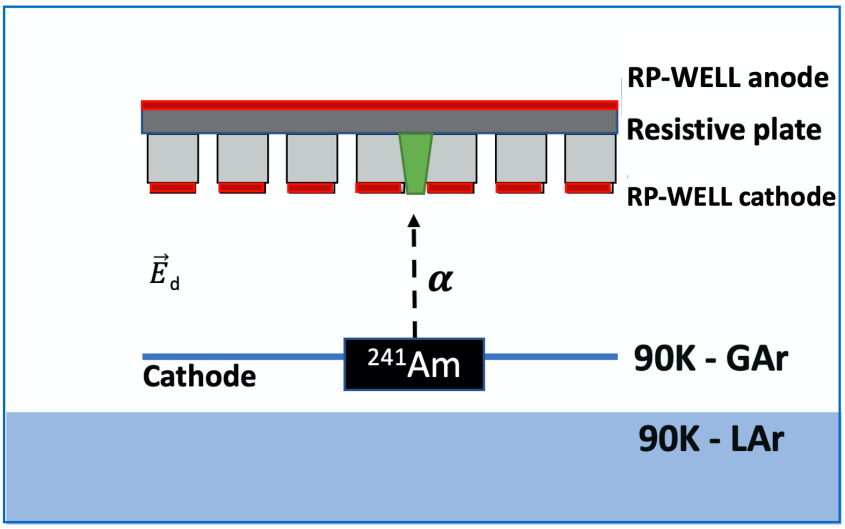

Figure 6.35: Scheme of the cryogenic experimental setup for investigating the RPWELL detector. The assembly was composed of a metallic-plate cathode equipped with a collimated ^{241}Am source fixed at 15 mm from the amplification stage (corresponding to E_d = 0.5 kV/cm). The multiplier consists of a 0.8 mm thick single-sided THGEM coupled to an anode via a resistive plate. The assembly was inserted into a Teflon cup and operated in the liquid argon vapor at 90 K, 1.2 bar.

The measurement methodology also follows closely the one described in Sec. 6.1.2 and consists of the following steps:

- Purification and thermal stabilization of the system (12 hours)

USC UNIVERSIDADE DE SANTIAGO DE COMPOSTELA

- Power adjustment and gain stabilization (minimum 5 hours)
- Measurement of the charge distribution in charge-collection mode and of the collection peak position from the RPWELL top electrode
- Effective gain estimation - charge-distribution peak position measured from the anode normalized to the collection peak.
- Discharge monitoring through the power supply currents (Labview SignalExpress).

For the gain stabilization measurement, the linear amplifier was set to a shaping time of 10 μs. Histograms were recorded using the MCA, during 120 s. All the spectra were normalized to their area and to the maximum at $\Delta V_{RPWELL} = 2.7$ kV. A data set of 5k waveforms was recorded for each measurement with the oscilloscope.

Gain stabilization

The drift field was set at $E_d = 0.5$ kV/cm and the voltage across the 75% Fe_2O_3-RPWELL, ΔV_{RPWELL}, was varied between 2.7 kV to 3.28 kV. The gain evolution during the scan is reported in Fig. 6.36, top. To correlate gain instabilities with discharges occurring in the RPWELL, the power supply currents monitored from the RPWELL top and the anode are reported in Fig. 6.36, bottom.

As can be seen, a gain drop of the order of 60% was recorded during the initial stabilization at $\Delta V_{RPWELL} = 2.7$ kV, due to the charging-up of the dielectric substrate of the THGEM [267, 295]. Stable operation was recorded in the range 2.7 kV $< \Delta V_{RPWELL} <$ 3.2 kV.
Unstable operation, as indicated by correlated spikes between the gain measurements and the current ones, were observed when the detector was operated in the range 3.2 kV $< \Delta V_{RPWELL} <$ 3.28 kV. Nevertheless, the detector was able to sustain these discharges. The measurement was stopped at $\Delta V_{RPWELL} = 3.28$ kV, above which discharges started piling-up causing a DC voltage drop across the amplification structure (detector tripping).

Typical spectra

In Fig. 6.37, the normalized charge-amplitude spectra are shown. The calibration was performed by injecting a known amount of charge through a

USC UNIVERSIDADE DE SANTIAGO DE COMPOSTELA

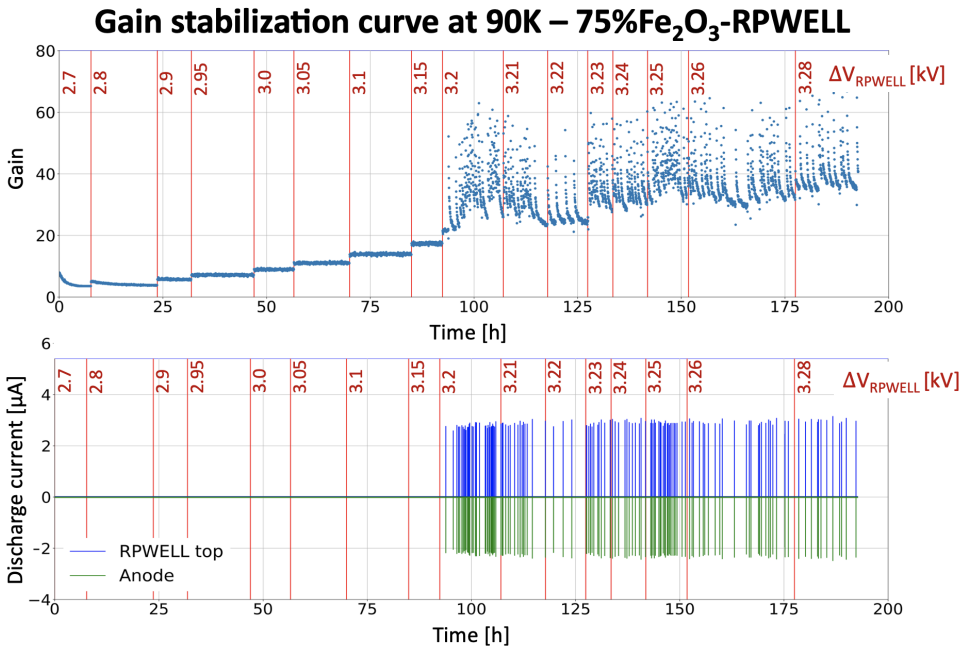

Figure 6.36: Top: Gain stabilization curve over approximately 200 hours of a 75% Fe_2O_3-RPWELL operated at 90 K, 1.2 bar. The voltage configurations are indicated by red vertical bars with the corresponding values of $\Delta V_{\mathrm{RPWELL}}$. Bottom: Power supply currents recorded from the RPWELL top electrode (blue) and anode (green) for the same measurement. Note the presence of discharges above $\Delta \mathrm{V}_{\mathrm{RPWELL}} = 3.2$ kV.

2 pF capacitor, as explained in Sec. 6.1.2. The mean value of each amplification spectrum was normalized over the mean value of the collection spectrum (see Fig. 6.18 right), the latter corresponding to ∼1.5 x 10^5 primary electrons. With increasing voltage, the general shape of the spectra was preserved, with no indication of distortions due to secondary effects or discharges.

Stable gain curve and discharge probability

In what follows we consider only measurements carried out in stable gain conditions, i.e., after initial gain stabilization and prior to the appearance of discharges (Sec. 6.2.2). Fig. 6.38 left shows the gain as a function of $\Delta V_{\mathrm{RPWELL}}$ for a 75%Fe_2O_3-RPWELL and a a 65%Fe_2O_3-RPWELL operated at 90 K, 1.2 bar of purified Ar. The results are compared to identical

USC UNIVERSIDADE DE SANTIAGO DE COMPOSTELA

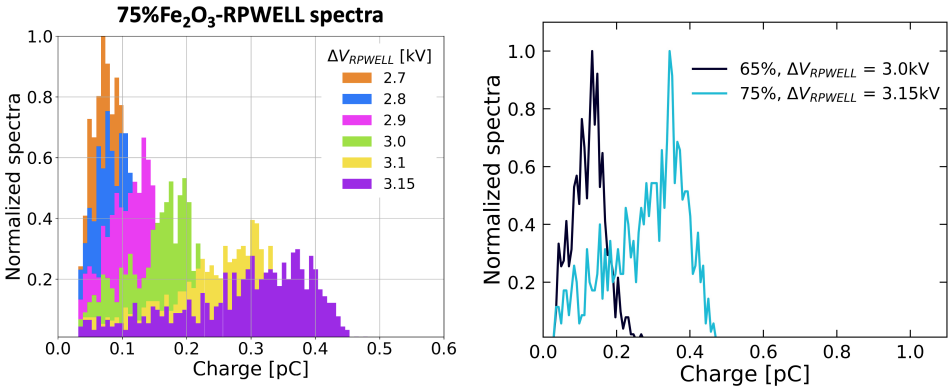

Figure 6.37: Left: example of reconstructed α-spectra obtained from a 75%Fe_2O_3-RPWELL operated at 90K, 1.2 bar. Right: example of charge spectra from an RP-WELL coupled to Fe_2O_3/YSZ ceramics at 65%wt Fe_2O_3 (dark blue) and 75%wt Fe_2O_3 (light blue), from [296].

measurement carried out on non-resistive THGEM/THWELL and on two RWELLs (see Sec. 6.1.2). For all the investigated configurations, the gains exponentially increase with $\Delta V_{\mathrm{RPWELL}}$. As it can be seen, the two resistive configurations outperform the non-resistive ones. A maximum gain value G ≈17 was reached at $\Delta V_{\mathrm{RPWELL}} = 3.15$ kV with the 75%Fe_2O_3-RPWELL, relative to a gain of 5 measured with the THGEM/THWELL in the same conditions. Beyond this value, the detector was still capable of operating in the presence of discharges.

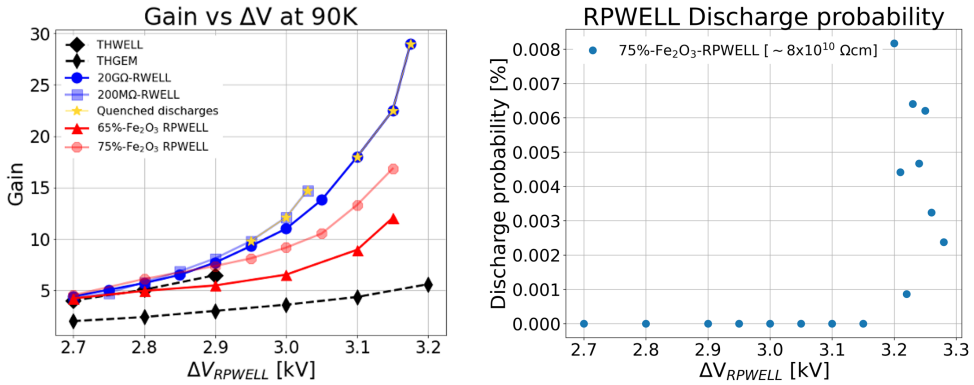

Figure 6.38: Left: stable gain as a function of Δ V_{RPWELL} for a 75% and a 65% Fe_2O_3-RPWELL at 90 K, 1.2 bar in purified Ar. Data from THGEM, THWELL and RWELL from 6.1.2 are included for comparison. Right: discharge probability of the 75%Fe_2O_3-RPWELL as a function of $\Delta V_{\mathrm{RPWELL}}$.

USC UNIVERSIDADE DE SANTIAGO DE COMPOSTELA

The discharge probability, like in Sec. 6.1.2, is defined as the number of discharges over the total number of events. It was estimated by normalizing the number of discharges recorded from the power supply current monitor over the elapsed time and the source counting rate. The discharge probability as a function of ΔV_{RPWELL} is depicted in Fig. 6.38 right for a 75% Fe_2O_3-RPWELL at 90 K, 1.2 bar in purified Ar.

One observes that in the stable region, of 2.7 kV $< \Delta V_{RPWELL} \leq$ 3.15 kV, the detectors with the different plates are discharge-free (discharge probability $< 0.005\%$). A phase transition occurs around $\Delta V_{RPWELL} \geq$ 3.15 kV. Beyond this voltage, a region of instability characterized by quenched discharges appeared. The latter occurred with a magnitude around 1-1.3 μC. The 75% Fe_2O_3-RPWELL could operate in the presence of quenched discharges albeit at an unstable gain condition. Beyond $\Delta V_{RPWELL} = 3.28$ kV, discharges led to a high DC current between the RPWELL-top and the grounded resistive plate, causing the tripping of the detector like in the non-protected ones. The described phenomenology could be caused by setup-related limitations, such as a bad coupling between the resistive plate and the THGEM due to non-perfect planarity. Additional investigation is ongoing to understand the origin of the aforementioned phenomenology.

Conclusions

For the first time, a cryogenic RPWELL detector incorporating a YSZ+Fe_2O_3 ceramic plate (with Fe_2O_3 in the concentration of 75%) was operated in argon vapor at cryogenic temperature (90 K, 1.2 bar). The detector was characterized with an alpha source. After an initial gain reduction of ≈60% imputable to charging-up, stable, discharge-free operation was recorded up to G ≈17. Above the maximal stable gain, the detector was still operable but, due to the presence of discharges, the gain became unstable. It is interesting to remark that the discharges in the RPWELL had a magnitude ≈ 3-fold smaller than the ones recorded for a THWELL ($\geq$ 3.75 μC) and they were able to destabilize the detector gain for ≈30 minutes. The transition from the discharge-free regime to the discharge one was sharp. In comparison to the results presented in Sec. 6.1.2, the cryogenic RPWELLs outperformed the non-protected configurations (THGEM, THWELL) of equal dimensions, operated in the same conditions. On the other hand, the cryogenic RWELL reached higher gains (up to ≈30) but at a cost of high discharge probability (≈1%). Both the RWELL and the RPWELL were found to have very low discharge probability, near zero, at equal gains of ≈17.

USC UNIVERSIDADE DE SANTIAGO DE COMPOSTELA

7 Bubble-assisted LHMs

The following chapter is based on the paper:

Bubble dynamics
in Liquid Hole Multipliers

A. Tesi[1], E. Segre[2], S. Leardini[3], A. Breskin[1], S. Kapishnikov[4], L. Moleri[5], D. Vartsky[1] and S. Bressler[1]

Author affiliations

[1] Department of Particle Physics and Astrophysics, Weizmann Institute of Science, Hertzl street 234, Rehovot, Israel

[2] Physics Core Facilities, Weizmann Institute of Science, Hertzl street 234, Rehovot, Israel

[3] Instituto Galego de Física de Altas Enerxías, Universidade de Santiago de Compostela, Rúa de Xoaquín Díaz de Rábago, Santiago de Compostela, Spain

[4] Department of Chemical Research Support, Weizmann Institute of Science, Hertzl street 234, Rehovot, Israel

[5] Department of Physics, Technion — Israel Institute of Technology, Technion City, Haifa, Israel

Journal and Article Information
Journal name: Journal of Instrumentation
Publisher: IOP Publishing
ISSN: 1748-0221
Year of publication: 2021
DOI: 10.1088/1748-0221/16/09/P09003

USC UNIVERSIDADE DE SANTIAGO DE COMPOSTELA

In the last years, advancements have been made in the field of noble-liquid radiation detectors based on the bubble-assisted Liquid Hole-Multipliers (LHM) concept [211, 216, 297, 298, 299]. The original LHM concept [300], presented in the context of rare-event searches, was proposed to perform a combined detection of ionization electrons and primary scintillation photons generated by the interaction of radiation within a single-phase noble liquids. In its present configuration, an LHM-based detector consists of a CsI-coated perforated electrode (e.g. a GEM or a THGEM) immersed in the noble liquid with a stable gas bubble formed and trapped underneath. As a reminder, a typical LHM-detector layout is shown in Fig. 7.1, and was described in Sec. 5.3. An unanswered question in the aforementioned works was a ∼5-fold discrepancy between the measured photon detection efficiency (PDE) and the simulated one, together with a lower-than-expected energy resolution [301]. Moreover, different hole geometries was seen to affect the EL yield [212]. One hypothesis to explain these observation was that a tangential component of the electric field on the liquid-bubble interface could hinder the transfer of electrons between the two phases: under this assumption, some electrons would be guided along the interface towards the electrode, instead of crossing the liquid-gas barrier. Otherwise, the bubble could have an equilibrium point at the bottom of the hole, hence not being able to exploit the region of highest field to produce electroluminescence. To probe this idea, it was essential to investigate the behaviour of the interface, understanding for example which are the accessible equilibrium configurations for the bubble, what are the properties of the liquid-gas interface within the electrode holes (shape of the meniscus, protrusion) and how does the presence of an external electric field affect the bubble properties.

In Sec. 7.1, a theoretical model was derived, based on hydrostatic considerations for the equilibrium configurations of a bubble trapped underneath an ideal single-hole electrode, without the presence of electric fields. The model depends on the surface tension of the gaseous-liquid interface (LAr and GAr in our case) and the contact angle associated with the gaseous-liquid-solid junction (liquid and gaseous argon, and the solid-material substrate supporting the bubble) [302]. A measurement of the latter is described in Sec. 7.2.

The equilibrium configurations of the bubble, in the LHM configuration (of Fig. 7.1), in the presence of an external electric field are studied in Sec. 7.3 using accurate COMSOL™[303] simulations. A set of micro-CT scans of a perforated electrode immersed in silicone oil permitted to observe the shape of the bubble-to-gas interface and its variation under electric field applied across the electrode. These measurements are described in Sec. 7.4. They permitted to validate the electrodynamical model and enable modeling the bubble properties in noble liquids, and to design optimal electrode and

USC UNIVERSIDADE DE SANTIAGO DE COMPOSTELA

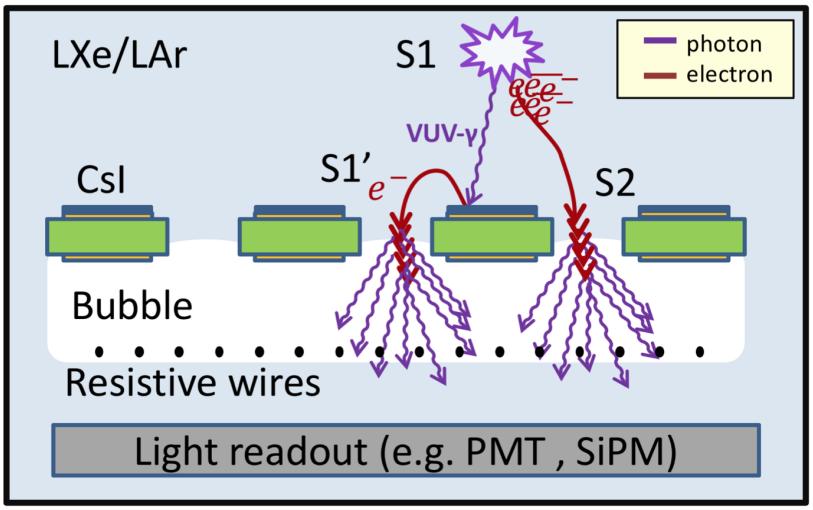

Figure 7.1: LHM operation principle - A bubble is formed using a set of heating wires placed underneath a perforated electrode (GEM or THGEM). The electrode top is coated with a CsI photocathode. Ionization electrons focused into the holes, or S1 scintillation-induced photoelectrons emitted from CsI, create electroluminescence photons after crossing the liquid-gas interface into the bubble. A position-sensitive photon detector (e.g. SiPMs, PMTs), located underneath the wires, detects the resulting S2 and S1' photons. Typical dimensions for a THGEM electrode employed in our setup are: electrode thickness 0.4 mm, hole diameter 0.3 mm and hole pitch 0.7 mm.

field configurations. This would allow optimizing both electron transfer into the bubble and the electroluminescence yield.

7.1 Equilibrium of the gas bubble under a THGEM-electrode hole: theory

The properties of a gas bubble formed and sustained under a THGEM-electrode determine the shape of the resulting bubble, and the conditions for its eventual stability. In particular, it is important to know whether the electrode's hole contains gas or liquid and what is the shape of the interface separating the two phases. We can then describe the electric field distributions in gas and liquid, under potentials applied to the electrodes (shown in Fig. 7.1), and discuss their role on the bubble stability and their effect on the detector performance. Thus, we consider the forces acting on the fluid, and examine the conditions that guarantee an equilibrium, taking into consideration the materials and geometrical parameters. In the following we assume that the fluid's gas and liquid phases are in static equilibrium. In an LHM-based detector, we might have to consider out-of-equilibrium con-

USC UNIVERSIDADE DE SANTIAGO DE COMPOSTELA

ditions, responsible for the formation, the movement, the coalescence and the escape of such bubbles, as well as convection and pressure fluctuations within the cryostat. The treatment of all these dynamical effects is out of the scope of the present work.

We schematize the situation considering an ideal single-hole electrode with axial symmetry, with a standing bubble formed underneath. For a matter of graphic convenience, a bubble protruding from the top side of the electrode is illustrated in Fig. 7.2 and discussed.

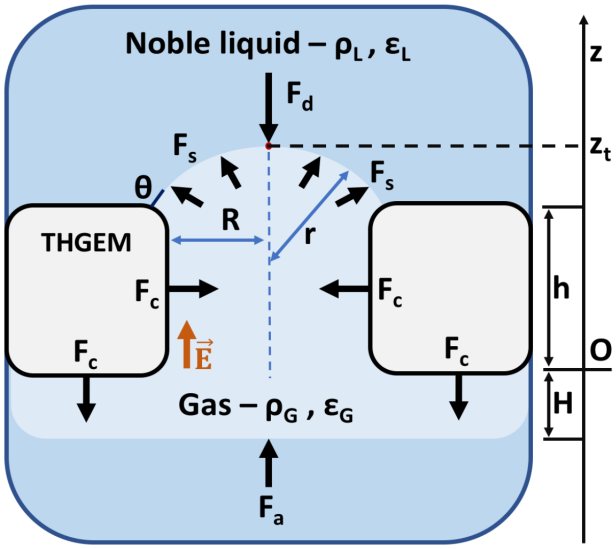

Figure 7.2: Scheme of a bubble protruding from the top side of a bore including all the main forces responsible for the dynamical equilibrium at the liquid-gas interface.

The bottom part of the bubble is considered flat and horizontal; its thickness H is imposed by the amount of gas trapped and is considered fixed. The top part of the bubble is contained by the lower face of the electrode plate; part of it may penetrate the hole, with or without protrusion out of it - depending on the equilibrium configuration. The gas-to-liquid interface-meniscus (from now on referred only as "meniscus" for simplicity) is the only material surface which we consider as dynamically free within the fluid, i.e. it re-adjusts its shape in order to satisfy the prescribed balance of forces. At rest, all forces, acting on the fluid in its bulk and at its boundaries, are in equilibrium. The relevant forces are (see Fig. 7.2): a) the dielectrophoretic force $\vec{F}_d$, due to the presence of a local electrical field $\vec{E}$ and to different values of the electrical permittivity ε in the liquid, ε_L, and in the gas, ε_G; b) the Archimedean lift $\vec{F}_a$, due to the different densities of the gas and the liquid phases; c) the containment forces exerted by the solid support $\vec{F}_c$,

USC UNIVERSIDADE DE SANTIAGO DE COMPOSTELA

and d) the surface tension $\vec{F}_s$, acting only at the interface between the two phases. Viscous forces, due to the differential motion of the fluid parcels, are absent in static conditions, and do not require consideration here.

The dielectrophoretic force acts throughout all the volume and it is generally expressed as the divergence of the Maxwell stress tensor, $\vec{F}_d = \vec{\nabla} \cdot \overline{\overline{T}}$, where $\overline{\overline{T}} = \varepsilon \vec{E} : \vec{E} - \frac{\varepsilon}{2}\vec{E}^2\overline{\overline{\delta}}$. We treat argon as an ideal dielectric, with neutral volume charge, and no charge accumulation at its interfaces between gas, liquid and solid boundaries. In this case, all terms related to the bulk drop out (see [304, 305]). The only remaining contributions arise from boundary terms at the material interfaces:

$$\vec{F}_d = -\frac{\varepsilon}{2}\vec{E}^2 \ \vec{n} \tag{7.1}$$

where $\vec{n}$ is the local normal at the domain boundaries.

We first discuss the stability conditions for the upper bubble meniscus, in the absence of electrical field ($\vec{F}_d = 0$). In first approximation we can derive an analytical expression for the meniscus position. The additional effect of the electrostatic field will be discussed later.

In purely hydrostatic conditions, the Archimedean lift $\vec{F}_a$ is compensated everywhere in the bulk of the fluid by the gradient of the local pressure p. We can therefore simplify the treatment, imposing only the equilibrium of the boundary forces, and reason in terms of the pressure p at the boundaries. On the solid immobile boundaries, a local constraint force balances the pressure, ensuring that the boundary remains fixed there, and we do not need to consider it explicitly. The force $\vec{F}_s$ acting on the surface element of the gas-to-liquid interface is described as the Young-Laplace pressure

$$\vec{p}_L = p_L\vec{n} = \frac{2\gamma}{r}\vec{n} \tag{7.2}$$

where γ is the surface tension between the two phases and r the local radius of curvature of the meniscus. To describe both concave or convex menisci, we adopt the convention $r > 0$ if the center of curvature of the meniscus is above it, i.e. if the concavity is oriented upwards - and vice versa. With this convention we consider p_L as positive if the force acts upwards. Referring to Fig. 7.3, all menisci depicted in green have $r < 0$, which implies downwards pressure forces and $p_L > 0$. A static meniscus implies

$$p_L = p_1 - p_2 \tag{7.3}$$

where p_1 is the relative hydrostatic pressure exerted by the liquid out of the bubble and p_2 is the one exerted by the gas. At the bottom of the bubble, which we assumed flat, $p_{L,b} = 0$, and thus $p_{1,b} = p_{2,b}$. This in turn is equal

USC UNIVERSIDADE DE SANTIAGO DE COMPOSTELA

to the hydrostatic pressure $\rho_l g H$ evaluated at the bottom side (ρ_l being the density of the liquid and g the acceleration of gravity). Inside the bubble, the pressure varies with height as $p(z) = p_{2,b} - \rho_g g(z + H)$. Here ρ_g is the density of gas; it is treated in first approximation as incompressible. The small vertical dimensions of the system and the small variations of absolute pressure, when compared to the ambient pressure (the saturation pressure of argon at the operating temperature, as described below in Sec. 7.2) justify this approximation. The z axis is drawn upward, with its origin at the bottom of the THGEM-electrode plate. At the top of the upper meniscus (z_t) we have thus

$$p_{L,t} = -\rho_l g z_t - p(z_t) = (\rho_g - \rho_l) g(z_t + H) \tag{7.4}$$

We interpret this as a condition imposing the radius of curvature of the meniscus as a function of its height z_t:

$$r = \frac{2\gamma}{(\rho_g - \rho_l) g(z_t + H)} \tag{7.5}$$

We note that even for the simple case of an axisymmetric meniscus within a circular vertical tube (e.g. a classical capillary rise problem), no general analytical solution for the actual shape of the surface exists (a reference numerical solution is given by [306]). To further simplify, we neglect the piezometric height differences along the meniscus. This is justified because in our case they are small, of the order of the radius of the THGEM hole R, and typically smaller than the capillary length $\sqrt{\gamma/g(\rho_l - \rho_g)}$. We thus approximate menisci as circular caps of homogeneous radius r.

The location of the upper meniscus is determined by a further geometrical constraint, the attachment line on the solid substrate at the hole's rim. On this contact line the meniscus forms a prescribed contact angle θ (defined here in the liquid side, see Fig. 7.3) with the wall. This angle is an intrinsic feature of the chosen materials, i.e. the gas, the liquid and the substrate material. Some relevant measurements of θ are presented in Sec. 7.2. Fig. 7.3 schematically shows possible meniscus locations. To define the attachment point at the edge of the hole, the bore edges are considered smooth. The meniscus settles on a position which, additionally to the prescribed θ, presents a downward concavity with the radius of curvature balancing the bubble pressure, and realizes a stable equilibrium with respect to movements normal to the interface center.

An approach for solving Eq.7.4 is presented in the appendix of [307], and is not reported here. In summary,

USC UNIVERSIDADE DE SANTIAGO DE COMPOSTELA

- for $\theta < 90°$, two equilibrium configurations are possible: the meniscus protruding from the top of the hole, or pinned at the bottom edge;
- for $\theta \geq 90°$, only a solution with the meniscus protruding from the top is acceptable.

Using experimental material parameters of argon, it was found that the bubble thickness evaluates to $0\,\text{mm} < H < 7.7\,\text{mm}$ if the meniscus is pinned at the bottom edge and to $7.3\,\text{mm} < H < 11.1\,\text{mm}$ if the meniscus protrudes from the top of the hole.

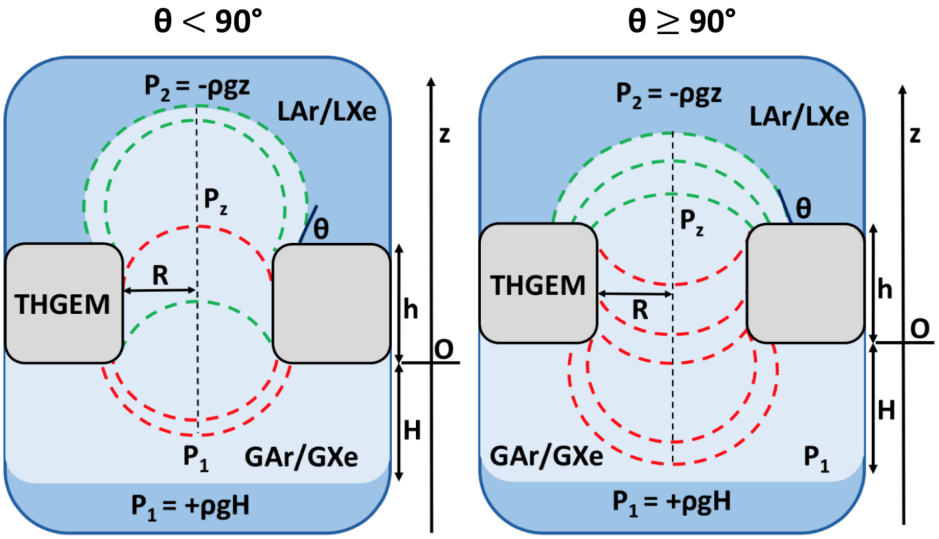

Figure 7.3: Meniscus configurations for Left) contact angle $\theta < 90°$; Right) contact angle $\theta \geq 90°$. In green, several acceptable equilibrium configurations are shown. Dashed red lines represent non-equilibrium configurations.

The electric field $\vec{E}$ applied across the hole (see Fig. 7.2) adds the term 7.1 to Eq. 7.3 and 7.4, transforming them into

$$p_L = p_1 - p_2 - \frac{1}{2}(\varepsilon_G \vec{E}_1^2 - \varepsilon_L \vec{E}_2^2) \tag{7.6}$$

It thus requires a different value of the radius of curvature r in order to satisfy Eq. 7.6.

Formally, the electric force $\vec{F}_d$, which also acts normally to the interface, can be assimilated to a local "electric" pressure force. In contrast to the piezometric term, the spatial dependence of the electric field is nontrivial for complex electrode geometries, and it is not as easy to define viable analytical

USC UNIVERSIDADE DE SANTIAGO DE COMPOSTELA

approximations as for pure hydrostatics. We therefore resort to numeric computation, as described below in Sec. 7.3.

7.2 Observation of captive bubbles in liquid Argon

The experimental characterizations of the bubble contact angles on different surfaces were conducted with the previously described LAr cryostat, WIS-ArD (Sec. 6.1.2). With respect to the bubble experiments performed in [211], the cryostat system was modified to include three of the aforementioned viewports, pointing at the inner experimental assembly; they were oriented perpendicular, $+60°$ and $-60°$ with respect to the chamber axis. The detector assembly was suspended from the topmost flange, equipped with an addional viewport.

The system was operated with LAr at the temperature of 90 K, with saturated vapor phase above, at a pressure $p_{sat} = 1.365$ bar. In these conditions, the expected properties of argon are: liquid density $\rho_l = 1395.4\,\mathrm{kg/m^3}$, gas density $\rho_g = 1.784\,\mathrm{kg/m^3}$, surface tension $\gamma = 11.83\,\mathrm{mN/m}$, dielectric coefficient of the liquid phase $\varepsilon_l = 1.504$, dielectric coefficient of the gaseous phase $\varepsilon_g = 1.000516$ [308].

The experiments were prepared adopting the following methodology:

- Planar 1.5 mm thick, 7 mm in diameter slabs of different materials were prepared: Copper, Epoxy Resin (FR4), Teflon and Kapton. Surface finishing was realized using super-fine sanding (600-grits) in order to grant an high-quality polishing. Prior to their installation, the samples underwent an ultrasonic cleaning cycle in petroleum ether, acetone (whereas possible) and ethanol;
- A grid of resistive wires (Ni-Fe, 55 μm in diameter, 2 mm spacing) was fixed at 5 mm below the sample. The wires were powered to form bubbles in the noble liquid via thermal emission (Joule effect);
- Bubbles were observed with a CALTEX VIP-50-HD60 camera via the viewport orthogonal to the chamber axis; illumination was introduced through the other viewports (Fig. 7.4).

A standard technique to measure contact angles is the so-called "captive bubble method" [309], where the angles are reconstructed from the images of the bubbles trapped underneath a surface. In order to reconstruct the contact angle formed between the bubble and the chosen substrate, we

USC UNIVERSIDADE DE SANTIAGO DE COMPOSTELA

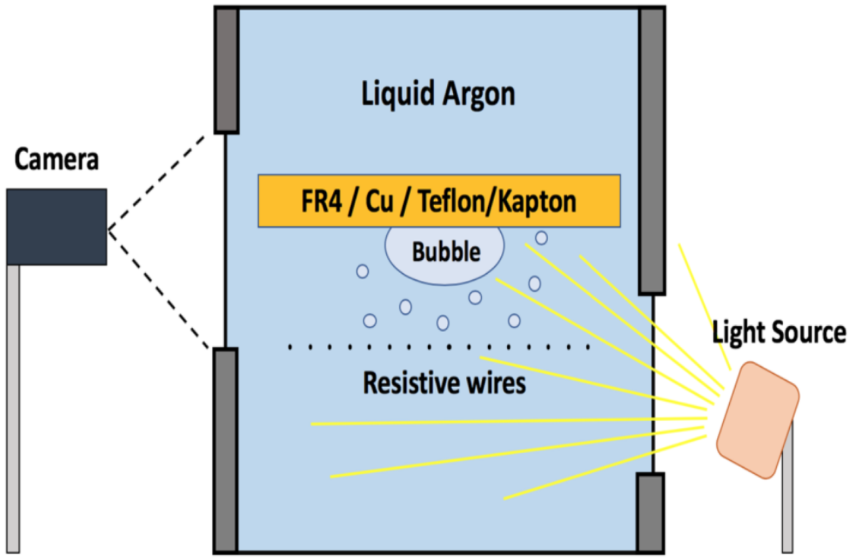

Figure 7.4: Scheme of the setup used to characterize the contact angles of bubbles trapped under different materials in LAr.

recorded multiple sets of images (1000 frames/set); the camera operated in an automatic acquisition mode (1 frame/second). The images were processed using a dedicated Python script, adjusting contrast and brightness, converting color into greyscale and cropping the frame around the bubble. Each set of images, consisting of 200 distinct bubbles (for a total of 400 contact angles) was subsequently manually analyzed, using the drop-shape analysis extension "DropSnake" [310] for the software ImageJ [311]. The shape reconstruction was done with an interactive spline method where the knots (see yellow dots in Fig. 7.5b, Fig. 7.5d) were placed by hand on the bubble interface [312]. This method offered us a rather straightforward and reliable way to reconstruct the bubble shape; it provided us with two, left and right, values of the contact angle for each frame. The distribution of each resulting statistical sample was fitted through a MATLAB script.

As discussed in Sec. 7.1, according to the contact angle value, different equilibrium configurations are allowed, affecting the liquid-to-gas interface (meniscus location and shape).
Conventionally, we will define the solid material to be:

- argon-phobic, if $\theta > 90°$, meaning that the local gaseous phase tends to adhere and spread over solid substrate (7.5d);

USC UNIVERSIDADE DE SANTIAGO DE COMPOSTELA

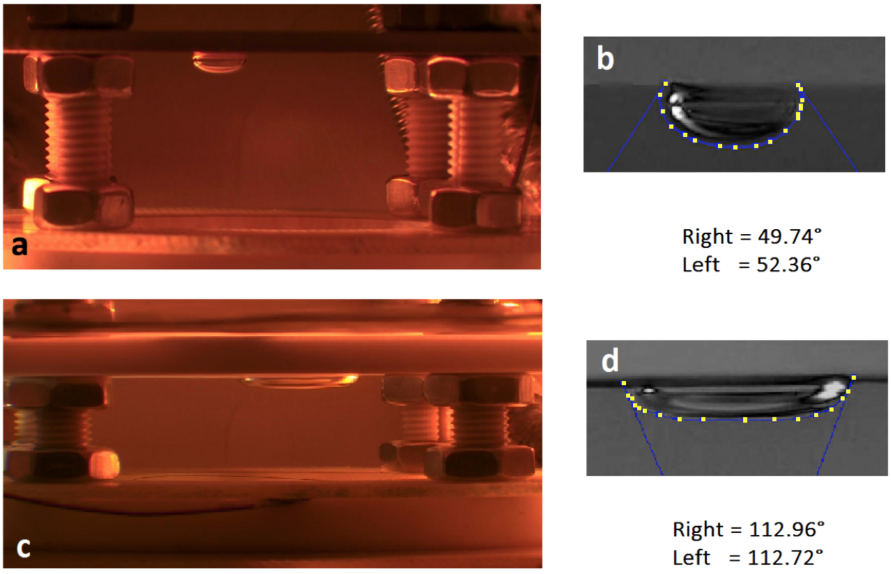

Figure 7.5: (a) Argon bubble trapped underneath a Copper slab surface, immersed in liquid argon; (b) Bubble reconstruction from the image depicted in a), processed according to the methodology discussed in the text; both, left and right contact angles were recorded. (c) A bubble trapped underneath a Teflon slab immersed in LAr; (d) Example of bubble reconstruction of the image depicted in c).

- argon-philic, if $\theta < 90°$, meaning that the liquid has the tendency to wet the solid material (7.5b).

The prefix "argon" in the definitions makes explicit reference to the liquid phase.

Our experiments were carried out with Copper, Epoxy resin (FR4), Teflon and Kapton. They revealed an argon-philic behaviour for bubbles sticking to FR4, Cu and Kapton (e.g. for Cu in Fig. 7.5 top); Teflon exhibited an argon-phobic tendency (e.g. Fig. 7.5 bottom). In the former case, the presence of small and escaping bubbles was favored while in the latter, the bubbles tended to coalesce into a large one and to spread over the substrate's surface.

Therefore, the measured contact angles are considered "dynamic" ones, since the bubbles did not remain static on a sufficiently long observation timescale. They rather represent an average between the "advancing" contact angle and the "receding" one. Precise values of "static" contact angles are therefore contained in an interval of values bounded by the advancing/re-

USC UNIVERSIDADE DE SANTIAGO DE COMPOSTELA

ceding contact-angle values [313].

An example shown in Fig. 7.6 depicts the Gaussian-fitted contact-angle histogram for bubbles sticking to a FR4 surface in LAr.

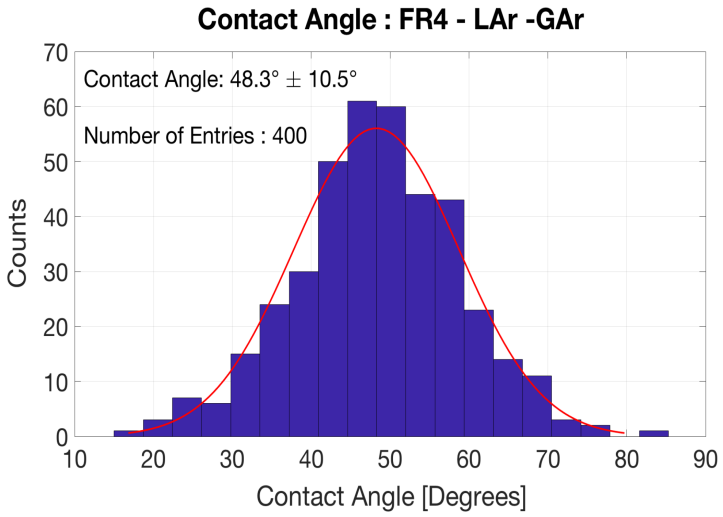

Figure 7.6: Example of a fitted histogram of contact angles measured with argon bubbles sustained underneath a slab of FR4 surface, immersed in LAr.

Table 7.1 summarizes the measured contact angles of bubbles sticking to Cu, FR4, Teflon and Kapton surfaces in LAr.

Material	Measured θ	Behaviour
Copper	$45.5° \pm 8.5°$	Argon-philic
FR4	$48.3° \pm 10.5°$	Argon-philic
Teflon	$108° \pm 6.5°$	Argon-phobic
Kapton	$59.3° \pm 9.3°$	Argon-philic

Table 7.1: Contact angles measured in LAr, for bubbles sticking to different substrate-material surfaces.

Little can be said in quantitative terms about the effects of the environment surrounding the bubble (presence of fluid motions, convection, pressure gradients, spontaneous-bubbles background etc.). It was observed that the bubbles were "breathing" (cyclic deflation and swelling) [216] and occasionally escaping from the field-of-view during the measurements.

The dynamic contact angles (Table 1) measured here for the first time,

USC UNIVERSIDADE DE SANTIAGO DE COMPOSTELA

are important parameters - implemented below in our numerical simulations.

7.3 Numerical simulations of the bubble electrodynamics

Determining the equilibrium conditions for the bubble in presence of an electrostatic field is crucial. The field, induced by the potentials applied to the various electrodes, depends on the medium (liquid, gas or substrate material), and on the geometrical layout. At the same time, the dielectric forces on the fluid boundary affect the shape of the bubble, determining which parts of the domain are occupied by gas or liquid, changing the layout itself. In order to solve the problem, these two effects need to be coupled. Because of the non-trivial spatial dependence of the electric field, the problem is addressed computationally. Numerical simulations were carried out using the microfluidics module of the commercial package COMSOL™(v. 5.4). The numerical solution provides, in addition to the liquid-to-gas interface equilibrium shapes, full characterization of the electrical field in the vicinity of the hole rim. Full details about the protocol of the numerical simulations, and the methodology used to determine the stable bubble profile for given parameter values, are reported in the appendix of [307].

Fig. 7.7 depicts equilibrium positions of the meniscus in argon, obtained varying the electrode potentials, for menisci pinned at the top and bottom of the hole. Both sets use values H of the bubble depth, and different applied-voltage range, for which pure hydrostatics guarantees stable solutions at $V_0 = 0\,\mathrm{V}$.

In the present geometry, both for meniscus locations at the top and at the bottom of the hole, the electric pressure (eq. 7.1) always acts downwards from the upper liquid phase towards the gas one. Consequently, its effect is always that of increasing the value of the curvature $\kappa = 1/r$ (cfr. eq. 7.2).

For increasing V_0 values, the concavity κ is negative and is oriented downwards; in the case of the bottom meniscus, stable solutions with reversed and positive concavity exist for higher values of V_0.

Detailed analysis of the electric field, not reported here, shows local variations of the electric pressure ($P_E \sim E^2$), causing the formation of a non-uniform curvature. In a real experiment, deviations from the idealized geometrical shape induce discrepancies with respect to the computed profiles. For $\theta < 90°$, the meniscus can attach around the bottom edge of the hole to different points than at the top. This implies a larger range of ad-

USC UNIVERSIDADE DE SANTIAGO DE COMPOSTELA

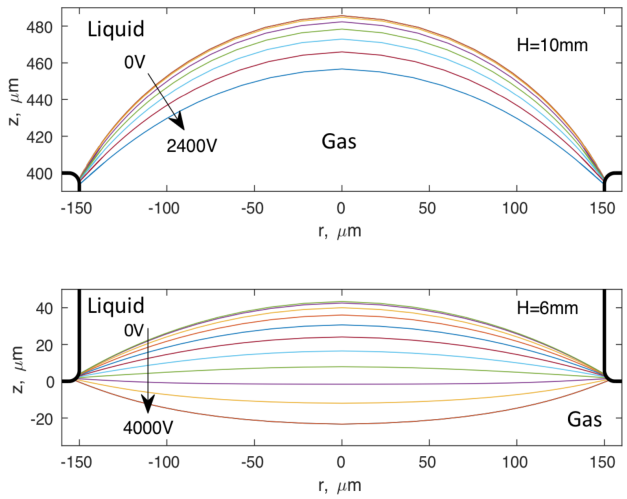

Figure 7.7: Relaxed meniscus profiles in argon at (a) top and (b) bottom of the hole. Profiles are obtained at fixed bubble depths H, and varying V_0 values in steps of 400 V as indicated on the figure.H and V_0 were chosen to satisfy equilibrium solutions.

missible curvatures satisfying the contact angle constraint and means that it is physically possible, tuning parameters like H and V_0, to cause a larger variation of the meniscus concavity if the same is attached to the bottom of the hole rather than at the top. On the lower face, both convex and concave menisci are allowed. This is reflected in the larger range of applicable voltages to maintain equilibrium at the bottom, albeit for different values of the gas layer thickness H (keeping all other material parameters equal).

We remark that the method used here is essentially one that searches for the relaxation to a static bubble equilibrium, and serves only to determine the parameter ranges for which the one or the other meniscus solution is stable, and the resulting actual bubble shape. The numerical procedure adopted here does not reveal which of the two positions of the meniscus is more likely to appear when the bubble is formed, and does not guarantee that a bubble destabilized by a large perturbation will return to the same equilibrium shape. It is for example possible that a bubble collapses to a given different position once some amount of gas is added at the bottom or escapes through the hole. Such effects can only be assessed by full fluid dynamics simulations, which are beyond the scope of this work.

USC UNIVERSIDADE DE SANTIAGO DE COMPOSTELA

7.4 Experimental validations by X-ray micro-CT

The validation of the results derived from the model presented in Sec. 7.1 requires a direct observation of the bubble interface location and shape in a perforated structure. While not simple in a noble liquid, a way was found to observe the interface in a perforated electrode immersed in water or in silicone oil, at room temperature – applying X-ray microtomography (μ-CT) [314, 315]. This technique, widely employed in the fields of biomedicine, materials research and in industry [316, 317, 318], offers the possibility to reconstruct with micrometric precision 3D tomographic images of an object using X-rays; these represent a 3D distribution of the mass attenuation coefficients within the object.

A successful validation in these materials of the bubble hydrostatics and electrodynamic models, described above, is expected to predict the behavior of bubbles in the noble liquid.

7.4.1 Validation of the bubble hydrostatics in water and in silicone oil

The perforated-electrode sample used in the hydrostatic experiments was composed by a 0.4 mm thick FR4-made bare (no Cu) THGEM-like disc of 13.9 mm diameter with 0.5 mm diameter holes , spaced by 1 mm. The disc was installed in a dedicated Plexiglas container, with a side aperture for inflating a gas bubble underneath. Two liquids were selected for the investigations: water (with 5% KI added to improve the contrast) and silicone oil (Dow Corning diffusion pump oil - 704); the latter was chosen because of its electrical insulating properties (for further experiments under electric fields). The assembly is depicted in Fig. 7.8. An air-bubble was injected underneath the electrode immersed in the liquid. Then, the container was introduced into a ZEISS Xradia 520 Versa micro-CT scanner (up to 0.7μm spatial resolution, X-ray source: 30-160kV). The tomographic sets of X-ray transmission images were acquired in 1201 consecutive steps over an angular range of 360 degrees at the X-ray source voltage of 110kV and the current of 91 μA. Each transmission image with the pixel size of 2.1μm was acquired over 22 s, whereas an entire tomographic set was collected over ca. 8 h.

Reconstructions of the bubble-interface protrusions into the holes obtained in the two investigated liquids are illustrated in Fig. 7.9. The bubble interface penetrates into the 0.5mm diameter holes by $\approx$ 16.5 μm and $\approx$ 37 μm in water and oil, respectively. These values are in good agreement with

USC UNIVERSIDADE DE SANTIAGO DE COMPOSTELA

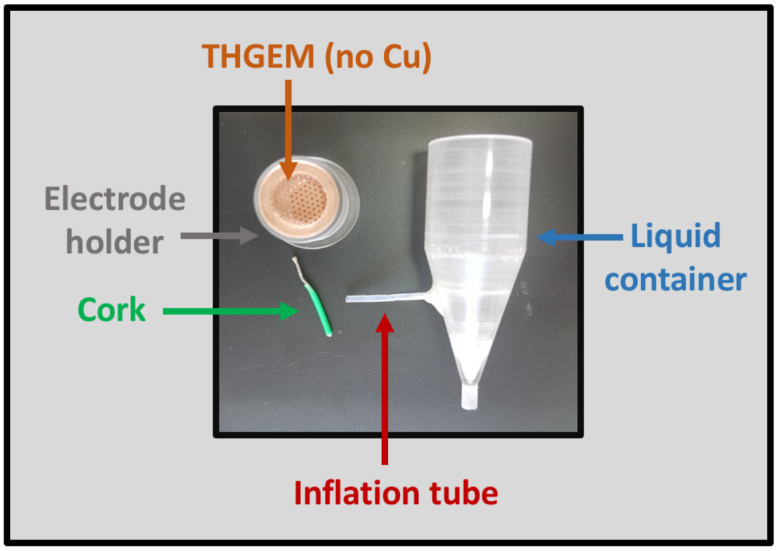

Figure 7.8: Bare THGEM sample installed into a dedicated Plexiglass electrode holder.

the respective model predictions of 16 μm and 35 μm. The thickness of the gas in these experiments was $\approx$ 4 mm. Estimations of the expected protrusions were computed for both liquids using the values of the contact angles measured on a FR4-substrate surface with a sessile drop method [319, 320]. From the contact angle measurements, it was found: $\sim$39° and $\sim$24° for water and silicone oil, respectively. Possible causes for the very small deviations ($\approx$ 6%) in the interface protrusion from our model prediction, might be related to uncertainties in the measured contact angles or other experimental systematic errors.

7.4.2 Validation of the bubble electrodynamics in silicone oil

Following the hypothesis that the electric field at the interface should have an impact on its shape and the model-simulation results, led our experimental efforts to validate the bubble electrodynamics. Experiments were carried out in silicone oil, using the same container. To avoid X-ray beam hardening artifacts in the μ-CT reconstruction process, metal coating of the perforated electrode had to be avoided. Instead, the two surfaces were evaporated with thin (10nm) graphite films prior to hole drilling. In addition, the 1mm-thick FR4 perforated-electrode disc was designed with a 0.1 narrow Cu HV-contact ring.

USC UNIVERSIDADE DE SANTIAGO DE COMPOSTELA

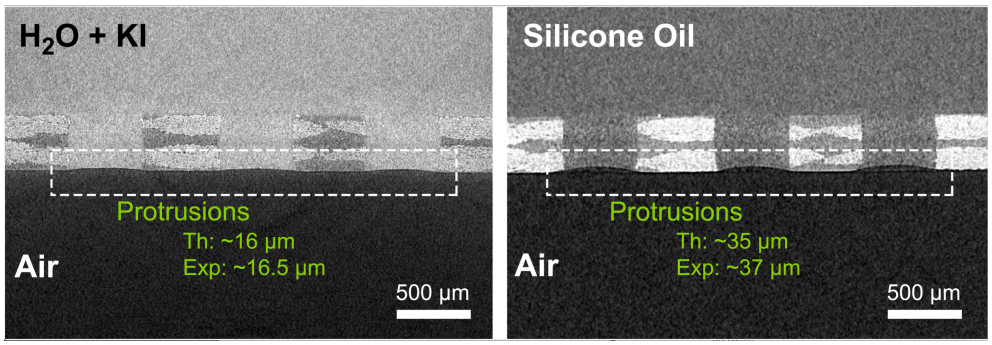

Figure 7.9: μ-CT cross-section images of air bubbles trapped underneath a bare perforated electrode immersed in Left) H_2O+5%KI; Right) Silicone oil. The theoretical and experimental values for the bubble protrusion into the 0.5mm diameter holes are displayed. Note the laminated structure of the FR4 epoxy-resin plate.

After graphite-film evaporation, holes of 0.8 mm diameter were drilled on the disc. The experimental μ-CT procedure is similar to the one described above. The voltage was supplied to the electrode by a CAEN N8315 NIM Power Supply. Tomographic scans were run at two different voltage configurations: ΔV= 0 kV and 3kV (E = 0-30kV/cm over the 1mm thick disc). The tomographic scans were of 8h duration and of an intrinsic resolution of 2.5μm.

It should be added that the contact angle of an air bubble trapped in silicon oil underneath a graphite surface was measured by x-ray transmission (see Fig. 7.10) in the microtomography system; it is an important parameter for the model simulations.

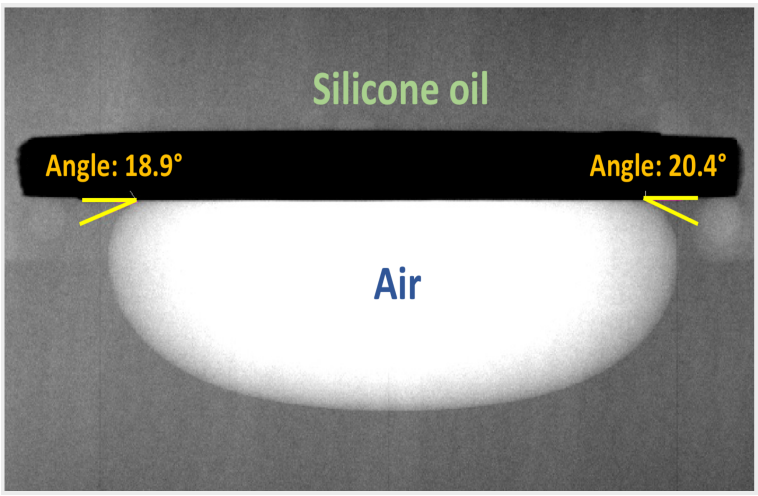

Figure 7.10: μ-CT reconstruction of an air bubble trapped underneath a graphite-coated disc immersed in silicone oil. The average measured contact angle equals to 19.6°.

USC UNIVERSIDADE DE SANTIAGO DE COMPOSTELA

The measured average value for the contact angle of the air bubble sustained below a graphite-coated disc immersed in silicone oil is 19.6° and the measured bubble thickness is ≈ 3.4 mm.

In order to implement our simulations, the following parameters were taken into account: the measured contact angle, the dielectric constant of air $\varepsilon_{air} = 1$, of silicone oil $\varepsilon_{SO} = 2.8$ ($\Delta\varepsilon_r = \varepsilon_{air} - \varepsilon_{SO} = 1.8$) and the surface tension of silicone oil $\gamma_{SO} = 37.3$ mN/m, as reported in [321, 322].

A direct comparison of the reconstructed protrusions via μ-CT with the simulations was not possible because of the presence of surface imperfections stemming from the drilling process. Instead, we opted for the comparison of the reconstructed protrusion variations measured at the center with the electric field assuming ideal edges. The reconstructed images for the applied voltage ΔV=0kV and 3kV are shown in Fig. 7.11.

The difference between the expected protrusion variation within the 0-3 kV range in simulations, ∼28 μm, and the measured one, ∼34 μm, is in agreement within ∼16% error. It is possible to observe that not only the interface re-adjusts itself to satisfy the new equilibrium set by the presence of the electric field, but also that the preferential configuration corresponds to a bubble protrusion into the hole from the bottom of the electrode. No bubble protrusion was observed in this work from the top side of the electrode.

In Fig. 7.11, the reconstructed images for the applied voltage ΔV = 0kV and 3kV are shown.

7.5 Conclusions

In this work, we aimed at evaluating the nature of the interface of a gas bubble trapped in liquid under a perforated electrode. The subject is of high relevance for understanding the physical processes in bubble-assisted Liquid Hole Multiplier (LHM) noble-liquid radiation detectors. Starting from the hydrostatic equations describing a bubble trapped in liquid argon underneath an electrode, the possible bubble equilibrium configurations were computed and the distinct behaviors (argon-philic/-phobic) dictated by the value of the contact angle were discussed. For the first time, bubbles in liquid argon were optically observed and their dynamical contact angles were measured in liquid argon on potential materials forming LHM electrodes: Cu, FR4, Teflon and Kapton. The experimental results opened the way to investigate with numerical simulations the effects of external electric fields

USC UNIVERSIDADE DE SANTIAGO DE COMPOSTELA

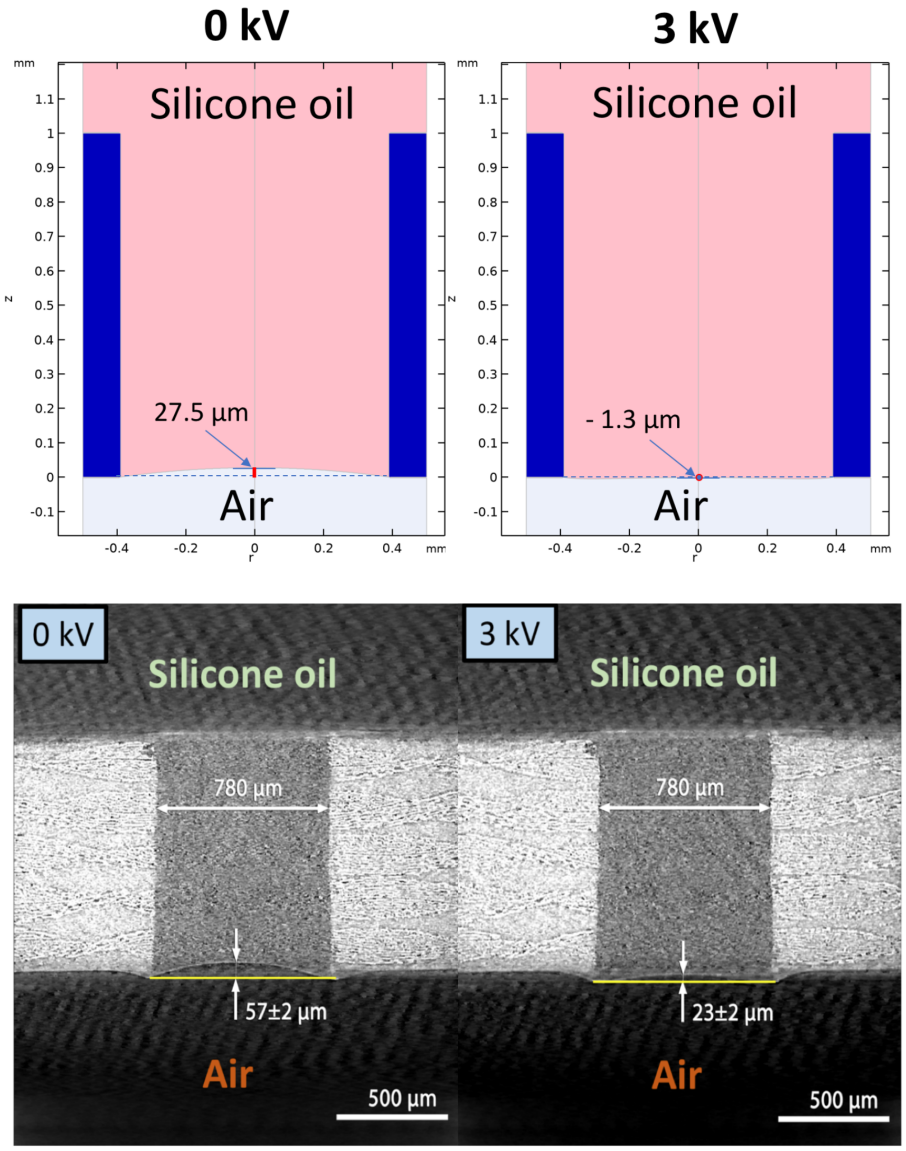

Figure 7.11: Top: results of the simulation of an air bubble trapped under a graphite-coated THGEM hole immersed in silicone oil for two different voltage configurations; Left: 0 kV; Right: 3 kV. Bottom: reconstructions of an air bubble trapped under a graphite-coated THGEM immersed in silicone oil for two different voltage configurations; $2.5\mu m$ resolution scans. Estimations of the experimental bubble protrusion variations are displayed on each panel. Left: 0 kV; Right: 3 kV.

on the bubble equilibrium configurations and on the meniscus-like liquid-to-gas interface in the presence of holes. As a result, it was clarified that the electric fields at the interface vicinity contribute to the equilibrium balance

USC UNIVERSIDADE DE SANTIAGO DE COMPOSTELA

as an additional pressure term. This translates into a downwards thrust and into deformations of the bubble interface according to the intensity of the applied field. The results of the model-simulated bubble hydrostatics and electrodynamics in room-temperature water and silicone oil, were validated by μ-CT imaging experiments. It is of interest to report here that in all the experiments performed at room temperature no stable bubble protruding from the top side of the electrode was observed for $\theta < 90°$. The presence of a liquid-to-gas interface located at the bottom of the hole was also outlined in [212] in the context of LXe-LHM. Therefore it would be reasonable to assume that also in LAr, for $\theta < 90°$, the expected equilibrium configuration corresponds to a bubble protruding from the bottom side of the electrode's hole. Using μCT it was shown that it is possible to reconstruct the interface of an air bubble trapped underneath an electrode immersed in water or in silicone oil within 6% agreement with the theoretical predictions. A validation of our bubble electrodynamics model was achieved in silicone oil, under different electric-field conditions; the observed interface-protrusion variations with the field were in 16% agreement with the simulations. The successful validation of our model in room-temperature liquids, should lay the groundwork for inferring the bubble-interface configuration in noble liquids. Further model-simulations studies are expected to shed more light on the interface modifications induced by shaping the electric fields at the holes' vicinity. These could serve as a solid base for the enhancement of the electron transfer efficiency from a noble liquid to the bubble in LHM detectors.

An optimal field (and interface) shaping could also play a role in enhancing their electroluminescence (EL) photon yield. While currently most of the EL-photons are emitted within a small portion of the bubble, at the vicinity of the bottom of a hole [212], conditions may be found to push the interface deeper into the high-field region within a hole, thus enhancing the EL-photon yield. To this regard, an optimization of the electrode geometry allowing for an equilibrium configuration of the meniscus located at the hole center could be investigated (e.g. SC-GEM, [212]).

USC UNIVERSIDADE DE SANTIAGO DE COMPOSTELA

USC
UNIVERSIDADE
DE SANTIAGO
DE COMPOSTELA

8 Ar/CF_4 secondary scintillation

As mentioned in sec. 4.4.1, a mixture of argon and CF_4 would be ideal for operating DUNE NDGAr as an OTPC. Moreover, throughout the thesis it has been widely discussed about all the advantages brought by this kind of gas mixture. With this in mind, a spectroscopic study of primary scintillation has been already carried out [86]. Since, as explained in Sec. 2.2, a different population of states is expected for the secondary scintillation, it is important to extend the study [86] by including it. Moreover, a study of charge and optical gain in the parallel plates configuration could be performed. Additionally, it was possible to perform comparative studies with pure CF_4 and He/CF_4, a gas mixture selected for example for the CYGNO experiment, a gaseous TPC aiming at detecting low energy nuclear recoils [323, 324]. Since this study has not been published yet and I cannot give proper credit by means of a paper's author list, I acknowledge the fundamental contribution for this work of Florian Brunbauer (who additionally made the GDD lab facilities available for me) and Pablo Amedo.

8.1 Experimental setup

The measurements were taken at the Gaseous Detectors Development (GDD) laboratory at CERN, using the same setup described in [86], with small modifications (Fig. 8.1). The electrodes were placed in a parallel plate configuration: the cathode was made of an aluminium foil, while the anode

USC UNIVERSIDADE DE SANTIAGO DE COMPOSTELA

was a semi-transparent chromium mesh, evaporated on top of a fused silica plate. The two electrodes were kept 1 mm apart by means of four 0.25 mm FR4 spacers. The anode was grounded through a picoammeter (Keithley 6487), allowing for a current reading during the experiment. Behind the anode, a collimating lens (OceanOptics 74-UV) was placed, connected to an optical fiber (UV-VIS, 600 µm core). The fiber was ultimately coupled to a CCD spectrometer (OceanOptics FX UV-VIS), sensitive to wavelengths in the range 220-800 nm. In front of the cathode, on the other hand, an X-ray gun made of a copper tube, with tunable voltage and current, could irradiate the setup through a 1-cm-diameter aluminium window.

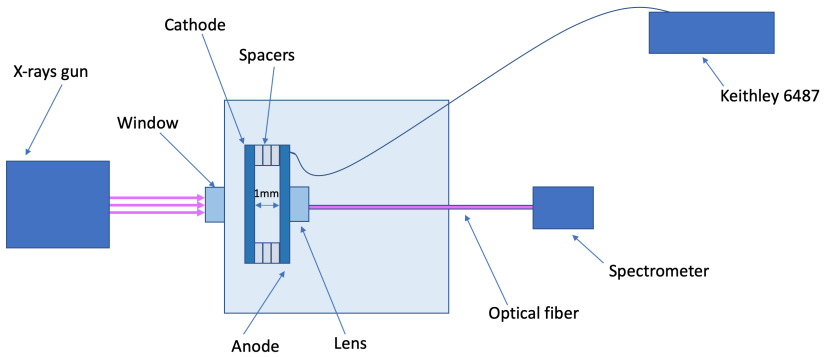

Figure 8.1: Setup for the Ar/CF_4 secondary scintillation measurements. From left to right: an X-ray gun irradiating the setup through a 1-cm-diameter collimating aluminium window; the electrodes in parallel-plate configuration, 1 mm apart one from the other; a collimating lens directing the scintillation light into an optical fiber and ultimately to a CCD spectrometer; a picoammeter measuring the current from the anode.

Before mounting the full setup, the response of the anode-lens-fiber-spectrometer chain was calibrated by using an external lamp, able to emit UV and visible light of known spectra. The two calibrations were automatically merged at around 300 nm by the OceanView software associated with the spectrometer.
Previously to any gas filling, the system was pumped with a primary pump down to $\sim 10^{-2}$ mbar; thereafter, CF_4 gas was inserted first, until the required partial pressure was achieved. Subsequently, the argon was added, relying on the forced flow of a dominant quantity of argon for the mixing, following the approach described in [86]. For every CF_4 concentration under study, the system was initially filled with 4 bar of total gas, and then the gas was evacuated out of the system via a leak valve in steps of 1 bar until 1 bar inside the chamber was reached; an additional set of data at P = 0.5 bar was then taken. The pressure was monitored during the filling procedure with an opportunely calibrated MKS pressure transducer for the highest pressures,

USC UNIVERSIDADE DE SANTIAGO DE COMPOSTELA

and otherwise with a Pfeiffer Vacuum PCR 280 Pirani/Capacitance gauge, which gets saturated at P $\geq$ 1.5 bar.
Additional data was taken with a He/CF_4 mixture and pure CF_4 at 1 bar, following analogous filling procedures.

8.2 Data taking and analysis

Before taking S2 data, some spectra of the primary scintillation (no electric field applied) were taken with Ar/CF_4 99/1 to make sure the spectral response was in agreement with [86]. Although the spectra were much fainter, as expected since the gap between the electrodes had been reduced by a factor of 7.5, the peaks were observed in the same wavelength, and compatible UV-vis ratios. Calibration of the setup in different conditions gave confidence about the lack of serious issues in the system that could affect the spectra. The main source of contamination was assessed to be H_2O, inferred from the peak centered at $\sim$ 310 nm, corresponding to the transition $OH^*(A^2\Sigma^+) \rightarrow OH(X^2\Pi)$; this is generated by charge transfer between Ar^+ and H_2O^+ ($Ar^+ + H_2O \rightarrow Ar + H_2O^+$), followed by dissociative recombination [325, 86]. The prominence of the peak was pressure-dependent, as it was observed to become more dominant at low pressures; a dependence with time was ruled out with a dedicated scan at 0.5 bar with Ar/CF_4 99/1, excluding that the 310 nm peak was due to system leakage. A minor source of contamination was nitrogen, whose lines in the 335-380 nm range are barely visible in the spectra.

For each combination of concentration and pressure, the electric field was increased until reaching breakdown inside the gas; applying an electric field slightly below breakdown conditions, a scan of current at the anode against x-ray intensity was then performed: in fact, to avoid space-charge effects, it was necessary to work at x-rays intensities below the saturation point (see Fig. 8.2). The choice of x-ray intensity was mainly pressure-dependent: while saturation was easily reached at the lowest pressures under study, at pressures of 3-4 bar the setup was limited by the feedthrough breakdown voltage, and by the presence of strong feedback effects at high fields; to compensate for the low gains reachable, it was necessary to use a higher x-ray intensity. Due to the instabilities encountered at 4 bar for Ar/CF_4 80/20 and 90/10, the related data require more in-depth analysis and are omitted in this work.

Once established the optimal x-ray intensity, a scan in gain was performed, taking 10 spectra at the highest electric field achievable, and the values of current at the anode for the whole scan; at 1 bar extra sets of 10 spectra

USC UNIVERSIDADE DE SANTIAGO DE COMPOSTELA

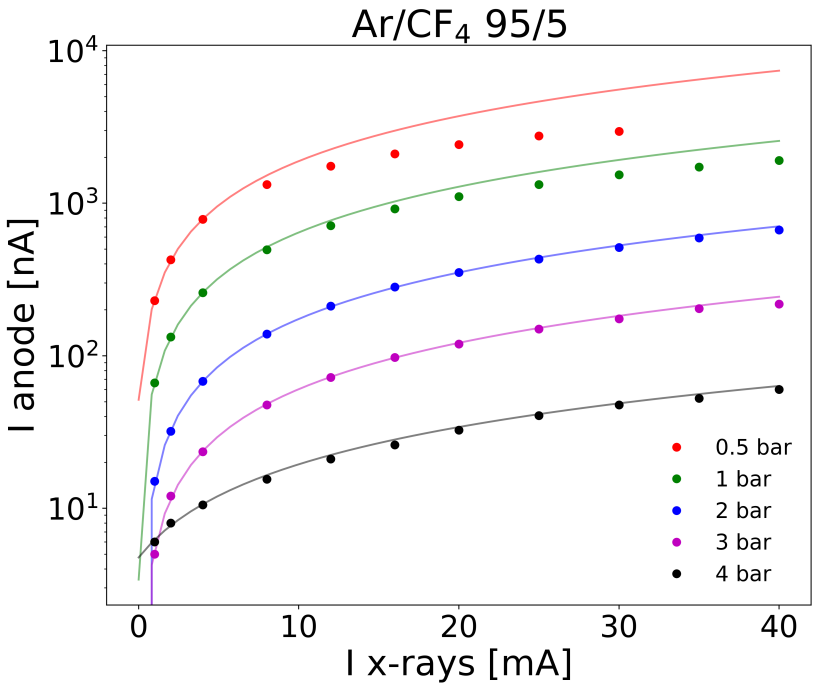

Figure 8.2: Example of saturation curve for Ar/CF_4 95/5: the effect is more prominent for low pressures (0.5 - 1 bar), where it was necessary to set a low x-ray intensity to avoid space-charge effects; on the contrary, a high x-ray intensity (typically 30 mA) was used for higher pressures (3 - 4 bar), where the electric field (hence the gain) was limited by breakdown at the feedthrough and feedback effects.

were taken at different electric field values.
At the end of each scan, 10 spectra of the primary scintillation were recorded, in order to subtract from the secondary scintillation spectra the contribution from the background, constituted by the primary scintillation and spurious effects from the spectrometer. As no significant effects from recombination were observed in [86], these spectra were taken at zero electric field.

The 10 collected spectra for each scan were then averaged, background-subtracted, corrected for the calibration factor, and finally converted in number of photons. A smoothening of the spectra was also performed by means of a moving average.

USC UNIVERSIDADE DE SANTIAGO DE COMPOSTELA

8.3 Results

8.3.1 Spectra at different concentrations

Fig. 8.3 (top) shows the spectra taken for Ar/CF_4 mixtures at different concentrations (respectively 20%, 10%, 5%, 2%, 1% and 0.5% CF_4), normalized to the peak appearing in the visible region (∼630 nm). While an absolute comparison of the yields in this case would be pointless, since the data was taken in different conditions of gain and x-ray intensity, considerations can be made about the peaks that are seen and the transitions that produce them. The spectra, for all concentrations and pressures, show two major peaks, one centered in the UV region (∼260 nm), and the one aforementioned in the visible (∼630 nm). The two peaks are attributed, respectively, to the transitions $CF_3^*(2A_1^{'}) \rightarrow CF_3(1A_2^{''})$ and $CF_3^*(2A_2^{''}, 1E^{'}) \rightarrow CF_3(1A_1^{'})$ [326, 327]; both peaks show a systematic broadening towards shorter wavelengths at low pressure. The yields ratio between the visible and UV peaks, if properly defined in order to exclude the emission from OH and the emission lines appearing in the IR region (stemming from argon [328]), remains constant (∼10:1) for the pressures and concentrations investigated, and looks independent from the field applied (Fig. 8.4).

The shape of the spectra displays significant differences with the spectra of primary scintillation observed in [86] (Fig. 8.3 bottom): in this case, a double peak in the UV region was reported, attributed to transitions stemming from $CF_4^{+*}(\widetilde{C})$ states, which require a higher energy to be formed, as expected (see Sec. 2.2). An additional peak present at 400nm, and attributed to transitions from the D state, requires of even higher electron energies and is also absent in the spectra of secondary scintillation.
A comparison can also be made with pure CF_4 and He/CF_4 80/20 mixtures, whose spectra at 1 bar are shown in Fig. 8.5: in the case of pure CF_4, the UV transition stemming from the CF_3^* still looks dominant; this is in agreement with [330], where a significant contribution from this state was observed in the UV region in secondary scintillation spectra obtained with a GEM and a MSGC. On the other hand, the He/CF_4 80/20 mixture displays a very clear double peak structure in the UV region, which is even predominant with respect to the visible emission. A possible explanation could be the higher electron energies in helium, which could lead to the formation of excited states with higher energy. Superimposed to the spectra taken with the He/CF_4 80/20 mixture, a spectrum taken with He/CF_4 60/40 from [71] is shown: as for the case of Ar/CF_4, the concentration of CF_4 doesn't seem to play a role on the spectral shape of He/CF_4 mixtures.

USC UNIVERSIDADE DE SANTIAGO DE COMPOSTELA

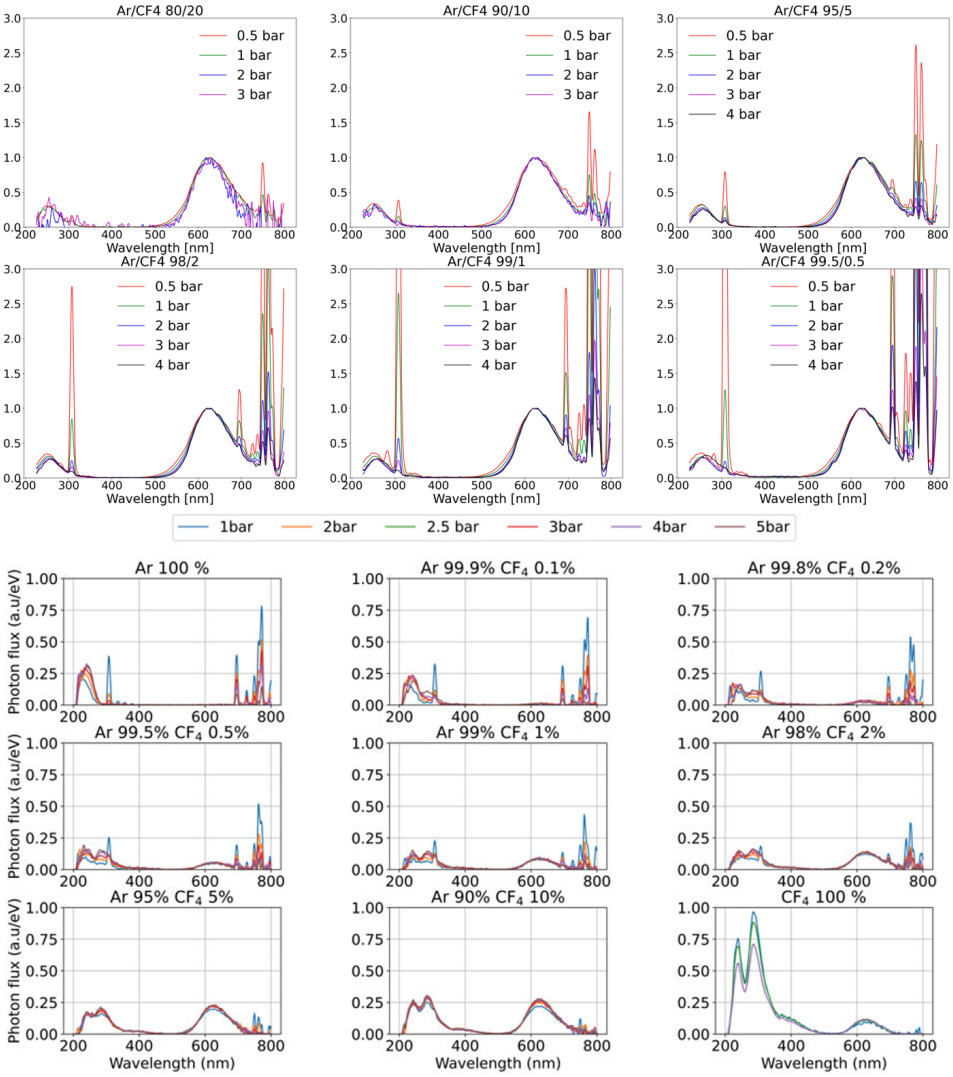

Figure 8.3: Top: secondary scintillation spectra in the pressure range 0.5-4 bar for Ar/CF_4 mixtures with different concentrations. Each spectrum is normalized to the maximum of the visible peak. Bottom: for comparison, spectra of primary scintillation of Ar/CF_4 mixtures at different concentrations, from [86].

8.3.2 Charge and optical gain

As the ionization of the gas occurred throughout the whole gap between the cathode and the anode, the calculation for the gain shown in Chapter 3 didn't hold, as anticipated, as it described an avalanche started from an electron at the cathode. In this case we can define an experimental average gain:

USC UNIVERSIDADE DE SANTIAGO DE COMPOSTELA

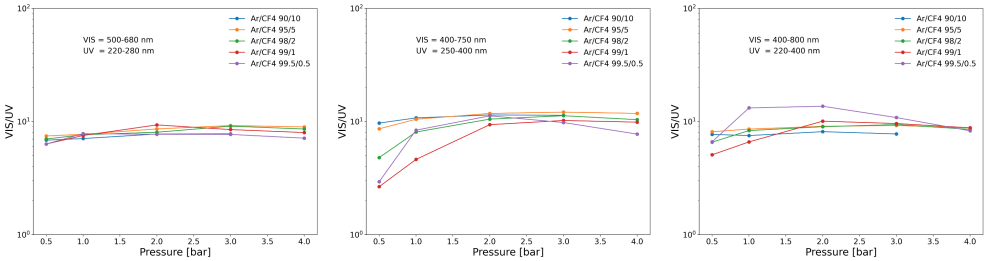

Figure 8.4: Ratio between the visible peak yield and the UV peak yield, defined as the integrated signal in three different couples of intervals. Left: the visible range is taken between 500 and 680 nm, and the UV between 220 and 280 nm, in order to exclude the argon lines in the IR and the OH peak at 310 nm. Center: the visible range is taken between 400 and 750 nm, and the UV between 250 and 400 nm, coherently with the definition used in [226]; in this case, the prominent OH peak at low pressures, included in the UV range, causes a decrease in the ratio at low concentrations of CF_4. Right: the visible range is taken between 400 and 800 nm, and the UV between 220 and 400 nm, to include also the IR emission from argon; this could be an interesting source of extra scintillation at relatively low concentrations of CF_4, its use having been already proposed in pure argon for dark matter search, coherent neutrino-nucleus scattering experiments and also for ion beam radiotherapy [329]. Results for the Ar/CF_4 80/20 mixture are not shown, as the UV peak was too weak to provide meaningful results.

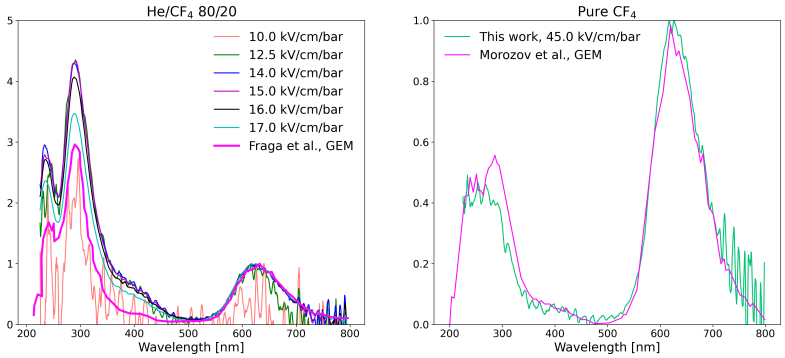

Figure 8.5: Spectra of secondary scintillation from a He/CF_4 80/20 mixture (left) and pure CF_4 (right) normalized to the maximum of the visible peak, all taken at 1 bar. Spectra from [71], taken in a He/CF_4 60/40 mixture, and from [330], taken in pure CF_4 with a GEM, are superimposed on the left and right figure, respectively, showing little dependence of the spectral shape on the electric field or the concentration. The spectrum of He/CF_4 at 10 kV/cm/bar, despite the low amout of light collected, is included to show the trend.

$$I = I_0 < G >= I_0 \frac{1}{d} \int_0^d e^{\alpha_{SST} x} dx \tag{8.1}$$

where d is the length of the gap, and α_{SST} is the steady-state Townsend

USC UNIVERSIDADE DE SANTIAGO DE COMPOSTELA

coefficient [332, 333, 334], related to the Townsend coefficient α through the relation

$$D_L \alpha_{SST}^2 - v_d \alpha_{SST} + v_d \alpha = 0, \tag{8.2}$$

D_L being the longitudinal diffusion and v_d the drift velocity. α_{SST} takes into account the back-flow of some electrons, which have more chance to multiply; hence, it is higher than the Townsend coefficient. One could then consider the maximum gain obtained in the setup as $e^{\alpha_{SST} d}$, keeping in mind that in the applications for which this study was planned, such as the OTPC for NDGAr, the gains are expected to be higher, since the presence of GEM-type multiplication structures would reduce feedback effects by hiding the cathode of the amplification structure from direct photon impact.

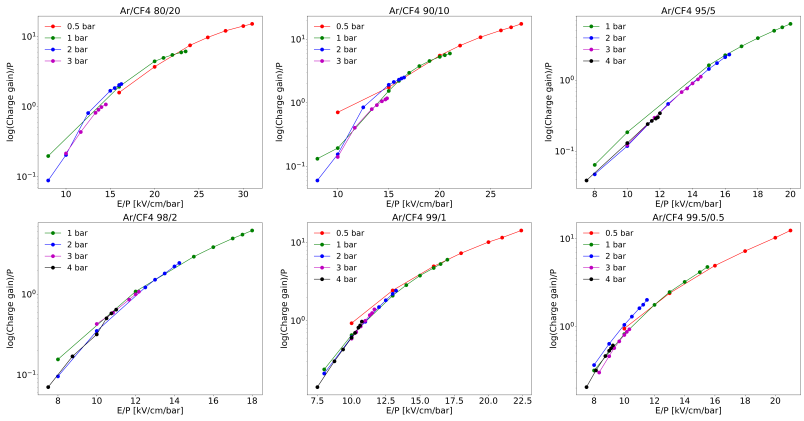

Figure 8.6: Charge gain (defined as $e^{\alpha_{SST} d}$) for the different Ar/CF_4 mixtures at different pressures, scaled with pressure, as a function of the reduced field.

Fig. 8.6 shows the gains defined as $e^{\alpha_{SST} d}$, scaled with pressure. The good scaling displayed gives reassurance on the experimental procedure as well as on the formula for extracting the gain. Deviations of some of the curves from the P-scaling point to experimental artifacts (such as the 2 bar curve for 99.5/0.5 concentrations, or the low-field 1 bar-data for 95/5 and 98/2 ones). Deviations observed at low fields for the case of 90/10 and 80/20 deserve more detail scrutiny, though, and are not fully understood at the moment. In general, the noise level at low current values is known to have an effect in the estimated gain, but it has not been quantified yet.
Spectra at different electric field were taken at 1 bar for the different Ar/CF_4 mixtures under study: Fig. 8.7 shows the spectra normalized to the current (defined as I - I_0), with the corresponding charge gain. While at high CF_4

USC UNIVERSIDADE DE SANTIAGO DE COMPOSTELA

concentrations (10-20%) the shape of the spectra does not change (within 20%), mixtures with lower concentrations show a significantly lower efficiency in producing light as the gain increases. The observation of a decrease of photons per electron at high fields was also reported in [331] for Ar/CF_4 mixtures. However, the absolute number of photons per primary electron produced for concentrations of CF_4 1-5% turns out to be significantly higher, despite reaching similar charge gains (Fig. 8.8).

8.4 Discussion and conclusions

In this work, a systematic study of secondary scintillation spectra of Ar/CF_4 mixtures was performed, in terms of CF_4 concentration and gas pressure. The study confirmed that the UV emission is produced from lower-energy states than the primary scintillation emission, which was previously studied in a similar setup [86]. The secondary scintillation spectra shape showed little dependence with the electrical field applied, the gas pressure and the CF_4 concentration; this observation holds even when comparing the results in He/CF_4 mixtures and pure CF_4 with works in literature taken in different configurations. On the other hand, the efficiency of light production seems to decrease with charge gain for low concentrations of CF_4, which could be in principle compatible with previous observations found in literature, such as [331]; however, this observation needs to be studied in more detail in order to be confirmed. Even if this were the case, the optical gain obtained in low-concentration mixtures (1-5% CF_4) is the highest observed in the mixtures under study. Provided that keeping the highest possible purity of Ar is fundamental for DUNE NDGAr, the choice of 1% CF_4 is confirmed to be optimal for the proposed OTPC [226, 335]. In the case of parallel plates used in this work, the inversion point, at which a further addition of Ar causes a decrease of optical gain, was even observed at concentrations of $CF_4 \sim 2$, while for GEMs it was observed to occur between 20% and 5% CF_4 [335]. Further analysis of the data taken in this work will aim at studying the scaling of optical gain with pressure, in order to establish its role on the scintillation dynamics, and at developing a kinetic model to describe the observations for both the primary and the secondary scintillation spectra in Ar/CF_4 and He/CF_4.

USC UNIVERSIDADE DE SANTIAGO DE COMPOSTELA

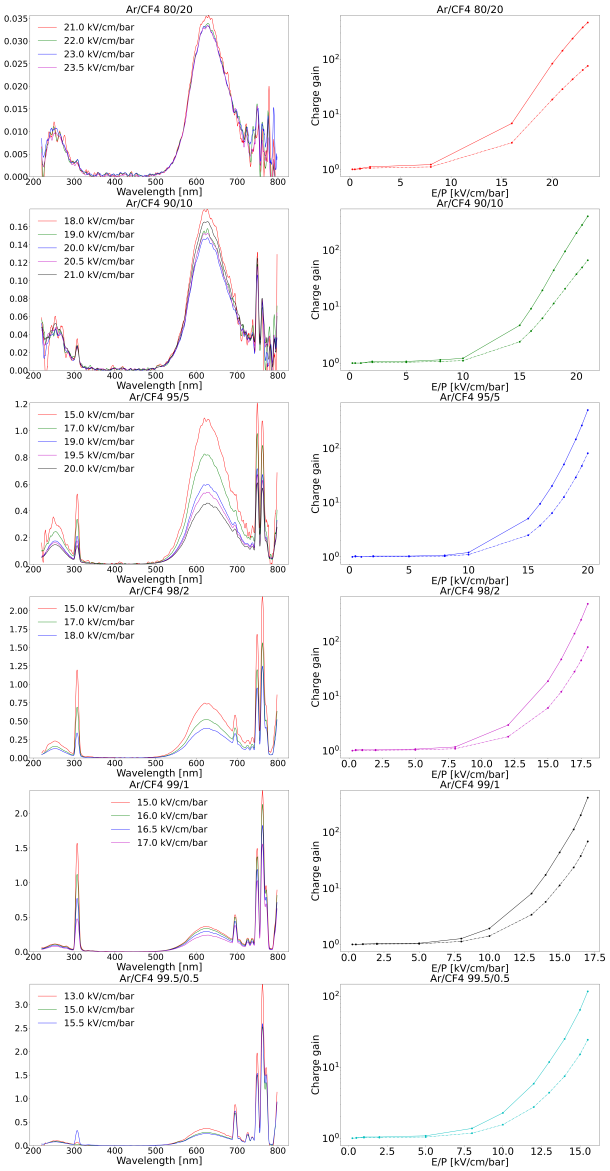

Figure 8.7: Left column: spectra (in arbitrary units) at different electric fields for different CF_4 concentrations at 1 bar, normalized at (I-I_0); right column: corresponding charge gain curve (solid line); the dashed line represents the ratio I/I_0, which is lower than the effective gain, as expected.

USC UNIVERSIDADE DE SANTIAGO DE COMPOSTELA

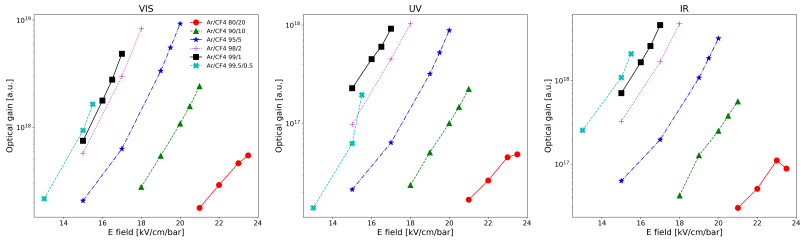

Figure 8.8: Optical gain (in arbitrary units) normalized for the number of primary electrons for the visible peak (left) and the UV peak (center) according to the formula $(\int_{\lambda_{min}}^{\lambda_{max}} n_{ph}(\lambda)d\lambda) \cdot e^{\alpha_{SST}d}/(I - I_0)$, where I is the current measured at the corresponding electric field; this formula is compensating for the production of photons at different positions in the gap, analogously with the charge gain calculation. The two regions are defined as VIS: 400-750 nm, UV: 250-400 nm, coherently with [226]. On the right, the optical gains for the infrared region (700-800 nm), including most of the argon lines and the tail of the CF_3 peak, is shown separately, as a potential channel of interest on its own.

USC UNIVERSIDADE DE SANTIAGO DE COMPOSTELA

USC
UNIVERSIDADE
DE SANTIAGO
DE COMPOSTELA

9 FAT-GEMs for electroluminescence

In the state-of-the-art sections, it was widely explained how advantageous the usage of electroluminescence is for a range of applications, and the technical challenges that it poses. It has been already mentioned that a proposed structure, which may overcome the sagging problem of meshes, together with providing an excellent light yield, is the FAT-GEM (Field Assisted Transparent Gaseous Electroluminescence Multiplier), introduced for the first time in [188]. Since then, the concept has evolved to make the structures optically active, whether with TPB coating inside the FAT-GEM holes, or with a bulk made of a wavelength-shifting material (Polyethylene Naphthalate, PEN). The ideas for a better transmission of light have also flourished, thinking about coupling the wavelength-shifter concept to transparent electrodes (improved S2 and S1), and/or to a reflector (improved S2). During my PhD I have characterized different concepts, and the following sessions will present PMMA-based FAT-GEMs (Sec. 9.1) and PEN-based FAT-GEMs (Sec. 9.2). In particular, Sec. 9.1 will present a comprehensive performance study of different PMMA-based FAT-GEM structures under 5.9 keV X-rays, involving different fabrication procedures, different processing (adding wavelength-shifting coating or an internal reflective layer), different geometries (hole sizes), different gases (xenon and argon), and different pressures (2-10 bar); comparisons with simulations and with a simple 2-mesh configuration will be given, too. Sec. 9.2, on the other hand, will describe a PEN-based structure, designed in a way which maximizes the S1 light collection and simplifies the wavelength-shifting procedure. The concept and its possible configurations, fabrication process, a simulation of the main optical

USC UNIVERSIDADE DE SANTIAGO DE COMPOSTELA

properties (yields and point spread function) and first functionality tests of the prototype devices will be introduced.

USC
UNIVERSIDADE DE SANTIAGO DE COMPOSTELA

The following section (9.1) is based on the paper:

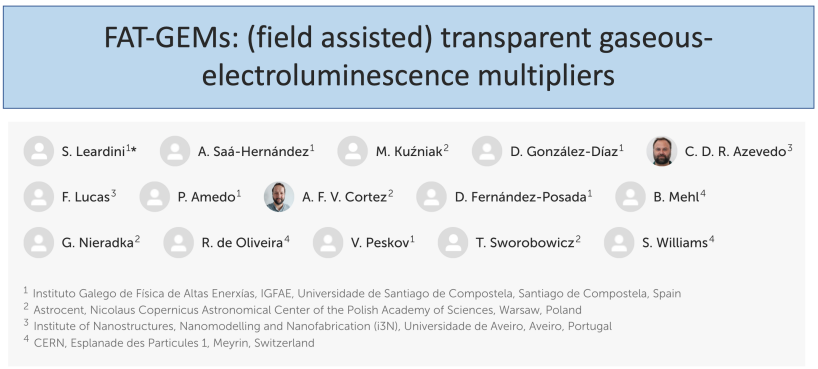

Journal and Article Information
Journal name: Frontiers in Detector Science and Technology
Publisher:
ISSN: 2813-8031
Year of publication: 2024
DOI: 10.3389/fdest.2024.1373235

9.1 PMMA-based FAT-GEMs

9.1.1 Fabrication process

As already seen, electroluminescence thrives in regions where the product of the number density, N, times gas gap, d, is large. Geometries with large values of the product $N \cdot d$ can sustain higher breakdown voltages [336] and therefore provide higher optical gains in avalanche-free conditions. In regard to the electric field configuration, an uniform field region is preferable in terms of intrinsic energy resolution [337] and maximum optical throughput before the onset of multiplication (e.g. [338, 57]). Coincidentally, a high $N \cdot d$ enhances neutral bremsstrahlung radiation below the E_{EL} threshold, too [74, 102]. Thus, in order to create a large-gap, uniform-field, sagging-free structure, PMMA plates of about 5 mm-thickness were procured and drilled at different hole diameters (1-4 mm) on an hexagonal pattern, with a pitch of 5-6 mm. Two additional structures were prepared based on the 2 mm-hole geometry, this time having TPB coated inside the holes. One of them had an additional 3M™ Enhanced Specular Reflector (ESR) layer [339, 340] placed underneath the cathode. A compilation of the structures

USC UNIVERSIDADE DE SANTIAGO DE COMPOSTELA

studied is provided in table 9.1.

Regular (uncoated) structures were produced in the RD51 workshop at CERN: a bare PMMA plate (7 cm × 7 cm) was thermally bonded to two circular copper electrodes (6 cm diameter). The metallization area was increased with respect to the structures used earlier in [188], leaving the active area unchanged, to eliminate possible fringe-fields stemming from charging-up. Holes were then CNC-drilled, and a rim around them (0.2 mm) was created in a chemical bath, to mitigate corona discharges. Finally, a hatched pattern (inner square side 0.35 mm, trace width 0.1 mm) was made through photolithography on the cathode of the structure. Two things were noticed: on the positive side, electric field simulations showed a negligible change in the electric field compared to the geometry with a solid cathode; on the negative side, thermal-bonding rendered the structure translucent and sub-optimal for further optical treatment, something that was pursued through an alternative fabrication process that is discussed below. Two microscope photos of the resulting structures are provided in Fig. 9.1 (a and b), and the fabrication procedures are sketched in Fig. 9.1c.

Descriptor	Hole size (mm)	Pitch (mm)	Thickness (mm)	Number of holes	TPB	ESR
A	1	5	4.5	30	No	No
B	2	5	4.7	30	No	No
C	3	5	4.75	30	No	No
D	4	6	4.8	18	No	No
E	2	5	5.33	31	Yes	No
F	2	5	5.47	31	Yes	Yes

Table 9.1: Compilation of the FAT-GEM structures characterized in this work.

The TPB-coated structures were produced at AstroCeNT (Poland), starting from the application of thin PET films coated with indium tin oxide (ITO) to the two faces of the bare tile, by means of an adhesive film. Compared to the thermally-bonded hatched electrode (transparency 60%), the PET+ITO resulted in a larger transparency of 79% (according to the producer [341]), with the benefit of preserving the optical properties of the plate. Once the PET-ITO films were adhered, holes were made with a manual milling machine equipped with precision drill bits, and finally TPB evaporated inside them (Fig. 9.1d). In order to further increase light collection, an ESR layer was interleaved in between the PMMA and the ITO electrode for one of the structures (Fig. 9.1e). The thickness of the plates was around 4.7 mm for the uncoated structure and 5.4 mm for the coated ones.

USC UNIVERSIDADE DE SANTIAGO DE COMPOSTELA

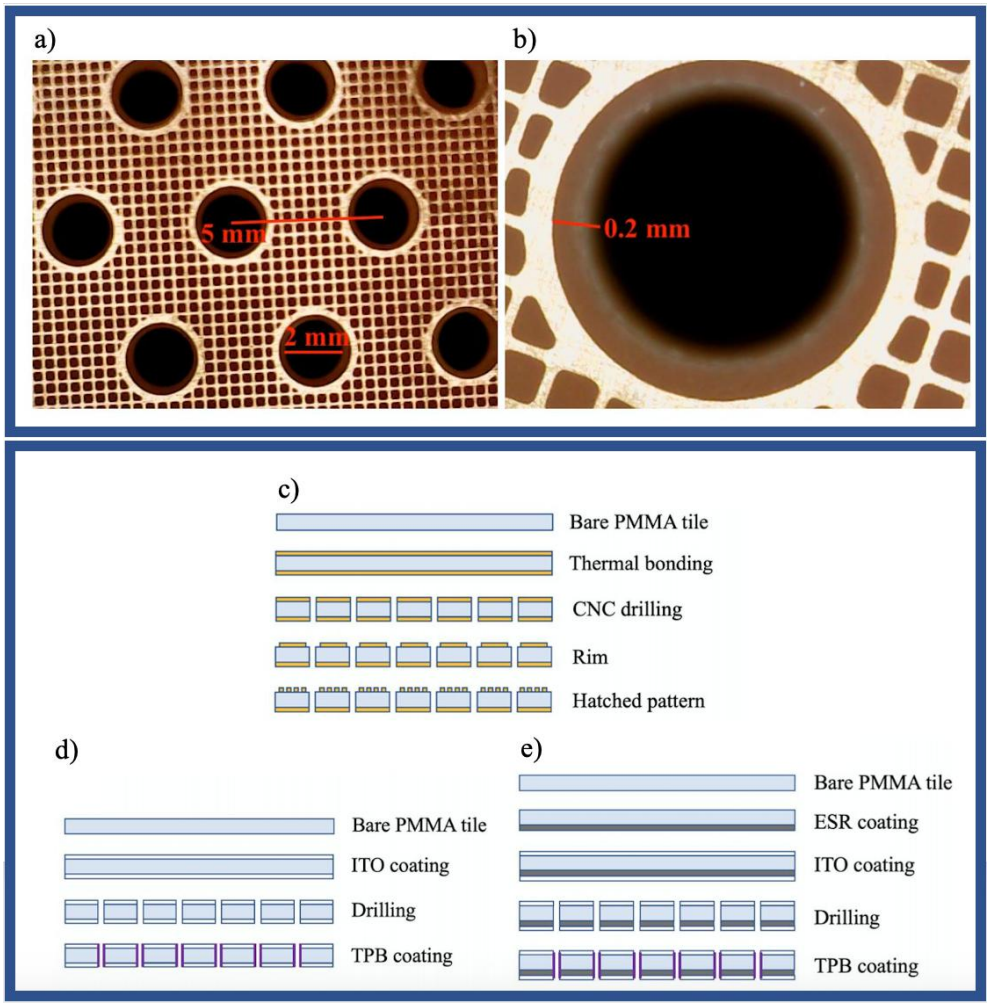

Figure 9.1: *a* and *b*: uncoated FAT-GEM 'B' (the hatched-electrode technique was employed in this particular case). *c*, *d* and *e*: Sketch of the fabrication process for FAT-GEMs produced at CERN (*c*) and at AstroCeNT (*d* and *e*). FAT-GEMs produced at CERN have thermal-bonded copper electrodes, one of them made semi-transparent through chemical etching of a hatched pattern. For the structures produced at AstroCeNT, ITO electrodes were applied in order to increase the structure transparency; moreover, TPB was coated inside the holes. Procedures *d* and *e* differ for the presence of a reflecting ESR layer.

9.1.2 Radiopurity

A mid-size FAT-GEM of 18 cm diameter (Fig. 9.2 right) was purposely built at the CERN-RD51 workshop and screened mainly to show that the production process did not result in strong contamination. The raw PMMA material (Fig. 9.2 left) was Polycast provided by Spartech (as used in the DEAP-3600 detector), with measured activities as low as 0.11 mBq/kg of ^{235}U [342]. The radiopurity screening was performed at Laboratorio Sub-

USC UNIVERSIDADE DE SANTIAGO DE COMPOSTELA

terráneo de Canfranc over a practical time of a bit over a month (50.76 days at GeAnayet for the bare PMMA plate, 47.7 days at GeTobazo for the FAT-GEM). The sensitivity of the measurements, presented in Table 9.2, was mainly limited by the mass of the amplification structure. While competitive radiopurity levels would still need to be demonstrated (especially for a structure that is expected to face the interaction volume), the present fabrication techniques seem promising.

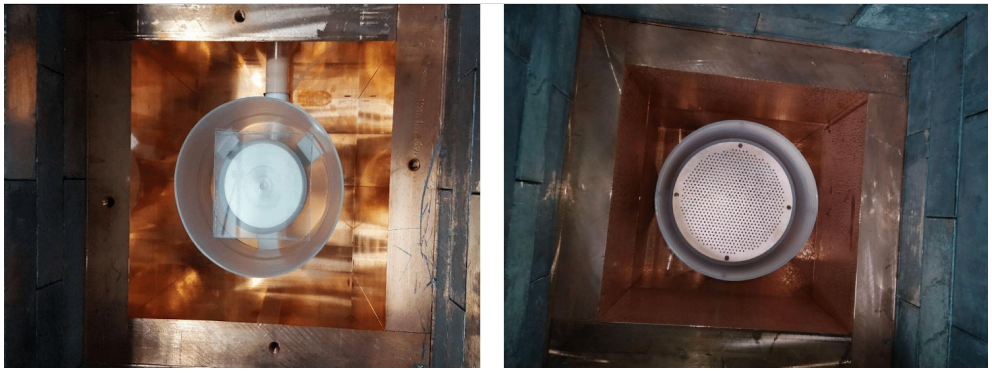

Figure 9.2: Bare PMMA plate (left) and FAT-GEM (right) inside the copper shielding of the setups used for radioactivity screening at Laboratorio Subterráneo de Canfranc.

9.1.3 Working principle

Having a cutoff typically in the range of 300 nm [343], PMMA is not a VUV-transparent material. Therefore, without further treatment, it is not optimal for use under noble gas scintillation as the amount of light detected would be limited by the solid angle defined by the holes' walls. In principle, coating the walls with TPB should allow to make use of such a 'lost' light at near 100% efficiency [196], re-emitting it isotropically in a band (peaked at λ ∼420 nm, with a cutoff around λ ∼350 nm [195]), to which the PMMA is fully transparent. Additionally, a reflective layer would help recovering part of the wavelength-shifted light that is emitted in the opposite direction with respect to the light sensor (Fig. 9.3).

9.1.4 Setup

The setup used was the same as in [188]: the electroluminescent structures served as the anode of a drift/conversion region of 15 mm in length, closed by an aluminum cathode with an x-ray source (^{55}Fe) placed behind it (Fig. 9.4). Initially, a high-transparency mesh was placed covering the anode of the amplification structures, but it was removed once assessed, comparing

USC UNIVERSIDADE DE SANTIAGO DE COMPOSTELA

Isotope	PMMA (mBq/kg) (mBq/kg)	FAT-GEM (mBq/kg) [(mBq/cm^2)]	PMMA, DEAP-3600 (mBq/kg)
U-238/Pa-234m	<340	<791 [<0.741]	
U-238/Pb-214	<2.8	<6.9 [<0.006]	
U-238/Bi-214	<2.3	<7.0 [<0.007]	
U-238/Ra-226			<0.1
U-238/Th-234			<9.0
Th-232/Ac-228	<8.8	<22 [<0.021]	
Th-232/Pb-212	<2.9	<7.4 [<0.007]	
Th-232/Tl-208	<6.3	<15 [<0.014]	
Th-232			<0.3
U-235/U-235	<1.9	<6.1 [<0.006]	<0.6
K-40	<17	<38 [<0.036]	<1.1
Co-60	<0.74	<2.5 [<0.002]	
Cs-137	<1.1	<1.9 [<0.002]	

Table 9.2: Measurements of radiopurity performed at the Canfranc Underground Laboratory for the bare PMMA (second column) and for a FAT-GEM with thermally-bonded copper electrodes (third column). The last column shows the measurements of the PMMA light guide from the DEAP-3600 detector [342]. Only upper limits are reported, driven by the sensitivities of the respective assays.

the yield curve of the same structure with and without it, that it had a negligible impact on the performance. At 15 mm from the FAT-GEM anode, a Hamamatsu R7378 PMT was placed, covered with a grounded mesh to eliminate fringe-fields from the buffer region leaking into the PMT vacuum. The PMT was then connected to a pre-amplifier (ORTEC 142), an amplifier (ORTEC 572A) and finally to an MCA (Amptek 8000D) to collect the spectra. In order to convert from MCA channels to photoelectrons, a calibration run was performed by connecting the PMT directly to an acquisition card (CAEN DT5725), as described later.

A sketch of the experimental setup and a description of the acquisition system can be seen in Fig. 9.4. The container vessel was connected to a pressure/vacuum system and, before filling, it was pumped down to 10^{-4} mbar. During operation the gas was circulated through a cold getter (Entegris GPU80) specified to trap H_2O and O_2, with a KNF compressor (N286.15) at around 20 Nl/min[1].

During the argon measurements, high-purity fresh gas (6N bottle, i.e.,

[1]Normal liters per minute.

USC UNIVERSIDADE DE SANTIAGO DE COMPOSTELA

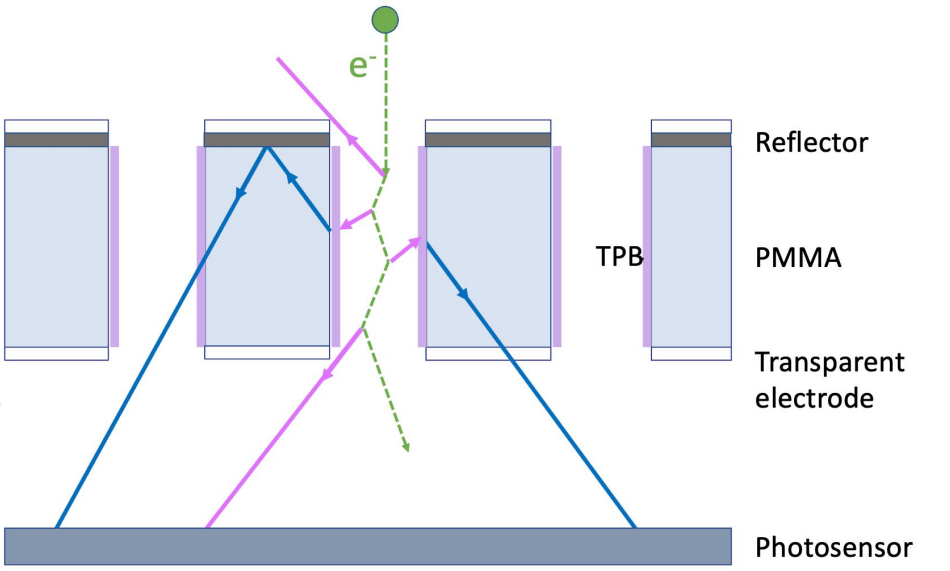

Figure 9.3: Illustration of the FAT-GEM concept. The electron enters from above into the channels due to the intense electric field, and produces electroluminescence (VUV). The light is subsequently wavelength-shifted into the visible range through TPB-coating of the holes' walls, reflected at the cathode inner surface and transmitted through the transparent anode until it reaches the photosensor.

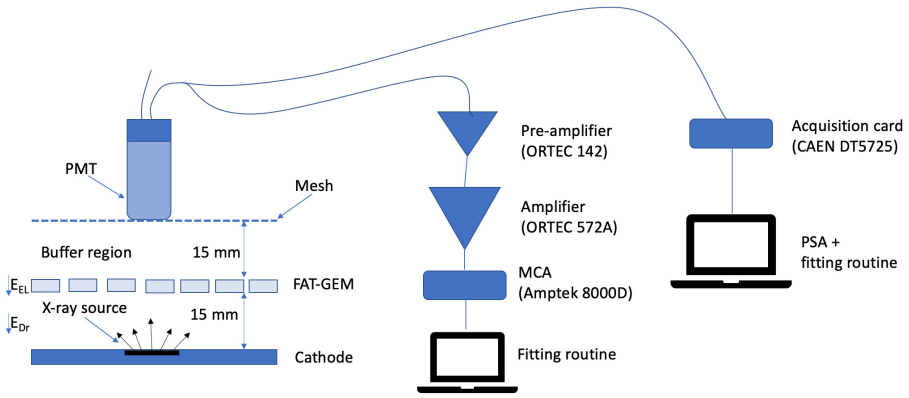

Figure 9.4: Sketch of the experimental setup and the two acquisition modes employed during the measurements. The central one was used regularly for most measurements, while the right one was employed to calibrate from MCA channels to photoelectrons.

ppm-level contamination) was used for each run (namely, for each EL-field series). During the measurements with xenon, on the other hand, the gas was cryorecovered after each run and residual impurities were pumped away.

USC UNIVERSIDADE DE SANTIAGO DE COMPOSTELA

Variations in the yields were observed during the measurements and estimated to typically represent a 15%. They were attributed to gas contamination and PMT drifts.

9.1.5 Data taking and analysis

For each structure, the electroluminescence field (E_{EL}) was kept fixed while scanning the drift field (E_{Dr}), to achieve the highest electron transmission (a detailed explanation is provided in Sec. 9.1.7). With the drift field fixed at that value, a scan for different electroluminescence field values was performed. MCA spectra were then stored, rebinned, background-subtracted and finally fitted to a gaussian (Fig. 9.5). Apart from the electronic noise at low channel count, there was a second source of background on the left hand-side of the spectra correlated with activity in the buffer region (between the structure and the PMT-mesh) when the anode of the FAT-GEM was positively biased (Fig. 9.5-a). Although the size of the buffer region was chosen such that the electric field there was above the electroluminescence threshold at all times (maximum value of 533 V/cm/bar), the background was seen to increase with pressure, pointing to the presence of a scintillation mechanism different from electroluminescence. The only available phenomenon outside corona effect stemming from the connection points (not expected as those were smoothed and screened with black tape), is the direct radiative emission of the drifting electrons in the form of neutral/dipolar bremsstrahlung [74]. This source of background was assessed by a dedicated run with the 2 mm-hole structure, taking spectra at the same drift and electroluminescence fields, but with the anode of the structure grounded (Fig. 9.5-b). Fig. 9.5-c shows for reference a spectra taken close to the optimal electric field (maximum transmission and highest electroluminescence field). At the highest pressures, when bipolar biasing of the FAT-GEMs was unavoidable due to power supply limitations, the background subtraction was implemented to extract the energy resolution[2].

In order to convert from MCA channels to photoelectrons, the following procedure was followed: first, the PMT was calibrated according to the procedure described in [57]: a green LED was powered with a fast pulser

[2]The analysis procedure is as follows: i) an iterative gaussian fit was performed, over a running window defined from the width of the ^{55}Fe energy distribution; ii) once the algorithm converged to the estimates of the peak position and width, the background was defined as any entry outside a $\pm 2.5\sigma$ band around the peak position; iii) the background was then fitted to a straight line and the interpolated value subtracted from the energy distribution; iv) the gaussian fit was repeated, providing the final values. Studies performed in equivalent conditions, with and without background, allowed to assign the uncertainty of the procedure to be about 1%, that is included in the uncertainty of the energy-resolution data.

USC UNIVERSIDADE DE SANTIAGO DE COMPOSTELA

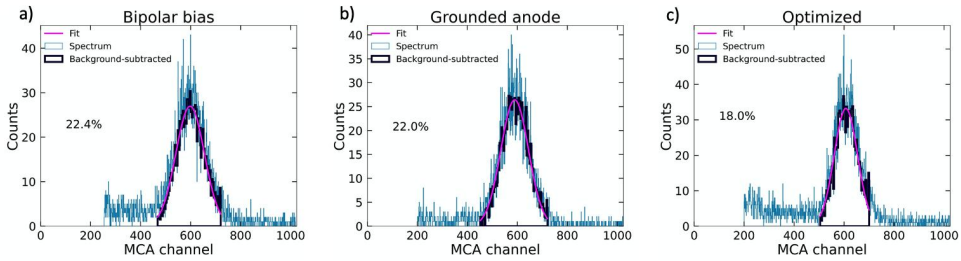

Figure 9.5: a) and b) exemplary spectra taken with the MCA (2 mm structure, P=2 bar, E_{Dr}=167 V/cm/bar, E_{EL} = 4.6 kV/cm/bar), with a Gaussian fit superimposed (22.4% FWHM -a), and 22.0% FWHM -b), respectively). This run corresponds to a control measurement performed with bipolar bias (a) and grounded anode (b). The difference in background activity is attributed to the buffer region and was subtracted during analysis. c) MCA spectrum taken for the 2 mm structure at P=2 bar, E_{Dr}=167 V/cm/bar, E_{EL} = 6.9 kV/cm/bar, corresponding to an energy resolution of 18% FWHM. The PMT voltage was lower for this point than for the spectra in a) and b), in order to match the MCA range.

(Agilent 81130A), adjusting the bias voltage until it resulted in a light intensity around the single-photon level. Data was then taken with an acquisition card (CAEN DT5725) and then analysed through a Matlab script: the result is a multi-peak distribution in charge as depicted in Fig. 9.6 (top), given by the detection of zero photons, a single photon, two photons and so on. The peaks are then fitted with gaussians whose integral values were bound by Poisson statistics.
Afterwards, a dedicated run with the 2-mm uncoated structure was performed, setting the same values of drift and electroluminescence fields as for the data taken with the MCA. Through a pulse-shape analysis and fitting routine, and resorting to the single-photon calibration, the number of photoelectrons/electron was obtained. Finally, the slope between the number of photoelectrons/electron and the peak position in the MCA data was found by performing a linear fit, providing the calibration value (Fig. 9.6, bottom left).
Since different PMT biases were used during the measurements, the relation between gain and voltage was also assessed with the LED. The data was then fitted to a power-law, showing agreement with the data-sheet from the manufacturer (Fig. 9.6, bottom right).

9.1.6 Simulations

Simulations were performed according to the following steps. First, the electric field maps ensuing from an elementary amplification cell were created

USC UNIVERSIDADE DE SANTIAGO DE COMPOSTELA

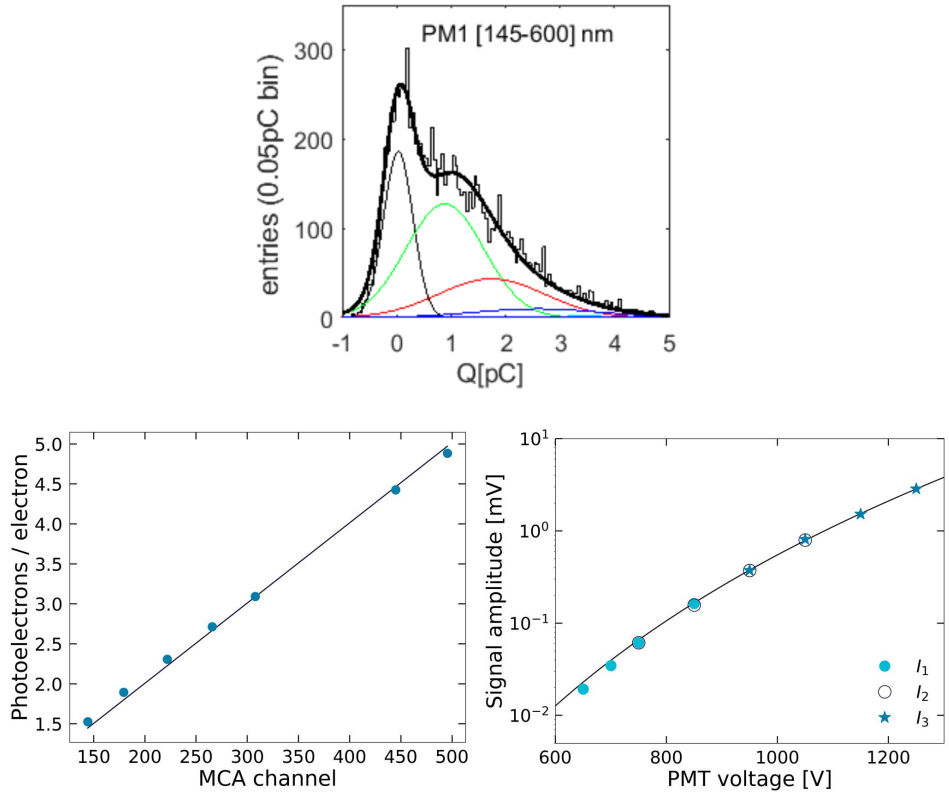

Figure 9.6: Top: example of single-photon calibration for a Hamamatsu R7378 PMT performed in our lab for another study [57]; the calibration for this specific PMT and experiment yielded analogous results. Bottom left: calibration of the MCA spectra for the 2-mm uncoated structure: $P = 8$ bar, V_{PMT}=550 V. The y-axis shows the ^{55}Fe X-ray peak position obtained from pulse shape analysis, and the x-axis the one from the peak obtained from the MCA. The best-fit parameter is 0.01 photoelectron/electron per MCA channel at V_{PMT}=550 V. Bottom right: average amplitude of the PMT signals as a function of the bias voltage for three LED intensities. Each LED intensity series was taken so as to keep the PMT charge per pulse within the same range, and re-scaled afterwards.

with Ansys [344], (Fig. 9.7a). Field and geometry maps were then imported into Garfield++ [345] and extended in the x and y axis (axes parallel to the electrode plane), building the FAT-GEM structure (Fig. 9.7b). The position of the primary electrons was generated following an uniform x, y distribution centered at the middle of the detector, extending over a $\pm$5 mm region and placed at 0.1 mm from the cathode plane. The impact of considering a distributed ionization source corresponding to the X-ray mean free path (around 2.7 mm/bar) was evaluated but the differences dimmed too small. In Fig. 9.7c the path of an electron is shown: as expected, most of the collisions that produce an excited state happen inside the FAT-GEM hole.

USC UNIVERSIDADE DE SANTIAGO DE COMPOSTELA

The Garfield++ simulation provided the 3D-distribution of excited states over the entire array of holes. This was then imported into Geant4 [346] and used to sample the initial positions of the scintillation photons, that were subsequently launched isotropically.[3] Photon ray-tracing was handled by a Geant4 model with optical properties implemented for all materials, extending the model used in Ref. [189]. New wavelength-dependent optical properties added to the model included the transparency of ITO (approx. 79%, based on the suppliers' specification [341]), measured reflectivity for the laminated ESR foil, and TPB properties as in [200]. This allowed us to estimate the geometrical efficiency of the experimental setup (Fig. 9.7d). A two-mesh configuration was simulated using similar techniques, except that the mesh transparency was introduced as an effective number and the reflectivity of the aluminum cathode [347] was included too (yielding about a 10% increase, an effect negligible for FAT-GEMs).

Finally, photon detection efficiency (PDE) curves were considered for four illustrative sensors: Hamamatsu R7378 [348] (employed in these measurements), R11410-21 (used in XENON1T [349]) PMTs, and two representative SiPMs: FBK NUV-HD-SF [350] and Hamamatsu VUV4 (S13370) [351].

9.1.7 Results for untreated FAT-GEMs

In Fig. 9.8, the characterization of the uncoated 2 mm-structure is reported. Data were taken with xenon gas at 2, 4, 6, 8, and 10 bar. The plots labeled as a and b refer to the drift-scan measurements: on the left the energy resolution (FWHM), on the right the light yield normalized to the maximum (*transmission curve*). The decrease of transmission at high drift fields can be explained by the loss of field-focusing: the electron, under a strong drift field, hits the surface of the structure instead of being channeled into the holes. The decrease of transmission at low fields is qualitatively reproduced by simulations too (Fig. 9.9) and can be attributed partly to electroluminescence extending outside of the hole region and increasing as the drift field increases. However the much stronger trend in data suggests the presence of additional contributions (presumably due to attachment to impurities).

Fig. 9.8(c and d) shows the results of the electroluminescence scan: on the left the energy resolution, on the right the detected number of photons/electron, namely photoelectrons/electron (n_{pe}). One can see that the scintillation yield increases with pressure as expected, except for 10 bar where the voltage limit of our power supplies is reached. The voltage drop

[3] A control simulation considering excited states produced only in the central hole yielded little differences.

USC UNIVERSIDADE DE SANTIAGO DE COMPOSTELA

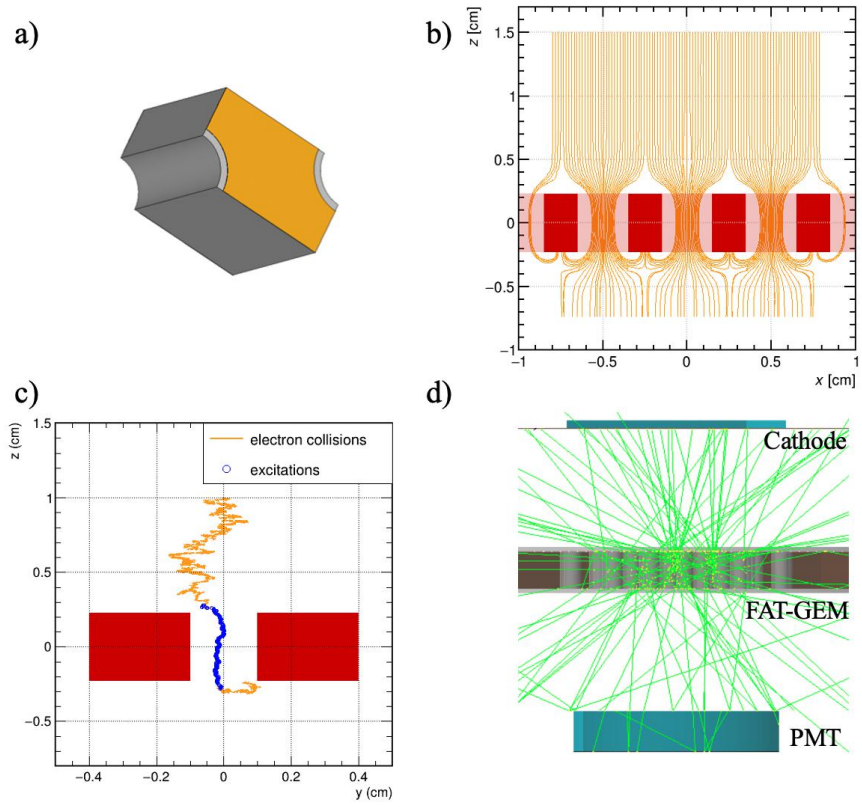

Figure 9.7: Simulations steps: (a) elementary cell in Ansys, (b) Ansys field maps loaded in Garfield++, (c) electron tracking in Garfield++, and (d) photon-tracing in Geant4.

across the FAT-GEM amounts to 15 kV in those conditions.

The typical best energy resolution was 17-17.5%, obtained for virtually any structure and pressure, at high E_{EL} fields (Fig. 9.10, a). A dedicated run with xenon at 4 bar and meshes (electroluminescence gap of 5 mm) yielded an energy resolution a bit over 15% despite the much increased scintillation (the mesh results are shown through the continuous line in Fig. 9.10, a).

In Fig. 9.10 (b) the pressure-reduced yields are shown for the three uncoated structures and all pressures. All points fall on a line, showing that operation takes place in pure EL-mode, i.e., largely free from avalanche multiplication. Comparing the results with simulations (Fig. 9.10, c), the latter predict slightly larger yields: 15% (2 mm), 22% (3 mm), 30% (4 mm). Remarkably, both in simulation and measurements, the threshold to have scintillation light is observed to be 1 kV/cm/bar (above the

USC UNIVERSIDADE DE SANTIAGO DE COMPOSTELA

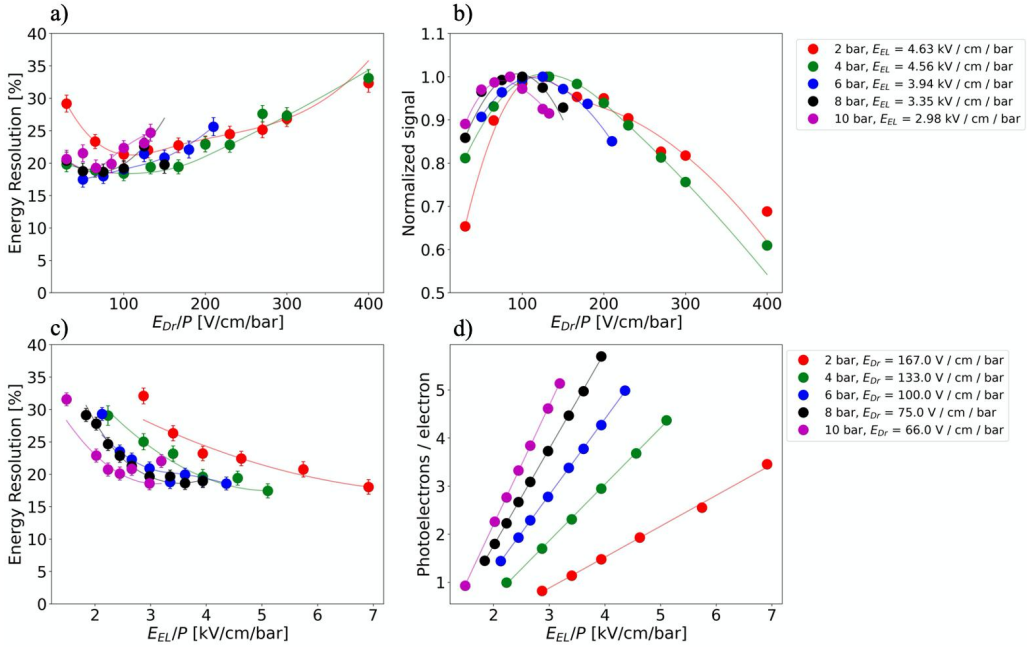

Figure 9.8: Drift field (*a* and *b*) and EL field (*c* and *d*) scans for the uncoated 2 mm-hole FAT-GEM. The lines for the energy resolution and the transmission curves are splines meant to guide the eye.

canonical 0.7 kV/cm/bar for uniform-field conditions in xenon [74]) for all structures. The increase can be interpreted as the lower effective field in the central axis of the hole (where electrons are field-focused) compared to a parallel-electrode configuration. In data, a small deviation is observed for 2 mm structures, providing a hint that the yields at high E_{EL}/P and low P might have a small contribution from avalanche multiplication, biasing the linear fit towards higher threshold values.

An additional structure with 1 mm hole size was characterized, yielding a factor $\times 3$ less light than the 2 mm structure. This seems to support the expectation from simulation, where a minimum diameter size of 1.75 mm is needed in order to reach 100% 'entrance $\times$ transmission' probability for the impinging electron, on a 5 mm-long xenon channel at typical EL fields.

9.1.8 Results for TPB-coated FAT-GEMs

A direct assessment of the impact of TPB at the holes' walls was made for the 2 mm structure under argon, since our PMT has a fused-silica window and is therefore blind to its scintillation. As expected, no signal was observed

USC UNIVERSIDADE DE SANTIAGO DE COMPOSTELA

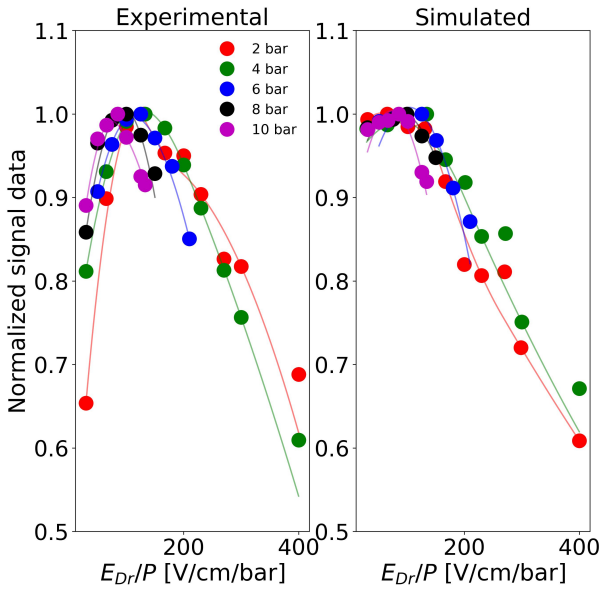

Figure 9.9: Experimental (left) and simulated (right) electron-transmission curve for the uncoated 2-mm-hole FAT-GEM. The decrease of transmission is reproduced at high fields and partially at low fields. An extra contribution is suspected to come from attachment to impurities.

before coating with TPB, however a clear spectrum was formed after doing so (Fig. 9.11, dark-blue circles).

A run with xenon at 4 bar showed a 125% average increase of detected light with respect to the uncoated structure, resulting on a mere 25% deficit with respect to meshes at the maximum operating field of 3.5 kV/cm/bar (Fig. 9.11, light-blue circles). Such a field was significantly lower than the 5 kV/cm/bar applied to the uncoated structures and was chosen simply to fully preserve the structure for further studies, avoiding risk of discharges and TPB damage. At that field, the energy resolution was comparable with the one provided by the two-mesh setup (Fig. 9.11, left).

A structure with ESR was also tested in xenon at 4 bar (pink circles), providing just 6% more light than the coated structure without reflector. As discussed later in text, such a modest increase can be understood largely due to the presence of internal reflection inside the PMMA, due to the specular-reflection characteristics of ESR, and/or a bad optical coupling. A path to improve this performance is discussed later in text.

Short-term aging of the TPB-coated FAT-GEMs was studied in xenon at 4 bar, operating the structure with ΔV=6.8 kV continuously over 20 hours (event rate ∼5 Hz). Non-monotonous variations within a maximum of 25%

USC UNIVERSIDADE DE SANTIAGO DE COMPOSTELA

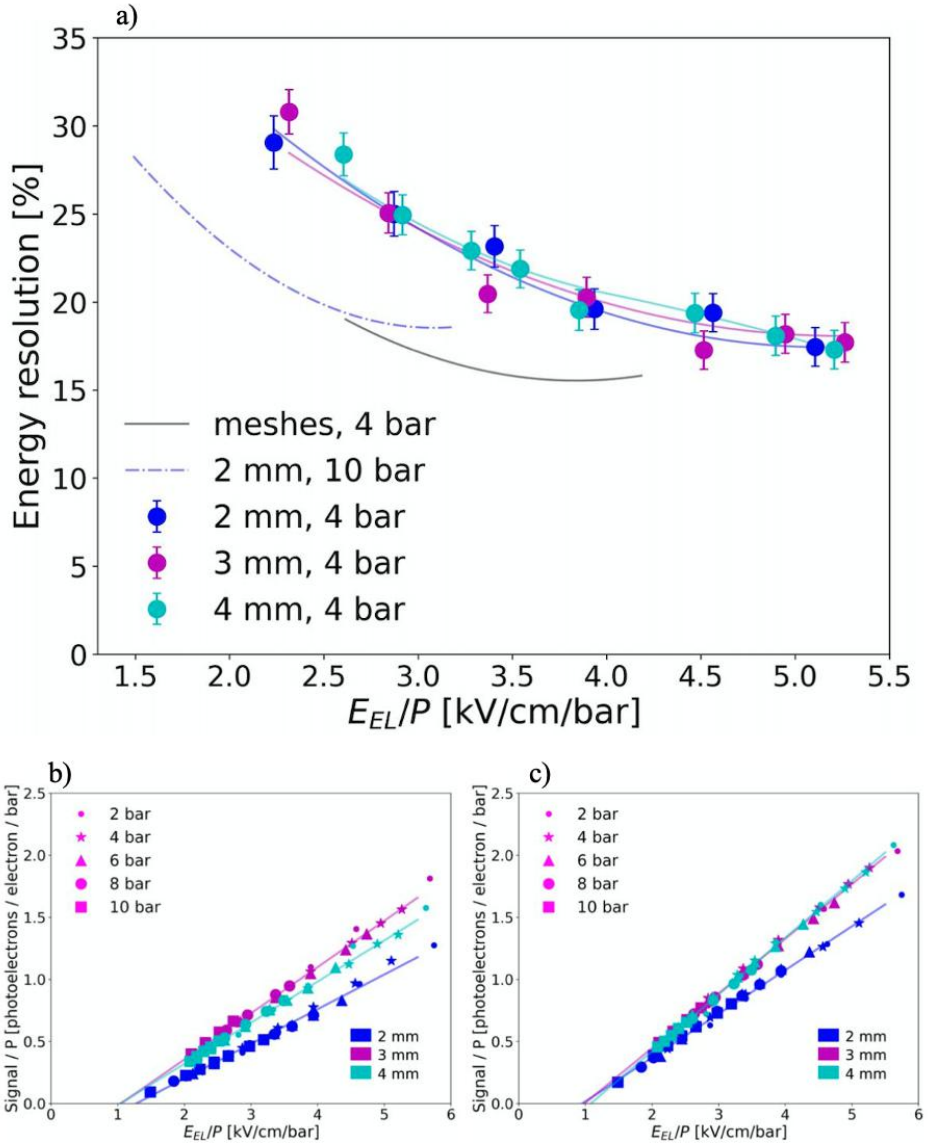

Figure 9.10: *a*: energy resolution at 4 bar for FAT-GEM structures of different hole dimensions (blue - 2 mm 'B', purple - 3 mm 'C', light blue - 4 mm 'D'). For reference, the splines corresponding to the double-mesh data (black, continuous) and 10 bar data (blue, dot-dashed) are given too (and data-points can be found elsewhere in this document). *b*: pressure-reduced scintillation yields measured for FAT-GEM structures of different hole dimensions (dark blue 2 mm - 'B', purple 3 mm - 'C', light blue 4 mm - 'D'). *c*: pressure-reduced scintillation yields simulated for FAT-GEM structures of different hole dimensions. (Measurements and simulations performed for drifts fields corresponding to the transmission plateau).

were observed, attributed mainly to PMT drifts. The strong correlation with the temperature variation during a day-night cycle suggests that this

USC UNIVERSIDADE DE SANTIAGO DE COMPOSTELA

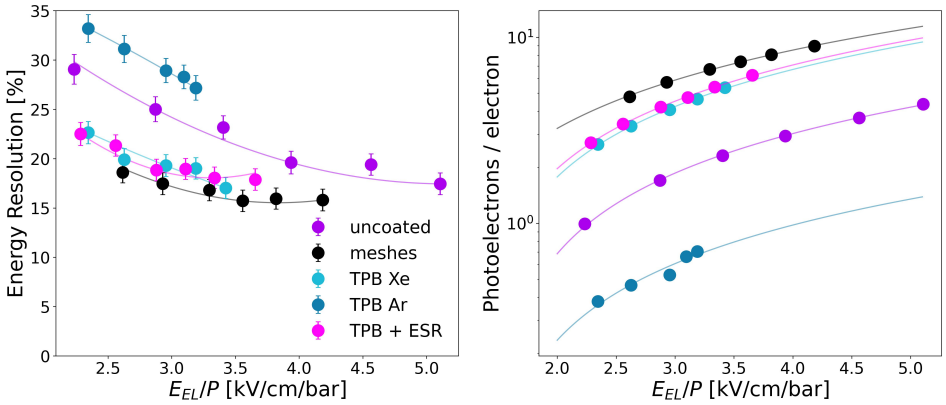

Figure 9.11: Performance studies of the TPB-coated FAT-GEMs (light and dark blue - 'E', pink - 'F'), including results for the uncoated structure ('B'), and two parallel meshes (black circles). These studies were performed at 4 bar, in xenon and argon.

transient behaviour arises from small variations in the electrical properties of the passive components of the base (Fig. 9.12). No indication of permanent damage was evident after the test.

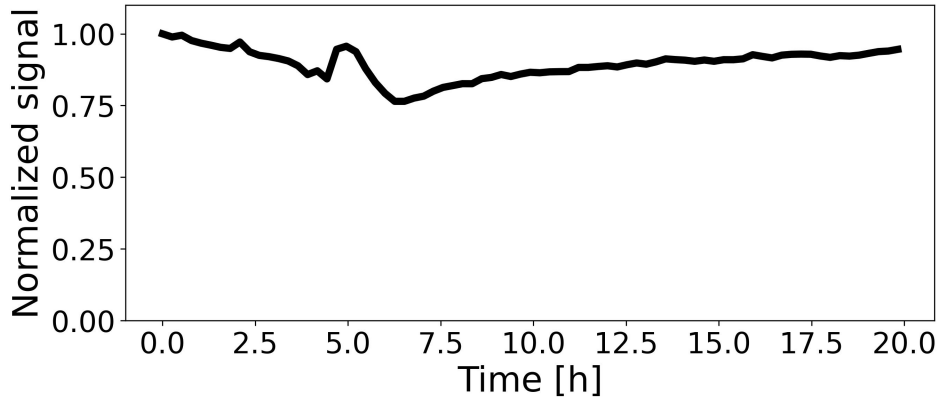

Figure 9.12: Study of possible TPB-damage induced by sustained operation under high voltage (ΔV = 6.8 kV). The optical gain of the FAT-GEM was monitored over 20 h in xenon at 4 bar and, except for a non-monotonous variation (attributed to the PMT drift), no strong short-term deterioration could be seen.

9.1.9 Discussion

The best energy resolution that was measured for FAT-GEMs in this work was 17% (FWHM), at the 5.9 keV peak of ^{55}Fe. This represents almost a factor two increase with respect to the value expected from the Fano factor alone [352, 353, 354, 355, 356, 357]. The measurement is not photon statis-

USC UNIVERSIDADE DE SANTIAGO DE COMPOSTELA

tics -limited, as similar asymptotic values were obtained for different optical gains (up to a number of detected photoelectrons per electron $n_{pe} = 10$). Further, similar results were obtained both with a double-mesh and with a drift-less configuration (the latter being more immune to attachment). The deviation from the Fano limit can be qualitatively understood from the afterpulsing of this PMT model (as observed during the LED characterization): it appears with a delay of about 250 ns, and can reach about 10% of the signal; as the ionization cloud spreads over at least a few µs due to the combined effects of the photoelectron range and diffusion, afterpulsing can not be removed and its event-by-event fluctuations are not correctable.

Notwithstanding, an extrapolation of present results up to the $Q_{\beta\beta}$-scale of ^{136}Xe (2.45 MeV) indicates that the achieved energy resolution is competitive with the ones reached by current experiments and other R&D efforts (Fig. 9.13). The recent result of 0.73% at 1.836 MeV (star), reported for Teflon-based perforated structures in [359], gives further support to the notion that, in practical applications, this type of EL-structures are already within the double-mesh performance limit in terms of optical gain and energy resolution.

To better understand the present technology limits, it is relevant to estimate the wavelength-shifting-efficiency (WLSE) achieved for the TPB-coating process inside the structure channels. The ratio of the TPB-coated structure to the non-coated one has been used for this purpose, as the ratio should be more immune to mis-modeling effects (Fig. 9.14). The uncertainty band was taken to be 15%. As shown, the estimated WLSE of the TPB lies within the 74% to 128% range, centered at 105%, in line with the literature results [196, 363]. Simulations performed for the structure with ESR produced slightly lower values of the WLSE of around 94%, that could point to a bad optical coupling (or modeling) of the ESR reflector.

The process of wavelength-shifting results in a different spectral content for the FAT-GEM and double-mesh configurations, so it is interesting to perform a comparison for different photosensors, based on the results achieved in this work. Fig. 9.15 shows the simulated number of photoelectrons (normalized to cm·bar) assuming the nominal PDE of each of the four exemplary photosensors discussed here (meshes in black, FAT-GEM (present) in pink, FAT-GEM (enhanced) in green). Moreover, a flat-response light sensor with 30% PDE is also shown. The 'enhanced' version of the FAT-GEM assumes a diffuse reflector instead of ESR to minimize the effect of photon trapping due to internal reflection inside the PMMA. Experimental data obtained in this work are given by stars ($P = 4$ bar). All comparisons have been made at a pressure-reduced electric field of $E_{EL} = 3.65$ kV/cm/bar for which discharge-free operation of the FAT-GEM was comfortably achieved. Ex-

USC UNIVERSIDADE DE SANTIAGO DE COMPOSTELA

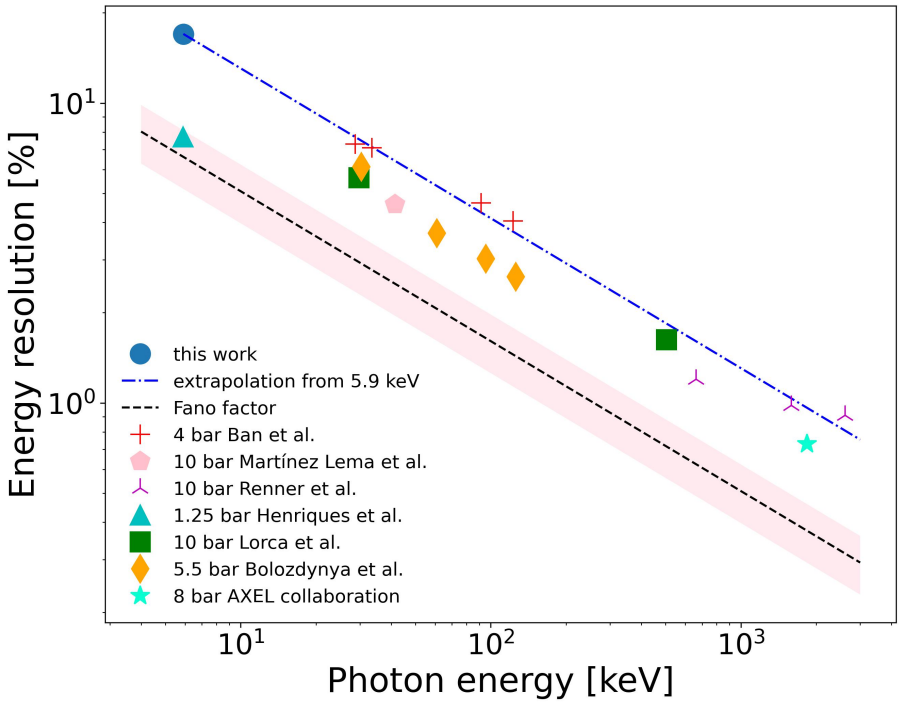

Figure 9.13: Energy resolution in this work (dark-blue circle) and comparison with other experiments (Figure adapted from [358], with data from [187, 359, 360, 180, 77, 361, 362]). The Fano factor represented by the dashed line is an average value from [352, 353, 354, 355, 356, 357], while the band shows the region comprising the highest and lowest values, considering the entire energy range involved.

trapolations to a half-hemisphere photosensor plane are shown by the empty bar.

9.1.10 Conclusions

The use of 'ad hoc' perforated structures for electroluminescence is reaching maturity. Here we present performances for the FAT-GEM technology (Field-Assisted Transparent Gaseous Electroluminescence Multipliers), that are already matching those achievable for double-meshes, our proxy for the 'ideal' uniform-field situation. The optical gain achieved in xenon at 4 bar, at a pressure-reduced electric field of 3.65 kV/cm/bar, is within 18% of the value achieved in a double-mesh configuration with the same photosensor coverage, a bit over the systematic uncertainty of present data (15%). Further, a good description of the observed yields can be achieved if assuming a WLSE of 105% for the TPB-coated channels. The structure is electrically stable at 3.65 kV/cm/bar (4 bar) and 2.8 kV/cm/bar (10 bar), the latter

USC UNIVERSIDADE DE SANTIAGO DE COMPOSTELA

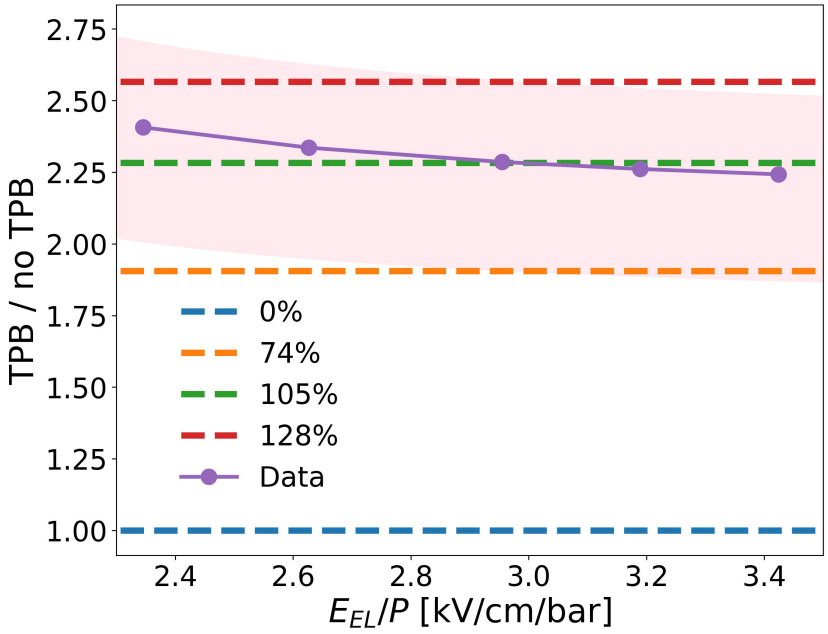

Figure 9.14: Ratio of the light yield of the TPB-coated FAT-GEM to the uncoated one (purple circles), as a function of the pressure-reduced electric field, obtained in xenon at 4 bar. The light-red band accounts for the systematic uncertainty in data. Wavelength-shifting-efficiency (WLSE) has been estimated by comparison with the ratio predicted in simulations (WLSE values indicated by dashed lines).

limited by the maximum power supply of our equipment. Despite being in a high-field region, no systematic TPB degradation was observed during 20 h of continuous operation. Assuming complete hemispherical coverage, the above WLSE figure extrapolates to a number of detected photoelectrons (at 4 bar) in the range of: 29(41) for Hamamatsu R7378 PM, 43(57) for Hamamatsu R11410-21 PM, 60(92) for FBK NUV-HD-SF SiPM and 66(99) for Hamamatsu VUV4 SiPM when considering the present (or enhanced) FAT-GEM structures. Higher values are anticipated at higher pressures. The observed energy resolution, on the other hand, extrapolates to 0.84% (0.91%) FWHM for 4 bar (10 bar) at the $Q_{\beta\beta}$ of ^{136}Xe, competitive for next-generation $\beta\beta0\nu$ experiments. Evidence has been presented, pointing to the intrinsic resolution of the structure being better than that.

The FAT-GEM concept combines the properties of gas scintillation and light-guides, being radiopure, versatile in design and intrinsically transparent from the hard VUV up to visible and near-IR regions (1600 nm). It is called to solve the scaling issues for large-volume chambers and perhaps offer an universal technique to implement electroluminescence readouts in noble-elements.

USC UNIVERSIDADE DE SANTIAGO DE COMPOSTELA

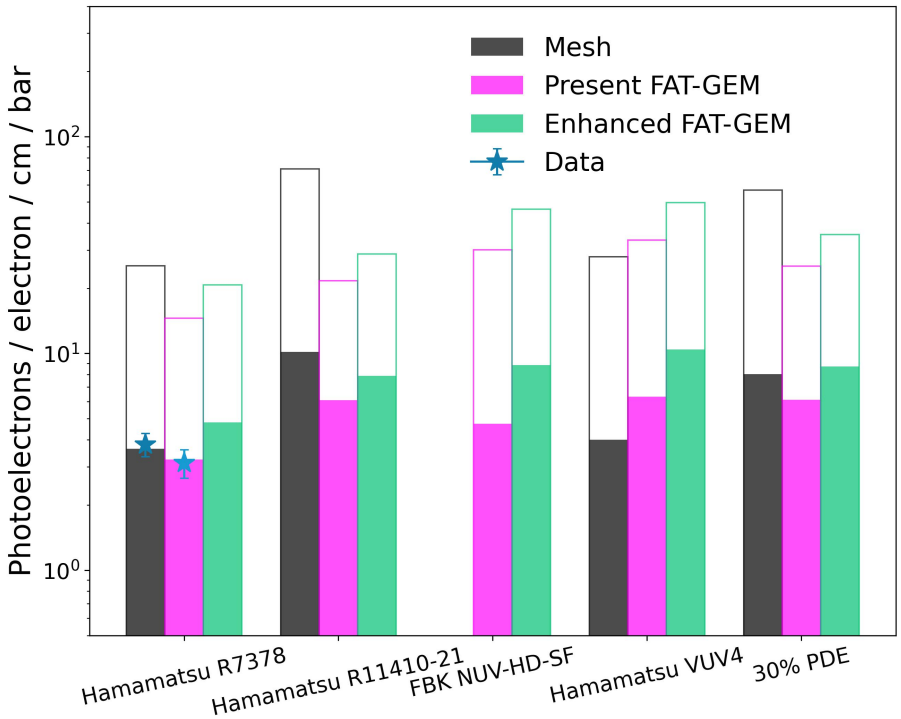

Figure 9.15: Simulated light yields in phe/e/cm/bar when considering the PDE's of different photosensors, for a pressure-reduced field of 3.65 kV/cm/bar, $P = 4$ bar and a gas gap of 5 mm. The empty bars refer to a half-hemisphere sensor, while the full bars assume the geometry in this work (2.1 cm diameter photosensor at 1.5 cm distance). The structures considered are a double-mesh (black), the FAT-GEM developed in this work (pink), and an 'enhanced' FAT-GEM after the modifications discussed in text (green). The blue stars refer to experimental data in this work.

USC UNIVERSIDADE DE SANTIAGO DE COMPOSTELA

The following section (9.2) is based on the paper:

Development of very-thick transparent GEMs with wavelength-shifting capability for noble element TPCs

M. Kuźniak[1,a], D. González-Díaz[2,b], P. Amedo[2], C. D. R. Azevedo[3], D. J. Fernández-Posada[2], M. Kuźwa[1], S. Leardini[2], A. Leonhardt[8], T. Łęcki[5], L. Manzanillas[6], D. Muenstermann[7], G. Nieradka[1], R. de Oliveira[4], T. R. Pollmann[8,9], A. Saá Hernández[2], T. Sworobowicz[1], C. Türkoğlu[1], S. Williams[4]

[1] AstroCeNT, Nicolaus Copernicus Astronomical Center of the Polish Academy of Sciences, Rektorska 4, 00-614 Warsaw, Poland
[2] Instituto Galego de Física de Altas Enerxías, Univ. de Santiago de Compostela, Campus Vida, Rúa Xosé María Sufez Núñez, s/n, 15782 Santiago de Compostela, Spain
[3] Institute of Nanostructures, Nanomodelling and Nanofabrication (i3N), Universidade de Aveiro, Aveiro, Portugal
[4] CERN, Esplanade des Particules 1, Meyrin, Switzerland
[5] Biological and Chemical Research Centre, Faculty of Chemistry, University of Warsaw, Żwirki i Wigury 101, 02-089 Warsaw, Poland
[6] Max Planck Institute for Physics, Munich, Germany
[7] Physics Department, Lancaster University, Lancaster, UK
[8] Department of Physics, Technische Universität München, 80333 Munich, Germany
[9] *Present address:* Nikhef and the University of Amsterdam, Science Park, 1098XG Amsterdam, The Netherlands

Journal and Article Information
Journal name: The European Physical Journal C
Publisher: EDP Sciences, Società Italiana di Fisica and Springer Berlin Heidelberg
ISSN: 1434-6052
Year of publication: 2023
DOI: 10.1140/epjc/s10052-021-09316-0

9.2 PEN-based FAT-GEMs

9.2.1 Concept and possible configurations

In TPCs, the VUV component of S1 can be collected from the full solid angle by walls covered with an efficient reflector. For xenon scintillation, PTFE provides sufficient reflectivity, while in case of argon a layer of WLS on the reflectors is additionally required (typically TPB-coated ESR or PTFE are used [196]). S1 light can therefore reach the amplification structure directly as VUV, or after multiple reflections from the walls, either as VUV or visible photons, if the WLS coating on the walls is present. In this work, the idea of wavelength shifting S1 light using the bulk of the amplification structure was explored. For this purpose, FAT-GEM structures with the bulk made of PEN, presented in Fig. 9.16, were prepared at AstroCeNT (Poland). In fact, given that PEN has been identified as an efficient wavelength-shifter, and taking advantage of the fact that injection moulding technology for production of up to 5 mm plates has been recently established [364], using

USC UNIVERSIDADE DE SANTIAGO DE COMPOSTELA

it as the bulk material for the amplification structure represents a natural choice. Therefore, several PEN-based tiles have been manufactured to optimize the design and decouple possible light production mechanisms, as shown in Tab. 9.3. In particular, since injection moulded PEN [365] has at the moment a reduced WLS efficiency (WLSE) compared to PEN foils, an additional commercial layer was applied to the surface, aimed at higher S1 sensitivity. PMMA-based structures were prepared as well, for comparison.

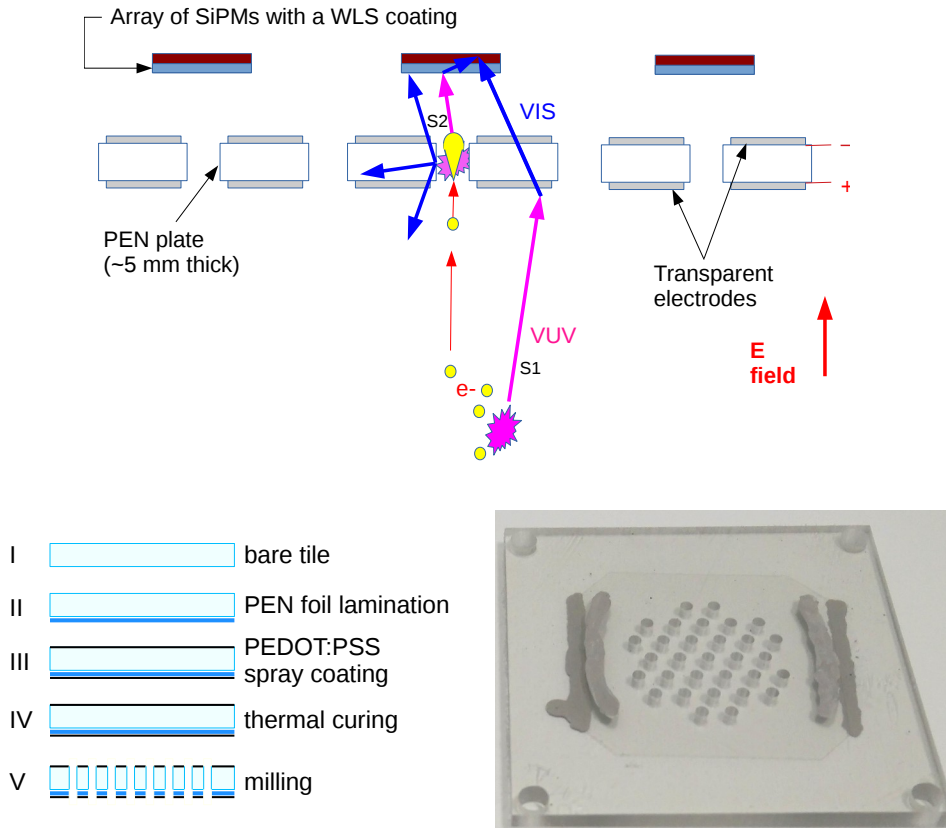

Figure 9.16: (Top) Cross-sectional scheme illustrating the operation of the new WLS-transparent amplification structure, showing photon tracks from S1 and S2 emissions, with VUV in magenta and visible in blue. (Bottom-left) Steps of the fabrication sequence for structure 'e'. (Bottom-right) Fabricated structure 'e', with deposited silver-based epoxy contacts.

Both PMMA and PEN are transparent to visible light; in addition, the electrodes were made either of a semi-transparent mesh, as in [188], or of a transparent coating of 3,4-ethylene dioxythiophene: poly(styrene sulfonate), PEDOT: PSS [366], as in NEXT-White [367]. All these materials have low outgassing characteristics, are vacuum and HV compatible, radiopure, and have been previously used in the context of ultra-low background cryogenic

USC UNIVERSIDADE DE SANTIAGO DE COMPOSTELA

experiments. Collection efficiency for S1 is increased due to the WLS effect at the surface facing the drift region, while for S2 it is increased due to the WLS effect of the holes' walls. In this way, the array of photosensors placed after the structure becomes easily sensitive to both S2 and S1 components, which is useful for background mitigation purposes, e.g. for discrimination of pileup of S1-only and S2-only events [368].

9.2.2 Production

The production of 5 mm-thick injection moulded PEN plates has been developed as part of the R&D effort for LEGEND [369]. The plate used in this work was made starting from a commercial PEN granulate (TN-8065 S) acquired from Tejin-DuPont under the brand name of Teonex [370]. For configurations 'e', 'f', 'g', additional patches of wavelength-shifting foil (PEN Teonex Q51, 25 μm-thick, see [199]), or specular reflector (ESR from 3M) were laminated on the TPC-side of the tile with an adhesive film, 467MP from 3M (PEN laminates have already been used in LAr [257]).

Two types of transparent electrodes were tried: (1) a stainless steel or copper mesh with 0.5 mm-pitch and 0.1 mm-wide tracks (71% transparent), similar to [188], and (2) a thin air-brushed PEDOT:PSS coating, based on Clevios F ET (Heraeus). Otherwise, the geometry of the tiles follows the FAT-GEM design [188]: 7 cm $\times$ 7 cm$\times$ 0.5 cm tiles with 2 mm diameter cylindrical holes arranged in a 5 mm pitch hexagonal pattern.

Fabrication steps are shown in Fig. 9.16(bottom-left), taking as a reference structure 'e'. The production of transparent conductive coatings was performed in an ISO7 cleanroom. Before applying the coatings, the substrates were ultrasonically washed for 1 hour in a solution of Alconox® in ultrapure water (UPW) at 40°C, followed by a ultrasonic wash and rinse in UPW alone and drying. Edges of each tile were then masked with adhesive tape in order to ensure lack of electrical contact with the support structure. After diluting PEDOT with a solution of isopropanol and ultrapure water (UPW), coatings were deposited using a hand-held commercial airbrush (Paasche Talon TG-3F), supplied with a fan head permitting to uniformly deposit up to a 3-inch wide beam. The target thickness of the coatings, approximately 50 nm, was achieved by adjusting the amount of PEDOT in the solution relative to the area of the substrate. Deposition was performed in three passes for each substrate side. Coatings were then cured in an oven at 85°C for 30 minutes. The behaviour of the coating down to LN_2 temperature, for two different target values of the surface resistivity, was measured with a purposely-designed setup at IGFAE, showing an increase in resistivity by a factor of approx. 50 (3) between room temperature

USC UNIVERSIDADE DE SANTIAGO DE COMPOSTELA

	TPC — side		Base mat.: WLSE	PD — side	S1 ε_{vuv}: 1.5% ε_{vis} [%]	S1 f	S2 ε_{vuv}: 10% ε_{vis} [%]	S2 f
a		PEDOT	PMMA:0	PEDOT	0	1	0	1
b			PEN:0.09		1.1(5)	2.5	1.3(5)	1.2
c			PEN:1		12(5)	17	14(5)	4.9
d			PMMA:1		32	44	36	8.1
e	PEDOT	Q51	PEN:0.09	PEDOT	4(2)	6.6	1.4(6)	1.2
f		Q51	PMMA:0		2.3	4.2	0	1
g		ESR	PMMA:1		7.7	11	58	13
h		mesh	PEN:0.09	mesh	0.8(3)	2.1	1.0(3)	1.1
i			PMMA:1		19	26	25	6.0
j			Ar/Xe:0		0	60	0	4.5

Table 9.3: Considered and fabricated (bold label) structures, detailing the TPC and photodetector (PD) sides, and base material configurations with the assumed base material WLSE ('g' so far prototyped only with non-WLS PMMA). Light collection efficiencies, ε_{vuv} (VUV) and ε_{vis} (visible), obtained from Geant4 simulations (Sec. 9.2.3), are given in the right columns (for 'j', which is a special case, ε_{vuv}^{S1}=88% and ε_{vuv}^{S2}=45%). For the PEN base material, two visible light absorption lengths are considered, 1 cm and 5 cm, with the resulting central value and systematic uncertainty given for ε_{vis}. The figure of merit, f, defined later in text, is also shown (central value only).

and 77 K for the 20 MΩ/sq. (5 kΩ/sq.) coating, see Fig. 9.17(top). While this aspect is of importance for detector stability and spark immunity, its optimization was not part of the present study. Coatings used were in the range of MΩ/sq.

For the case of transparent electrodes based on PEDOT (structures 'a', 'e', 'f'), the coating was applied directly to the PEN and PMMA tiles (with additional Q51 and ESR films depending on the case), and the holes milled out. Finally, electrical leads were attached to the sides of the transparent electrodes with silver-based epoxy (Technicqll R-082), see Fig. 9.16(bottom-right). Apart from the production process, the PEN and Teonex materials and the final tiles were stored in the dark.

For the case of semi-transparent electrodes based on meshes (structure 'h'), two different methods were attempted: thermal bonding of copper-substrate followed by photolithographic etching of the mesh (at RD51 workshops, as in [188]) and contact by pressure with stainless steel woven meshes.

USC UNIVERSIDADE DE SANTIAGO DE COMPOSTELA

9.2.3 Expected light collection performance

A Geant4 [346] simulation model was used to quantify light collection. Optical properties were taken from the literature, including: PEN and PMMA attenuation lengths of 1–5 cm [369] and ∼3 m [371], respectively, PEN emission spectrum [199], refractive indices of PEN and PMMA, and ESR reflectivity of 0.98. The literature results for PEN WLSE are typically relative to TPB, which itself has a debated absolute yield [196]. For the sake of this discussion we treat the published PEN WLS efficiencies as if they were absolute: 9.1% for the PEN tile and 34% for Teonex Q51 film, as recently measured for a similar grade in a LAr environment [365]. Assumed WLSE are constant in the entire VUV range, which again is debated [195, 372] and makes the results nominally valid for both Ar and Xe and easy to scale to a more realistic WLSE in presence of new data.

The least known parameter is the transparency of PEDOT coatings. On the one hand, technical specifications state up to 99% for visible light [373], which is used in the simulation. On the other hand, VUV-transparency is not known. In order to assess this effect, an integrating sphere (LISR-3100) measurement in a diffuse reflectivity mode was performed with a Shimadzu UV-3600 spectrophotometer down to 190 nm, and with a fixed-detection-angle vacuum monochromator (Acton VM-502) setup down to 128 nm. Following the method described in [199], we evaluated the apparent WLSE reduction caused by VUV losses in the conductive coating, see Fig. 9.17(bottom). The more conservative 128 nm value of 75% was chosen, also due to the large uncertainty on the 175 nm data point (caused by a low intensity of the light source at that wavelength).

For reference, we consider some limiting cases, assuming 100% WLSE for PEN or PMMA ('c', 'd', 'g', 'i'). Such a situation could be approached in practice by optimizing the base material properties, or application of thin evaporated, painted or spin-coated [372] TPB layers covering the plate surfaces. Additionally, configuration 'j' in Tab. 9.3 approximates the optical configuration of a dual-phase TPC, with a gas pocket replacing the tile and placed between 95% and 98% transparent meshes - inspired by DarkSide-50 [374], but adapted for the considered geometry, for comparison.

The light collection efficiency of the structures was simulated for both S1 and S2 components. For S1, photons were generated isotropically into the cone containing the hole pattern from a point fixed centrally 15 mm from the tile, into the TPC side (1.80 sr solid angle). S2 photons were generated isotropically from the central FAT-GEM hole, with vertex positions following a 2D Gaussian distribution centered at the hole axis, which follows from simulations of the electron transport and generation of excited

USC UNIVERSIDADE DE SANTIAGO DE COMPOSTELA

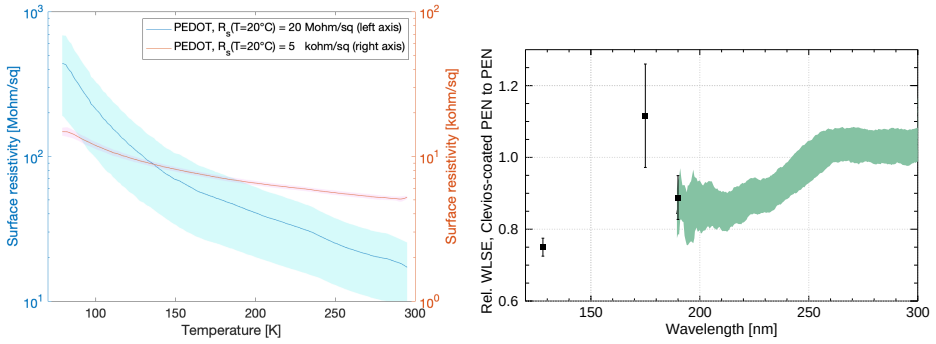

Figure 9.17: Characterization of the PEDOT coating. (Top) Measurements of the sheet resistivity vs. temperature for two extreme cases, obtained from the average on different spots. Surface resistivities on the range of 10-1000 MΩ/sq are interesting because they offer spark quenching, however they are thinner and less uniform (illustrated by the larger error band). (Bottom) Ratio of WLSE measurements of PEN foils with and without PEDOT electrodes. Performed using a Shimadzu UV-3600 spectrophotometer equipped with an integrating sphere in a diffuse reflection configuration (green band) and with a fixed-detection-angle vacuum monochromator setup (black points).

states in the gas performed with the Garfield++ toolkit [345]. Collection efficiencies ε were calculated separately for VUV and visible photons by dividing the number of photons reaching a plane located 3 mm away, on the photodetector (PD) side of the FAT-GEM tile, by the number of initially generated VUV photons. With such definition, photons leaving the tile in the opposite direction are lost; although in a real detector they would still have a chance to be detected on the opposite side of the TPC (or reflected back), improving the overall light yield and energy resolution, they would contribute little information to x-y position reconstruction. VUV collection efficiencies are driven by the solid angles and approximately the same for all considered configurations (except for 'j'): ε^{S1}_{vuv}=1.5% and ε^{S2}_{vuv}=10%. ε^{S1}_{vis} and ε^{S2}_{vis} strongly depend on the optical properties of the model and are summarized in Tab. 9.3.

It is observed that ε^{S1}_{vis} scales with the PEDOT transparency and the WLSE of the face material, while ε^{S2}_{vis} scales with the WLSE of the bulk material. The efficiency increases by a factor of approx. 2 with the PEN absorption length increased from 1 to 5 cm, and by another factor of 2 when switching to PMMA, which has negligible absorption losses. We have verified that the conclusions are robust against changing the S2 vertex distributions inside the FAT-GEM hole to uniform (which results in a 9% reduction of ε^{S2}_{vuv} and 2% increase of ε^{S2}_{vis}), and for VUV Ar and Xe scintillation.

USC UNIVERSIDADE DE SANTIAGO DE COMPOSTELA

Compared to ε_{vuv}, even the simplest WLS configuration, 'b', additionally brings a matching amount of visible light for S1, yet approximately eight times lower for S2. With enhanced WLS properties, the number of visible photons can exceed the VUV one by up to a factor of 19 for S1 (structure 'd') and up to a factor 6 for S2 (structure 'g', which makes use of ESR reflector to maximize S2 collection).

For a more practical comparison one should also consider the typical SiPM photodetection efficiencies (PDEs) of 50% for blue visible light, significantly higher than 20% for VUV [375]. We assume, for simplicity, a blue-sensitive sensor coated with a perfect WLS layer, effectively reducing ε_{vuv} by a factor of two due to isotropic re-emission of wavelength-shifted light. Consequently, a figure-of-merit parameter, representing the enhancement in optical output relative to a non-WLS configuration 'a', is defined as:

$$f \equiv \frac{\varepsilon_{vuv}/2 + \varepsilon_{vis}}{\varepsilon^{(a)}_{vuv}/2}, \tag{9.1}$$

Based on this metric, and relying on the current optical properties of PEN plates, it is possible to anticipate an increase of the photoelectron yield by a factor of approximately 2 for S1 and 20% for S2, with respect to conventional FAT-GEMs (structure 'b'). In the limiting cases of WLSE approaching one, the enhancement factor could reach up to 44 for S1 (only 35% shy of the value achievable for a meshes) and 8 for S2, as in structure 'd' in Tab. 9.3 – almost twice the value achievable with meshes (represented by configuration 'j'). Such a significant improvement has a purely geometrical origin: in a FAT-GEM configuration, S2 VUV light emitted into nearly full solid angle is isotropically wavelength-shifted, with up to a half reaching PDs, while in the case of meshes only half of the S2 VUV emission can reach the WLS-coated PDs, with only a quarter left after conversion. If a reflector foil is added to the TPC-side of the FAT-GEM, as in structure 'g', nearly all wavelength shifted light can be collected (at the expense of losing S1 light), resulting in the optical gain tripled relative to meshes (as long as the same WLSE can be achieved in both cases).

Finally, distributions of photon hits in an x-y-plane placed 3 mm after the tile are shown in Fig. 9.18(top and middle), together with the point spread function (PSF) for S2 (bottom). The visible photon PSF is 2-3 times wider than for VUV, yet recent results show that optical PSFs even wider than the one in Fig. 9.18(bottom-right) are compatible with track reconstruction with 1-2 mm accuracy [376].

USC UNIVERSIDADE DE SANTIAGO DE COMPOSTELA

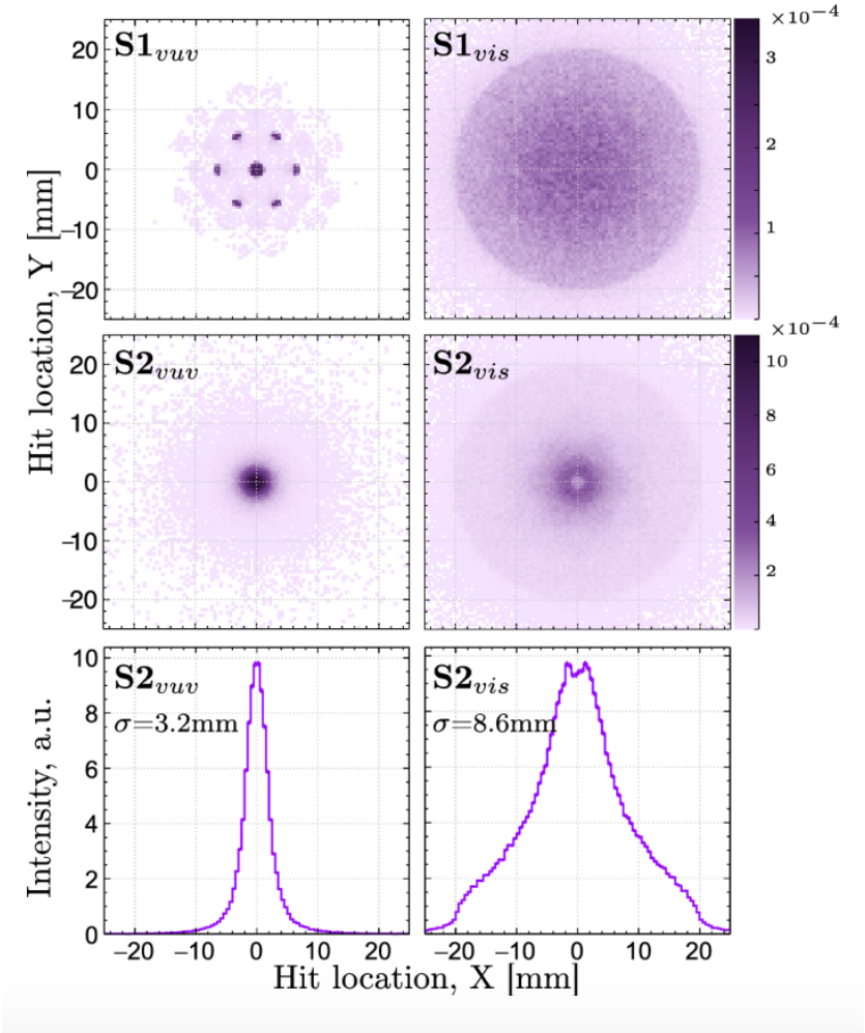

Figure 9.18: Photon hit locations at a photodetection plane placed 3 mm after the WLS FAT-GEM. Shown separately: x-y maps for VUV (left column) and visible (right column), photons from S1 (top) and S2 (middle), and x-axis projections of S2 hits (bottom). The standard deviation, σ, is given for S2 projections. The histograms are divided by the initial 10^6 of generated VUV photons and have 0.5 mm-wide bins. Clusters of VUV hits from photons transmitted directly through GEM holes are visible on top of a broader distribution caused by diffuse reflections.

9.2.4 High voltage tests and validation in xenon gas

High voltage stability was first tested in room air, with no adverse effects observed up to 6 kV drop across the structure. In xenon at 2 bar, conditions

USC UNIVERSIDADE DE SANTIAGO DE COMPOSTELA

used for characterization, 4 kV voltage drop could be applied reliably. The setup employed was the same one described in Sec. 9.1.4, see Fig. 9.19(top-left). X-ray events from an ^{55}Fe source were produced at the cathode, with a characteristic mean free path around 1.5 mm in xenon at 2 bar (5 mm in argon at 4 bar). Since most events come from the cathode, the shape of the waveforms is diffusion dominated, see Fig. 9.19(top-right). The PMT used (PM7378) is blind to argon scintillation, so the relatively high yields observed in this latter case hint at WLS taking place on the PEN plate. The behaviour of the optical gain (in photoelectrons/electron) in xenon is shown in Fig. 9.19(bottom-left) for structures 'h' and 'e', and the energy spectrum corresponding to the highest EL field used for structure 'e' is shown in Fig. 9.19(bottom-right), giving 32% (FWHM). These values are comparable to the ones obtained previously for acrylic structures in this setup, for this gas, field and pressure conditions. They cannot be interpreted directly in terms of those achievable in a final experiment, however, since the purity levels, sensor type and geometrical coverage are setup dependent.
This is to our knowledge the first instance of a micropattern gaseous detector directly bulked on a WLS material. While further optimization is needed, including the WLSE itself, this work shows that the concept is sound, not being limited by surface discharges, outgassing or charge collection/loss at the channels.

9.2.5 Conclusions

Transparent/wavelength-shifting amplification structures based on PEN and PEDOT:PSS (Clevios F ET) for the simultaneous light and charge detection in noble gas and dual-phase detectors can bring substantial improvements over conventional wires/meshes as well as other MPGD readouts. As shown by the simulation results based either on the literature or directly measured optical parameters, 20% more S2 photoelectrons and several times more S1 compared to PMMA-based structures can be anticipated, if resorting to injection moulded PEN plates developed as part of the R&D program of the LEGEND experiment. With more efficient WLS, and a base material with negligible losses, an order of magnitude enhancement for S2 (and a factor 44 for S1) could be obtained. It is in principle possible to achieve such a performance with commercial WLS plates or optimized configurations of PMMA base plates coated with PEN or TPB, that allow WLSE's in the range 0.5-1, depending on the source. Comparison with a TPC supplied with wire mesh electrodes, on the other hand, show that such optimized structures could achieve a similar S1-light collection yield (up to 75%) and up to 2-3 times higher for S2, due to a much more favourable geometry for collection and wavelength shifting of VUV electroluminescence.

USC UNIVERSIDADE DE SANTIAGO DE COMPOSTELA

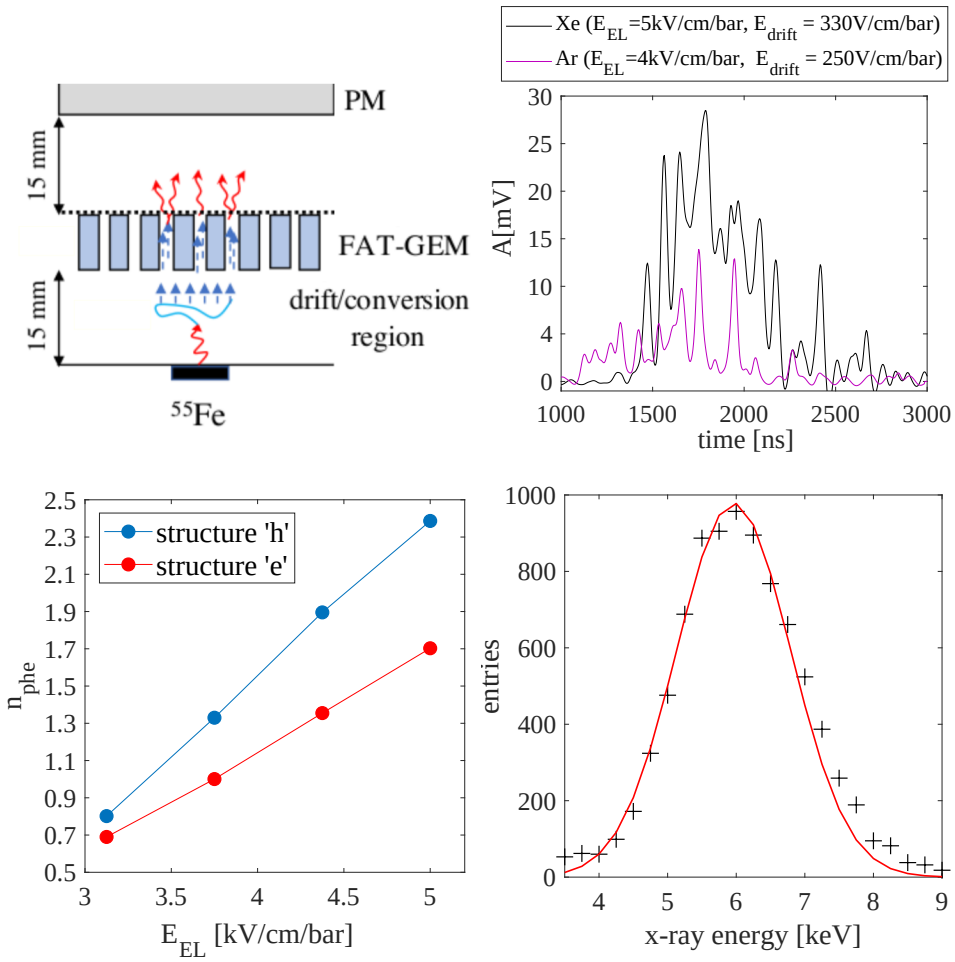

Figure 9.19: (Top-left) Experimental setup used at IGFAE for the characterization of the WLS FAT-GEMs [188]. (Top-right) X-ray waveforms for xenon (2 bar) and argon (4 bar) after cuts. (Bottom-left) Light yield in photoelectrons per electron for xenon at 2 bar. (Bottom-right) Reconstructed energy spectrum at a reduced field in the EL region of 5 kV/cm/bar, for structure 'e'.

Several transparent/WLS amplification structures (with 3.5 cm diameter of active region) were made, using mesh or PEDOT electrodes, showing for the latter: good scalability potential, adequate sheet resistivity for temperatures between 87 K and room temperature, and high transparency for VUV light. High voltage tests and a proof-of-principle run in 2 bar gaseous Xe TPC were performed, permitting to register first light from the structures, hints of wavelength shifting, and demonstrating adequate performance of the PEDOT coatings.

USC UNIVERSIDADE DE SANTIAGO DE COMPOSTELA

Future plans include the detailed empirical characterization of S1 and S2 collection efficiencies, further HV optimization of the transparent electrodes, implementation of the TPB-doped polymeric coatings and longer term and larger scale performance and stability tests. Based on the projections presented in this work, and the promising first tests, future optimized structures could offer sufficient S1 yield, better S2 yield and, above all, a higher scalability and uniformity of response, needed by the upcoming generations of large noble-element based detectors.

USC
UNIVERSIDADE DE SANTIAGO DE COMPOSTELA

Results and Conclusions

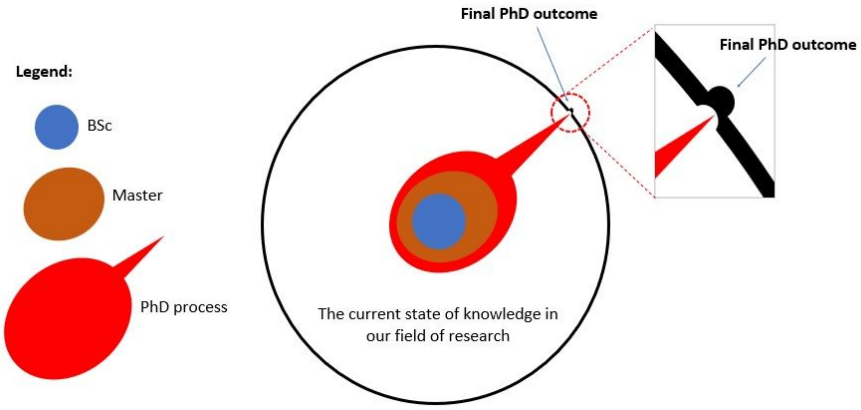

The essence of a PhD (image from [377]).

TPCs are an amazing concept, and their use is widespread, other than in neutrino physics (a glimpse of which was given in Chapter 1) also in searches for other particles, other fields of physics, and in totally unrelated aspects of life, such as homeland security and medical imaging.
To operate or design a TPC, a lot of aspects have to be known: the scintillation mechanism of the chosen active material, explained in Chapter 2 for noble elements, which are often the primary choice, either in the gaseous or in the liquid phase; the risks of reaching breakdown voltages, and discharge mechanisms inside a gas, addressed in Chapter 3, since you will have to apply electric fields in the detector; the possibilities you have in terms of TPC concept, readout mechanism, and amplification structures, described in Chapter 4.

Despite all the TPC wonders, there are still unresolved issues and room for new technologies, especially to accommodate the needs of contemporary and future big-scale experiments; in Chapter 5 some of the main challenges were listed, such as finding alternatives to the classic dual-phase interface, building easily scalable amplification structures, protect your detector from sparks, and many others.

USC UNIVERSIDADE DE SANTIAGO DE COMPOSTELA

In this spirit, my PhD work aimed to develop possible solutions to some of these challenges:

- Chapter 6 focused on spark protection of detectors in cryogenic conditions, especially in liquid argon dual-phase TPCs. For this purpose, two materials were investigated: DLC and Fe_2O_3/YSZ ceramics. These choices allowed to produce samples with different resistivity values, as it is possible to act on the thickness of the deposited material (in first approximation) for the case of DLC and on the concentration of Fe_2O_3 for the ceramics to tune this parameter. The two materials were characterized in terms of behavior as a function of temperature, voltage applied, and aging. The materials displayed excellent results in terms of robustness to aging, and samples in the right range of resistivities (10-10^4 Mohm / sq for DLCs, 10^9 - 10^{12} Ω·cm for ceramics) were identified. These samples were then tested inside the WISArD detector at the Weizmann Institute of Science, in saturated argon gas at 90 K, using an RWELL configuration for the DLC, and an RPWELL configuration for the ceramics. For all the samples tested a gain higher than for the configurations (a THGEM and a THWELL) with bare structures were achieved: with the THGEM and the THWELL configurations the maximum gain was 6 and 8 respectively, while with the RWELL and the RPWELL the maximum gain was 30 for the former, and 16 for the latter. In the case of the RWELL it was also possible to operate the detector in a stable way in the presence of sparks, which was impossible with the unprotected structures.

- Chapter 7 contained an attempt of shedding light to an aspect of bubble-assisted liquid hole multipliers. This idea, which could be an alternative to dual-phase TPCs by creating a local gaseous phase under the multiplication structure (a THGEM), already explored in previous works, suffered from a lower photon detection efficiency than expected. For this reason the dynamics of the bubble in liquid argon was explored: starting from the hydrostatic equations, the possible equilibrium points of the bubble underneath an electrode hole were identified, in the case of an argon-philic or an argon-phobic behavior. The effect of an electric field on the equilibrium points was also studied, finding that it exerts a downward thrust on the bubble. The nature of the contact angle was first observed in the WISArD detector at Weizmann Institute of Science, showing an argon-philic behavior for the materials that a THGEM is made of (copper and FR4). The predictions for the hydrostatic and electrodynamic cases were subsequently validated at room temperature using silicone oil and air by means of μCT imaging, finding an agreement within 6% with the predictions. Based on the results, it is likely that the gas-liquid interface

USC UNIVERSIDADE DE SANTIAGO DE COMPOSTELA

is located at the bottom of a hole, thus not exploiting fully the region with the highest electric field inside the THGEM to produce electroluminescence. An optimization of the hole geometry could be explored in order to push the bubble further inside the hole and improve the light yield.

- Chapter 8 investigated the secondary scintillation emission of Ar/CF_4 gas mixtures. This kind of gas mixtures provide at the same time quenching and wavelength shifting, even at low concentrations of CF_4; for this reason, it could be a precious asset for gaseous TPCs such as DUNE NDGAr. The measurements, taken at GDD at CERN in different pressures and concentrations, aimed at understanding which excited states contribute to the secondary scintillation, and provided an occasion to study the optical gain of these mixtures more in depth. The study confirmed that the secondary scintillation spectra shows peaks in the UV region stemming from less energetic states than the primary scintillation, and showed little dependence with pressure, electric field, and concentration. The optical gain obtained with Ar/CF_4 99/1 looked ideal for applications such as the optical TPC proposed for NDGAr, since it provides one of the highest gains while preserving the high purity of argon required for the application; this confirms previous results, which already indicated that a 1% concentration of CF_4 is the ideal choice.

- Chapter 9 showed the characterization of sturdy, radiopure and scalable structures (FAT-GEMs) for electroluminescence in gaseous TPCs, which could be an alternative to meshes, in that the latter present some difficulties if big sized, and tend to suffer from sagging. Three different kinds of FAT-GEMs were studied: the first one had a PMMA bulk and copper electrodes, while the second one had improved transparency in that the electrodes were made of ESR (and, optionally, a reflector). These structures were optimized for S2, in particular the second kind had TPB evaporated inside the electrodes, allowing to wavelength-shift the VUV EL light emitted by xenon and argon gas into visible light, to which PMMA is transparent. The presence of the reflector on the cathode side makes the FAT-GEM act as a light guide, in principle recovering part of the photons emitted away from the light sensor. With the TPB-coated structure equipped with a reflector it was possible to achieve an optical gain within 18% the one achieved with a double-mesh configuration in xenon at 4 bar (pressure-reduced electric field of 3.65 kV/cm). Further improvement is expected by refining the reflector-FAT-GEM coupling. For all the structures, the extrapolated energy resolution up to the $Q_{\beta\beta}$-scale of ^{136}Xe was competitive with the results obtained with meshes found in literature. Finally, the third

USC UNIVERSIDADE DE SANTIAGO DE COMPOSTELA

kind of structure was designed to detect both S1 and S2, by using a bulk made of PEN, a natural wavelength-shifter, and transparent PEDOT electrodes. The FAT-GEMs made of PEN were tested in both xenon (2 bar) and argon (4 bar) gas, showing promising wavelength-shifting capabilities.

I hope the little bubble in the current state of knowledge I created with this work will be helpful to someone in the future.

USC UNIVERSIDADE DE SANTIAGO DE COMPOSTELA

Bibliography

[1] C. D. Anderson, *The Positive Electron*, Phys. Rev. 43, 491 (1933), DOI: 10.1103/PhysRev.43.491

[2] C. D. Anderson and S. H. Neddermeyer, *Cloud Chamber Observations of Cosmic Rays at 4300 Meters Elevation and Near Sea-Level*, Phys. Rev. 50, 263 (1936), DOI: 10.1103/PhysRev.50.263

[3] S. B. Heard, *On whimsy, jokes, and beauty: can scientific writing be enjoyed?*, Ideas in Ecology and Evolution 7: 64–72 (2014), DOI: 10.4033/iee.2014.7.14.f

[4] MissMJ, `https://en.wikipedia.org/wiki/Standard_Model`, link opened on 03/11/2023

[5] Y. Fukuda et al. (Super-Kamiokande Collaboration), *Evidence for Oscillation of Atmospheric Neutrinos*, Phys. Rev. Lett. 81, 1562 (1998), DOI: 10.1103/PhysRevLett.81.1562

[6] Q. R. Ahmad et al. (SNO Collaboration), *Measurement of the Rate of* $\nu_e + d \rightarrow p + p + e^-$ *Interactions Produced by* ^8B *Solar Neutrinos at the Sudbury Neutrino Observatory*, Phys. Rev. Lett. 87, 071301 (2001), DOI: 10.1103/PhysRevLett.87.071301

[7] K. Eguchi, et al., (KamLAND Collaboration), *First Results from KamLAND: Evidence for Reactor Antineutrino Disappearance*, Phys. Rev. Lett. 90, 021802 (2003), DOI: 10.1103/PhysRevLett.90.021802

[8] L. Stanco et al., *A new way to determine the neutrino mass hierarchy at reactors*, arXiv:1707.07651 (2017)

[9] I. Esteban et al., *The fate of hints: updated global analysis of three-flavor neutrino oscillations*, J. High Energ. Phys. 09 178 (2020), DOI: 10.1007/JHEP09(2020)178

[10] Planck Collaboration, *Planck 2018 results. VI. Cosmological parameters*, Astronomy & Astrophysics, 641, A6 (2020), [arXiv:2007.14792], DOI: 10.1051/0004-6361/201833910

USC UNIVERSIDADE DE SANTIAGO DE COMPOSTELA

[11] KATRIN collaboration, *KATRIN: status and prospects for the neutrino mass and beyond*, J. Phys. G: Nucl. Part. Phys. 49 100501 (2022), DOI: 10.1088/1361-6471/ac834e

[12] NuFIT 5.2 (2022), www.nu-fit.org, opened on 28/03/2024

[13] M. Moe, *The First Direct Observation of Double-Beta Decay*, Annual Review of Nuclear and Particle Science 64:1, 247-267 (2014), DOI: 10.1146/annurev-nucl-102313-025411

[14] A. Balysh et al., *Double Beta decay of* ^{48}Ca, Phys. Rev. Lett. 77 5186 (1996), DOI: 10.1103/PhysRevLett.77.5186

[15] A. A. Vasenko et al., *New Results in the Itep / Yepi Double Beta Decay Experiment With Enriched Germanium Detector*, Mod. Phys. Lett. A 05, 1299 (1990), DOI: 10.1142/S0217732390001475

[16] T. Kirsten et al., *Massenspektrometrischer Nachweis von* $\beta\beta$*-Zerfallsprodukten*, Z. Phys. 202, 273 (1967), DOI: 10.1007/BF01331214

[17] A. Kawashima et al., *Geochemical estimation of the half-life for the double beta decay of* ^{96}Zr, Phys. Rev. C, 47, p. 2452 (1993), DOI: 10.1103/PhysRevC.47.R2452

[18] A. S. Barabash et al., *Two neutrino double-beta decay of* ^{100}Mo *to the first excited* 0^+ *state in* ^{100}Ru, Phys. Lett. B, 345, p. 408 (1995), DOI: 10.1016/0370-2693(94)01657-X

[19] K. Kume et al., *Double beta decays of* ^{116}Cd, Nucl. Phys. A 577, 405 (1994), DOI: 10.1016/0375-9474(94)90888-5

[20] E. W. Hennecke, O. K. Manuel, and D. D. Sabu, *Double beta decay of* ^{128}Te, Phys. Rev. C 11, 1378 (1975), DOI: 10.1103/PhysRevC.11.1378

[21] M. G. Inghram and J. H. Reynolds, *Double Beta-Decay of* ^{130}Te, Phys. Rev. 78, 822 (1950), DOI: 10.1103/PhysRev.78.822.2

[22] N. Ackerman et al., *Observation of Two-Neutrino Double-Beta Decay in* ^{136}Xe *with the EXO-200 Detector*, Phys. Rev. Lett. 107, 212501 (2011), DOI: 10.1103/PhysRevLett.107.212501

[23] V. A. Artemiev et al., *Observation of* $2\nu\beta\beta$ *decay of* ^{150}Nd *in an experiment with the Time Projection Chamber*, JETP Lett. 58, 262 (1993)

USC UNIVERSIDADE DE SANTIAGO DE COMPOSTELA

[24] A. L. Turkevich, T. E. Economou and G. A. Cowan, *Double-beta decay of* ^{238}U, Phys. Rev. Lett. 67, 3211 (1991), DOI: 10.1103/PhysRevLett.67.3211

[25] K. Zuber, *Double beta decay*, Contemporary Physics, volume 45, number 6, pages 491 - 502 (2004), DOI: 10.1080/00107510412331283540

[26] S. Dell'Oro et al., *New expectations and uncertainties on neutrinoless double beta decay*, Phys. Rev. D90, 033005 (2014), DOI: 10.1103/PhysRevD.90.033005

[27] A. Guliani, *Neutrinoless double beta decay experiments*, lecture at ISAPP, Valencia (2021)

[28] L. Wolfenstein, *Neutrino oscillations in matter*, Physical Review D, vol. 17, no. 9, pp. 2369–2374 (1978), DOI: 10.1103/PhysRevD.17.2369

[29] S. Mikheev and A. Y. Smirnov, *Resonance enhancement of oscillations in matter and solar neutrino spectroscopy*, Soviet Journal of Nuclear Physics, vol. 42, pp. 913–917 (1985)

[30] SNO collaboration, *Combined analysis of all three phases of solar neutrino data from the Sudbury Neutrino Observatory*, Phys. Rev. C 88 025501 (2013), DOI: 10.1103/PhysRevC.88.025501

[31] Borexino collaboration, *Final results of Borexino Phase-I on low-energy solar neutrino spectroscopy*, Phys. Rev. D 89 112007 (2014), DOI: 10.1103/PhysRevD.89.112007

[32] IceCube collaboration, *Measurement of Atmospheric Neutrino Oscillations at 6–56 GeV with IceCube DeepCore*, Phys. Rev. Lett. 120 071801 (2018), DOI: 10.1103/PhysRevLett.120.071801

[33] Super-Kamiokande collaboration, *Atmospheric neutrino oscillation analysis with improved event reconstruction in Super-Kamiokande IV*, PTEP 053F01 (2019), DOI: 10.1093/ptep/ptz015

[34] NOvA collaboration, *New constraints on oscillation parameters from* ν_e *appearance and* ν_μ *disappearance in the NOvA experiment*, Phys. Rev. D 98 032012 (2018), DOI: 10.1103/PhysRevD.98.032012

[35] T2K collaboration, *Search for Electron Antineutrino Appearance in a Long-Baseline Muon Antineutrino Beam*, Phys. Rev. Lett. 124 161802 (2020), DOI: 10.1103/PhysRevLett.124.161802

[36] J. Datta et al., *Matter vs vacuum oscillations in atmospheric neutrinos*, Nuclear Physics B, Volume 961, 2020, 115251, ISSN 0550-3213

USC UNIVERSIDADE DE SANTIAGO DE COMPOSTELA

[37] Kamioka Observatory, ICRR (Institute for Cosmic Ray Research), The University of Tokyo, https://www-sk.icrr.u-tokyo.ac.jp/en/sk/about/research/?doing_wp_cron=1712153325.4204099178314208984375, link opened on 03/04/2024

[38] Image by Batmann, https://en.wikipedia.org/wiki/Accelerator_neutrino#/media/File:Neutrino_beam_production.svg, link opened on 03/04/2024

[39] Image by APS/Alan Stonebraker, https://physics.aps.org/articles/v10/66, opened on 03/04/2024

[40] Daya Bay collaboration, *Measurement of the Electron Antineutrino Oscillation with 1958 Days of Operation at Daya Bay*, Phys. Rev. Lett. 121 241805 (2018), DOI: 10.1103/PhysRevLett.121.241805

[41] RENO collaboration, *Measurement of Reactor Antineutrino Oscillation Amplitude and Frequency at RENO*, Phys. Rev. Lett. 121 201801 (2018), DOI: 10.1103/PhysRevLett.121.201801

[42] P. F. de Salas et al., *2020 global reassessment of the neutrino oscillation picture*, J. High Energ. Phys. 02, 71 (2021), DOI: 10.1007/JHEP02(2021)071

[43] The MiniBooNE Collaboration, *Significant Excess of Electron-Like Events in the MiniBooNE Short-Baseline Neutrino Experiment*, Physical Review Letters. 121 (22): 221801 (2018), DOI: 10.1103/PhysRevLett.121.221801

[44] S. R. Elliott, V. Gavrin and W. Haxton, *The Gallium Anomaly*, Progress in Particle and Nuclear Physics, Vol. 134 (2023), DOI: 10.1016/j.ppnp.2023.104082

[45] COHERENT Collaboration, *Observation of coherent elastic neutrino-nucleus scattering*, Science Sep 15;357(6356):1123-1126 (2017), DOI: 10.1126/science.aao0990

[46] I. Manthos (on behalf of the DarkSide-20k Collaboration), *DarkSide-20k: Next generation Direct Dark Matter searches with liquid Argon*, The European Physical Society Conference on High Energy Physics, arXiv:2312.03597 (2023)

[47] C. Amsler et al., PL B667, 1 (2008) and 2009 partial update for the 2010 edition (http://pdg.lbl.gov)

[48] W. R. Leo, *Passage of Radiation Through Matter. In: Techniques for Nuclear and Particle Physics Experiments*, Springer, Berlin, Heidelberg (1994) DOI: 10.1007/978-3-642-57920-2_2

USC UNIVERSIDADE DE SANTIAGO DE COMPOSTELA

[49] N. Duarte, *Proportional counters equipped with thin B4C conversion layers for the detection of slow neutrons*, PhD thesis at University of Coimbra (2021)

[50] C. D. R. Azevedo et al., *Microscopic simulation of xenon-based optical TPCs in the presence of molecular additives*, Nuclear Inst. and Methods in Physics Research, A 877 157–172 (2018) DOI: 10.1016/j.nima.2017.08.049

[51] F. Marchal et al., *Temperature dependence of xenon excimer formations using two-photon absorption laser-induced fluorescence*, J. Phys. B: At. Mol. Opt. Phys. 43 235210 (2010), DOI: 10.1088/0953-4075/43/23/235210

[52] H. D. Wenck et al., *Time and spectrally resolved fluorescence of Xe_2 molecules excited with synchrotron radiation*, Chemical Physics Letters, volume 66, number I (1979), DOI: 10.1016/0009-2614(79)80384-X

[53] R. Santorelli et al., *Spectroscopic analysis of the gaseous argon scintillation with a wavelength sensitive particle detector*, Eur. Phys. J. C 81, 622 (2021), DOI: 10.1140/epjc/s10052-021-09375-3

[54] E. Audouard et al., *Pressure effects on kinetics and decay processes in krypton after selective photoexcitation*, J. Chem. Phys. 89, 6176–6188 (1988), DOI: 10.1063/1.455434

[55] M. Suzuki et al., *Time dependence of the recombination luminescence from high-pressure argon, krypton and xenon excited by alpha particles*, Nucl. Instr. Meth. 192 565-574 (1982), DOI: 10.1016/0029-554X(82)90874-6

[56] M. Suzuki et al., *Electric field dependence of the decay curves of high pressure xenon scintillators excited by alpha particles*, Nucl. Instr. Meth. 192 623-625 (1982), DOI: 10.1016/0029-554X(82)90884-9

[57] S. Leardini et al., *Time and band-resolved scintillation in time projection chambers based on gaseous xenon*, Eur. Phys. J. C 82, 425 (2022), DOI: 10.1140/epjc/s10052-022-10385-y

[58] R. Hammann et al., *Investigating the slow component of the infrared scintillation time response in gaseous xenon*, JINST 19 C02080 (2024), DOI: 10.1088/1748-0221/19/02/C02080

[59] J. Wieser et al., *Novel pathways to the assignment of the third rare gas excimer continua*, Optics Communications 173(1-6):233-245 (2000), DOI: 10.1016/S0030-4018(99)00610-0

USC UNIVERSIDADE DE SANTIAGO DE COMPOSTELA

[60] A. Boichenko et al., *The Nature of Third Continua in Rare Gases*, Laser Physics. 9. 1004-1020 (1999)

[61] P. Millet et al., *Time resolved study of the uv and near uv continuums of xenon*, J. Chem. Phys., 69, 92 (1978), DOI: 10.1063/1.436349

[62] A. Birot et al., *Continuous emissions of argon and krypton in the near ultraviolet*, The Journal of Chemical Physics, 63(4) (1975), DOI: 10.1063/1.431509

[63] A. B. Treshchalov and A. A. Lissovski, *Multi-band spectral structure and kinetics of the third continua in Ar, Kr and Xe gases excited by a pulsed discharge*, Eur. Phys. J. D 66:95 (2012), DOI: 10.1140/epjd/e2012-20662-y

[64] A. F. Borghesani et al., *Infrared emission spectrum and potentials of 0_u^+ and 0_g^+ states of Xe_2 excimers produced by electron impact*, J. Phys B: At. Mol. Opt. Phys. 40 4551 (2007), DOI: 10.1088/0953-4075/40/24/001

[65] M. Piotter et al., *First time-resolved measurement of infrared scintillation light in gaseous xenon*, The European Physical Journal C 83(6) (2023), DOI: 10.1140/epjc/s10052-023-11618-4

[66] C. A. N. Conde and A. J. P. L. Policarpo, *A gas proportional scintillation counter*, Nucl. Instr. Meth. 53 7-12 (1967), DOI: 10.1016/0029-554X(67)91323-7

[67] S. Leardini et al., *FAT-GEMs: (field assisted) transparent gaseous-electroluminescence multipliers*, Front. Detect. Sci. Technol 2:1373235 (2024), DOI: 10.3389/fdest.2024.1373235

[68] C. M. B. Monteiro et al., *Secondary scintillation yield in pure argon*, Phys. Lett. B 668, 167–170 (2008), DOI: 10.1016/j.physletb.2008.08.030

[69] E. Aprile et al., *Noble gas detectors*, Wiley VCH (2006), ISBN: 978-3-527-60963-5

[70] C. M. B. Monteiro et al., *Secondary scintillation yield from GEM and THGEM gaseous electron multipliers for direct dark matter search*, Physics Letters B, Volume 714, Issue 1, Pages 18-23 (2012), DOI: 10.1016/j.physletb.2012.06.066

[71] M. M. F. R. Fraga et al., *The GEM scintillation in He CF-4, Ar CF-4, Ar TEA and Xe TEA mixtures*, Nucl. Instr. Meth. A, 504 88-92 (2003), DOI: 10.1016/S0168-9002(03)00758-7

USC UNIVERSIDADE DE SANTIAGO DE COMPOSTELA

[72] P. Amedo, D. González-Díaz and B. J. P. Jones, *Neutral bremsstrahlung in TPCs*, JINST 17 C02017 (2022), DOI: 10.1088/1748-0221/17/02/C02017

[73] A.Buzulutskov et al., *Revealing neutral bremsstrahlung in two-phase argon electroluminescence*, Astropart. Phys. 103 29 (2018), DOI: 10.1016/j.astropartphys.2018.06.005

[74] C. A. O. Henriques, P. Amedo, et al. (NEXT Collaboration), *Neutral Bremsstrahlung Emission in Xenon Unveiled*, Phys. Rev. X 12, 021005 (2022), DOI: 10.1103/PhysRevX.12.021005

[75] A.S. Barabash and A.I. Bolozdynya, *Liquid ionization detectors*, Moscow, Energoatomizdat (1993, in Russian)

[76] Y. Li et al., *Measurement of longitudinal electron diffusion in liquid argon*, Nucl. Instrum. Meth. A, Volume 816, Pages 160-170 (2016), DOI: 10.1016/j.nima.2016.01.094

[77] C. A. O. Henriques et al. (The NEXT collaboration), *Electroluminescence TPCs at the thermal diffusion limit*, J. High Energ. Phys. 27 (2019), DOI: 10.1007/JHEP01(2019)027

[78] F. Sauli, *Gaseous detectors handbook*, freely distributed on `http://fabio.home.cern.ch/fabio/handbook.html`

[79] G. G. Raju, *Gaseous electronics. Tables, Atoms, and Molecules*, CRC Press (2012), DOI: 10.1201/9781315217437

[80] C. A. O. Henriques et al. (the NEXT collaboration), *Secondary scintillation yield of xenon with sub-percent levels of CO_2 additive for rare-event detection*, Physics Letters B, 733 663-671 (2017), DOI: 10.1016/j.physletb.2017.09.017

[81] B. Al Atoum et al., *Electron transport in gaseous detectors with a Python-based Monte Carlo simulation code*, Computer Physics Communications, Volume 254, 107357 (2020), DOI: 10.1016/j.cpc.2020.107357

[82] R. Felkai et al., *Helium–Xenon mixtures to improve the topological signature in high pressure gas xenon TPCs*, Nucl. Instrum. Meth. A, Volume 905, Pages 82-90 (2018), DOI: 10.1016/j.nima.2018.07.013

[83] A. D. McDonald et al. (the NEXT collaboration), *Electron drift and longitudinal diffusion in high pressure xenon-helium gas mixtures*, JINST 14 P08009 (2019), DOI: 10.1088/1748-0221/14/08/P08009

USC UNIVERSIDADE DE SANTIAGO DE COMPOSTELA

[84] The NEXT collaboration, *Low-diffusion Xe-He gas mixtures for rare-event detection: electroluminescence yield*, JHEP 04 034 (2020), DOI: 10.1007/JHEP04(2020)034

[85] S. Cebrián et al., *Micromegas-TPC operation at high pressure in xenon-trimethylamine mixtures*, JINST 8 P01012 (2013), DOI: 10.1088/1748-0221/8/01/P01012

[86] P. Amedo et al., *Observation of strong wavelength-shifting in the argon-tetrafluoromethane system*, Front. Detect. Sci. Technol. 1:1282854 (2023), DOI: 10.3389/fdest.2023.1282854

[87] I. Murayama and S. Nakamura, *Time profile of the scintillation from liquid and gaseous xenon*, Nucl. Instrum. Meth. A, Volume 763, Pages 533-537 (2014), DOI: 10.1016/j.nima.2014.07.003

[88] S. Kubota et al., *Evidence for a triplet state of the self-trapped exciton states in liquid argon, krypton and xenon*, J. Phys. C: Solid State Phys. 11 2645 (1978), DOI: 10.1088/0022-3719/11/12/024

[89] XMASS collaboration, *A measurement of the scintillation decay time constant of nuclear recoils in liquid xenon with the XMASS-I detector*, JINST 13 P12032 (2018), DOI: 10.1088/1748-0221/13/12/P12032

[90] E. Segreto, *Properties of liquid argon scintillation light emission*, Phys. Rev. D 103, 043001 (2021), DOI: 10.1103/PhysRevD.103.043001

[91] T. Heindl et al., *The scintillation of liquid argon*, EPL 91 62002 (2010), DOI: 10.1209/0295-5075/91/62002

[92] E. Aprile et al., *Measurements of proportional scintillation and electron multiplication in liquid xenon using thin wires*, JINST 9 P11012 (2014), DOI: 10.1088/1748-0221/9/11/P11012

[93] G. Martinez-Lema et al., *First observation of liquid xenon electroluminescence with a microstrip plate*, JINST 19 P02037 (2024), DOI: 10.1088/1748-0221/19/02/P02037

[94] Q. Lin, *Proposal of a Geiger-geometry single-phase liquid xenon Time Projection Chamber as potential detector technique for dark matter direct search*, JINST 16 P08011 (2021), DOI: 10.1088/1748-0221/16/08/P08011

[95] Y. Wei et al., *Performance of a radial time projection chamber with electroluminescence in liquid xenon*, JINST 17 C02002 (2022), DOI: 10.1088/1748-0221/17/02/C02002

USC UNIVERSIDADE DE SANTIAGO DE COMPOSTELA

[96] J. Qi et al., *Low energy electronic recoils and single electron detection with a liquid Xenon proportional scintillation counter*, JINST 18 P07027 (2023), DOI: 10.1088/1748-0221/18/07/P07027

[97] J. Qi et al., *Feasibility of Liquid-phase Xenon Proportional Scintillation for Low-energy Physics*, arXiv:2408.01646 (2024)

[98] F. Tönnies et al., *Proportional scintillation in liquid xenon: demonstration in a single-phase liquid-only time projection chamber*, arXiv:2405.10687v1 (2024)

[99] P. K. Lightfoot et al., *Optical readout tracking detector concept using secondary scintillation from liquid argon generated by a thick gas electron multiplier*, JINST 4, P04002 (2009), DOI: 10.1088/1748-0221/4/04/P04002

[100] A. Buzulutskov, *Advances in cryogenic avalanche detectors*, JINST 7, C02025 (2012), DOI: 10.1088/1748-0221/7/02/C02025

[101] A. Buzulutskov, *Electroluminescence and Electron Avalanching in Two-Phase Detectors*, Instruments 4(2), 16 (2020), DOI: 10.3390/instruments4020016

[102] A. Bondar et al., *First Observation of Neutral Bremsstrahlung Electroluminescence in Liquid Argon*, Phys. Rev. Lett. 131, 241001 (2023), DOI: 10.1103/PhysRevLett.131.241001

[103] V. V. Petrov, *Announcements on Galvano-Voltaic experiments, conducted by the Professor of Physics Vasilii Petrov, based on an enormous battery, consisting of 20 4200 copper and zinc disks, located at St. Petersburg's Medical and Surgical Academy* (in Russian). St. Petersburg, Russia: St. Petersburg's Medical and Surgical Academy (1803)

[104] H. Davy, *Additional experiments on Galvanic electricity*, in a letter to Mr. Nicholson, dated September 22, 1800, (Nicholson's) Journal of Natural Philosophy, Chemistry, and the Arts, vol. IV, pp. also in The Collected Works of Sir Humphry Davy, edited by his brother John Davy, vol. II, Early Miscellaneous Papers, London: Smith, Elder, and Cornhill, 1839, pp. 155-163 (1800)

[105] Kirlian photo: Robin Noorda, Tropism Art & Science Collective, `https://www.tropism.eu/flora-volta-kirlian.html`, and `https://www.robin-noorda.com/kirlian-photograms.html`, opened on 30/04/2024

USC UNIVERSIDADE DE SANTIAGO DE COMPOSTELA

[106] J. M. Jenkins et al., *Prodigious Amounts of Hydrogen Oxides Generated by Corona Discharges on Tree Leaves*, Journal of Geophysical Research: Atmospheres 127(16) (2022), DOI: 10.1029/2022JD036761

[107] Alessandro Piazza, `https://www.meteotornado.it/temporali-tra-il-5-e-il-17-agosto-2022/`, opened on 30/04/2024

[108] A. E. Dubinov et al., *Glow discharge based device for solving mazes*, Physics of Plasmas, 21(9) (2014), DOI: 10.1063/1.4894677

[109] R. F. Yunusov and E. R. Yunusova, *Investigation of the electric field of the plasma ball*, J. Phys.: Conf. Ser. 1683 032006 (2020), DOI: 10.1088/1742-6596/1683/3/032006

[110] Fir0002/Flagstaffotos `https://en.wikipedia.org/wiki/Tesla_coil#/media/File:Lightning_simulator_questacon02.jpg`

[111] F. Sauli, *Principles of operation of multiwire proportional and drift chambers*, CERN 77 09 (1977), DOI: 10.5170/CERN-1977-009

[112] F. Paschen, *Über die zum Funkenübergang in Luft, Wasserstoff und Kohlensäure bei verschiedenen Drucken erforderliche Potentialdifferenz*, Annalen der Physik. 273 (5): 69–96 (1889)

[113] A. Küchler, *Elektrische Festigkeit, in Hochspannungstechnik*, VDI-Buch. Springer Vieweg, Berlin, Heidelberg (2017), DOI: 10.1007/978-3-662-54700-7_3

[114] Y. P. Raizer, *Gas Discharge Physics*, Berlin, Germany: Springer (1991), ISBN 9783642647604

[115] P. Gasik, *Beyond stability point*, lecture at RD51 MPGD School, CERN (2023)

[116] P. Fonte, V. Peskov and F. Sauli, *Feedback and breakdown in parallel-plate chambers*, Nuclear Instruments and Methods in Physics Research Section A, 305(1), 91-110 (1991), DOI: 10.1016/0168-9002(91)90522-R

[117] H. Raether, *Electron Avalanches and Breakdown in Gases*, Butterworths (1964)

[118] D. Xiao, *Fundamental Theory of Streamer and Leader Discharge, in Gas Discharge and Gas Insulation*, Energy and Environment Research in China, vol 6, Springer, Berlin, Heidelberg (2016), DOI: 10.1007/978-3-662-48041-0_4

USC UNIVERSIDADE DE SANTIAGO DE COMPOSTELA

[119] V. Peskov et al., *The study and optimization of new micropattern gaseous detectors for high-rate applications*, IEEE Trans. Nucl. Sci., 48, 1070 (2001), DOI: 10.1109/23.958725

[120] B. V. Magaldi et al., *Control and data acquisition system to study dielectric breakdown in low-pressure DC plasma reactor with parallels electrodes*, Revista Brasileira de Aplicações de Vácuo 40(1) (2022), DOI: 10.17563/rbav.v40.1216

[121] E. M. Bazelyan, Y. P. Raizer, *Spark discharge*, CRC Press (1998), ISBN 9780849328688

[122] G. Lobov, *Study of the corona discharge phenomenon for application in pathogen and narcotic detection in aerosol*, master thesis at Stockholm university (2012)

[123] Wikigian, `https://en.wikipedia.org/wiki/Electric_discharge_in_gases#/media/File:Glow2arc.jpg`, opened on 05/04/2024

[124] M. D. R. Silva, *Ionizing Radiation Detectors*, Evolution of Ionizing Radiation Research, InTech (2015), DOI: 10.5772/60914

[125] G. F. Knoll, *Radiation Detection and Measurement*, 3rd edition, John Wiley & Sons, Inc. (2000), ISBN 9780470131480

[126] J. Miyamoto, A. Breskin and V. Peskov, *Gain limits of a Thick GEM in high-purity Ne, Ar and Xe*, JINST 5 P05008 (2010), DOI: 10.1088/1748-0221/5/05/P05008

[127] M. Ageron et al., *ANTARES: The first undersea neutrino telescope*, Nucl. Instr. Meth. A, Volume 656, Issue 1, Pages 11-38 (2011), DOI: 10.1016/j.nima.2011.06.103

[128] M.G. Aartsen et al., *The IceCube Neutrino Observatory: instrumentation and online systems*, JINST 12 P03012 (2017), DOI: 10.1088/1748-0221/12/03/P03012

[129] D. R. Nygren, *Proposal to Investigate the Feasibility of a Novel Concept in Particle Detection*, LBL internal report, February 1974

[130] D. R. Nygren, *The Art of Experiment and the Pace of Discovery in Particle Physics*, Severo Ochoa Colloquium at IFIC, `https://www.youtube.com/watch?v=G5VDZJ90srM` (2019)

[131] A. H. Walenta, J. Heintze and B. Schürlein, *The multiwire drift chamber a new type of proportional wire chamber*, Nucl. Instr. Meth., 92 (3) 373-380 (1971), DOI: 10.1016/0029-554X(71)90413-7

USC UNIVERSIDADE DE SANTIAGO DE COMPOSTELA

[132] J. S. Townsend, *The Diffusion and Mobility of Ions in a Magnetic Field*, Proceedings of the Royal Society of London, Series A, Containing Papers of a Mathematical and Physical Character 86, no. 590: 571–77 (1912)

[133] D. González-Diaz, F. Monrabal, and S. Murphy, *Gaseous and dual-phase time projection chambers for imaging rare processes*, Nucl. Instr. Meth. A, Volume 878, Pages 200-255 (2018), DOI: 10.1016/j.nima.2017.09.024

[134] L. Manenti, *Liquid Argon Time Projection Chambers for Dark Matter and Neutrino Experiments*, PhD thesis at University College London (2016)

[135] J. Alme et al., *The ALICE TPC, a large 3-dimensional tracking device with fast readout for ultra-high multiplicity events*, Nucl. Instr. Meth. A, Volume 622 Issue 1, Pages 316-367 (2010), DOI: 10.1016/j.nima.2010.04.042

[136] B. Yu et al., *Designs of Large Liquid Argon TPCs — from MicroBooNE to LBNE LAr40*, Physics Procedia Volume 37, Pages 1279-1286 (2012), DOI: 10.1016/j.phpro.2012.03.737

[137] A. Simón on behalf of the NEXT Collaboration, *Status of the NEXT experiment*, Journal of Physics: Conference Series 2374 012033 (2022), DOI: 10.1088/1742-6596/2374/1/012033

[138] D. S. Akerib et al., *The Large Underground Xenon (LUX) experiment*, Nucl. Instr. Meth. A, Vol. 704, Pages 111-126, (2013), DOI: 10.1016/j.nima.2012.11.135

[139] G. Charpak et al., *The use of multiwire proportional counters to select and localize charged particles*, Nucl. Instr. and Meth. 62, 262 (1968), DOI: 10.1016/0029-554X(68)90371-6

[140] F. Sauli, *Gaseous Radiation Detectors*, Cambridge University Press (2014), DOI: 10.1017/9781009291200

[141] S. Tangwancharoen et al., *A gating grid driver for time projection chambers*, Nucl. Instr. and Meth. A, Volume 853, Pages 44-52 (2017), DOI: 10.1016/j.nima.2017.02.001

[142] A. Oed, *Position-sensitive detector with microstrip anode for electron multiplication with gases*, Nucl. Instr. Meth. 263 351 (1988), DOI: 10.1016/0168-9002(88)90970-9

[143] S. Bressler et al., *The Thick Gas Electron Multiplier and its derivatives: Physics, technologies and applications*, Progress

USC UNIVERSIDADE DE SANTIAGO DE COMPOSTELA

in Particle and Nuclear Physics 130 104029 (2023), DOI: 10.1016/j.ppnp.2023.104029

[144] Y. Giomataris et al., *MICROMEGAS: a high-granularity position-sensitive gaseous detector for high particle-flux environments*, Nucl. Instr. Meth. A, Volume 376, Issue 1, Pages 29-35 (1996), DOI: 10.1016/0168-9002(96)00175-1

[145] F. Sauli, *The gas electron multiplier (GEM): Operating principles and applications*, Nucl. Instr. Meth. A, Volume 805, Pages 2-24 (2016), DOI: 10.1016/j.nima.2015.07.060

[146] S. Bachmann et al., *Discharge studies and prevention in the gas electron multiplier (GEM)*, Nucl. Instr. Meth. A, Volume 479, Issues 2–3, Pages 294-308 (2002), DOI: 10.1016/S0168-9002(01)00931-7

[147] E. Erdal et al., *First demonstration of VUV-photon detection in liquid xenon with THGEM and GEM-based Liquid Hole Multipliers*, Nucl. Instr. Meth. A, Volume 845, Pages 218-221 (2017), DOI: 10.1016/j.nima.2016.05.105

[148] A. Breskin, *Novel electron and photon recording concepts in noble-liquid detectors*, JINST 17 P08022 (2022), DOI: 10.1088/1748-0221/17/08/P08002

[149] L. Rolandi et al., *Particle Detection with Drift Chambers*, Springer-Verlag Berlin Heidelberg (2008) DOI: 10.1007/978-3-540-76684-1

[150] S. N. Ahmed, *Signal processing, in Physics and Engineering of Radiation Detection*, Second Edition, ELSEVIER, Pages 477-540 (2014), eBook ISBN: 9780128016442, DOI: 10.1016/B978-0-12-801363-2.00008-5

[151] CREMAT website, `https://www.cremat.com/CR-200-R2.1.pdf`, opened on 30/04/2024

[152] `https://www.amptek.com/products/multichannel-analyzers/mca-8000d-digital-multichannel-analyzer`, opened on 30/04/2024

[153] S. R. Cherry, J. A. Sorenson and M. E. Phelps, *chapter 7 - Radiation Detectors, in Physics in Nuclear Medicine*, Fourth Edition, W.B. Saunders, Pages 87-106 (2012) ISBN 9781416051985, DOI: 10.1016/B978-1-4160-5198-5.00007-1

[154] Lab Book of RD51 Micro Pattern Gaseous Detectors School (2023)

[155] D. Pinci, *Optical and hybrid readout techniques*, lecture at RD51 MPGD school (2023)

USC UNIVERSIDADE DE SANTIAGO DE COMPOSTELA

[156] T. Poikela et al., *Timepix3: a 65K channel hybrid pixel readout chip with simultaneous ToA/ToT and sparse readout*, JINST 9 C05013 (2014), DOI: 10.1088/1748-0221/9/05/C05013

[157] A. J. Lowe et al., *Optical Readout of the ARIADNE LArTPC Using a Timepix3-Based Camera*, Instruments 4 35 (2020), DOI: 10.3390/instruments4040035

[158] A. J. Lowe et al., *ARIADNE^{+}: Large Scale Demonstration of Fast Optical Readout for Dual-Phase LArTPCs at the CERN Neutrino Platform*, Phys. Sci. Forum, 8(1), 46 (2023), DOI: 10.3390/psf2023008046

[159] E. Aprile et al. (XENON collaboration), *The XENONnT Dark Matter Experiment*, arXiv:2402.10446 (2024)

[160] K. Micko, P. Papcun and I. Zolotová, *Review of IoT Sensor Systems Used for Monitoring the Road Infrastructure*, Sensors 23(9):4469 (2023), DOI: 10.3390/s23094469

[161] C. Palomares and the DUNE Collaboration, *DUNE Physics Program and Status*, Journal of Physics: Conference Series 2156 012107 (2021), DOI: 10.1088/1742-6596/2156/1/012107

[162] B. Abi et al. (DUNE collaboration), *Long-baseline neutrino oscillation physics potential of the DUNE experiment*, Eur. Phys. J. C 80, 978 (2020), DOI: 10.1140/epjc/s10052-020-08456-z

[163] B. Abi et al. (DUNE collaboration), *Supernova neutrino burst detection with the Deep Underground Neutrino Experiment*, Eur. Phys. J. C 81, 423 (2021), DOI: 10.1140/epjc/s10052-021-09166-w

[164] B. Abi et al., *Volume I. Introduction to DUNE*, JINST 15 T08008 (2020), DOI: 10.1088/1748-0221/15/08/T08008

[165] Credit: Fermilab, link to original image: `https://vms.fnal.gov/asset/detail?recid=1965410`

[166] A. A. Abud et al., *Deep Underground Neutrino Experiment (DUNE) Near Detector Conceptual Design Report*, Instruments 5, 31 (2021), DOI: 10.3390/instruments5040031

[167] A. Abed Abud et al., *Deep Underground Neutrino Experiment (DUNE) Near Detector Conceptual Design Report*, arXiv:2103.13910 (2021), DOI: 10.48550/arXiv.2103.13910

[168] A. A. Abud et al., *DUNE Phase II: Scientific Opportunities, Detector Concepts, Technological Solutions*, arXiv:2408.12725 (2024)

USC UNIVERSIDADE DE SANTIAGO DE COMPOSTELA

[169] A. Saá-Hernández et al., *On the determination of the interaction time of GeV neutrinos in large argon gas TPCs*, arXiv:2401.09920 (2024)

[170] P. Amedo et al., *Scintillation of Ar/CF_4 mixtures: glass-THGEM characterization with 1% CF_4 at 1-1.5 bar*, JINST 19 05 (2024), DOI: 10.1088/1748-0221/19/05/C05001

[171] C. Touramanis, *DUNE at LBNF*, talk at the XX International Workshop on Neutrino Telescopes (2023) `https://agenda.infn.it/event/33107/contributions/206487/attachments/112268/160347/NEUTEL23-DUNE-CT.pdf`

[172] P. Amedo et al., *Letter of Intent: Large-scale demonstration of the ARIADNE LArTPC optical readout system at the CERN Neutrino Platform*, CERN-SPSC-2020-026; SPSC-I-255 (2020)

[173] D. Hollywood et al., *ARIADNE-A novel optical LArTPC: technical design report and initial characterisation using a secondary beam from the CERN PS and cosmic muons*, JINST 15 P03003 (2020), DOI: 10.1088/1748-0221/15/03/P03003

[174] A. Lowe et al., *A Novel Manufacturing Process for Glass THGEMs and First Characterisation in an Optical Gaseous Argon TPC*, Appl. Sci., 11(20), 9450 (2021), DOI: 10.3390/app11209450

[175] S. Kubota et al. (Q-Pix Collaboration), *Enhanced low-energy supernova burst detection in large liquid argon time projection chambers enabled by Q-Pix*, Phys. Rev. D 106, 032011 (2022), DOI: 10.1103/PhysRevD.106.032011

[176] D. A. Dwyer et al., *LArPix: demonstration of low-power 3D pixelated charge readout for liquid argon time projection chambers*, JINST 13 P10007 (2018), DOI: 10.1088/1748-0221/13/10/P10007

[177] P. Novella on behalf of the NEXT Collaboration, *NEXT-White results and roadmap towards a ton-scale detector* , J. Phys.: Conf. Ser. 2502 012005 (2023), DOI: 10.1088/1742-6596/2502/1/012005

[178] NEXT collaboration, *The NEXT-100 experiment for neutrinoless double beta decay searches (Conceptual Design Report)*, arXiv:1106.3630 (2011)

[179] P. Ferrario et al. (the NEXT collaboration), *First proof of topological signature in the high pressure xenon gas TPC with electroluminescence amplification for the NEXT experiment*, JHEP 104 (2016), DOI: 10.1007/JHEP01(2016)104

USC UNIVERSIDADE DE SANTIAGO DE COMPOSTELA

[180] J. Renner et al. (the NEXT collaboration), *Energy calibration of the NEXT-White detector with 1% resolution near $Q\beta\beta$ of ^{136}Xe*, J. High Energy Phys. 230 (2019), DOI: 10.1007/JHEP10(2019)230

[181] L. Rogers et al. (the NEXT collaboration), *High voltage insulation and gas absorption of polymers in high pressure argon and xenon gases*, JINST 13 P10002 (2018), DOI: 10.1088/1748-0221/13/10/P10002

[182] P. Agnes et al., *Search for low-mass dark matter WIMPs with 12 ton-day exposure of DarkSide-50*, Phys. Rev. D 107 063001 (2023), DOI: 10.1103/PhysRevD.107.063001

[183] H. Takahashi et al., *Development of a glass GEM*, Nucl. Instr. Meth. A 724 1-4 (2013), DOI: 10.1016/j.nima.2013.04.089

[184] F.A.F. Fraga et al., *Optical readout of GEMs*, Nucl. Instrum. Meth. A 471 125-130 (2001), DOI: 10.1016/S0168-9002(01)00972-X

[185] F. M. Brunbauer et al., *Radiation imaging with optically read out GEM-based detectors*, JINST 13 T02006 (2018), DOI: 10.1088/1748-0221/13/02/T02006

[186] S. Roy et al., *Stability study of gain and energy resolution for GEM detector*, Nucl. Instrum. Methods Phys. Res. A, 936, p. 485 (2019), DOI: 10.1016/j.nima.2018.10.060

[187] S. Ban et al., *Electroluminescence collection cell as a readout for a high energy resolution Xenon gas TPC*, Nucl. Instr. Meth. A, 875 185 (2017), DOI: 10.1016/j.nima.2017.09.015

[188] D. González-Díaz et al., *A new amplification structure for time projection chambers based on electroluminescence*, J. Phys. Conf. Ser., 1498 012019 (2020), DOI: 10.1088/1742-6596/1498/1/012019

[189] M. Kuźniak et al., *Development of very-thick transparent GEMs with wavelength-shifting capability for noble element TPCs*, Eur. Phys. J. C, 81 609 (2021), DOI: 10.1140/epjc/s10052-021-09316-0

[190] `https://pdf.datasheet.live/6432b002/hamamatsu.com/R7378.pdf`, opened on 16/02/2024

[191] `https://www.hamamatsu.com/content/dam/hamamatsu-photonics/sites/documents/99_SALES_LIBRARY/etd/High_energy_PMT_TPMZ0003E.pdf`, opened on 16/02/2024

[192] S. F. Pate et al., *A model for the Global Quantum Efficiency for a TPB-based wavelength-shifting system used with photomultiplier*

USC UNIVERSIDADE DE SANTIAGO DE COMPOSTELA

tubes in liquid argon in MicroBooNE, JINST 13 P02034 (2018), DOI: 10.1088/1748-0221/13/02/P02034

[193] M. Spanu et al., *Study on TPB as wavelength shifter for the new ICARUS T600 light collection system in the SBN program*, J. Phys.: Conf. Ser. 956 012016 (2018), DOI: 10.1088/1742-6596/956/1/012016

[194] B. Broerman et al., *Application of the TPB Wavelength Shifter to the DEAP-3600 Spherical Acrylic Vessel Inner Surface*, JINST 12 P04017 (2017), DOI: 10.1088/1748-0221/12/04/P04017

[195] C. Benson, G. D. Orebi Gann, and V. Gehman, *Measurements of the intrinsic quantum efficiency and absorption length of tetraphenyl butadiene thin films in the vacuum ultraviolet regime*, Eur. Phys. J. C 78, 329 (2018), DOI: 10.1140/epjc/s10052-018-5807-z

[196] M. Kuźniak and A. M. Szelc, *Wavelength Shifters for Applications in Liquid Argon Detectors*, Instruments 5(1) 4 (2021), DOI: 10.3390/instruments5010004

[197] P. Sanguino et al., *Stability of tetraphenyl butadiene thin films in liquid xenon*, Thin Solid Films, 600, 65 – 70 (2016), DOI: 10.1016/j.tsf.2016.01.006

[198] J. Asaadi et al., *Emanation and bulk fluorescence in liquid argon from tetraphenyl butadiene wavelength shifting coatings*, JINST 14 P02021 (2019), DOI: 10.1088/1748-0221/14/02/P02021

[199] M. Kuźniak et al., *Polyethylene naphthalate film as a wavelength shifter in liquid argon detectors*, Eur. Phys. J. C 79(4), 291 (2019), DOI: 10.1140/epjc/s10052-019-6810-8

[200] M. G. Boulay et al., *Direct comparison of PEN and TPB wavelength shifters in a liquid argon detector*, Eur. Phys. J. C 81, 1099 (2021), DOI: 10.1140/epjc/s10052-021-09870-7

[201] C. A. B. Oliveira et al., *Measurements of Charge and Light in Pure High Pressure Xe towards the Study of Xe+TMA Mixtures with Dark Matter Directionality Sensitivity and Supra-intrinsic Energy Resolution for $0\nu\beta\beta$ Decay Searches*, Physics Procedia, Volume 61, Pages 742-749 (2015), DOI: 10.1016/j.phpro.2014.12.093

[202] B. Krylov et al., *Channels of energy transfer to atomic nitrogen in excited argon–nitrogen mixtures*, J. Phys. B 35, 4257 (2002), DOI: 10.1088/0953-4075/35/20/311

[203] C. G. Wahl et al., *Pulse-shape discrimination and energy resolution of a liquid-argon scintillator with xenon doping*, JINST 9 P06013 (2014), DOI: 10.1088/1748-0221/9/06/P06013

USC UNIVERSIDADE DE SANTIAGO DE COMPOSTELA

[204] K. Aouame et al., *Spectroscopic and kinetic analysis of the krypton VUV continuum in neon-krypton mixtures* , J. Phys. B 31, 4929 (1998), DOI: 10.1088/0953-4075/31/22/006

[205] P. Peiffer et al., *Pulse shape analysis of scintillation signals from pure and xenon-doped liquid argon for radioactive background identification*, JINST 3 P08007 (2008), DOI: 10.1088/1748-0221/3/08/P08007

[206] S. Kubota et al., Nuc. Instrum. Meth. 196, 101 (1982)

[207] E. Conti et al., *Time behaviour of the scintillation light in mixtures of liquid argon and xenon*, Nucl. Instr. Meth. A, Volume 382, Issue 3, Pages 475-478 (1996), DOI: 10.1016/S0168-9002(96)00810-8

[208] C. M. Ignarra, *A Demonstration of Light Guides for Light Detection in Liquid Argon TPCs*, Physics Procedia 37 1217 – 1222 (2012), DOI: 10.1016/j.phpro.2012.02.455

[209] G. Martínez-Lema et al., *Electron transfer efficiency in liquid xenon across THGEM holes*, JINST 19 P01030 (2024), DOI: 10.1088/1748-0221/19/01/P01030

[210] L. Arazi et al., *Liquid Hole Multipliers: bubble-assisted electroluminescence in liquid xenon*, JINST 10 P08015 (2015), DOI: 10.1088/1748-0221/10/08/P08015

[211] E. Erdal et al., *First demonstration of a bubble-assisted Liquid Hole Multiplier operation in liquid argon*, JINST 14 P11021 (2019), DOI: 10.1088/1748-0221/14/11/P11021

[212] E. Erdal et al., *Recent advances in bubble-assisted Liquid Hole-Multipliers in liquid xenon*, JINST 13 P12008 (2018), DOI: 10.1088/1748-0221/13/12/P12008

[213] E. Erdal et al., *Bubble-assisted Liquid Hole Multipliers in LXe and LAr: towards "local dual-phase TPCs"*, JINST 15 C04002 (2020), DOI: 10.1088/1748-0221/15/04/C04002

[214] V. Chepel et al., *First results on FHM — a Floating Hole Multiplier* , JINST 18 P05013 (2023), DOI:10.1088/1748-0221/18/05/P05013

[215] R. Acciarri et al., *Design and construction of the MicroBooNE detector*, JINST 12 P02017 (2017), DOI: 10.1088/1748-0221/12/02/P02017

[216] E. Erdal et al., *Direct observation of bubble-assisted electroluminescence in liquid xenon*, JINST 10 P11002 (2015), DOI: 10.1088/1748-0221/10/11/P11002

USC UNIVERSIDADE DE SANTIAGO DE COMPOSTELA

[217] A. P. L. Policarpo et al., *Observation of electron multiplication in liquid xenon with a microstrip plate*, Nucl. Instr. Meth. A, Volume 365, Issues 2–3, Pages 568-571 (1995), DOI: 10.1016/0168-9002(95)00457-2

[218] S. E. Derenzo et al., *Electron avalanche in liquid xenon*, Physical Review A, 9(6), 2582–2591 (1974), DOI: 10.1103/PhysRevA.9.2582

[219] J. Prunier et al., Nucl. Instrum. Meth. 109, 257 (1973)

[220] J. G. Kim et al., *Studies of electron avalanche behavior in liquid argon*, IEEE Transactions on Nuclear Science 49(4):1851 - 1856 (2002), DOI: 10.1109/TNS.2002.801490

[221] G. Bressi et al., *Electron multiplication in liquid argon on a tip array*, Nucl. Instrum. Meth. A, 310 613-617 (1991), DOI: 10.1016/0168-9002(91)91107-7

[222] V. Chepel and H. Araújo, *Liquid noble gas detectors for low energy particle physics*, JINST 8 R04001 (2013), 10.1088/1748-0221/8/04/R04001

[223] D. Caratelli et al., *Nuclear Recoil Imaging in Argon*, talk at Magnificent CEνNS (2024), `https://indico.cern.ch/event/1342813/contributions/5950997/attachments/2877730/5040123/LArCADe_NR_imaging.pdf`

[224] J. Galán et al., *Aging studies of Micromegas prototypes for the HL-LHC*, JINST 7 C01041 (2012), DOI: 10.1088/1748-0221/7/01/C01041

[225] J. Galán, 7th RD51 Collaboration Meeting, 2011, `https://indico.cern.ch/event/132080/contributions/1357035/attachments/98111/140040/SparksPresentation.pdf`, opened on 01/03/2024

[226] P. Amedo, S. Leardini, A. Sáa Hernández and D. González Díaz, *Primary scintillation yields induced by α particles in gas mixtures of Argon/CF4 at 9.5 bar*, paper in preparation

[227] V. V. Parkhomchuck et al., *Spark counter with large area*, Nucl. Instrum. Methods 93: No. 2, 269-70 (1971), DOI: 10.1016/0029-554X(71)90475-7

[228] R. Santonico and R. Cardarelli, *Development of resistive plate counters*, Nucl. Instrum. Meth. 187 377-380 (1981), DOI: 10.1016/0029-554X(81)90363-3

USC UNIVERSIDADE DE SANTIAGO DE COMPOSTELA

[229] M. Abbrescia et al., *Resistive Gaseous Detectors: Designs, Performance, and Perspectives*, Wiley-VCH (2018) ISBN: 978-3-527-34076-7

[230] R. Oliveira et al., *First tests of thick GEMs with electrodes made of a resistive kapton*, Nucl. Instr. Meth. A 576, 362-366 (2007), DOI: 10.1016/j.nima.2007.03.010

[231] G. Bencivenni et al., *The micro-Resistive WELL detector: a compact spark-protected single amplification-stage MPGD*, JINST 10 P02008 (2015), DOI: 10.1088/1748-0221/10/02/P02008

[232] R. Oliveira et al., *First Tests of MICROMEGAS and GEM-Like Detectors Made of a Resistive Mesh*, IEEE Nucl. Sci. 57, 3744 (2010), DOI: 10.1109/TNS.2010.2073483

[233] T. Alexopoulos et al., *A spark-resistant bulk-micromegas chamber for high-rate applications*, Nucl. Instr. Meth. A 640, 110 (2011), DOI: 10.1016/j.nima.2011.03.025

[234] V. Peskov et al., *An improved design of spark-protected microstrip gas counters (R-MSGC)*, arXiv:1107.5512 (2011)

[235] A. Jash et al., *Electrical breakdown in Thick-GEM based WELL detectors*, JINST 17 P11004 (2022), DOI: 10.1088/1748-0221/17/11/P11004

[236] S. Leardini et al., *Diamond-like carbon coatings for cryogenic operation of particle detectors*, Nuc. Inst. and Meth. A, Volume 1049, 168104 (2023), DOI: 10.1016/j.nima.2023.168104

[237] M. S. Dixit and A. Rankin, *Simulating the charge dispersion phenomena in Micro Pattern Gas Detectors with a resistive anode*, Nucl. Instr. Meth. A, 566, p. 281 (2006), DOI: 10.1016/j.nima.2006.06.050

[238] W. Riegler, *Electric fields, weighting fields, signals and charge diffusion in detectors including resistive materials*, JINST 11 P11002 (2016), DOI: 10.1088/1748-0221/11/11/P11002

[239] D. Attié et al., *Performances of a resistive Micromegas module for the Time Projection Chambers of the T2K Near Detector upgrade*, Nucl. Instr. Meth. A, 957 163286 (2020), DOI: 10.1016/j.nima.2019.163286

[240] I. Giomataris et al., *A resistive ACHINOS multi-anode structure with DLC coating for spherical proportional counters*, JINST 15 P11023 (2020), DOI: 10.1088/1748-0221/15/11/P11023

USC UNIVERSIDADE DE SANTIAGO DE COMPOSTELA

[241] R. Bouclier et al., *High rate operation of micro-strip gas chambers on diamond coated glass*, Nucl. Inst. Meth. A 369, p. 328 (1996), DOI: 10.1016/0168-9002(95)00812-8

[242] Y. Lv et al., *Production and performance study of Diamond-Like Carbon resistive electrode in MPGD*, Nucl. Inst. Meth. A 958 162759 (2020), DOI: 10.1016/j.nima.2019.162759

[243] T. Francke et al., *Potential of RPCs for tracking*, Nucl. Instr. Meth. A 508, p. 83 (2003), DOI: 10.1016/S0168-9002(03)01282-8

[244] G. Bencivenni et al., *Performance of μ-RWELL detector vs resistivity of the resistive stage*, Nucl. Instr. Meth. A 886, p. 36 (2018), DOI: 10.1016/j.nima.2017.12.037

[245] H. Ito et al., *Optical transmittance measurements of sheet resistors for the CF4 scintillating light in a gaseous time-projection chamber*, arXiv:2202.08983 (2022)

[246] M. Morales et al., *Conductivity and charge depletion aging of resistive electrodes for high rate RPCs*, JINST 8 P01022 (2013), DOI: 10.1088/1748-0221/8/01/P01022

[247] A. Jash et al., *Discharge quenching mechanism and performance of RPWELL with tunable 3D printed resistive plates, charge evacuation in semiconductive glass RPWELL and discharge quenching for Cryogenic-RWELL over a wide range of resistivity*, Nucl. Inst. Meth. A, Volume 1064, 169319 (2024), DOI: 10.1016/j.nima.2024.169319

[248] D. González-Díaz et al., *The effect of temperature on the rate capability of glass timing RPCs*, Nucl. Inst. Meth. A, Volume 555, Issues 1–2, Pages 72-79 (2005), DOI: 10.1016/j.nima.2005.09.005

[249] A. Tesi, S. Leardini et al., *Cryogenic RPWELL: a novel charge-readout element for dual-phase argon TPCs*, JINST 19 P02019 (2024), DOI: 10.1088/1748-0221/19/02/P02019

[250] A. Roy et al., *First results of Resistive-Plate Well (RPWELL) detector operation at 163 K*, JINST 14 P10014 (2019), DOI: 10.1088/1748-0221/14/10/P10014

[251] D. Zavazieva et al., *Towards a large-area RPWELL detector: design optimization and performance* , JINST 18 P08009 (2023), DOI: 10.1088/1748-0221/18/08/P08009

[252] I. Miccoli et al., *The 100th anniversary of the four-point probe technique: the role of probe geometries in isotropic and anisotropic systems*, J. Phys. Cond. Mat., 27 (2015), DOI: 10.1088/0953-8984/27/22/223201

USC UNIVERSIDADE DE SANTIAGO DE COMPOSTELA

[253] https://docs.rs-online.com/eb29/0900766b8013a21d.pdf, opened on 11/05/2023

[254] B. I. Shklovskii, A. L. Efros, *Electronic Properties of Doped Semiconductors*, Springer, Berlin (1984)

[255] N. F. Mott, *Metal Insulator Transitions*, Taylor & Francis, London (1974)

[256] J. J. Hauser, *Electrical, structural and optical properties of amorphous carbon*, Journal of Non-Crystalline Solids 23, 21-41 (1977), DOI: 10.1016/0022-3093(77)90035-7

[257] B. Abi et al., *Volume IV. The DUNE far detector single-phase technology*, JINST 15 T08010 (2020), DOI: 10.1088/1748-0221/15/08/T08010

[258] J. Maneira (private communication)

[259] P. Benetti et al., *Measurement of the specific activity of ^{39}Ar in natural argon*, Nucl. Instr. Meth. A, 574, p. 1 (2006), DOI: 10.1016/j.nima.2007.01.106

[260] R. Bitter et al., *LabVIEW: Advanced programming techniques*, Crc Press (2006) ISBN 9780849333255

[261] A. Tesi, *Development of novel light and charge light readout concepts for liquid argon particle detectors*, PhD thesis, Weizmann Institute of Science (2023)

[262] E. Aprile and T. Doke, *Liquid xenon detectors for particle physics and astrophysics*, Reviews of Modern Physics 82 2053 (2010), DOI: 10.1103/RevModPhys.82.2053

[263] K. Majumdar and K. Mavrokoridis, *Review of Liquid Argon Detector Technologies in the Neutrino Sector*, Applied Sciences 11 2455 (2021), DOI: 10.3390/app11062455

[264] J. F. Ziegler, M. Ziegler and J. Biersack, *SRIM – The stopping and range of ions in matter*, Nucl. Instr. Meth. B 268, 1818 (2010), DOI: 10.1016/j.nimb.2010.02.091

[265] E. W. Lemmon et al., *Thermophysical Properties of Fluid Systems*, NIST Chemistry WebBook (2023)

[266] H. Tawara et al., *Measurements of the W values in argon, nitrogen, and methane for 0.93 to 5.3 MeV alpha particles*, Nucl. Instr. Meth. B 29 447 (1987), DOI: 10.1016/0168-583X(87)90055-3

USC UNIVERSIDADE DE SANTIAGO DE COMPOSTELA

[267] D. S. Renous et al., *Gain stabilization in Micro Pattern Gaseous Detectors: methodology and results*, JINST 12 P09036 (2017), DOI: 10.1088/1748-0221/12/09/P09036

[268] S. Biagi, *Monte Carlo simulation of electron drift and diffusion in counting gases under the influence of electric and magnetic fields*, Nucl. Instr. Meth. A 421 234 (1999), DOI: 10.1016/S0168-9002(98)01233-9

[269] D. Herrera, *Study of columnar recombination in xe+trymethilamine mixtures using a micromegas-tpc*, PoS TIPP2014 057 (2014), DOI: 10.22323/1.213.0057

[270] V. Peskov et al., *Further evaluation of a THGEM UV-photon detector for RICH – comparison with MWPC*, JINST 5 P11004 (2010), DOI: 10.1088/1748-0221/5/11/P11004

[271] P. Traldi, *Some basic concepts on ion mobility in gas phase*, `https://www.waters.com/webassets/cms/library/docs/local_seminar_presentations/01_Some_basic_concepts_on_ion_mobility_in_gas_Pietro_Traldi.pdf`, opened on 01/05/2024

[272] A. Tesi, L. Moleri, S. Leardini et al., *Novel resistive charge-multipliers for dual-phase LAr-TPCs: towards stable operation at higher gains*, JINST 18 C06017 (2023), DOI: 10.1088/1748-0221/18/06/C06017

[273] S. Wu, *Study of alternative double phase LAr TPC charge readout systems*, PhD. thesis, Zurich, ETH (2017), DOI: 10.3929/ethz-b-000172413

[274] L. Arazi et al., *Laboratory studies of THGEM-based WELL structures with resistive anode*, J. Instrum. 9, P04011 (2014), DOI: 10.1088/1748-0221/9/04/p04011

[275] C. Cantini et al., *Performance study of the effective gain of the double phase liquid Argon LEM Time Projection Chamber*, JINST 10, P03017 (2015), DOI: 10.1088/1748-0221/10/03/P03017

[276] WA105 Collaboration, *Performance study of a 3x1x1 m^3 dual phase liquid Argon Time Projection Chamber exposed to cosmic rays*, JINST 16, P08063 (2021),DOI: 10.1088/1748-0221/16/08/P08063

[277] G. Song et al., *Development of THGEM-like detectors with diamond-like carbon resistive electrodes*, J. Instrum. 15, P11013 (2020), DOI: 10.1088/1748-0221/15/11/P11013

[278] I. Deppner et al., *The CBM time-of-flight wall*, Nucl. Inst. Meth. A 661 S121 (2012), DOI: 10.1016/j.nima.2010.09.165

USC UNIVERSIDADE DE SANTIAGO DE COMPOSTELA

[279] IEC 62631-3-1, *Dielectric and resistive properties of solid insulating materials*, https://cdn.standards.iteh.ai/samples/18943/e80e151d026146ef9b0cc1301f575e4e/IEC-62631-3-1-2016.pdf (2016)

[280] M. Lisowski and R. Kacprzyk, *Changes proposed for the IEC 60093 standard concerning measurements of the volume and surface resistivities of electrical insulating materials*, IEEE Trans. Diel. Elec. Insul. 13 139 (2006), DOI: 10.1109/tdei.2006. 1593412

[281] https://docs.rs-online.com/1f82/0900766b815feb3d.pdf, opened on 11/05/2023

[282] D. González Díaz et al., *Signal coupling and signal integrity in multi-strip resistive plate chambers used for timing applications*, Nucl. Instrum. Meth. A 648 52 (2011), DOI: 10.1016/j.nima.2011.05.039

[283] X.Y. Xie et al., *Measuring attenuation in signal propagation in Resistive-Plate Chambers*, JINST 16 P01001 (2021), DOI: 10.1088/1748-0221/16/01/P01001

[284] D. González-Díaz et al., *An analytical description of rate effects in timing RPCs*, Nucl. Phys. B Proc. Suppl. 158 111-117 (2006), DOI: 10.1016/j.nuclphysbps.2006.07.026

[285] D. González Díaz, *Simulation of resistive plate chambers with multi-strip readout*, Nucl. Instrum. Meth. A 661, S172–S176 (2012), DOI: 10.1016/j.nima.2010.09.067

[286] J. Wang et al., *Development of high-rate MRPCs for high resolution time-of-flight systems*, Nucl. Instrum. Meth. A 713, 40–51 (2013), DOI: 10.1016/j.nima.2013.02.036

[287] R. A. Lunt et al., *Dielectric response of Fe2O3 crystals and thin films*, Chem. Phys. Lett. 586, 67–69 (2013), DOI: 10.1016/j.cplett.2013.09.023

[288] B. Boukamp et al., *Electrochemical characterisation of 3Y-TZP–Fe_2O_3 composites* Solid State Ion. 158 381 (2003), DOI: 10.1016/S0167-2738(02)00841-X

[289] V. V. Kharton et al., *Research on the electrochemistry of oxygen ion conductors in the former Soviet Union. I. ZrO_2-based ceramic materials*, J. Solid State Electrochem. 3 61 (1999)

[290] M. J. Verkerk et al., *Effect of impurities on sintering and conductivity of yttria-stabilized zirconia*, J. Matter Sci. 17 3113 (1982), DOI: 10.1007/bf01203473

USC UNIVERSIDADE DE SANTIAGO DE COMPOSTELA

[291] P. Liao et al., *Electron transport in pure and doped hematite*, Nano Lett. 11 1775 (2011), DOI: 10.1021/nl200356n

[292] R. M. Slilaty et al., *Electrical conductivity of Yttria Stabilized Zirconia doped with transitions metals*, Bol. Esp. Ceram. Vidrio 35 109 (1996)

[293] F. Guo et al., *Cobalt-catalyzed highly selective hydroxylation of organohydrosilanes and hydrosiloxanes*, J. Am. Chem. Soc. 104 4642 (2021), DOI: 10.1039/D2QO01294D

[294] C. S. Ahart et al., *Electron and hole mobilities in bulk hematite from spin-constrained density functional theory*, J. Am. Chem. Soc. 144 4623 (2022), DOI: 10.1021/jacs.1c13507

[295] M. Pitt et al., *Measurements of charging-up processes in THGEM-based particle detectors*, JINST 13 P03009 (2018), DOI: 10.1088/1748-0221/13/03/P03009

[296] L. Olano Vegas, I. Pardo, S. Leardini et al., *Development of Fe_2O_3/YSZ ceramic plates for cryogenic operation of resistive-protected gaseous detectors*, Front. Detect. Sci. Technol., volume 1 (2023), DOI: 10.3389/fdest.2023.1234229

[297] L. Arazi, et al., *First observation of liquid-xenon proportional electroluminescence in THGEM holes*, JINST 8 C12004 (2013), DOI: 10.1088/1748-0221/8/12/C12004

[298] E. Erdal et al., *First demonstration of VUV-photon detection in liquid xenon with THGEM and GEM-based Liquid Hole Multipliers*, Nucl. Instr. Meth. A, vol. 845, pp. 218–221 (2017), DOI: 10.1016/j.nima.2016.05.105

[299] E. Erdal et al., *First imaging results of a bubble-assisted Liquid Hole Multiplier with SiPM readout in liquid xenon*, JINST 14 P01028 (2019), DOI: 10.1088/1748-0221/14/01/P01028

[300] A. Breskin, *Liquid Hole-Multipliers: A potential concept for large single-phase noble-liquid TPCs of rare events*, Journal of Physics: Conference Series, vol. 460, p. 012020 (2013), DOI: 10.1088/1742-6596/460/1/012020

[301] E. Erdal., *Development of novel concepts of noble-liquid detectors for rare-event searches*, PhD thesis, Weizmann Institute of Science (2021)

[302] P. Vadgama, *Surfaces and interfaces for biomaterials*, Woodhead Publishing (2005) ISBN 9781855739307

USC UNIVERSIDADE DE SANTIAGO DE COMPOSTELA

[303] COMSOL Multiphysics, *Introduction to comsol multiphysics®*, Burlington, MA, vol. 9, p. 2018 (1998)

[304] D. A. Saville, *Electrohydrodynamics: the Taylor-Melcher leaky dielectric model*, Annual Review of Fluid Mechanics, Volume 29, pages 27-64 (1997), DOI: 10.1146/annurev.fluid.29.1.27

[305] Y. Lin, P. Skjetne and A. Carlson, *A phase field model for multiphase electro-hydrodynamic flow*, International Journal of Multiphase Flow, Volume 45, pages 1-11 (2012), DOI: 10.1016/j.ijmultiphaseflow.2012.04.002

[306]] P. Concus, *Static menisci in a vertical right circular cylinder*, J. Fluid Mech. 34 481 (1968), DOI: 10.1017/s002211206800203x

[307] A. Tesi, E. Segre, S. Leardini et al., *Bubble dynamics in Liquid Hole Multipliers*, JINST 16 P09003 (2021), DOI: 10.1088/1748-0221/16/09/P09003

[308] A. Marchionni, *Status and new ideas regarding liquid argon detectors*, Ann. Rev. Nucl. Part. Sci., vol. 63, pp. 269–290 (2013), DOI: 10.1146/annurev.nucl.012809.104445

[309] K. Y. Law and H. Zhao, *Contact Angle Measurements and Surface Characterization Techniques*, pp. 7–34., Springer, Cham, Switzerland (2015), DOI: 10.1007/978-3-319-25214-8_2

[310] A. Stalder et al., *A snake-based approach to accurate determination of both contact points and contact angles*, Colloids and Surfaces A: Physicochemical and Engineering Aspects, vol. 286, no. 1, pp. 92 – 103 (2006), DOI: 10.1016/j.colsurfa.2006.03.008

[311] C. A. Schneider, W. S. Rasband and K. W. Eliceiri, *NIH image to ImageJ: 25 years of image analysis*, Nat Meth, vol. 9, pp. 671–675 (2012), DOI: 10.1038/nmeth.2089

[312] D. Salomon, *Curves and surfaces for computer graphics*, Springer, New York (2006), DOI: 10.1007/0-387-28452-4

[313] M. Miyama et al., *Static and dynamic contact angles of water on polymeric surfaces*, Langmuir, vol. 13, no. 20, pp. 5494–5503 (1997), DOI: 10.1021/la960870n

[314] A. C. Kak and M. Slaney, *Principles of Computerized Tomographic Imaging*, Society for Industrial and Applied Mathematics (2001), DOI: 10.1137/1.9780898719277

[315] S. Stock, *MicroComputed Tomography: Methodology and Applications*, CRC Press, Boca Raton, FL, U.S.A. (2008)

USC UNIVERSIDADE DE SANTIAGO DE COMPOSTELA

[316] R. Mizutani and Y. Suzuki, *X-ray microtomography in biology*, Micron, vol. 43, no. 2, pp. 104–115 (2012), DOI: 10.1016/j.micron.2011.10.002

[317] S. R. Stock, *Recent advances in X-ray microtomography applied to materials*, International Materials Reviews, vol. 53, no. 3, pp. 129–181 (2008), DOI: 10.1179/174328008x277803

[318] A. du Plessis, S. G. le Roux and A. Guelpa, *Comparison of medical and industrial X-ray computed tomography for non-destructive testing*, Case Studies in Nondestructive Testing and Evaluation, vol. 6, pp. 17–25 (2016), DOI: 10.1016/j.csndt.2016.07.001

[319] L. M. Lander et al., *A systematic comparison of contact angle methods*, Langmuir, vol. 9, pp. 2237–2239 (1993), DOI: 10.1021/la00032a055

[320] J. W. Drelich, *Guidelines to measurements of reproducible contact angles using a sessile-drop technique*, Surface Innovations, vol. 1, no. 4, pp. 248–254 (2013), DOI: 10.1680/si.13.00010

[321] Silicone oil properties, `https://vacuumoil.com/wp-content/uploads/2016/08/Dow-Corning-Diffusion-Pump-Fluid.pdf`

[322] T. Widyanugraha et al., *Dielectric properties of silicone oil, natural ester, and mineral oil under accelerated thermal aging*, IEEE International Conference on Condition Monitoring and Diagnosis, vol. 1, pp. 1139–1142 (2012), 10.1109/CMD.2012.6416360

[323] E. Baracchini et al., *First evidence of luminescence in a He/CF_4 gas mixture induced by non-ionizing electrons* , JINST 15 P08018 (2020), DOI: 10.1088/1748-0221/15/08/P08018

[324] F. D. Amaro et al., *Enhancing the light yield of He:CF4 based gaseous detector*, arXiv:2406.05713v1 (2024)

[325] A. Maslaáni and V. Sember, *Emission spectroscopy of OH radical in water-argon arc plasma jet*, J. Spectrosc. 952138 (2014), DOI: 10.1155/2014/952138

[326] N. Washida et al., *Emission spectra of CF3 radicals. IV. Excitation spectra, quantum yields, and potential energy surfaces of the CF3 fluorescences*, J. Chem. Phys. 78 (3), 1025–1032 (1983), DOI: 10.1063/1.444902

[327] L. C. Lee, X. Wang, and M. Suto, *Fluorescence from extreme ultraviolet photoexcitation of CF4*, J. Chem. Phys. 85 (11), 6294–6300 (1986), DOI: 10.1063/1.451459

USC UNIVERSIDADE DE SANTIAGO DE COMPOSTELA

[328] P. Lindblom and O. Solin, *Atomic near-infrared noble gas scintillations I: Optical spectra*, Nucl. Inst. Meth. A, Volume 268, Issue 1, Pages 204-208 (1988), DOI: 10.1016/0168-9002(88)90607-9

[329] A. Bondar et al., *Study of infrared scintillations in gaseous and liquid argon – Part II: light yield and possible applications*, JINST 7 P06014 (2012), DOI: 10.1088/1748-0221/7/06/P06014

[330] A. Morozov et al., *Secondary scintillation in CF_4: emission spectra and photon yields for MSGC and GEM*, JINST 7 P02008 (2012), DOI: 10.1088/1748-0221/7/02/P02008

[331] M. M. R. Fraga et al., *Pressure Dependence of Secondary NIR Scintillation in Ar and Ar/CF_4*, IEEE TRANSACTIONS ON NUCLEAR SCIENCE, VOL. 48, NO. 3 (2001), DOI: 10.1109/23.940075

[332] L. G. Huxley, and R. W. Crompton, *The diffusion and drift of electrons in gases*, Wiley, New York (1974), ISBN 978-0471425908

[333] J. Brambring, *Der Stromverlauf einer Elektronenlawine mit Diffusion*, Zeitschrift für Physik, Volume 179, pages 532–538 (1964), DOI: 10.1007/BF01380826

[334] R. W. Crompton, *Comments on Some Recent Analyses of the Pulsed Townsend Discharge*, J. Appl. Phys. 38, 4093–4094 (1967), DOI: 10.1063/1.1709082

[335] D. González-Díaz, *A survey on GEM-based readouts and gas mixtures for optical TPCs*, Vienna Conference (2016), `https://indico.cern.ch/event/391665/contributions/1827205/`

[336] L. Norman et al., *Dielectric strength of noble and quenched gases for high pressure time projection chambers*, Eur. Phys. J. C 82:52 (2022), DOI: 10.1140/epjc/s10052-021-09894-z

[337] J. Escada et al., *A Monte Carlo study of the fluctuations in Xe electroluminescence yield: pure Xe vs Xe doped with CH_4 or CF_4 and planar vs cylindrical geometries*, J. Instrum. 6, P08006 (2011), DOI: 10.1088/1748-0221/6/08/p08006

[338] E. D. C. Freitas et al., *Secondary scintillation yield in high-pressure xenon gas for neutrinoless double beta decay search*, Phys. Lett. B 684, 205–210 (2010), DOI: 10.1016/j.physletb.2010.01.013

[339] Application Guidelines ESR Family (2018) `https://multimedia.3m.com/mws/media/1389248O/application-guide-for-esr.pdf`, opened on 01/11/2023

USC UNIVERSIDADE DE SANTIAGO DE COMPOSTELA

[340] M. F. Weber et al., *Giant birefringent optics in multilayer polymer mirrors*, Science 287 2451–2456 (2000), DOI: 10.1126/science.287.5462.2451

[341] `https://www.visionteksystems.co.uk/ito_conductive_film.htm`, opened on 15/10/2023

[342] P. A. Amaudruz et al., *Design and construction of the DEAP-3600 dark matter detector*, Astroparticle Physics 108, 1-23 (2019), DOI: 10.1016/j.astropartphys.2018.09.006

[343] Y. Tameda et al., *Air shower observation by a simple structured Fresnel lens telescope with a single pixel for the next generation of ultra-high-energy cosmic ray observatories*, Progress of Theoretical and Experimental Physics 4 (2019), DOI: 10.1093/ptep/ptz025

[344] ANSYS (2023), `https://www.ansys.com/products`, opened on 19/09/2023

[345] H. Schindler, Garfield++ (2019), `https://garfieldpp.web.cern.ch/garfieldpp/`, opened on 19/09/2023

[346] S. Agostinelli et al., *Geant4—a simulation toolkit*, Nucl. Instrum. Methods Phys. Res., Sect. A 506.3, pp. 250–303 (2003), DOI: 10.1016/S0168-9002(03)01368-8

[347] I. Lindseth, A. Bardal and R. Spooren, *Reflectance measurements of aluminium surfaces using integrating spheres*, Opt. Lasers Eng., 32, 5 419-435 (1999), DOI: 10.1016/S0143-8166(00)00010-5

[348] `https://www.datasheet.live/pdfviewer?url=https%3A%2F%2Fpdf.datasheet.live%2F6432b002%2Fhamamatsu.com%2FR7378.pdf`, opened on 09/01/2024

[349] `https://www.hamamatsu.com/content/dam/hamamatsu-photonics/sites/documents/99_SALES_LIBRARY/etd/High_energy_PMT_TPMZ0003E.pdf`, opened on 10/01/2024

[350] C. E. Aalseth et al., *DarkSide-20k: A 20 tonne two-phase LAr TPC for direct dark matter detection at LNGS*, Eur. Phys. J. Plus 2018, 133 (2018), DOI: 10.1140/epjp/i2018-11973-4

[351] G. Gallina et al., *Characterization of the Hamamatsu VUV4 MPPCs for nEXO*, Nucl. Instr. Meth. A 940, 371 (2019), DOI: 10.1016/j.nima.2019.05.096

[352] E. P. De Lima et al., *Fano factors of rare gases and their mixtures*, Nucl. Instr. Meth. 192(s 2–3):575–581 (1982), DOI: 10.1016/0029-554X(82)90875-8

USC UNIVERSIDADE DE SANTIAGO DE COMPOSTELA

[353] C. Henriques, *Studies of xenon mixtures with molecular additives for the NEXT electroluminescence TPC*, PhD thesis (2018)

[354] D. F. Anderson et al., *A large area, gas scintillation proportional counter*, Nucl. Instr. Meth. 163, 125-134 (1979), DOI: 10.1016/0029-554x(79)90040-5

[355] `https://degrad.web.cern.ch/degrad/`, opened on 09/01/2024

[356] T. H. V. T. Dias et al., *The Fano factor in gaseous xenon: a Monte Carlo calculation for X-rays in the 0.1 to 25 keV energy range*, Nucl. Instr. Meth. A 307, 341-346 (1991), DOI: 10.1016/0168-9002(91)90202-2

[357] D. Nygren, *Can the "intrinsic" energy resolution in xenon be surpassed?*, J. Phys. Conf. Ser. 309 012006 (2011), DOI: 10.1088/1742-6596/309/1/012006

[358] A. Saa-Hernández et al., *Xenon-Based EL-TPCs for 4π Detection of X-Rays in the Energy Range 10–100 keV in Radiation Detection Systems*, 2nd Edition, CRC Press (2021), DOI: 10.1201/9781003218364

[359] S. Akiyama, *Status and prospects of the AXEL experiment*, talk at Workshop on Xenon Detector $0\nu\beta\beta$ Searches, SLAC (2023)

[360] G. Martínez-Lema et al., *Calibration of the NEXT-White detector using 83 mKr decays*, JINST 13 P10014 (2018), DOI: 10.1088/1748-0221/13/10/p10014

[361] D. Lorca et al., *Characterisation of NEXT-DEMO using xenon K_α X-rays*, JINST 9 P10007 (2014), DOI: 10.1088/1748-0221/9/10/P10007

[362] A. Bolozdynya et al., *A high pressure xenon self-triggered scintillation drift chamber with 3D sensitivity in the range of 20-140 keV deposited energy*, Nucl. Instr. Meth. A 385 225–238 (1997), DOI: 10.1016/S0168-9002(96)01035-2

[363] G. R. Araujo, L. Baudis, N. McFadden et al., *R&D of wavelength-shifting reflectors and characterization of the quantum efficiency of tetraphenyl butadiene and polyethylene naphthalate in liquid argon*, Eur. Phys. J. C 82, 442 (2022), DOI: 10.1140/epjc/s10052-022-10383-0

[364] Y. Efremenko et al., *Use of poly(ethylene naphthalate) as a self-vetoing structural material*, JINST 14 P07006 (2019), DOI: 10.1088/1748-0221/14/07/P07006

USC UNIVERSIDADE DE SANTIAGO DE COMPOSTELA

[365] Y. Abraham, et al., *Wavelength-Shifting Performance of Polyethylene Naphthalate Films in a Liquid Argon Environment*, arXiv:2103.03232 (2021)

[366] G. Huseynova et al., *Rising advancements in the application of PEDOT:PSS as a prosperous transparent and flexible electrode material for solution-processed organic electronics*, J. Inf. Disp. 21, 71 (2020), DOI: 10.1080/15980316.2019.1707311

[367] F. Monrabal et al., *The NEXT White (NEW) detector*, JINST 13 P12010 (2018), DOI: 10.1088/1748-0221/13/12/P12010

[368] P. Agnes, et al., *DarkSide-50 532-day dark matter search with low-radioactivity argon*, Phys. Rev. D 98, 102006 (2018), DOI: 10.1103/PhysRevD.98.102006

[369] Y. Efremenko, et al., *Use of poly(ethylene naphthalate) as a self-vetoing structural material*, J. Phys. Conf. Ser. 1468, 012225 (2020), DOI: 10.1088/1742-6596/1468/1/012225

[370] Teijin, Polyethylene Naphthalate (PEN) Resin Teonex (2020), `www.teijin.com/products/resin/teonex`

[371] P. A. Amaudruz et al, *Design and construction of the DEAP-3600 dark matter detector Author links open overlay panel* , Astropart. Phys. 108, 1 (2019), DOI: 10.1016/j.astropartphys.2018.09.006

[372] J. R. Graybill et al., *Extreme ultraviolet photon conversion efficiency of tetraphenyl butadiene*, Appl. Opt. 59, 1217 (2020), DOI: 10.1364/AO.380185

[373] Heraeus, Clevios™ antistatic and conductive glass coatings, (2021) `www.heraeus.com/\media/media/hec/documents_hec/brochures_en/Clevios_EMI.pdf`

[374] P. Agnes et al., *First results from the DarkSide-50 dark matter experiment at Laboratori Nazionali del Gran Sasso*, Phys. Lett. B 743, 456 (2015), 10.1016/j.physletb.2015.03.012

[375] A. Gola et al., *NUV-Sensitive Silicon Photomultiplier Technologies Developed at Fondazione Bruno Kessler*, Sensors 19, 308 (2019), DOI: 10.3390/s19020308

[376] A. Simón et al., *Boosting background suppression in the NEXT experiment through Richardson-Lucy deconvolution*, JINST 17 C01014 (2022), DOI: 10.1088/1748-0221/17/01/C01014

[377] `https://www.wasyresearch.com/what-is-the-essence-of-phd/`

USC UNIVERSIDADE DE SANTIAGO DE COMPOSTELA

[378] L. Olano Vegas, *Development of ceramic materials for gaseous detectors in HEP*, bachelor thesis, Universidad de Cantabria (2022), https://repositorio.unican.es/xmlui/bitstream/handle/10902/26602/OlanoVegasLuc%C3%ADa_TFGF%C3%ADsica_Desarrollo_Materiales_Cer%C3%A1micos.pdf

[379] F. M. Lucas, *Initial simulation of a gaseous compton camera with electroluminescence amplification*, master thesis, Universidade de Aveiro (2023), https://ria.ua.pt/bitstream/10773/39489/1/Documento_Francisco_Lucas.pdf

USC UNIVERSIDADE DE SANTIAGO DE COMPOSTELA

List of publications

Diamond-like carbon coatings for cryogenic operation of particle detectors

S. Leardini [a], Y. Zhou [c d], A. Tesi [b], M. Morales [a], D. González-Díaz [a], A. Breskin [b], S. Bressler [b], L. Moleri [b], V. Peskov [a]

[a] IGFAE, Universidade de Santiago de Compostela, Spain
[b] Weizmann Institute of Science, Department of Particle Physics and Astrophysics, Rehovot, Israel
[c] State Key Laboratory of Particle Detection and Electronics, University of Science and Technology of China, Hefei 230026, China
[d] Department of Modern Physics, University of Science and Technology of China, Hefei 230026, China

PhD Student Contribution
For the part reproduced in the thesis: contribution in experiment design (hardware and software); responsible for data taking with the in-house cryostat, whole data analysis and modeling.
Used (with some modifications) in Chapter: 6.1.1

Journal and Article Information
Journal name: Nuclear Instruments and Methods in Physics Research Section A: Accelerators, Spectrometers, Detectors and Associated Equipment
Publisher: Elsevier
ISSN: 1872-9576
Year of publication: 2023
DOI: 10.1016/j.nima.2023.168104
Impact factor in 2023: 1.5
Quartile in 2023: Q2

The article is distributed under the terms of the Creative Commons Attribution License (CC-BY-NC-ND 4.0), which permits any use, distribution and reproduction in any medium, provided the original author(s) and source are credited.

USC UNIVERSIDADE DE SANTIAGO DE COMPOSTELA

The cryogenic RWELL: a stable charge multiplier for dual-phase liquid argon detectors

A. Tesi[1,a], **S. Leardini**[1,2], **L. Moleri**[1], **D. Gonzalez-Diaz**[2], **A. Jash**[1], **A. Breskin**[1], **S. Bressler**[1]
[1] Department of Particle Physics and Astrophysics, Weizmann Institute of Science, Rehovot, Israel
[2] Instituto Galego de Física de Altas Enerxías, Univ. de Santiago de Compostela, Santiago de Compostela, Spain

PhD Student Contribution
Contribution in code writing and data analysis.
Used (with some modifications) in Chapter: 6.1.2

Journal and Article Information
Journal name: The European Physical Journal C
Publisher: EDP Sciences, Società Italiana di Fisica and Springer Berlin Heidelberg
ISSN: 1434-6052
Year of publication: 2023
DOI: 10.1140/epjc/s10052-023-12162-x
Impact factor in 2023: 4.2
Quartile in 2023: Q1

The article is distributed under the terms of the Creative Commons Attribution License (CC-BY 4.0), which permits any use, distribution and reproduction in any medium, provided the original author(s) and source are credited.

USC UNIVERSIDADE DE SANTIAGO DE COMPOSTELA

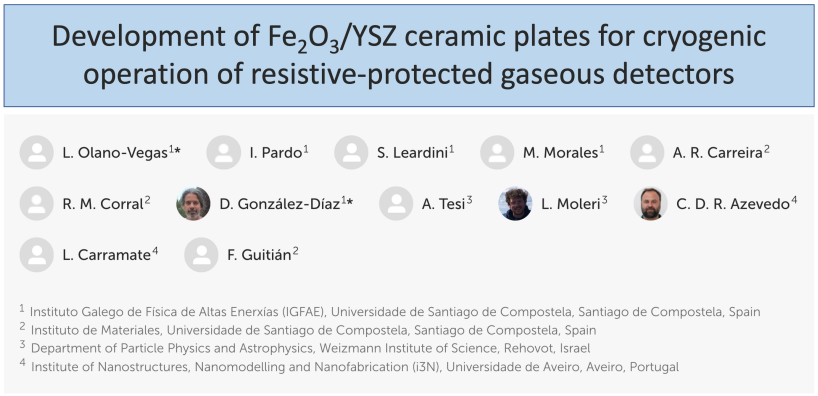

PhD Student Contribution
For the part reproduced in the thesis: responsible for overseeing the experimental activities, and contributed to the experimental characterisation of the ceramics.
Used (with some modifications) in Chapter: 6.2.1

Journal and Article Information
Journal name: Frontiers in Detector Science and Technology
Publisher:
ISSN: 2813-8031
Year of publication: 2023
DOI: 10.3389/fdest.2023.1234229
Impact factor in 2023: N/A (it is a new journal)
Quartile in 2023: N/A (it is a new journal)

The article is distributed under the terms of the Creative Commons Attribution License (CC-BY 4.0), which permits any use, distribution and reproduction in any medium, provided the original author(s) and source are credited.

USC UNIVERSIDADE DE SANTIAGO DE COMPOSTELA

Cryogenic RPWELL: a novel charge-readout element for dual-phase argon TPCs

A. Tesi[3,1], S. Leardini[3,1,2], L. Moleri[1], M. Morales[2], D. Gonzalez-Diaz[2], A. Jash[1], A. Breskin[1] and S. Bressler[1]

Author affiliations

[1] Department of Particle Physics and Astrophysics, Weizmann Institute of Science, Rehovot, Israel

[2] Instituto Galego de Física de Altas Enerxías, Universidad de Santiago de Compostela, Santiago de Compostela, Spain

Author notes

[3] Contributed equally.

PhD Student Contribution
Contributed in detector operation, code writing and data analysis.
Used (with some modifications) in Chapter: 6.2.2

Journal and Article Information
Journal name: Journal of Instrumentation
Publisher: IOP Publishing
ISSN: 1748-0221
Year of publication: 2024
DOI: 10.1088/1748-0221/19/02/P02019
Impact factor in 2023: 1.3
Quartile in 2023: Q2

The article is distributed under the terms of the Creative Commons Attribution License (CC-BY 4.0), which permits any use, distribution and reproduction in any medium, provided the original author(s) and source are credited.

USC UNIVERSIDADE DE SANTIAGO DE COMPOSTELA

Bubble dynamics in Liquid Hole Multipliers

A. Tesi[1], E. Segre[2], S. Leardini[3], A. Breskin[1], S. Kapishnikov[4], L. Moleri[5], D. Vartsky[1] and S. Bressler[1]

Author affiliations

[1] Department of Particle Physics and Astrophysics, Weizmann Institute of Science, Hertzl street 234, Rehovot, Israel

[2] Physics Core Facilities, Weizmann Institute of Science, Hertzl street 234, Rehovot, Israel

[3] Instituto Galego de Física de Altas Enerxías, Universidade de Santiago de Compostela, Rúa de Xoaquín Díaz de Rábago, Santiago de Compostela, Spain

[4] Department of Chemical Research Support, Weizmann Institute of Science, Hertzl street 234, Rehovot, Israel

[5] Department of Physics, Technion — Israel Institute of Technology, Technion City, Haifa, Israel

PhD Student Contribution
Contributed for the experimental measurements inside the cryostat in experiment design, data taking; contributed for all the experimental measurements in code writing and data analysis.
Used (with some modifications) in Chapter: 7

Journal and Article Information
Journal name: Journal of Instrumentation
Publisher: IOP Publishing
ISSN: 1748-0221
Year of publication: 2021
DOI: 10.1088/1748-0221/16/09/P09003
Impact factor in 2023: 1.3
Quartile in 2023: Q2

The article is distributed under the terms of the Creative Commons Attribution License (CC-BY 4.0), which permits any use, distribution and reproduction in any medium, provided the original author(s) and source are credited.

USC UNIVERSIDADE DE SANTIAGO DE COMPOSTELA

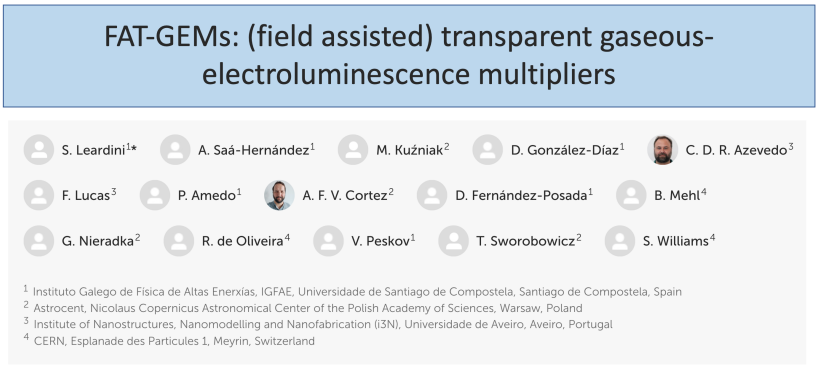

PhD Student Contribution
Responsible for data taking and analysis; contributed for writing analysis code.
Used (with some modifications) in Chapter: 9.1

Journal and Article Information
Journal name: Frontiers in Detector Science and Technology
Publisher:
ISSN: 2813-8031
Year of publication: 2024
DOI: 10.3389/fdest.2024.1373235
Impact factor in 2023: N/A (it is a new journal)
Quartile in 2023: N/A (it is a new journal)

The article is distributed under the terms of the Creative Commons Attribution License (CC-BY 4.0), which permits any use, distribution and reproduction in any medium, provided the original author(s) and source are credited.

USC UNIVERSIDADE DE SANTIAGO DE COMPOSTELA

Development of very-thick transparent GEMs with wavelength-shifting capability for noble element TPCs

M. Kuźniak[1,a], D. González-Díaz[2,b], P. Amedo[2], C. D. R. Azevedo[3], D. J. Fernández-Posada[2], M. Kuźwa[1], S. Leardini[2], A. Leonhardt[8], T. Łęcki[5], L. Manzanillas[6], D. Muenstermann[7], G. Nieradka[1], R. de Oliveira[4], T. R. Pollmann[8,9], A. Saá Hernández[2], T. Sworobowicz[1], C. Türkoğlu[1], S. Williams[4]

[1] AstroCeNT, Nicolaus Copernicus Astronomical Center of the Polish Academy of Sciences, Rektorska 4, 00-614 Warsaw, Poland
[2] Instituto Galego de Física de Altas Enerxías, Univ. de Santiago de Compostela, Campus Vida, Rúa Xosé María Sufez Núñez, s/n, 15782 Santiago de Compostela, Spain
[3] Institute of Nanostructures, Nanomodelling and Nanofabrication (i3N), Universidade de Aveiro, Aveiro, Portugal
[4] CERN, Esplanade des Particules 1, Meyrin, Switzerland
[5] Biological and Chemical Research Centre, Faculty of Chemistry, University of Warsaw, Żwirki i Wigury 101, 02-089 Warsaw, Poland
[6] Max Planck Institute for Physics, Munich, Germany
[7] Physics Department, Lancaster University, Lancaster, UK
[8] Department of Physics, Technische Universität München, 80333 Munich, Germany
[9] *Present address:* Nikhef and the University of Amsterdam, Science Park, 1098XG Amsterdam, The Netherlands

PhD Student Contribution
Characterization of the PEDOT:PSS coating resistivity. Contribution to measurements in xenon and argon gas.
Used (with some modifications) in Chapter: 9.2

Journal and Article Information
Journal name: The European Physical Journal C
Publisher: EDP Sciences, Società Italiana di Fisica and Springer Berlin Heidelberg
ISSN: 1434-6052
Year of publication: 2023
DOI: 10.1140/epjc/s10052-021-09316-0
Impact factor in 2023: 4.2
Quartile in 2023: Q1

The article is distributed under the terms of the Creative Commons Attribution License (CC-BY 4.0), which permits any use, distribution and reproduction in any medium, provided the original author(s) and source are credited.

USC UNIVERSIDADE DE SANTIAGO DE COMPOSTELA

Contributions from other authors that also appeared in their theses

All the papers used in chapters 6 and 7 have also been used in the PhD thesis of Andrea Tesi [261], who is a co-author of the papers.
For Chapter 6 he was responsible for the experiment design for the operation in a detector of the RWELL and RPWELL structures and for the data taking with the RWELL structure. He contributed in the detector operation with the RPWELL structure and in the data analysis of the RWELL and RPWELL structures.
For Chapter 7 he contributed for the experimental measurements inside the cryostat in: experiment design, data taking. He was responsible for the experimental measurements with the μCT in: experiment design, data taking. He contributed for all the experimental measurements in the data analysis.

Preliminary results of the work presented in *Development of Fe_2O_3/YSZ ceramic plates for cryogenic operation of resistive-protected gaseous detectors* (reproduced in Chapter 6.2.1) have also been used in the bachelor thesis of Lucía Olano Vegas [378], who is a co-author of the paper. She has contributed in the experimental characterisation of the ceramics (data taking and analysis).

Preliminary results from the simulations presented in *FAT-GEMs: (field assisted) transparent gaseous-electroluminescence multipliers* (reproduced in Chapter 9) have also been used in the master thesis of Francisco Miranda Lucas [379], who is a co-author of the paper, as he has contributed in performing the simulations for this work.

USC UNIVERSIDADE DE SANTIAGO DE COMPOSTELA

Permission of content reuse

Images under Creative Commons Licenses

Figures 1.1, 3.1e, 3.7, 4.3c, 4.13 left, 5.2, are released under the The reproduction of these contents is allowed under the Creative Commons CC-BY 3.0 license.

Figures 1.8a, 1.9, 2.1left, 2.2, 2.4a,c,d, 2.5, 2.6 right, 2.8, 3.1f, 3.5, 4.5 right, 4.9, 4.10 bottom, 4.11, 4.13 right, 4.14, 5.6, 5.10, 6.22, 8.3, 9.6 top, bottom, are released under the terms of the Creative Commons CC-BY 4.0license.

Figure 1.8d is released under the terms of the Creative Commons CC-BY-SA 4.0 license.

Figure 3.6b is released under the terms of the Creative Commons CC BY-SA 3.0 license.

Figures 4.3a, 4.3b, 5.4, are released under the terms of the Creative Commons CC BY-NC-ND 3.0 license.

Figures 4.4 left, 5.7 left, 5.11, table 5.1, are released under the terms of the Creative Commons CC BY-NC-ND 4.0 license.

USC
UNIVERSIDADE DE SANTIAGO DE COMPOSTELA

Images with other permissions

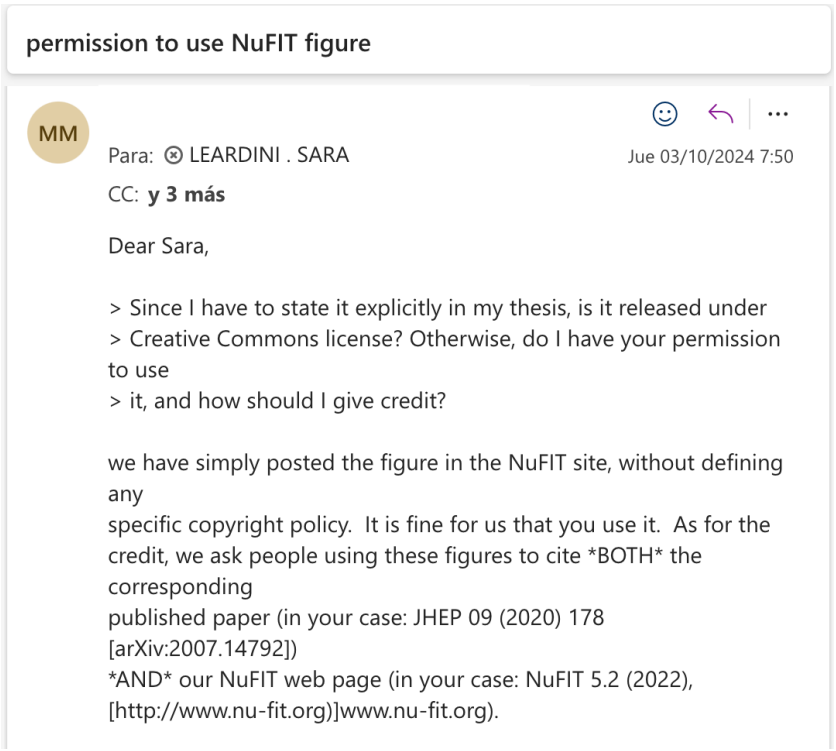

permission to use NuFIT figure

MM

Para: LEARDINI . SARA

Jue 03/10/2024 7:50

CC: **y 3 más**

Dear Sara,

> Since I have to state it explicitly in my thesis, is it released under
> Creative Commons license? Otherwise, do I have your permission to use
> it, and how should I give credit?

we have simply posted the figure in the NuFIT site, without defining any
specific copyright policy. It is fine for us that you use it. As for the credit, we ask people using these figures to cite *BOTH* the corresponding
published paper (in your case: JHEP 09 (2020) 178 [arXiv:2007.14792])
AND our NuFIT web page (in your case: NuFIT 5.2 (2022), [http://www.nu-fit.org)]www.nu-fit.org).

Permission to reuse Fig. 1.3

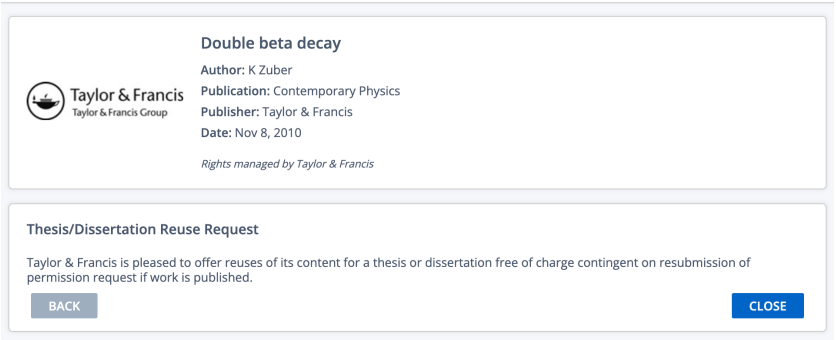

Taylor & Francis
Taylor & Francis Group

Double beta decay

Author: K Zuber
Publication: Contemporary Physics
Publisher: Taylor & Francis
Date: Nov 8, 2010

Rights managed by Taylor & Francis

Thesis/Dissertation Reuse Request

Taylor & Francis is pleased to offer reuses of its content for a thesis or dissertation free of charge contingent on resubmission of permission request if work is published.

BACK CLOSE

Permission to reuse Fig. 1.5

USC UNIVERSIDADE DE SANTIAGO DE COMPOSTELA

Order Date	02-Oct-2024	Type of Use	Republish in a thesis/dissertation
Order License ID	1532177-1	Publisher	ANNUAL REVIEWS
ISSN	1545-4134	Portion	Image/photo/illustration

LICENSED CONTENT

Publication Title	Annual review of nuclear and particle science	Publication Type	e-Journal
Article Title	The First Direct Observation of Double-Beta Decay	Start Page	247
		End Page	267
Date	01/01/1978	Issue	1
Language	English	Volume	64
Country	United States of America	URL	http://arjournals.annualreviews.org/loi/n...
Rightsholder	Annual Reviews, Inc.		

REQUEST DETAILS

Portion Type	Image/photo/illustration	Distribution	Worldwide
Number of Images / Photos / Illustrations	1	Translation	Original language of publication
Format (select all that apply)	Electronic	Copies for the Disabled?	No
Who Will Republish the Content?	Academic institution	Minor Editing Privileges?	Yes
Duration of Use	Life of current edition	Incidental Promotional Use?	No
Lifetime Unit Quantity	Up to 499	Currency	EUR
Rights Requested	Main product		

NEW WORK DETAILS

Title	NEW DETECTION CONCEPTS IN NOBLE-ELEMENT TPCS	Institution Name	University of Santiago de Compostela
		Expected Presentation Date	2024-12-16
Instructor Name	Diego Gonzalez Diaz		

ADDITIONAL DETAILS

Order Reference Number	N/A	The Requesting Person / Organization to Appear on the License	Sara Leardini / University of Santiago de Compostela

REQUESTED CONTENT DETAILS

Title, Description or Numeric Reference of the Portion(s)	Figure 2(c)	Title of the Article / Chapter the Portion Is From	The First Direct Observation of Double-Beta Decay
Editor of Portion(s)	Moe, Michael	Author of Portion(s)	Moe, Michael
Volume / Edition	64	Issue, if Republishing an Article From a Serial	1
Page or Page Range of Portion	247-267		
		Publication Date of Portion	2014-10-19

Permission to reuse Fig. 1.6

American Physical Society
Reuse and Permissions License

02-Oct-2024

This license agreement between the American Physical Society ("APS") and Sara Leardini ("You") consists of your license details and the terms and conditions provided by the American Physical Society and SciPris.

Licensed Content Information

License Number:	**RNP/24/OCT/084011**
License date:	02-Oct-2024
DOI:	10.1103/PhysRevD.90.033005
Title:	New expectations and uncertainties on neutrinoless double beta decay
Author:	Stefano Dell'Oro, Simone Marcocci, and Francesco Vissani
Publication:	Physical Review D
Publisher:	American Physical Society
Cost:	USD $ 0.00

Request Details

Does your reuse require significant modifications: No

Specify intended distribution locations:	Worldwide
Reuse Category:	Reuse in a thesis/dissertation
Requestor Type:	Student
Items for Reuse:	Figures/Tables
Number of Figure/Tables:	1
Figure/Tables Details:	Figure 1 left with some lines added to show different \tau_0 if 100Mo is a target
Format for Reuse:	Electronic

Information about New Publication:

University/Publisher:	University of Santiago de Compostela
Title of dissertation/thesis:	NEW DETECTION CONCEPTS IN NOBLE-ELEMENT TPCS
Author(s):	Sara Leardini
Expected completion date:	Dec. 2024

License Requestor Information

Name:	Sara Leardini
Affiliation:	Individual
Email Id:	
Country:	Spain

American Physical Society
Reuse and Permissions License

TERMS AND CONDITIONS

The American Physical Society (APS) is pleased to grant the Requestor of this license a non-exclusive, non-transferable permission, limited to Electronic format, provided all criteria outlined below are followed.

1. You must also obtain permission from at least one of the lead authors for each separate work, if you haven't done so already. The author's name and affiliation can be found on the first page of the published Article.
2. For electronic format permissions, Requestor agrees to provide a hyperlink from the reprinted APS material using the source material's DOI on the web page where the work appears. The hyperlink should use the standard DOI resolution URL, http://dx.doi.org/{DOI}. The hyperlink may be embedded in the copyright credit line.
3. For print format permissions, Requestor agrees to print the required copyright credit line on the first page where the material appears: "Reprinted (abstract/excerpt/figure) with permission from [(FULL REFERENCE CITATION) as follows: Author's Names, APS Journal Title, Volume Number, Page Number and Year of Publication.] Copyright (YEAR) by the American Physical Society."
4. Permission granted in this license is for a one-time use and does not include permission for any future editions, updates, databases, formats or other matters. Permission must be sought for any additional use.
5. Use of the material does not and must not imply any endorsement by APS.
6. APS does not imply, purport or intend to grant permission to reuse materials to which it does not hold copyright. It is the requestor's sole responsibility to ensure the licensed material is original to APS and does not contain the copyright of another entity, and that the copyright notice of the figure, photograph, cover or table does not indicate it was reprinted by APS with permission from another source.
7. The permission granted herein is personal to the Requestor for the use specified and is not transferable or assignable without express written permission of APS. This license may not be amended except in writing by APS.
8. You may not alter, edit or modify the material in any manner.
9. You may translate the materials only when translation rights have been granted.
10. APS is not responsible for any errors or omissions due to translation.
11. You may not use the material for promotional, sales, advertising or marketing purposes.
12. The foregoing license shall not take effect unless and until APS or its agent, Aptara, receives payment in full in accordance with Aptara Billing and Payment Terms and Conditions, which are incorporated herein by reference.
13. Should the terms of this license be violated at any time, APS or Aptara may revoke the license with no refund to you and seek relief to the fullest extent of the laws of the USA. Official written notice will be made using the contact information provided with the permission request. Failure to receive such notice will not nullify revocation of the permission.
14. APS reserves all rights not specifically granted herein.
15. This document, including the Aptara Billing and Payment Terms and Conditions, shall be the entire agreement between the parties relating to the subject matter hereof.

Permission to reuse Fig. 1.7

USC UNIVERSIDADE DE SANTIAGO DE COMPOSTELA

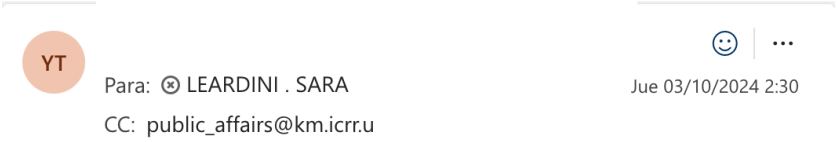

YT

Para: LEARDINI . SARA

Jue 03/10/2024 2:30

CC: public_affairs@km.icrr.u

Dear Sara,

Thank you for your email.

We are pleased to grant permission for you to use the image for your project.

Please provide these copyright;
Kamioka Observatory, ICRR(Institute for Cosmic Ray Research), The University of Tokyo

Permission to reuse Fig. 1.8c. The copyright belongs to Kamioka Observatory, ICRR(Institute for Cosmic Ray Research), The University of Tokyo.

AS

Alan Stonebraker<

Para: LEARDINI SARA <

;>

Mié 03/04/2024 18:11

Dear Sara,

Thank you for your inquiry. You have permission to use this image free of charge; please cite it in the same way that it appears on the website ("APS/Alan Stonebraker").

Permission to reuse Fig. 1.8e. The copyright belongs to APS/Alan Stonebraker.

USC UNIVERSIDADE DE SANTIAGO DE COMPOSTELA

SPRINGER NATURE LICENSE
TERMS AND CONDITIONS

Oct 03, 2024

This Agreement between Sara Leardini / university of Santiago de Compostela ("You") and Springer Nature ("Springer Nature") consists of your license details and the terms and conditions provided by Springer Nature and Copyright Clearance Center.

License Number	5881301002086
License date	Oct 03, 2024
Licensed Content Publisher	Springer Nature
Licensed Content Publication	Springer eBook
Licensed Content Title	Passage of Radiation Through Matter
Licensed Content Author	Dr. William R. Leo
Licensed Content Date	Jan 1, 1994
Type of Use	Thesis/Dissertation
Requestor type	academic/university or research institute
Format	electronic
Portion	figures/tables/illustrations
Number of figures/tables/illustrations	1
Will you be translating?	no
Circulation/distribution	200 - 499
Author of this Springer Nature content	no
Title of new work	NEW DETECTION CONCEPTS IN NOBLE-ELEMENT TPCS
Institution name	University of Santiago de Compostela
Expected presentation date	Dec 2024
Portions	Fig. 2.18
The Requesting Person / Organization to Appear on the License	Sara Leardini / university of Santiago de Compostela
Requestor Location	Santiago De Compostela, A Coruña Spain Attn: Sara Leardini
Billing Type	Invoice
Billing Address	
Total	0.00 EUR

Permission to reuse Fig. 2.1 right

License Number	5881310817237
License date	Oct 03, 2024

Printable Details

Licensed Content

Licensed Content Publisher	Elsevier
Licensed Content Publication	Nuclear Instruments and Methods in Physics Research Section A: Accelerators, Spectrometers, Detectors and Associated Equipment
Licensed Content Title	Microscopic simulation of xenon-based optical TPCs in the presence of molecular additives
Licensed Content Author	C.D.R. Azevedo,D. González-Díaz,S.F. Biagi,C.A.B. Oliveira,C.A.O. Henriques,J. Escada,F. Monrabal,J.J. Gómez-Cadenas,V. Álvarez,J.M. Benlloch-Rodríguez,F.I.G.M. Borges,A. Botas,S. Cárcel,J.V. Carrión,S. Cebrián,C.A.N. Conde,J. Díaz,M. Diesburg et al.
Licensed Content Date	Jan 1, 2018
Licensed Content Volume	877
Licensed Content Issue	n/a
Licensed Content Pages	16

Order Details

Type of Use	reuse in a thesis/dissertation
Portion	figures/tables/illustrations
Number of figures/tables/illustrations	2
Format	electronic
Are you the author of this Elsevier article?	No
Will you be translating?	No

About Your Work

Title of new work	NEW DETECTION CONCEPTS IN NOBLE-ELEMENT TPCS
Institution name	University of Santiago de Compostela
Expected presentation date	Dec 2024

Additional Data

Portions	Fig 1, Fig 2(bottom)
The Requesting Person / Organization to Appear on the License	Sara Leardini/university of Santiago de Compostela

Requestor Location

Requestor Location

Attn: Sara Leardini

Tax Details

Publisher Tax ID	GB 494 6272 12

Permission to reuse Fig. 2.3

USC UNIVERSIDADE DE SANTIAGO DE COMPOSTELA

License Number	5881311376622
License date	Oct 03, 2024

Printable Details

Licensed Content

Licensed Content Publisher	Elsevier
Licensed Content Publication	Nuclear Instruments and Methods in Physics Research
Licensed Content Title	Time dependence of the recombination luminescence from high-pressure argon, krypton and xenon excited by alpha particles
Licensed Content Author	Masayo Suzuki,Jian-zhi Ruan(Gen),Shinzou Kubota
Licensed Content Date	Feb 1, 1982
Licensed Content Volume	192
Licensed Content Issue	2-3
Licensed Content Pages	10

Order Details

Type of Use	reuse in a thesis/dissertation
Portion	figures/tables/illustrations
Number of figures/tables/illustrations	1
Format	electronic
Are you the author of this Elsevier article?	No
Will you be translating?	No

About Your Work

Title of new work	NEW DETECTION CONCEPTS IN NOBLE-ELEMENT TPCS
Institution name	University of Santiago de Compostela
Expected presentation date	Dec 2024

Additional Data

Portions	Fig 3 bottom
The Requesting Person / Organization to Appear on the License	Sara Leardini/university of Santiago de Compostela

Permission to reuse Fig. 2.4b

License Number	5881320409049
License date	Oct 03, 2024

Printable Details

Licensed Content

Licensed Content Publisher	Elsevier
Licensed Content Publication	Nuclear Instruments and Methods in Physics Research Section A: Accelerators, Spectrometers, Detectors and Associated Equipment
Licensed Content Title	The GEM scintillation in He–CF4, Ar–CF4, Ar–TEA and Xe–TEA mixtures
Licensed Content Author	M.M.F.R. Fraga,F.A.F. Fraga,S.T.G. Fetal,L.M.S. Margato,R.Ferreira Marques,A.J.P.L. Policarpo
Licensed Content Date	May 21, 2003
Licensed Content Volume	504
Licensed Content Issue	1-3
Licensed Content Pages	5

Order Details

Type of Use	reuse in a thesis/dissertation
Portion	figures/tables/illustrations
Number of figures/tables/illustrations	1
Format	electronic
Are you the author of this Elsevier article?	No
Will you be translating?	No

About Your Work

Title of new work	NEW DETECTION CONCEPTS IN NOBLE-ELEMENT TPCS
Institution name	University of Santiago de Compostela
Expected presentation date	Dec 2024

Additional Data

Portions	Fig 3
The Requesting Person / Organization to Appear on the License	Sara Leardini/university of Santiago de Compostela

Permission to reuse Fig. 2.6 left

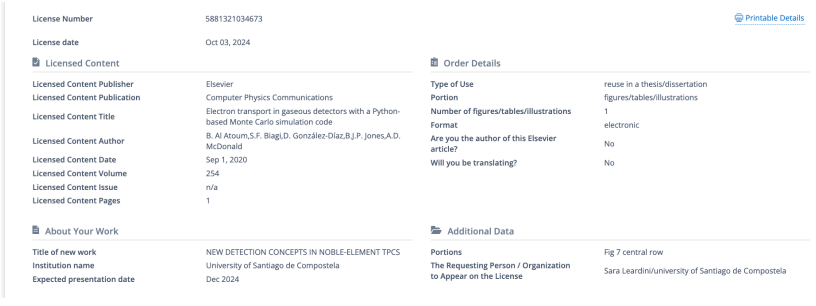

License Number	5881321034673
License date	Oct 03, 2024

Printable Details

Licensed Content

Licensed Content Publisher	Elsevier
Licensed Content Publication	Computer Physics Communications
Licensed Content Title	Electron transport in gaseous detectors with a Python-based Monte Carlo simulation code
Licensed Content Author	B. Al Atoum,S.F. Biagi,D. González-Díaz,B.J.P. Jones,A.D. McDonald
Licensed Content Date	Sep 1, 2020
Licensed Content Volume	254
Licensed Content Issue	n/a
Licensed Content Pages	1

Order Details

Type of Use	reuse in a thesis/dissertation
Portion	figures/tables/illustrations
Number of figures/tables/illustrations	1
Format	electronic
Are you the author of this Elsevier article?	No
Will you be translating?	No

About Your Work

Title of new work	NEW DETECTION CONCEPTS IN NOBLE-ELEMENT TPCS
Institution name	University of Santiago de Compostela
Expected presentation date	Dec 2024

Additional Data

Portions	Fig 7 central row
The Requesting Person / Organization to Appear on the License	Sara Leardini/university of Santiago de Compostela

Permission to reuse Fig. 2.7

USC UNIVERSIDADE DE SANTIAGO DE COMPOSTELA

De: Robin Noorda < .nl>
Enviado: miércoles, 25 de septiembre de 2024 13:50
Para: LEARDINI . SARA < .es>

Hi Sara,

Hereby permission to use the Kirlian photo for your PhD thesis under the condition of mentioning:
Kirlian photo: Robin Noorda, Tropism Art & Science Collective.

Permission to reuse Fig. 3.1a

License Number	5881431448865		Printable Details
License date	Oct 03, 2024		
Licensed Content		**Order Details**	
Licensed Content Publisher	John Wiley and Sons	Type of use	Dissertation/Thesis
Licensed Content Publication	Journal of Geophysical Research: Atmospheres	Requestor type	University/Academic
Licensed Content Title	Prodigious Amounts of Hydrogen Oxides Generated by Corona Discharges on Tree Leaves	Format	Electronic
Licensed Content Author	J. M. Jenkins, G. A. Olson, P. J. McFarland, et al	Portion	Figure/table
Licensed Content Date	Aug 16, 2022	Number of figures/tables	1
Licensed Content Volume	127	Will you be translating?	No
Licensed Content Issue	16		
Licensed Content Pages	12		
About Your Work		**Additional Data**	
Title of new work	NEW DETECTION CONCEPTS IN NOBLE-ELEMENT TPCS	Portions	Fig 1A
Institution name	University of Santiago de Compostela	The Requesting Person / Organization to Appear on the License	Sara Leardini/university of Santiago de Compostela
Expected presentation date	Dec 2024		

Permission to reuse Fig. 3.1b

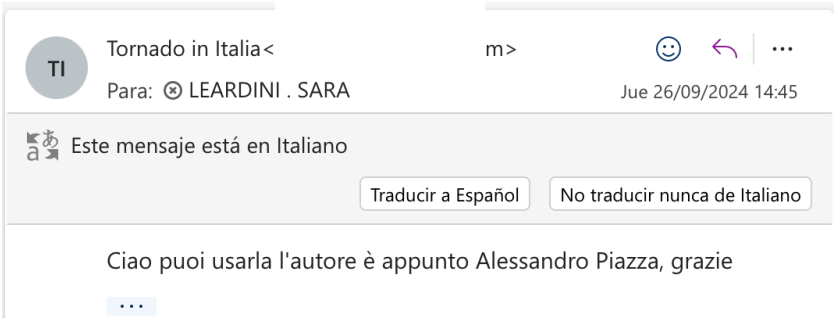

Permission to reuse Fig. 3.1c

USC UNIVERSIDADE DE SANTIAGO DE COMPOSTELA

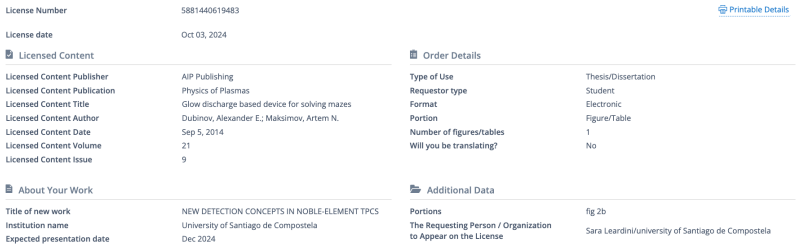

License Number	5881440619483
License date	Oct 03, 2024

Printable Details

Licensed Content

Licensed Content Publisher	AIP Publishing
Licensed Content Publication	Physics of Plasmas
Licensed Content Title	Glow discharge based device for solving mazes
Licensed Content Author	Dubinov, Alexander E.; Maksimov, Artem N.
Licensed Content Date	Sep 5, 2014
Licensed Content Volume	21
Licensed Content Issue	9

Order Details

Type of Use	Thesis/Dissertation
Requestor type	Student
Format	Electronic
Portion	Figure/Table
Number of figures/tables	1
Will you be translating?	No

About Your Work

Title of new work	NEW DETECTION CONCEPTS IN NOBLE-ELEMENT TPCS
Institution name	University of Santiago de Compostela
Expected presentation date	Dec 2024

Additional Data

Portions	fig 2b
The Requesting Person / Organization to Appear on the License	Sara Leardini/university of Santiago de Compostela

Permission to reuse Fig. 3.1d

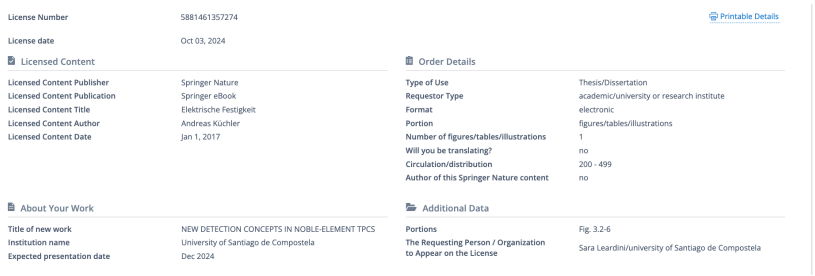

License Number	5881461357274
License date	Oct 03, 2024

Printable Details

Licensed Content

Licensed Content Publisher	Springer Nature
Licensed Content Publication	Springer eBook
Licensed Content Title	Elektrische Festigkeit
Licensed Content Author	Andreas Küchler
Licensed Content Date	Jan 1, 2017

Order Details

Type of Use	Thesis/Dissertation
Requestor Type	academic/university or research institute
Format	electronic
Portion	figures/tables/illustrations
Number of figures/tables/illustrations	1
Will you be translating?	no
Circulation/distribution	200 - 499
Author of this Springer Nature content	no

About Your Work

Title of new work	NEW DETECTION CONCEPTS IN NOBLE-ELEMENT TPCS
Institution name	University of Santiago de Compostela
Expected presentation date	Dec 2024

Additional Data

Portions	Fig. 3.2-6
The Requesting Person / Organization to Appear on the License	Sara Leardini/university of Santiago de Compostela

Permission to reuse Fig. 3.2

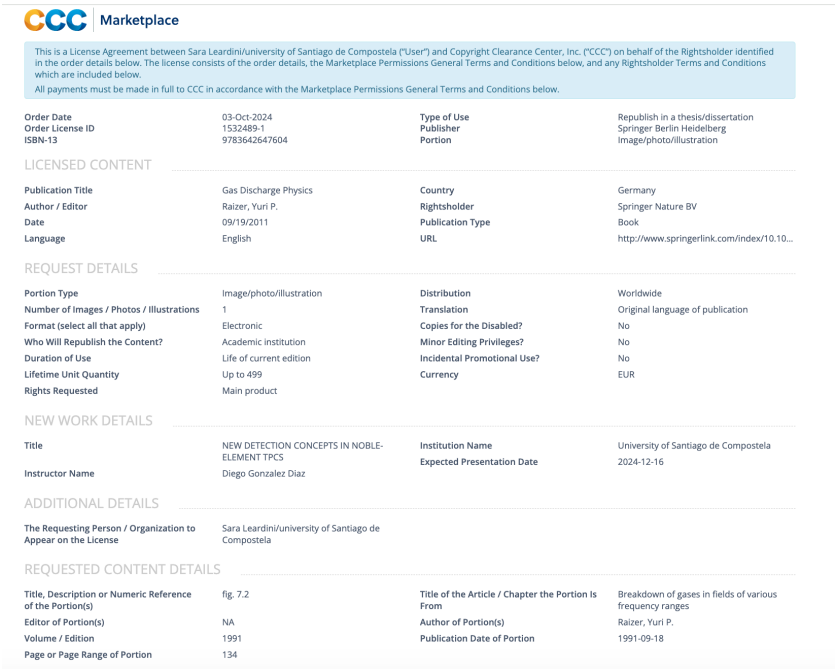

CCC Marketplace

This is a License Agreement between Sara Leardini/university of Santiago de Compostela ("User") and Copyright Clearance Center, Inc. ("CCC") on behalf of the Rightsholder identified in the order details below. The license consists of the order details, the Marketplace Permissions General Terms and Conditions below, and any Rightsholder Terms and Conditions which are included below.

All payments must be made in full to CCC in accordance with the Marketplace Permissions General Terms and Conditions below.

Order Date	03-Oct-2024	Type of Use	Republish in a thesis/dissertation
Order License ID	1532489-1	Publisher	Springer Berlin Heidelberg
ISBN-13	9783642647604	Portion	image/photo/illustration

LICENSED CONTENT

Publication Title	Gas Discharge Physics	Country	Germany
Author / Editor	Raizer, Yuri P.	Rightsholder	Springer Nature BV
Date	09/19/2011	Publication Type	Book
Language	English	URL	http://www.springerlink.com/index/10.10...

REQUEST DETAILS

Portion Type	Image/photo/illustration	Distribution	Worldwide
Number of Images / Photos / Illustrations	1	Translation	Original language of publication
Format (select all that apply)	Electronic	Copies for the Disabled?	No
Who Will Republish the Content?	Academic institution	Minor Editing Privileges?	No
Duration of Use	Life of current edition	Incidental Promotional Use?	No
Lifetime Unit Quantity	Up to 499	Currency	EUR
Rights Requested	Main product		

NEW WORK DETAILS

Title	NEW DETECTION CONCEPTS IN NOBLE-ELEMENT TPCS	Institution Name	University of Santiago de Compostela
Instructor Name	Diego Gonzalez Diaz	Expected Presentation Date	2024-12-16

ADDITIONAL DETAILS

The Requesting Person / Organization to Appear on the License	Sara Leardini/university of Santiago de Compostela

REQUESTED CONTENT DETAILS

Title, Description or Numeric Reference of the Portion(s)	fig. 7.2	Title of the Article / Chapter the Portion Is From	Breakdown of gases in fields of various frequency ranges
Editor of Portion(s)	NA	Author of Portion(s)	Raizer, Yuri P.
Volume / Edition	1991	Publication Date of Portion	1991-09-18
Page or Page Range of Portion	134		

Permission to reuse Fig. 3.3

USC UNIVERSIDADE DE SANTIAGO DE COMPOSTELA

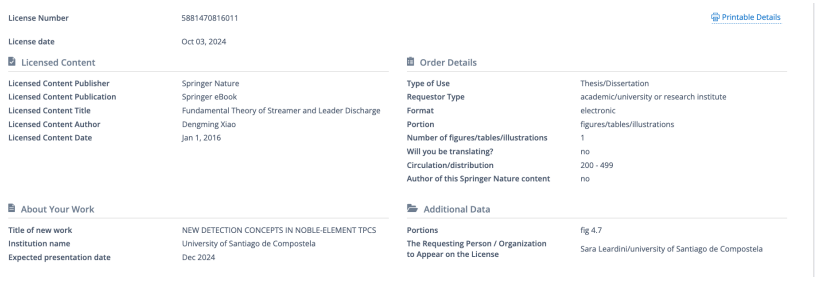

License Number	5881470816011		Printable Details
License date	Oct 03, 2024		
Licensed Content		**Order Details**	
Licensed Content Publisher	Springer Nature	Type of Use	Thesis/Dissertation
Licensed Content Publication	Springer eBook	Requestor Type	academic/university or research institute
Licensed Content Title	Fundamental Theory of Streamer and Leader Discharge	Format	electronic
Licensed Content Author	Dengming Xiao	Portion	figures/tables/illustrations
Licensed Content Date	Jan 1, 2016	Number of figures/tables/illustrations	1
		Will you be translating?	no
		Circulation/distribution	200 - 499
		Author of this Springer Nature content	no
About Your Work		**Additional Data**	
Title of new work	NEW DETECTION CONCEPTS IN NOBLE-ELEMENT TPCS	Portions	fig 4.7
Institution name	University of Santiago de Compostela	The Requesting Person / Organization to Appear on the License	Sara Leardini/university of Santiago de Compostela
Expected presentation date	Dec 2024		

Permission to reuse Fig. 3.4

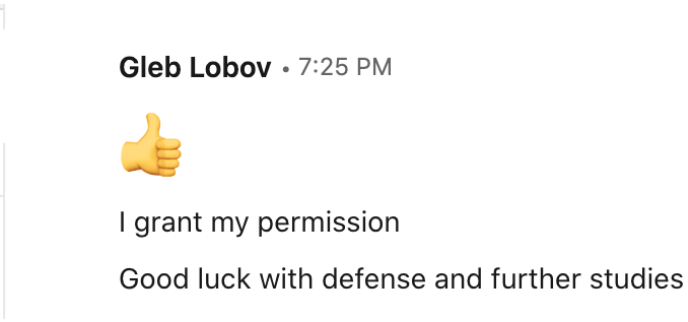

Permission to reuse Fig. 3.6a

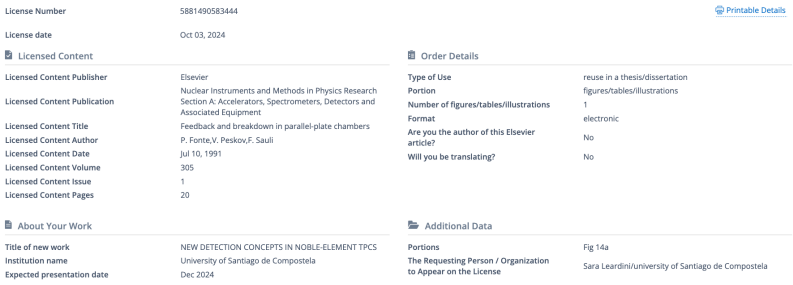

License Number	5881490583444		Printable Details
License date	Oct 03, 2024		
Licensed Content		**Order Details**	
Licensed Content Publisher	Elsevier	Type of Use	reuse in a thesis/dissertation
Licensed Content Publication	Nuclear Instruments and Methods in Physics Research Section A: Accelerators, Spectrometers, Detectors and Associated Equipment	Portion	figures/tables/illustrations
		Number of figures/tables/illustrations	1
Licensed Content Title	Feedback and breakdown in parallel-plate chambers	Format	electronic
Licensed Content Author	P. Fonte,V. Peskov,F. Sauli	Are you the author of this Elsevier article?	No
Licensed Content Date	Jul 10, 1991	Will you be translating?	No
Licensed Content Volume	305		
Licensed Content Issue	1		
Licensed Content Pages	20		
About Your Work		**Additional Data**	
Title of new work	NEW DETECTION CONCEPTS IN NOBLE-ELEMENT TPCS	Portions	Fig 14a
Institution name	University of Santiago de Compostela	The Requesting Person / Organization to Appear on the License	Sara Leardini/university of Santiago de Compostela
Expected presentation date	Dec 2024		

Permission to reuse Fig. 3.8

USC UNIVERSIDADE DE SANTIAGO DE COMPOSTELA

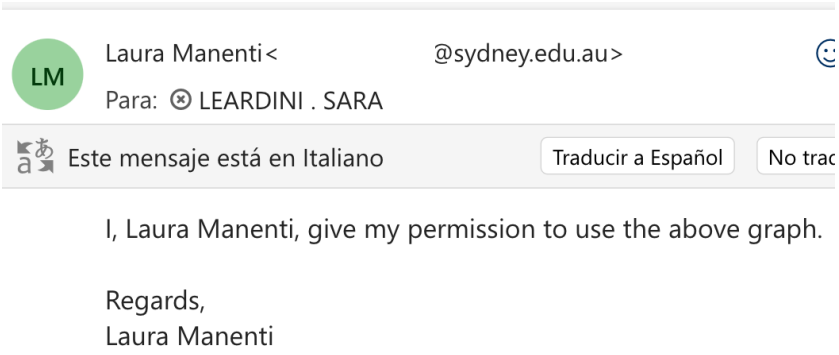

LM

Laura Manenti< @sydney.edu.au>

Para: ⊗ LEARDINI . SARA

Este mensaje está en Italiano Traducir a Español No trad

I, Laura Manenti, give my permission to use the above graph.

Regards,
Laura Manenti

Permission to reuse Fig. 4.2

License Number	58819801679 82		Printable Details
License date	Oct 04, 2024		
Licensed Content		**Order Details**	
Licensed Content Publisher	Elsevier	Type of Use	reuse in a thesis/dissertation
Licensed Content Publication	Nuclear Instruments and Methods in Physics Research Section A: Accelerators, Spectrometers, Detectors and Associated Equipment	Portion	figures/tables/illustrations
		Number of figures/tables/illustrations	1
Licensed Content Title	The Large Underground Xenon (LUX) experiment	Format	electronic
Licensed Content Author	D.S. Akerib,X. Bai,S. Bedikian,E. Bernard,A. Bernstein,A. Bolozdynya,A. Bradley,D. Byram,S.B. Cahn,C. Camp,M.C. Carmona-Benitez,D. Carr,J.J. Chapman,A. Chiller,C. Chiller,K. Clark,T. Classen,T. Coffey,A. Curioni,E. Dahl,S. Dazeley,L. de Viveiros et al.	Are you the author of this Elsevier article?	No
		Will you be translating?	No
Licensed Content Date	Mar 11, 2013		
Licensed Content Volume	704		
Licensed Content Issue	n/a		
Licensed Content Pages	16		
About Your Work		**Additional Data**	
Title of new work	NEW DETECTION CONCEPTS IN NOBLE-ELEMENT TPCS	Portions	Fig. 1
Institution name	University of Santiago de Compostela	The Requesting Person / Organization to Appear on the License	Sara Leardini/university of Santiago de Compostela
Expected presentation date	Dec 2024		

Permission to reuse Fig. 4.3d

License Number	5881981287061		Printable Details
License date	Oct 04, 2024		
Licensed Content		**Order Details**	
Licensed Content Publisher	Elsevier	Type of Use	reuse in a thesis/dissertation
Licensed Content Publication	Nuclear Instruments and Methods in Physics Research Section A: Accelerators, Spectrometers, Detectors and Associated Equipment	Portion	figures/tables/illustrations
		Number of figures/tables/illustrations	1
Licensed Content Title	A gating grid driver for time projection chambers	Format	electronic
Licensed Content Author	S. Tangwancharoen,W.G. Lynch,J. Barney,J. Estee,R. Shane,M.B. Tsang,Y. Zhang,T. Isobe,M. Kurata-Nishimura,T. Murakami,Z.G. Xiao,Y.F. Zhang	Are you the author of this Elsevier article?	No
		Will you be translating?	No
Licensed Content Date	1 May 2017		
Licensed Content Volume	853		
Licensed Content Issue	n/a		
Licensed Content Pages	9		
About Your Work		**Additional Data**	
Title of new work	NEW DETECTION CONCEPTS IN NOBLE-ELEMENT TPCS	Portions	Fig. 3
Institution name	University of Santiago de Compostela	The Requesting Person / Organization to Appear on the License	Sara Leardini/university of Santiago de Compostela
Expected presentation date	Dec 2024		

Permission to reuse Fig. 4.4center/right

USC UNIVERSIDADE DE SANTIAGO DE COMPOSTELA

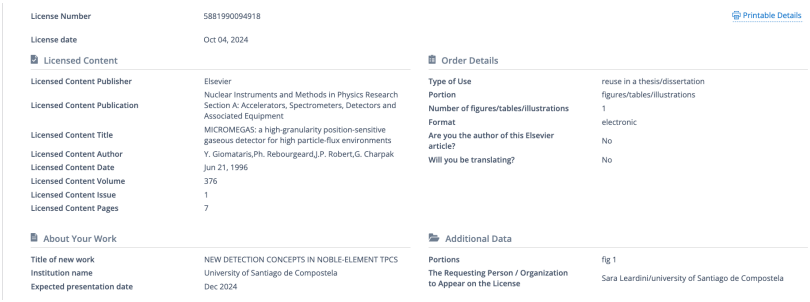

License Number	5881990094918
License date	Oct 04, 2024
Licensed Content	
Licensed Content Publisher	Elsevier
Licensed Content Publication	Nuclear Instruments and Methods in Physics Research Section A: Accelerators, Spectrometers, Detectors and Associated Equipment
Licensed Content Title	MICROMEGAS: a high-granularity position-sensitive gaseous detector for high particle-flux environments
Licensed Content Author	Y. Giomataris,Ph. Rebourgeard,J.P. Robert,G. Charpak
Licensed Content Date	Jun 21, 1996
Licensed Content Volume	376
Licensed Content Issue	1
Licensed Content Pages	7
Order Details	
Type of Use	reuse in a thesis/dissertation
Portion	figures/tables/illustrations
Number of figures/tables/illustrations	1
Format	electronic
Are you the author of this Elsevier article?	No
Will you be translating?	No
About Your Work	
Title of new work	NEW DETECTION CONCEPTS IN NOBLE-ELEMENT TPCS
Institution name	University of Santiago de Compostela
Expected presentation date	Dec 2024
Additional Data	
Portions	fig 1
The Requesting Person / Organization to Appear on the License	Sara Leardini/university of Santiago de Compostela

Permission to reuse Fig. 4.5 left

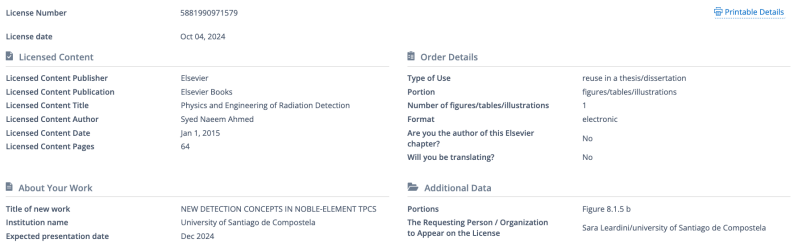

License Number	5881990971579
License date	Oct 04, 2024
Licensed Content	
Licensed Content Publisher	Elsevier
Licensed Content Publication	Elsevier Books
Licensed Content Title	Physics and Engineering of Radiation Detection
Licensed Content Author	Syed Naeem Ahmed
Licensed Content Date	Jan 1, 2015
Licensed Content Pages	64
Order Details	
Type of Use	reuse in a thesis/dissertation
Portion	figures/tables/illustrations
Number of figures/tables/illustrations	1
Format	electronic
Are you the author of this Elsevier chapter?	No
Will you be translating?	No
About Your Work	
Title of new work	NEW DETECTION CONCEPTS IN NOBLE-ELEMENT TPCS
Institution name	University of Santiago de Compostela
Expected presentation date	Dec 2024
Additional Data	
Portions	Figure 8.1.5 b
The Requesting Person / Organization to Appear on the License	Sara Leardini/university of Santiago de Compostela

Permission to reuse Fig. 4.6 left

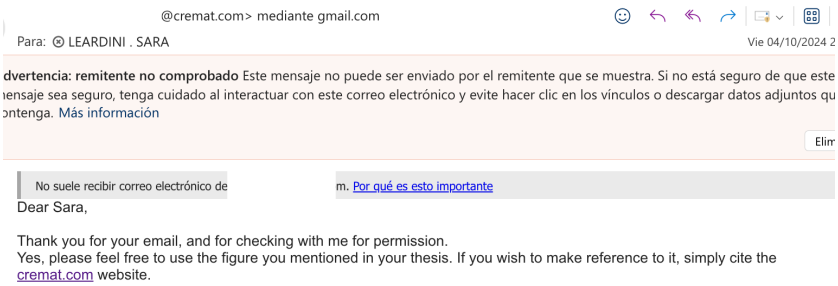

@cremat.com> mediante gmail.com

Para: LEARDINI . SARA Vie 04/10/2024 2

dvertencia: remitente no comprobado Este mensaje no puede ser enviado por el remitente que se muestra. Si no está seguro de que este ıensaje sea seguro, tenga cuidado al interactuar con este correo electrónico y evite hacer clic en los vínculos o descargar datos adjuntos qu ontenga. Más información

Elim

No suele recibir correo electrónico de m. Por qué es esto importante

Dear Sara,

Thank you for your email, and for checking with me for permission.
Yes, please feel free to use the figure you mentioned in your thesis. If you wish to make reference to it, simply cite the cremat.com website.

Permission to reuse Fig. 4.6 right

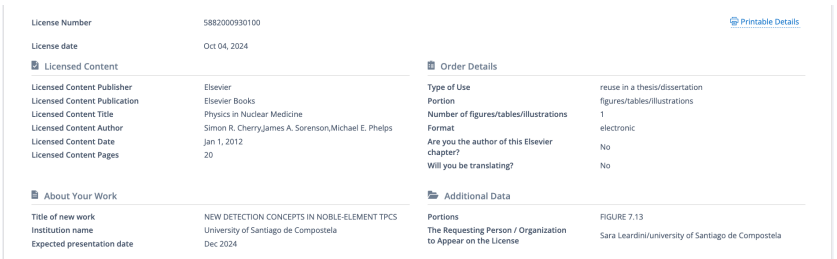

License Number	5882000930100
License date	Oct 04, 2024
Licensed Content	
Licensed Content Publisher	Elsevier
Licensed Content Publication	Elsevier Books
Licensed Content Title	Physics in Nuclear Medicine
Licensed Content Author	Simon R. Cherry,James A. Sorenson,Michael E. Phelps
Licensed Content Date	Jan 1, 2012
Licensed Content Pages	20
Order Details	
Type of Use	reuse in a thesis/dissertation
Portion	figures/tables/illustrations
Number of figures/tables/illustrations	1
Format	electronic
Are you the author of this Elsevier chapter?	No
Will you be translating?	No
About Your Work	
Title of new work	NEW DETECTION CONCEPTS IN NOBLE-ELEMENT TPCS
Institution name	University of Santiago de Compostela
Expected presentation date	Dec 2024
Additional Data	
Portions	FIGURE 7.13
The Requesting Person / Organization to Appear on the License	Sara Leardini/university of Santiago de Compostela

Permission to reuse Fig. 4.8 right

USC UNIVERSIDADE DE SANTIAGO DE COMPOSTELA

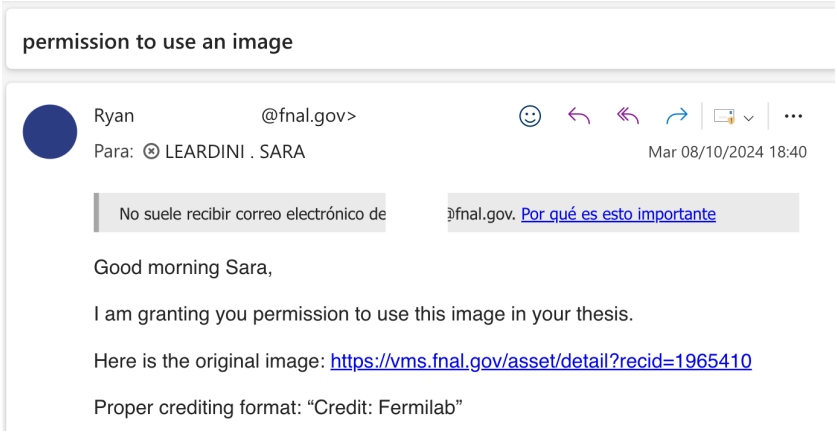
permission to use an image

Ryan @fnal.gov>

Para: LEARDINI . SARA

Mar 08/10/2024 18:40

No suele recibir correo electrónico de @fnal.gov. Por qué es esto importante

Good morning Sara,

I am granting you permission to use this image in your thesis.

Here is the original image: https://vms.fnal.gov/asset/detail?recid=1965410

Proper crediting format: “Credit: Fermilab”

Permission to reuse Fig. 4.10 top

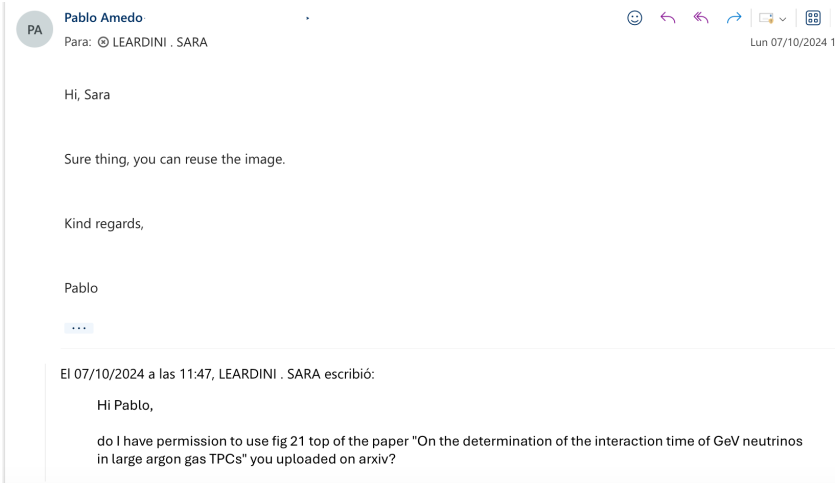
PA

Pablo Amedo

Para: LEARDINI . SARA

Lun 07/10/2024 1

Hi, Sara

Sure thing, you can reuse the image.

Kind regards,

Pablo

El 07/10/2024 a las 11:47, LEARDINI . SARA escribió:

Hi Pablo,

do I have permission to use fig 21 top of the paper "On the determination of the interaction time of GeV neutrinos in large argon gas TPCs" you uploaded on arxiv?

Permission to reuse Fig. 4.12 left

This is a License Agreement between Sara Leardini/university of Santiago de Compostela ("User") and Copyright Clearance Center, Inc. ("CCC") on behalf of the Rightsholder identified in the order details below. The license consists of the order details, the Marketplace Permissions General Terms and Conditions below, and any Rightsholder Terms and Conditions which are included below.

All payments must be made in full to CCC in accordance with the Marketplace Permissions General Terms and Conditions below.

Order Date	04-Oct-2024	**Type of Use**	Republish in a thesis/dissertation
Order License ID	1532814-1	**Publisher**	IOP Publishing
ISSN	1748-0221	**Portion**	Image/photo/illustration

LICENSED CONTENT

Publication Title	Journal of Instrumentation	**Country**	United Kingdom of Great Britain and Northern Ireland
Author / Editor	Institute of Physics (Great Britain), Institute of Physics Publishing., International School for Advanced Studies (Trieste, Italy)	**Rightsholder**	IOP Publishing, Ltd
		Publication Type	e-Journal
Date	01/01/2006	**URL**	http://www.iop.org/EJ/jinst/
Language	English		

REQUEST DETAILS

Portion Type	Image/photo/illustration	**Distribution**	Worldwide
Number of Images / Photos / Illustrations	1	**Translation**	Original language of publication
Format (select all that apply)	Electronic	**Copies for the Disabled?**	No
Who Will Republish the Content?	Academic institution	**Minor Editing Privileges?**	Yes
Duration of Use	Life of current edition	**Incidental Promotional Use?**	No
Lifetime Unit Quantity	Up to 499	**Currency**	EUR
Rights Requested	Main product		

NEW WORK DETAILS

Title	NEW DETECTION CONCEPTS IN NOBLE-ELEMENT TPCS	**Institution Name**	University of Santiago de Compostela
		Expected Presentation Date	2024-12-16
Instructor Name	Diego Gonzalez Diaz		

ADDITIONAL DETAILS

Order Reference Number	N/A	**The Requesting Person / Organization to Appear on the License**	Sara Leardini/university of Santiago de Compostela

REQUESTED CONTENT DETAILS

Title, Description or Numeric Reference of the Portion(s)	upper left fig.3	**Title of the Article / Chapter the Portion Is From**	Scintillation of Ar/CF4 mixtures: glass-THGEM characterization with 1% CF4 at 1-1.5 bar
Editor of Portion(s)	NA	**Author of Portion(s)**	P. Amedo
Volume / Edition	NA	**Issue, if Republishing an Article From a Serial**	N/A
Page or Page Range of Portion	4	**Publication Date of Portion**	2024-05-02

Permission to reuse Fig. 4.12right

This is a License Agreement between Sara Leardini/university of Santiago de Compostela ("User") and Copyright Clearance Center, Inc. ("CCC") on behalf of the Rightsholder identified in the order details below. The license consists of the order details, the Marketplace Permissions General Terms and Conditions below, and any Rightsholder Terms and Conditions which are included below.

All payments must be made in full to CCC in accordance with the Marketplace Permissions General Terms and Conditions below.

Order Date	05-Oct-2024	**Type of Use**	Republish in a thesis/dissertation
Order License ID	1532957-1	**Publisher**	IOP Publishing
ISSN	1748-0221	**Portion**	Image/photo/illustration

LICENSED CONTENT

Publication Title	Journal of Instrumentation	**Country**	United Kingdom of Great Britain and Northern Ireland
Author / Editor	Institute of Physics (Great Britain), Institute of Physics Publishing., International School for Advanced Studies (Trieste, Italy)	**Rightsholder**	IOP Publishing, Ltd
		Publication Type	e-Journal
Date	01/01/2006	**URL**	http://www.iop.org/EJ/jinst/
Language	English		

REQUEST DETAILS

Portion Type	Image/photo/illustration	**Distribution**	Worldwide
Number of Images / Photos / Illustrations	1	**Translation**	Original language of publication
Format (select all that apply)	Electronic	**Copies for the Disabled?**	No
Who Will Republish the Content?	Academic institution	**Minor Editing Privileges?**	Yes
Duration of Use	Life of current edition	**Incidental Promotional Use?**	No
Lifetime Unit Quantity	Up to 499	**Currency**	EUR
Rights Requested	Main product		

NEW WORK DETAILS

Title	NEW DETECTION CONCEPTS IN NOBLE-ELEMENT TPCS	**Institution Name**	University of Santiago de Compostela
		Expected Presentation Date	2024-12-16
Instructor Name	Diego Gonzalez Diaz		

ADDITIONAL DETAILS

Order Reference Number	N/A	**The Requesting Person / Organization to Appear on the License**	Sara Leardini/university of Santiago de Compostela

REQUESTED CONTENT DETAILS

Title, Description or Numeric Reference of the Portion(s)	Fig. 2 (top)	**Title of the Article / Chapter the Portion Is From**	High voltage insulation and gas absorption of polymers in high pressure argon and xenon gases
Editor of Portion(s)	NA	**Author of Portion(s)**	L. Rogers et al
Volume / Edition	NA	**Issue, if Republishing an Article From a Serial**	N/A
Page or Page Range of Portion	3	**Publication Date of Portion**	2018-10-01

Permission to reuse Fig. 5.1

USC UNIVERSIDADE DE SANTIAGO DE COMPOSTELA

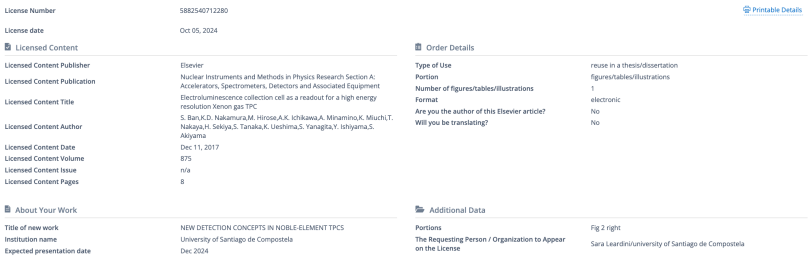

License Number	5882540712280		Printable Details
License date	Oct 05, 2024		
Licensed Content		**Order Details**	
Licensed Content Publisher	Elsevier	Type of Use	reuse in a thesis/dissertation
Licensed Content Publication	Nuclear Instruments and Methods in Physics Research Section A: Accelerators, Spectrometers, Detectors and Associated Equipment	Portion	figures/tables/illustrations
Licensed Content Title	Electroluminescence collection cell as a readout for a high energy resolution Xenon gas TPC	Number of figures/tables/illustrations	1
Licensed Content Author	S. Ban,K.D. Nakamura,M. Hirose,A.K. Ichikawa,A. Minamino,K. Miuchi,T. Nakaya,H. Sekiya,S. Tanaka,K. Ueshima,S. Yanagita,Y. Ishiyama,S. Akiyama	Format	electronic
Licensed Content Date	Dec 11, 2017	Are you the author of this Elsevier article?	No
Licensed Content Volume	875	Will you be translating?	No
Licensed Content Issue	n/a		
Licensed Content Pages	8		
About Your Work		**Additional Data**	
Title of new work	NEW DETECTION CONCEPTS IN NOBLE-ELEMENT TPCS	Portions	Fig 2 right
Institution name	University of Santiago de Compostela	The Requesting Person / Organization to Appear on the License	Sara Leardini/university of Santiago de Compostela
Expected presentation date	Dec 2024		

Permission to reuse Fig. 5.3

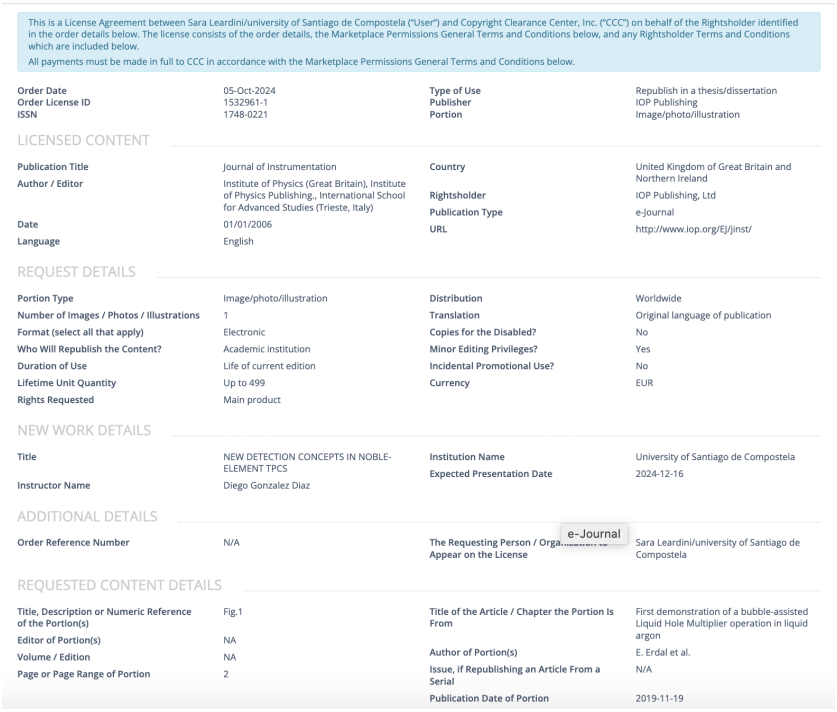

This is a License Agreement between Sara Leardini/university of Santiago de Compostela ("User") and Copyright Clearance Center, Inc. ("CCC") on behalf of the Rightsholder identified in the order details below. The license consists of the order details, the Marketplace Permissions General Terms and Conditions below, and any Rightsholder Terms and Conditions which are included below.

All payments must be made in full to CCC in accordance with the Marketplace Permissions General Terms and Conditions below.

Order Date	05-Oct-2024	Type of Use	Republish in a thesis/dissertation
Order License ID	1532961-1	Publisher	IOP Publishing
ISSN	1748-0221	Portion	Image/photo/illustration
LICENSED CONTENT			
Publication Title	Journal of Instrumentation	Country	United Kingdom of Great Britain and Northern Ireland
Author / Editor	Institute of Physics (Great Britain), Institute of Physics Publishing., International School for Advanced Studies (Trieste, Italy)	Rightsholder	IOP Publishing, Ltd
		Publication Type	e-Journal
Date	01/01/2006	URL	http://www.iop.org/EJ/jinst/
Language	English		
REQUEST DETAILS			
Portion Type	Image/photo/illustration	Distribution	Worldwide
Number of Images / Photos / Illustrations	1	Translation	Original language of publication
Format (select all that apply)	Electronic	Copies for the Disabled?	No
Who Will Republish the Content?	Academic institution	Minor Editing Privileges?	Yes
Duration of Use	Life of current edition	Incidental Promotional Use?	No
Lifetime Unit Quantity	Up to 499	Currency	EUR
Rights Requested	Main product		
NEW WORK DETAILS			
Title	NEW DETECTION CONCEPTS IN NOBLE-ELEMENT TPCS	Institution Name	University of Santiago de Compostela
		Expected Presentation Date	2024-12-16
Instructor Name	Diego Gonzalez Diaz		
ADDITIONAL DETAILS			
Order Reference Number	N/A	The Requesting Person / Orga...ation to Appear on the License	Sara Leardini/university of Santiago de Compostela
REQUESTED CONTENT DETAILS			
Title, Description or Numeric Reference of the Portion(s)	Fig.1	Title of the Article / Chapter the Portion Is From	First demonstration of a bubble-assisted Liquid Hole Multiplier operation in liquid argon
Editor of Portion(s)	NA		
Volume / Edition	NA	Author of Portion(s)	E. Erdal et al.
Page or Page Range of Portion	2	Issue, if Republishing an Article From a Serial	N/A
		Publication Date of Portion	2019-11-19

e-Journal

Permission to reuse Fig. 5.5 top left

USC UNIVERSIDADE DE SANTIAGO DE COMPOSTELA

This is a License Agreement between Sara Leardini/university of Santiago de Compostela ("User") and Copyright Clearance Center, Inc. ("CCC") on behalf of the Rightsholder identified in the order details below. The license consists of the order details, the Marketplace Permissions General Terms and Conditions below, and any Rightsholder Terms and Conditions which are included below.

All payments must be made in full to CCC in accordance with the Marketplace Permissions General Terms and Conditions below.

Order Date	05-Oct-2024	**Type of Use**	Republish in a thesis/dissertation
Order License ID	1532964-1	**Publisher**	IOP Publishing
ISSN	1748-0221	**Portion**	Image/photo/illustration

LICENSED CONTENT

Publication Title	Journal of Instrumentation	**Country**	United Kingdom of Great Britain and Northern Ireland
Author / Editor	Institute of Physics (Great Britain), Institute of Physics Publishing., International School for Advanced Studies (Trieste, Italy)	**Rightsholder**	IOP Publishing, Ltd
		Publication Type	e-Journal
Date	01/01/2006	**URL**	http://www.iop.org/EJ/jinst/
Language	English		

REQUEST DETAILS

Portion Type	Image/photo/illustration	**Distribution**	Worldwide
Number of Images / Photos / Illustrations	1	**Translation**	Original language of publication
Format (select all that apply)	Electronic	**Copies for the Disabled?**	No
Who Will Republish the Content?	Academic institution	**Minor Editing Privileges?**	Yes
Duration of Use	Life of current edition	**Incidental Promotional Use?**	No
Lifetime Unit Quantity	Up to 499	**Currency**	EUR
Rights Requested	Main product		

NEW WORK DETAILS

Title	NEW DETECTION CONCEPTS IN NOBLE-ELEMENT TPCS	**Institution Name**	University of Santiago de Compostela
		Expected Presentation Date	2024-12-16
Instructor Name	Diego Gonzalez Diaz		

ADDITIONAL DETAILS

Order Reference Number	N/A	**The Requesting Person / Organization to Appear on the License**	Sara Leardini/university of Santiago de Compostela

REQUESTED CONTENT DETAILS

Title, Description or Numeric Reference of the Portion(s)	Fig 4 c	**Title of the Article / Chapter the Portion Is From**	The International School for Advanced Studies (SISSA), find out more. Direct observation of bubble-assisted electroluminescence in liquid xenon
Editor of Portion(s)	NA		
Volume / Edition	NA	**Author of Portion(s)**	E. Erdal et al.
Page or Page Range of Portion	7	**Issue, if Republishing an Article From a Serial**	N/A
		Publication Date of Portion	2015-11-05

Permission to reuse Fig. 5.5 top right

This is a License Agreement between Sara Leardini/university of Santiago de Compostela ("User") and Copyright Clearance Center, Inc. ("CCC") on behalf of the Rightsholder identified in the order details below. The license consists of the order details, the Marketplace Permissions General Terms and Conditions below, and any Rightsholder Terms and Conditions which are included below.

All payments must be made in full to CCC in accordance with the Marketplace Permissions General Terms and Conditions below.

Order Date	05-Oct-2024	**Type of Use**	Republish in a thesis/dissertation
Order License ID	1532965-1	**Publisher**	IOP Publishing
ISSN	1748-0221	**Portion**	Image/photo/illustration

LICENSED CONTENT

Publication Title	Journal of Instrumentation	**Country**	United Kingdom of Great Britain and Northern Ireland
Author / Editor	Institute of Physics (Great Britain), Institute of Physics Publishing., International School for Advanced Studies (Trieste, Italy)	**Rightsholder**	IOP Publishing, Ltd
		Publication Type	e-Journal
Date	01/01/2006	**URL**	http://www.iop.org/EJ/jinst/
Language	English		

REQUEST DETAILS

Portion Type	Image/photo/illustration	**Distribution**	Worldwide
Number of Images / Photos / Illustrations	1	**Translation**	Original language of publication
Format (select all that apply)	Electronic	**Copies for the Disabled?**	No
Who Will Republish the Content?	Academic institution	**Minor Editing Privileges?**	Yes
Duration of Use	Life of current edition	**Incidental Promotional Use?**	No
Lifetime Unit Quantity	Up to 499	**Currency**	EUR
Rights Requested	Main product		

NEW WORK DETAILS

Title	NEW DETECTION CONCEPTS IN NOBLE-ELEMENT TPCS	**Institution Name**	University of Santiago de Compostela
		Expected Presentation Date	2024-12-16
Instructor Name	Diego Gonzalez Diaz		

ADDITIONAL DETAILS

Order Reference Number	N/A	**The Requesting Person / Organization to Appear on the License**	Sara Leardini/university of Santiago de Compostela

REQUESTED CONTENT DETAILS

Title, Description or Numeric Reference of the Portion(s)	fig. 6	**Title of the Article / Chapter the Portion Is From**	Bubble-assisted Liquid Hole Multipliers in LXe and LAr: towards "local dual-phase TPCs"
Editor of Portion(s)	NA		
Volume / Edition	NA	**Author of Portion(s)**	E. Erdal et al.
Page or Page Range of Portion	5	**Issue, if Republishing an Article From a Serial**	N/A
		Publication Date of Portion	2020-04-01

Permission to reuse Fig. 5.5 bottom

USC UNIVERSIDADE DE SANTIAGO DE COMPOSTELA

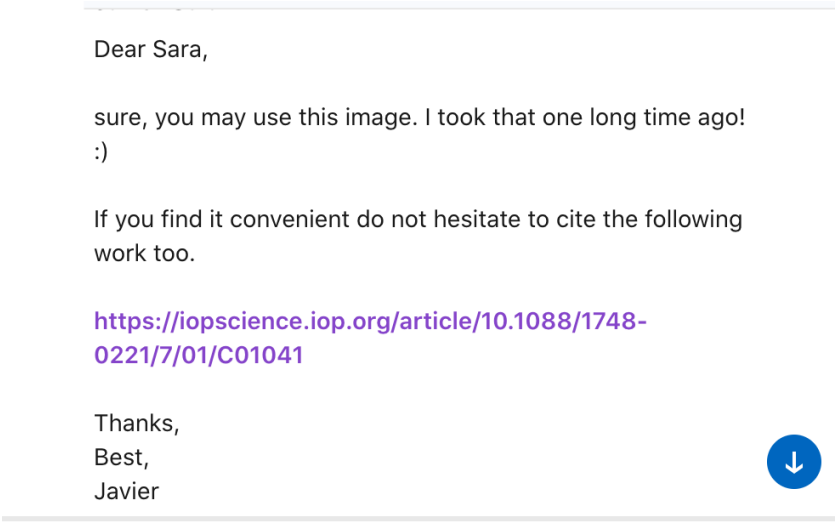

Dear Sara,

sure, you may use this image. I took that one long time ago! :)

If you find it convenient do not hesitate to cite the following work too.

https://iopscience.iop.org/article/10.1088/1748-0221/7/01/C01041

Thanks,
Best,
Javier

Permission to reuse Fig. 5.7 right

License Number	5882560980540
License date	Oct 05, 2024

Printable Details

Licensed Content

Licensed Content Publisher	John Wiley and Sons
Licensed Content Publication	Wiley Books
Licensed Content Title	Resistive Gaseous Detectors: Designs, Performance, and Perspectives
Licensed Content Author	Marcello Abbrescia,Paulo Fonte,Vladimir Peskov
Licensed Content Date	Jun 1, 2018
Licensed Content Pages	1

Order Details

Type of use	Dissertation/Thesis
Requestor type	University/Academic
Format	Electronic
Portion	Figure/table
Number of figures/tables	1
Will you be translating?	No

About Your Work

Title of new work	NEW DETECTION CONCEPTS IN NOBLE-ELEMENT TPCS
Institution name	University of Santiago de Compostela
Expected presentation date	Dec 2024

Additional Data

Portions	fig 1.14
The Requesting Person / Organization to Appear on the License	Sara Leardini/University of Santiago de Compostela

Permission to reuse Fig. 5.9

USC UNIVERSIDADE DE SANTIAGO DE COMPOSTELA

Permission to reuse Fig. 6.15

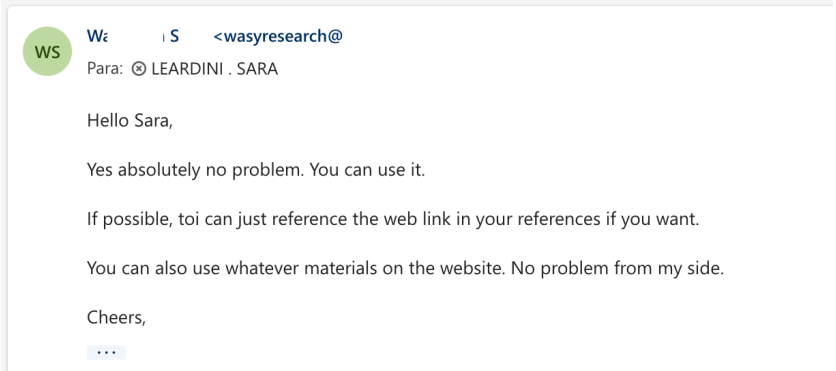

Permission to reuse the image in the conclusions section

USC UNIVERSIDADE DE SANTIAGO DE COMPOSTELA

Own images

Figures 1.2, 1.4, 1.8b, 1.10, 4.1, 4.7, 4.8 left, 5.8, 6.2, 6.38 left, 8.1, 8.2, 8.3 top, 8.4, 8.5, 8.6, 8.7, 8.8, are original works of the author.

All the other figures presented in this thesis reproduce contents from the papers of which I am co-author mentioned in the *List of publications* session. As already stated, the use of these figures is allowed under Creative Commons Attribution Licenses.

USC
UNIVERSIDADE DE SANTIAGO DE COMPOSTELA

Resumo

A busca de novas partículas sempre tivo que avanzar da man do desenvolvemento tecnolóxico, xa que a innovación e a tecnoloxía son fundamentais para a progresión no campo da física de partículas. Pasou moito tempo desde as primeiras cámaras de néboa, que foron pioneiras e permitiron descubrir partículas que son relativamente fáciles de detectar, como os positróns e os mións, que se convertiron en obxectivos importantes para os investigadores. Estes dispositivos baseábanse en imaxes visuais das trazas das partículas, que se formaban por partículas ionizadas que interactuaban co medio; aínda que eran innovadoras e unha gran novidade para a súa época, as cámaras de néboa tiñan limitacións inherentes en velocidade e resolución, o que levou a unha intensa búsqueda de métodos de detección máis eficaces e precisos. A chegada dos detectores electrónicos, por tanto, marcou un cambio revolucionario no campo da detección de partículas, pasando de sistemas de detección visual a sistemas baseados na carga eléctrica. Esta innovación permitiu a medición rápida e precisa das interaccións de partículas, aumentando significativamente as capacidades da física experimental e abrindo novas vías de investigación. Emerxeran varias tecnoloxías innovadoras, incluíndo cámaras de fío e cámaras de deriva, que son considerados precursores da Cámara de Proxección Temporal (TPC). Esta última é unha invención fundamental que combina a resolución espacial con capacidades de seguimento tridimensional, revolucionando así a forma en que se levan a cabo os experimentos na física de altas enerxías. Nos últimos anos, o enfoque da investigación en física de partículas cambiou notablemente cara ao descubrimento de eventos raros, como aqueles asociados coa materia escura ou as interaccións de neutrinos, que son fenómenos de gran interese na comunidade científica. Este cambio no enfoque da investigación require o desenvolvemento de novas tecnoloxías que sexan capaces de soportar TPCs que sexan máis grandes e máis sensibles. A medida que se intensifica a busca de fenómenos elusivos e difíciles de detectar, os investigadores están revisitando métodos de detección óptica, aproveitando novas técnicas de imaxe avanzadas e innovadoras que permiten unha mellor visualización dos eventos. Independentemente da elección do medio de lectura utilizado para os experimentos, a construción de tales experimentos é extremadamente desafiante e complexa, e require un enorme esforzo en I+D por parte dos equipos de investigación. O propósito deste traballo é abordar algúns problemas

USC
UNIVERSIDADE DE SANTIAGO DE COMPOSTELA

comúns que se atopan nos TPCs, como os estalos no detector, o manexo da interface gas-líquido en TPCs de fase dual, a detección de luz VUV e a produción de electroluminescencia con estruturas de amplificación a gran escala. Esta tese divídese da seguinte maneira. A primeira parte (capítulos 1-5) contén o estado da cuestión do coñecemento actual relevante para os TPCs. No Capítulo 1 ofrécese unha breve e concisa descrición da física dos neutrinos, xa que a detección de neutrinos é un dos principais obxectivos das búsquedas de Eventos Raros que están en marcha actualmente: os neutrinos son partículas elusivas detectadas por primeira vez na década de 1950, décadas despois de que a súa existencia fose hipotetizada para explicar o continuo espectro de enerxía dos electróns producidos a través da desintegración beta: se fose unha desintegración de dous corpos, o electrón debería ter unha enerxía fixa. Non obstante, atopar a solución ao enigma non foi fácil, xa que os neutrinos non interactúan nin a través da forza electromagnética nin da forza forte. Mesmo despois da súa descuberta, seguiron sorprendendo: inesperadamente, resultaron ter masa, o que obrigou aos investigadores a repensar como adaptar o Modelo Estándar da física de partículas ao novo feito; isto non é suficiente, xa que tanto a natureza desa masa como a xerarquía das diferentes masas dos neutrinos son, na actualidade, descoñecidas. Ademais, aprender a detectar o fondo cósmico de neutrinos (análogo ao fondo cósmico de microondas) podería proporcionar información sobre o universo cando só tiña un segundo de idade! Finalmente, moitos cren que os neutrinos teñen a clave para explicar por que no universo hai máis materia que antimateria: se a simetría de carga-paridade (CP) fose violada con suficiente intensidade polos neutrinos, unha cantidade inicial igual de materia e antimateria podería ter dado lugar á prevalencia actual da materia. No Capítulo 2 discútese a cintilación en elementos nobres, tanto en fase gasosa como en fase líquida, xa que o argón e o xenón, que poden ser utilizados puros ou en mesturas, son dos medios máis comúns e empregados nos TPCs grazas á alta transparencia á súa propia emisión de excímeros, ao alto rendemento de cintilación e á posibilidade de limpalos a niveis de alta pureza debido á súa baixa reactividade. O xenón é máis sensible aos retrocesos nucleares grazas ao seu núcleo máis pesado, non ten isótopo natural con tempos de decaemento problemáticos e posúe un espectro de lonxitude de onda máis longa, que é máis doado de detectar. Por outra banda, o argón é máis barato, e as interaccións nucleares elásticas con partículas de baixa masa son máis fáciles de detectar, xa que é un átomo máis lixeiro; o problema co isótopo natural ^{39}Ar, que constitúe unha fonte de ruído problemática, podería solucionarse recorrendo a argón subterráneo, cunha purificación química adicional. Para aproveitar ben estes elementos e extraer información física da súa interacción coas partículas de interese, é de suma importancia entender os seus mecanismos de cintilación. No Capítulo 3 preséntase a fascinante física do desprazamento de gas, un campo que inclúe fenómenos interesantes como os relámpagos e as fotografías de Kir-

USC UNIVERSIDADE DE SANTIAGO DE COMPOSTELA

lian, pero que tamén abarca eventos que son potencialmente destructivos para un detector, o que require unha coidada atención por parte dos investigadores. O Capítulo 4 describe os TPCs en detalle, afondando nas estruturas de amplificación dispoñibles e nas técnicas de lectura, que poden ser tanto electrónicas como ópticas. Como exemplos reais, presentaranse tamén dous experimentos de neutrinos: o primeiro é DUNE, un experimento multifuncional de neutrinos que está actualmente en construción nos Estados Unidos e que fará un uso extensivo de TPCs de argón líquido de fase simple. O segundo é NEXT, un experimento de desintegración beta dobre sen neutrinos que se está a levar a cabo en España, e que emprega un TPC de xenón gasoso a alta presión. O Capítulo 5, finalmente, explica algúns dos problemas comúns que se poden ter que resolver e afrontar nos TPCs para asegurar a súa eficacia. A segunda parte (capítulos 6-9) mostra as solucións propostas para algúns destes problemas: protección contra estalos para detectores que operan en condicións crioxénicas, discutido no Capítulo 6; unha configuración local de fase dual que supera o problema da interface, que se detalla no Capítulo 7; o estudo dunha mestura de gas que é capaz de cambiar a lonxitude de onda da luz VUV do argón a luz visible, manténdose unha adecuada quenched, que se analiza no Capítulo 8; e a caracterización dunha estrutura optimizada para electroluminescencia en TPCs gasosos, que se describe no Capítulo 9. En particular: Protección contra estoupidos: os detectores que operan en condicións de alta tensión poden sufrir estoupidos, que son eventos súbitos e inesperados que poden provocar unha operación inestable ou incluso danar permanentemente o propio detector. Unha solución coñecida e probada a temperatura ambiente é recorrer a materiais resistivos que proporcionen protección efectiva contra estoupidos; para este propósito específico, o material debe ter a resistividade adecuada, que se atopa dentro dun rango que vai desde 10 até 10^4 MΩ/sq para películas resistivas, e entre 10^9 e 10^12 Ω· cm para placas resistivas. Neste traballo, realizáronse estudos exhaustivos para buscar materiais analóxicos adecuados para a operación crioxénica, especialmente en argón líquido a temperaturas de 90 K; o foco centrouse en dous materiais específicos: carbono similar ao diamante (DLC) e cerámicas de Fe_2O_3/YSZ. As características e propiedades do DLC investigáronse a través do uso dun sistema de medición de propiedades físicas (PPMS) de Quantum Design, e dun criostato que foi feito na casa en atmosfera de hélio, conectado a un picoamperímetro para medicións precisas de resistividade e a un sensor PT100 para a monitorización continua de temperatura, estando mergullado nun baño de nitróxeno. As placas cerámicas medíronse a través do picoamperímetro e do PT100 en contacto directo co baño de nitróxeno para asegurar a precisión das medicións. As mostras adecuadas foron probadas dentro dun detector denominado WISArD, situado no Instituto Weizmann de Ciencia, na chamada configuración RWELL (para o material DLC) e na configuración RPWELL (para as cerámicas), na que o material resistivo está situado entre a estrutura de amplificación

USC UNIVERSIDADE DE SANTIAGO DE COMPOSTELA

(neste caso, un THGEM) e o ánodo de lectura. As medicións realizáronse a 90 K, en vapor de argón saturado, asegurando a pureza do argón a través da circulación continua do gas mediante un getter quente. A análise da caracterización dos materiais e da proba dentro do detector realizouse con scripts específicos programados en Python. Para todas as mostras que foron probadas, lograrouse unha ganancia superior á das configuracións anteriores (un THGEM e un THWELL) que utilizaban estruturas desprotexidas: coas configuracións THGEM e THWELL, a ganancia máxima foi de 6 e 8 respectivamente, mentres que coas RWELL e RPWELL a ganancia máxima foi de 30 para a primeira, e de 16 para a segunda. No caso da RWELL, tamén foi posible operar o detector de forma estable en presenza de estoupidos, o que resultaba completamente imposible coas estruturas desprotexidas, demostrando así a eficacia dos materiais utilizados para a protección.

Dual local de fase: nos últimos anos, realizáronse avances significativos no campo dos detectores de radiación de líquidos nobres, baseados no innovador concepto de multiplicadores de burbulla en líquidos (LHM, Liquid Hole-Multipliers). O concepto orixinal de LHM, que foi presentado no contexto das investigacións sobre eventos raros, foi proposto como un método para realizar unha detección combinada e simultánea dos electrones de ionización e dos fotóns de excitación primarios que se xeran pola interacción da radiación dentro de líquidos nobres en fase única. Na súa configuración actual, un detector que está baseado en LHM consiste nun eléctrodo perforado que está revestido de CsI (por exemplo, un GEM ou un THGEM) e que se mergulla no líquido noble, cunha burbulla de gas estable formada e atrapada por baixo. Unha pregunta que permanece sen resposta nos traballos mencionados anteriormente foi a discrepancia significativa de aproximadamente cinco veces entre a eficiencia de detección de fotóns medida (PDE) e a simulada, así como a resolución de enerxía que resultou ser inferior á esperada. Ademais, diferentes xeometrías de orificio foron observadas e comprobaron que afectaban de forma notable ao rendemento de electroluminescencia (EL). Unha hipótese que se propuxo para explicar estas observacións foi que un componente tangencial do campo eléctrico na interface burbulla-líquido podería obstaculizar de maneira considerable a transferencia de electrones entre as dúas fases: baixo esta suposición, algúns electrones serían guiados ao longo da interface cara ao eléctrodo, en lugar de cruzar a barreira líquido-gás como se esperaba inicialmente. En outro caso, a burbulla podería ter un punto de equilibrio no fondo do burato, non podendo así aproveitar a rexión de campo máis elevado para producir electroluminescencia. Para explorar esta idea en detalle, foi esencial investigar de forma exhaustiva o comportamento da interface, comprendendo, por exemplo, cales son as configuracións de equilibrio accesibles para a burbulla, cales son as propiedades da interface líquido-gás que se presentan dentro dos orificios do eléctrodo (como a forma do menisco e a protrusión) e como a presenza

USC UNIVERSIDADE DE SANTIAGO DE COMPOSTELA

dun campo eléctrico externo pode afectar ás propiedades da burbulla. Para isto, desenvolveron un modelo que se basea en ecuacións hidrostáticas e electrodinámicas, que foi simulado en COMSOL e validado a través de imaxes μCT. Para obter os puntos de equilibrio para a burbulla con este modelo, é fundamental contar co ángulo de contacto: a miña contribución a este traballo foi medir con precisión os ángulos de contacto da interface líquido-gás do argón con diferentes materiais, incluíndo cobre e FR4, dos cales están feitos os THGEMs. Para conseguir isto, as medicións realizáronse dentro do detector WISArD, que se atopa no Instituto Weizmann de Ciencia: as placas feitas de diferentes materiais mergulláronse en argón líquido, e formáronse burbullas estables de diferentes tamaños, que se capturaron e analizaron a través de imaxes de alta resolución para garantir a calidade dos datos obtidos. - Cambio de lonxitude de onda gasoso: A mezcla dun gas noble cun aditivo molecular específico pode resultar en significativas melloras, xa que pode reducir a difusión e estabilizar a operación do detector ao apagar o gas ou absorber fotóns VUV. Con todo, é importante destacar que algúns aditivos utilizados nesta aplicación poden causar que a sinal S1 desapareza, o que resulta na perda de información crítica sobre o tempo de interacción que é esencial para a precisión das medicións. As mesturas de Ar/CF_4 son especialmente efectivas e son capaces de manter a información S1 intacta, xa que permiten cambiar a lonxitude de onda da luz VUV emitida polos gases nobles a unha forma de luz visible, que é moito máis fácil de detectar e cuantificar utilizando sensores de luz comúns que se atopan na práctica habitual. Para comprender mellor a emisión e as características das mesturas de Ar/CF_4, realizouse un estudo espectroscópico detallado da cintilación secundaria no laboratorio GDD do CERN: un dispositivo que incluía unha placa de electrodos paralelos foi irradiado cunha pistola de raios X baixo diferentes condicións experimentais en termos de concentración de CF_4, presión do gas e campo eléctrico aplicado. Unha lente colimadora de precisión e unha fibra óptica dirixiron a luz emitida cara a un espectrómetro CCD, que foi previamente calibrado a través dunha lámpada visible e unha lámpada UV que emitían espectros coñecidos. A corrente no ánodo foi monitorizada de forma continua a través dun picoamperímetro, asegurando a precisión nas medicións. Os datos obtidos foron procesados posteriormente mediante scripts de Python, que facilitaron a análise detallada. O estudo confirmou que os espectros de cintilación secundaria mostran picos característicos na rexión UV, que proceden de estados excitados menos enerxéticos que os asociados á cintilación primaria, e mostraron unha baixa dependencia coidada da presión, do campo eléctrico e da concentración do gas. O ganho óptico obtido coa mestura de Ar/CF_4 na proporción 99/1 parece ideal para aplicacións como o TPC óptico que foi proposto para NDGAr, xa que proporciona un dos maiores ganhos medidos, ao tempo que preserva a alta pureza de argón que é fundamental para a aplicación; isto confirma resultados previos e estudos anteriores, que xa indicaban que unha concentración do 1% de

USC UNIVERSIDADE DE SANTIAGO DE COMPOSTELA

CF_4 é a opción ideal para maximizar o rendemento na aplicación práctica. Estructuras para electroluminescencia: Nas seccións de última tecnoloxía, explícase de forma amplamente detallada como a utilización da electroluminescencia resulta vantaxosa para unha ampla variedade de aplicacións, así como os numerosos retos técnicos que esta tecnoloxía presenta. Unha estrutura proposta, que pode superar eficazmente o problema da flexión das redes, ademais de proporcionar un excelente rendemento luminoso e eficiente, é o FAT-GEM (Multiplicador de Electroluminescencia Gasosa Transparente Asistido por Campo), que foi introducido por primeira vez na literatura científica en 2019. Desde ese momento, o concepto de FAT-GEM evolucionou para adaptar as estruturas e facelas ópticamente activas, xa sexa cun recubrimento de TPB que se aplica dentro dos orificios do FAT-GEM, ou cunha masa feita dun material que cambia de lonxitude de onda, que é o Nafatalato de Polietileno (PEN). As ideas para unha mellor transmisión da luz tamén floreceron, pensando en acoplar o concepto de cambiador de lonxitude de onda a eléctrodos transparentes, que se coñecen como S2 e S1 mellorados, e/ou a un reflector que tamén se considera mellorado (S2). Durante o meu doutoramento, caractericei diferentes conceptos e enfoques innovadores, e as seguintes sesións do meu traballo presentarán FAT-GEMs que están baseados en PMMA (Sec. 9.1) e FAT-GEMs que están baseados en PEN (Sec. 9.2). En particular, a Sec. 9.1 presentará un estudo de rendemento abrangente e detallado de diferentes estruturas FAT-GEM que están baseadas en PMMA, avaliadas baixo radiación de raios X de 5.9 keV, implicando diferentes procedementos de fabricación, así como distintos procesos (como engadir recubrimento de cambio de lonxitude de onda ou unha capa reflectante interna), diferentes xeometrías (en termos de tamaños de orificio), diferentes gases (incluíndo xenón e argón) e diferentes presións (que van de 2 a 10 bar); tamén se realizarán comparacións detalladas con simulacións e cunha simple configuración de dobre malla para ilustrar os resultados. A Sec. 9.2, por outro lado, describirá de maneira exhaustiva unha estrutura que está baseada en PEN, deseñada dunha maneira específica que maximiza a recollida de luz S1 e simplifica o procedemento de cambio de lonxitude de onda. O concepto e as súas posibles configuracións, o proceso de fabricación, unha simulación das principais propiedades ópticas (que inclúen rendemento e función de dispersión puntual) e as primeiras probas de funcionalidade dos dispositivos prototipo serán introducidos de forma clara e precisa. Para caracterizar as estruturas en termos de resolución de enerxía e rendemento luminoso, utilizouse un sistema altamente especializado equipado cunha fonte de ^{55}Fe que se situou no plano do cátodo. O recipiente encheuse adecuadamente con gas xenón ou argón a diferentes presións, e a luz foi recollida a través dunha cadea de PMT-preamplificador-amplificador-MCA. O PMT foi calibrado previamente cun LED verde e cun script de MATLAB que permitiu asegurar a precisión das medicións. O resto dos datos recollidos foron analizados mediante scripts de Python que facilitaron a interpretación

USC UNIVERSIDADE DE SANTIAGO DE COMPOSTELA

dos resultados. Coa estrutura recuberta de TPB, que estaba equipada cun reflector, foi posible lograr un rendemento óptico que se sitúa dentro do 18% do que se logrou cunha configuración de dobre malla en xenón a 4 bar (co campo eléctrico reducido por presión de 3.65 kV/cm). Espérase unha maior mellora na eficiencia ao refinar o acoplamento entre o reflector e o FAT-GEM. Para todas as estruturas analizadas, a resolución de enerxía extrapolada até a escala Q$\beta\beta$ de ^{136}Xe foi competitiva cos resultados obtidos con redes que se atopan na literatura científica actual. Os FAT-GEMs feitos de PEN foron probados tanto en xenón (a 2 bar) como en argón (a 4 bar), mostrando así capacidades prometedoras de cambio de lonxitude de onda que son moi interesantes para futuras investigacións. Os experimentos, a non ser que se especifique o contrario, foron realizados na USC. A tese remata cun capítulo sobre os resultados e conclusións.

USC
UNIVERSIDADE DE SANTIAGO DE COMPOSTELA

The field of Rare Event Searches can count on a great ally: the Time Projection Chamber (TPC). Despite all the technological advancements which already occurred, TPCs still have to adapt to more and more stringent requirements, as the experiments need more and more sensitivity. This implies a continuous R&D effort, which has driven this work, too. In particular, this thesis proposes some practical solutions to common problems encountered in TPCs: the development of tunable resistive materials capable of spark protection in cryogenic conditions, a local dual-phase concept (bubble-assisted LHMs), the study of secondary scintillation of Ar/CF4 mixtures, relevant, among others, for high pressure TPCs, and easily scalable, thick structures for electroluminescence with competitive light yields and energy resolutions.